Dynamics and Friction in Submicrometer Confining Systems

Dynamics and Friction in Submicrometer Confining Systems

Y. Braiman, Editor
Oak Ridge National Laboratory

J. M. Drake, Editor
Lubridyne Inc.

F. Family, Editor
Emory University

J. Klafter, Editor
Tel Aviv University

Dynamics and friction in submicrometer confining

Foreword

The ACS Symposium Series was first published in 1974 to provide a mechanism for publishing symposia quickly in book form. The purpose of the series is to publish timely, comprehensive books developed from ACS sponsored symposia based on current scientific research. Occasionally, books are developed from symposia sponsored by other organizations when the topic is of keen interest to the chemistry audience.

Before agreeing to publish a book, the proposed table of contents is reviewed for appropriate and comprehensive coverage and for interest to the audience. Some papers may be excluded to better focus the book; others may be added to provide comprehensiveness. When appropriate, overview or introductory chapters are added. Drafts of chapters are peer-reviewed prior to final acceptance or rejection, and manuscripts are prepared in camera-ready format.

As a rule, only original research papers and original review papers are included in the volumes. Verbatim reproductions of previously published papers are not accepted.

ACS Books Department

Preface

Recent years have witnessed a rapid development in nanoscience and nanotechnology. This remarkable growth has been fueled by the expectation that unusual properties of matter may become evident as the dimensions of the structural components of a device shrink. This book is based on papers presented at the American Chemical Society (ACS) national meeting symposium *Dynamics and Friction in Submicrometer Confining Systems,* held in Orlando, Florida, April 7–11, 2002. This book provides the most comprehensive and up-to-date review and original chapters on frictional dynamics at the nanoscale and also on fluid behavior under confinement. The chapters discuss some of the most recent advances in understanding and controlling dynamical properties of materials at the submicrometer scales. Some of the key questions addressed are the following: (1) redistribution and release of energy at the nanoscale due to confinement, (2) frictional dynamics and properties under confinement, and (3) control of frictional properties at the nanoscale level.

The primary topic of interest throughout the book is the question of how nearby surfaces of ultra-small geometries can force a system to behave in ways significantly different from its bulk behavior. The chapters in this book cover many important aspects of frictional behavior, including the origin of the stick–slip behavior, effects of thermal fluctuations, noise, and instabilities in boundary lubricants on the static and kinetic friction, and in situ control of friction. The dynamics of nanomechanical devices, which is a topic of major importance in the development of new technology at the atomic scale, is also discussed. Finally, a comprehensive analysis of liquid properties under confinement, including wetting, drainage, viscosity, and other dynamical properties, is presented.

All the chapters of this book are written in an accessible language and will be valuable for both graduate students and professionals, in the fields of chemistry, chemical engineering, mechanical engineering, materials science, and physics.

Y. Braiman
Center for Engineering Sciences Advanced Research
Computer Science and Mathematics Division
Oak Ridge National Laboratory
Oak Ridge, TN 37831

J. M. Drake
Lubridyne, Inc.
102 Leffler Hill Road
Flemington, NJ 08822

F. Family
Department of Physics
Emory University
Atlanta, GA 30322

J. Klafter
School of Chemistry
Tel Aviv University
Tel Aviv, Israel 69978

Dynamics and Friction in Submicrometer Confining Systems

Chapter 1

Scanning Tunneling Microscope–Quartz Crystal Microbalance Studies of "Real World" and Model Lubricants

J. Krim[1], M. Abdelmaksoud[1], B. Borovsky[1,2], and S. M. Winder[1]

[1]Physics Department, North Carolina State University, Box 8202, Raleigh, NC 27695
[2]Current address: Physics Department, Grinnell College, Grinnell, IA 50112

Abstract:

Applications of the Quartz Crystal Microbalance (QCM) for studies of tribology at atomistic time and length scales are described herein. Employing QCM as the sole technique, we report measurements on vapor phase lubricants for "real world" applications, and rare-gas systems that are of more fundamental interest. We also report on QCM measurements that have been recorded in conjunction with a Scanning Tunneling Microscope (STM). The QCM-STM apparatus allows unique and detailed investigations of a simple nanomechanical system formed by a contacting tip and surface. Both STM images of the contact and the response of the QCM are monitored throughout the course of the measurements, which are performed at realistic sliding speeds of over 1 m/s.

1

Introduction

Studies of the atomic-scale origins of friction and adhesion have undergone rapid progress in recent years with the development of new experimental and computational techniques for measuring and simulating tribological phenomena at atomic length and time scales.[1] Employing established technologies, such as ultra-high vacuum, for the preparation of crystalline samples. nanotribologists have been gathering information in situations where the nature of the contacting surfaces is determined in advance of the measurement. They have collectively measured friction forces per unit true contact area which span twelve orders of magnitude,[1] with no wear or damage occurring at the sliding interface. Faster computers have in turn allowed large scale molecular dynamics (MD) simulations of condensed systems to be performed for physically significant time periods, enabling numerical results to be increasingly comparable to experiment.[2]

If the precise nature of the contacting asperities between macroscopic objects in sliding contact could be determined (such studies do in fact represent an area of high research activity within the tribological community), then the results of nanotribological studies could begin to be directly implemented into mainstream tribological considerations. Meanwhile, the results are most applicable to friction at the interface between liquid and solid materials,[3,4] where the complicating factors associated with asperity contacts are less of an issue, and to the MEMS community,[5] where machine components with astoundingly small dimensions are rapidly approaching the length scales routinely probed by the nanotribological community. Indeed, solid surface nanocontacts abound among MEMS devices, and a myriad of device complications and failures are associated with their friction, adhesive and wear characteristics.[6] Because each of these contact areas is small, perhaps a few tens of atoms in extent,[7] both the topology and the mechanics of the contacting asperities must be investigated at the atomic scale in order to optimize device performance.

We describe herein how the Quartz Crystal Microbalance (QCM) is applied for studies of tribology at atomistic length and time scales. Examples of measurements employing QCM as the sole technique are first described, followed by examples recorded by means of a Scanning Tunneling Microscope (STM) operating in conjunction with the QCM. The STN allows a single asperity contact to be formed, and allows the buried contact to be imaged in both stationary and sliding conditions. The microbalance, whose surface is oscillating in transverse shear motion at speeds near 1 m/s, can be employed to measure the uptake rate and frictional properties of adsorbed lubricant species. The STM-QCM combination [8,9] allows access to a range of contact pressures and sliding speeds that traditional nanotribological instruments, such as the Atomic Force Microscope (AFM) and the Surface Forces Apparatus (SFA), fail to access. Furthermore, the use of STM avoids the problem of jump-to-contact associated with AFM, allowing the applied normal force to be varied continuously in a controlled fashion.

The Quartz Crystal Microbalance

The versatility of the QCM makes it an important experimental tool for studying a myriad of physical phenomena [10], including tribology, at atomistic length and time scales. It was used for decades, for microweighing purposes. before being adapted for friction measurements in 1986-88 by Widom and Krim. [11-14] A QCM consists of a single crystal of quartz that oscillates in transverse shear motion with a quality factor Q near 105. The driving force (supplied by a Pierce oscillator circuit) has constant magnitude and is periodic with frequency f = 4 to 10 MHz, the series resonant frequency of the oscillator. A metal electrode is deposited in ultra-high vacuum conditions onto each major face of the QCM, the quartz itself being polished to better than optical flatness. In general, the (111) surfaces of metals are studied, characterized by Auger electron spectroscopy, x-ray diffraction, scanning tunneling microscopy, and the verticality of stepwise adsorption of xenon monolayers. We have also studied of adsorption on graphene layers that were synthesized on the surface of the metal electrodes.

Sliding friction measurements are carried out in situ by transferring the sample, within the ultra-high vacuum chamber, to a tip that can be cooled to as little as 4K, or alternatively heated to 450 C. Adsorption occurs under equilibrium conditions as adsorbate gas is admitted to the chamber. This produces a change in the resonant frequency of the microbalance that is proportional to the fraction of the mass of the condensed film that is able to track the oscillatory motion of the underlying substrate. (Sensitivities of tenths to hundredths of a monolayer are typical.) Since the condensation occurs under equilibrium conditions, the film thickness is dependent only on the vapor pressure of the adsorbate gas surrounding the sample. Under these conditions, there is a continuous exchange of gas and film-phase particles. Individual particles remain in the film phase for periods that are at least (and usually orders of magnitude longer) two orders of magnitude longer than the period of oscillation of the microbalance. An additional consequence of the equilibrium adsorption conditions is the prevention of three-dimensional droplet or crystal condensation at pressures less than the three-dimensional saturation pressure.

For the systems discussed here, the binding forces perpendicular to the surface are, at a minimum, 1014 times stronger than corresponding gravitational forces. "Popping up" out of the plane due to the shaking action of the substrate is therefore not expected to occur as it might in a system governed by gravitational forces. Strong perpendicular forces do not, however, prevent horizontal motion of the film, which is governed only by frictional forces that arise from substrate corrugation. The binding energy of the second monolayer is in many cases significantly lower than that of the first, [14] so that at sufficiently low temperature the second layer does not begin to form until the first is essentially complete. The formation of such discrete second and higher layers adjacent to the substrate is evidenced by a "stepwise" structure in the adsorption isotherm, present only on highly uniform substrates.

The frequency and amplitude of a QCM are dependent on a variety of physical phenomena (temperature. ambient pressure, etc.). [15] The measurements reported here were recorded in controlled conditions that, unless otherwise noted, reflect contributions to frequency and amplitude shifts attributable uniquely to film slippage phenomenon.

Frequency and vibrational amplitude shifts that occur when a film adsorbs onto the surface electrode of the QCM are in general recorded simultaneously either as a function of pressure or time. Amplitude shifts are due to frictional shear forces exerted on the surface electrode by the adsorbed film (or alternatively by a three dimensional vapor or fluid phase). The microbalance in its present arrangement can detect shear forces in excess of 2.5 x 10-7 N. Characteristic slip times τ, and friction coefficients (i.e. shear stresses per unit velocity) η, are determined via:[12-14]

$$\delta\left(Q^{-1}\right)= 4\pi\delta f_{o} \qquad\qquad \eta = \frac{\rho_2}{\tau}$$

where $\rho2$ is the mass per unit area of the adsorbate, and τ corresponds to the time for an object's speed to fall to $1/e$ of its original value, assuming that it has been pushed at constant speed and then released, allowing frictional forces to bring it to a stop. (Amplitude shifts are converted to quality factor shifts $\delta(Q\text{-}1)$ through calibration with a gas that does not condense at 77.4 K) The "object" of interest is the film adsorbed on the oscillatory substrate, and τ represents an average over all film particles. Substantial decoupling effects occur whenever the slip time exceeds the period of oscillation. Partial decoupling is also quite evident for values $\tau = 2\pi f o \tau \geq 0.5$ where the percent of film mass which effectively couples to the oscillation is 80% or less. This decoupling behavior occurs for incommensurate solid Kr films adsorbed on gold, [16] consistent with experimental reports of extremely low surface corrugation levels for Au(111).[17]

Slip times measured by means of QCM are closely linked to the more general topic of energy transfer at an interface, and the vibrational properties of adsorbed molecules.[18] Such vibrations, which underlie heat transfer at an interface, have been studied by means of infrared-reflection-absorption spectroscopy, electron-energy-loss spectroscopy, and inelastic helium scattering. The lifetimes that these techniques determine for the damping of parallel frustrated translations are of the same order of magnitude, if not identical to, the slip times measured by means of the QCM.[19] The damping rate appears to be little changed in these systems regardless of the fact that in the QCM measurements the vibrational amplitude is larger than several lattice spacings. The fundamental energy dissipative mechanism involving electronic and phononic effects also appear to be equally viable. Indeed, the QCM slip time is frequently written in terms of separate phonon τph and electron-hole τeh contributions according to $\tau^{-1} = \tau\text{ph}^{-1} + \tau\text{eh}^{-1}$. [20-23]

QCM Studies of "Real World" and Model Lubricants

Vapor phase lubrication is an emerging technology [24,25] targeted at extreme environment applications that preclude the use of conventional liquid-phase lubricants (high and low temperature, space/vacuum applications, MEMS). The concept of lubricating high temperature bearing surfaces with organic vapors has existed for at least forty years, and as such, the surface reaction chemistry and macrotribological performance of a number of candidate materials has been extensively studied.[24-32] Vapor phase lubrication occurs via three distinct forms: (a) organic films that are intentionally reacted with a surface to form a solid lubricating film, (b) vapors which condense to form a lubricating liquid film on the surface of interest, and (c) light weight hydrocarbon vapors deposited onto hot catalytic nickel surfaces.

TCP (tricresylphosphate) is a candidate molecule for vapor phase lubrication whose surface reaction chemistry and macrotribological performance have been particularly well documented. Its uptake on iron at room temperature is limited to two adsorbed layers of intact molecules. [27] Above 200 C, the molecules fragment, through breakage of either the C-O, or P-O bonds [29] and thick reaction films form through partial corrosion of the underlying substrate. Studies of TCP uptake at elevated temperature on iron oxide containing materials have revealed the reaction films to be highly lubricious [27] polymers that can withstand temperatures in excess of 600 C. While much progress has been achieved in recent years concerning the chemical nature of the reaction films, the exact mechanisms underlying of the lubricity of TCP remain to be established.[32]

Modern nanotribological techniques can be brought to bear on these issues by examining in detail the properties of a known (macroscopic-scale) vapor phase lubricant. The knowledge gained is extremely likely to be applicable to NEMS/MEMS operations as well. Indeed, the vapor phase may ultimately prove to be the most effective, if not only, means to deliver and/or replenish a lubricant in the case of a submicron scale device.[30]

Figure 1 presents frequency, amplitude and sliptime data for TCP adsorption on iron at room temperature. The stepwise nature of the frequency shift data is indicative of intact molecular layers (assuming the molecules occupy the same volume as in the bulk liquid), adsorbing somewhat sequentially on the surface. Uptake of TCP on iron at room temperature: The frequency drop indicates mass adsorption. Shifts in amplitude are related to adsorbate motion, either slippage or internal molecular motion of the adsorbed species. Slip times are obtained via Eq. (1)

The Fig. 1 data are similar in both magnitude and form to those of physisorbed monolayers and monolayers having no internal degrees of freedom,
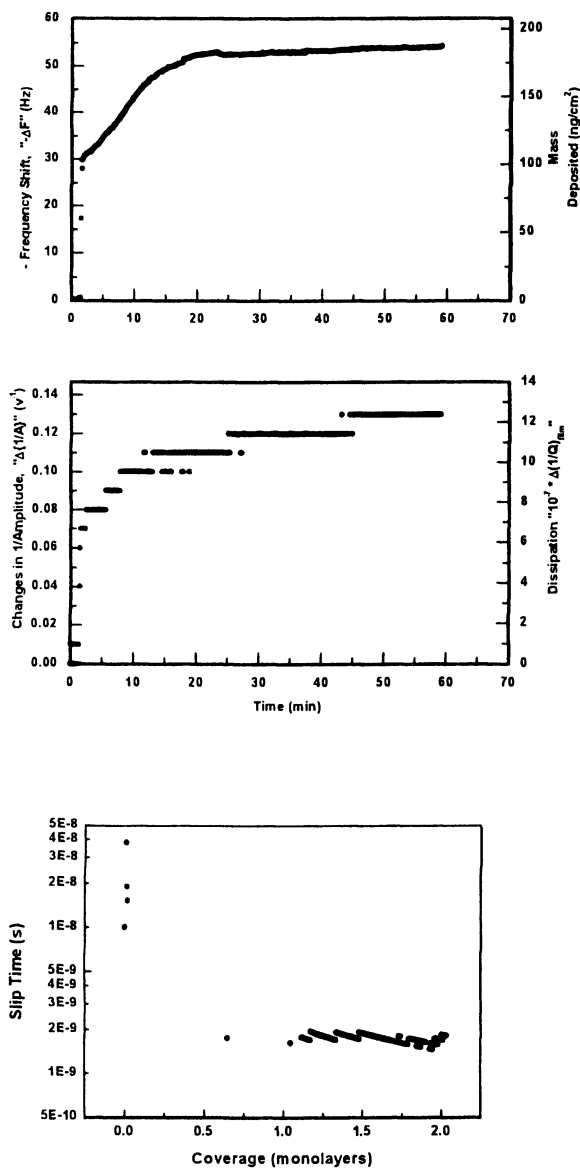
Figure 1: Frequency, amplitude and sliptime data for TCP uptake
on iron at room temperature.

for example the Xe/graphene data presented in Figure 2. The intact TCP molecules are therefore likely to be physisorbed, with no significant contributions to the dissipation arising from motion within the film.

For temperatures above 200 C, TCP uptake on iron is qualitatively quite distinct from that in the lower temperature regime. [29] Amplitude shifts become negligibly small in this regime, indicating that the reaction film is moving in unison with the substrate without slippage. Frequency reversals in directions opposite to that associated with mass uptake are also in evidence, attributable to tensile stress arising in the film. (Figure 3)

STM Imaging of a Moving QCM Electrode

The frequency shifts observed during the uptake of TCP are negative, simply due to the added mass of the film to the oscillating system. For the more complicated geometry of the STM-QCM the frequency shifts may be either positive or negative. A remarkable consequence of the STM-QCM combination is that the amplitude of vibration at the surface of the QCM may be directly measured using the STM images.[16] Such measurements are an important prelude to our studies of friction with this apparatus, allowing accurate determination of the maximum sliding speed of the tip-surface interface. We note that the QCM frequency response to applied forces plays no role in this measurement. In fact, we observe no frequency shift upon engaging the tip into tunneling contact, to within the resolution of +/- 0.1 Hz out of 5 MHz. This indicates that there is no observable normal load on the crystal when the tip is in tunneling contact, provided that both the tip and electrode surfaces are bare metals in high vacuum (~10-8 Torr in our experiments). As will be discussed in Section 5, the presence of even a thin adsorbed layer on the tip and electrode surfaces results in a QCM frequency shift during tunneling contact, due to the normal load required to squeeze the two metal surfaces sufficiently close together for tunneling.

The ability to image a vibrating surface with an STM, while unexpected, may be attributed to the three widely separated time scales involved, and the exponential dependence of the tunneling current on tip-surface separation. The characteristic frequencies of the scanner (Hz), the feedback loop (kHz), and the QCM (MHz) are each separated by three orders of magnitude. Conventional STM operation relies on the feedback loop being much faster than the scanner (in constant-current mode). For STM-QCM, the fact that the vibrations of the QCM are in turn much faster than the feedback loop causes the tip to be held at a separation from the surface which on average (over many surface oscillation cycles) gives the desired tunneling current (typically 1 nA). Qualitatively, the closest approach of the surface to the tip during each cycle is weighted most heavily in this average, due to the exponential dependence of the tunneling current on separation, so the tip is held at an altitude sufficient to avoid direct
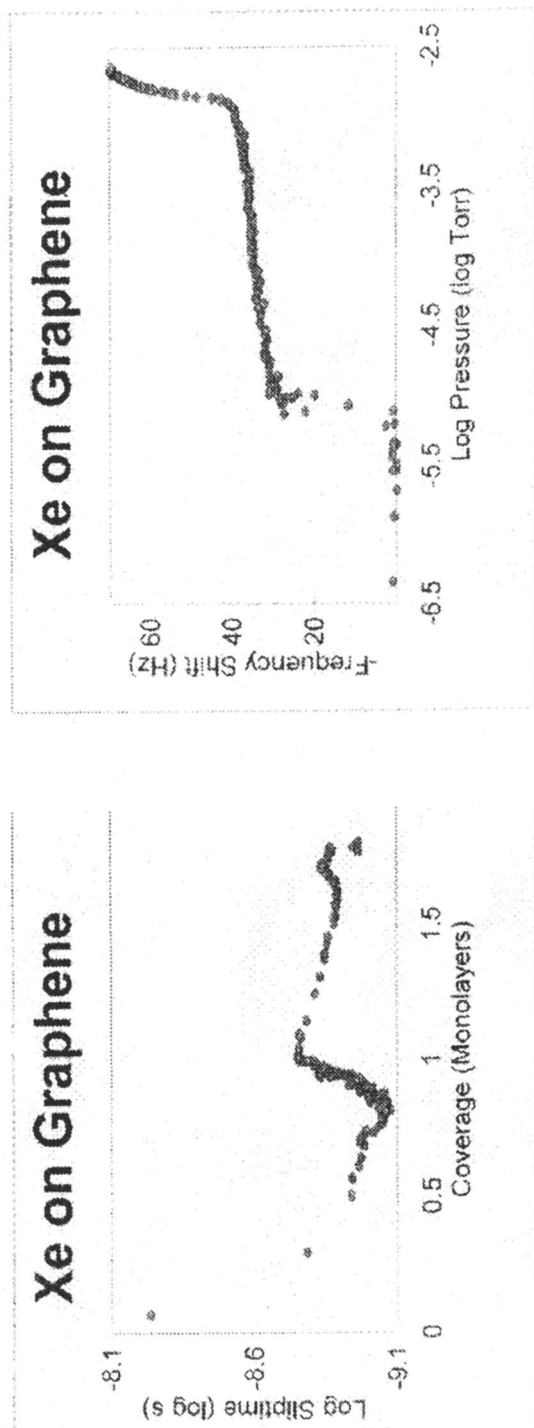
Figure 2. Sliptime and frequency shift data for Xe adsorption on Graphene at 77K.
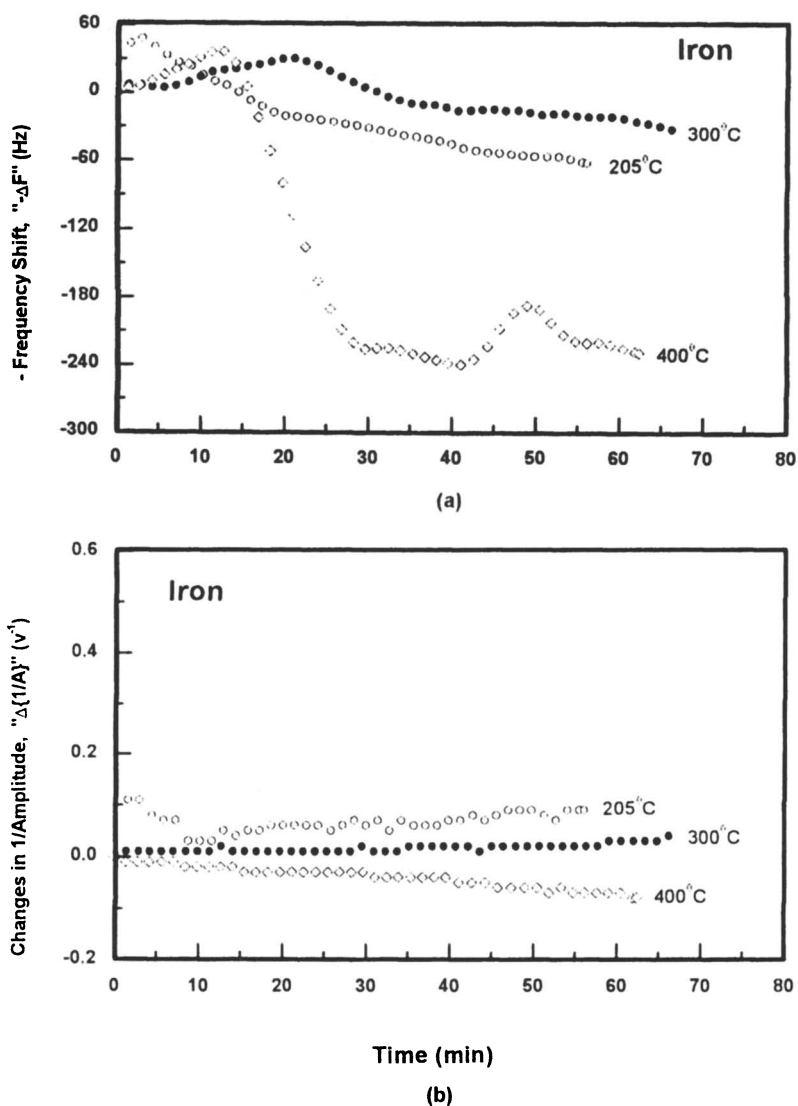
Figure 3. Frequency and amplitude shift data for TCP uptake on Iron at temperatures exceeding 200 C.

contact of the tip and surface. This allows the STM tip to image the vibrating surface without crashing into it, as is evident from a lack of damage to the surface.

The amplitude measurements proceed as follows: We employ an AT-cut quartz crystal for our QCM, which oscillates in transverse shear mode whereby displacements are in the plane of the surface. The STM tip is held in tunneling contact (in constant current mode) with the QCM electrode. Simultaneous operation of STM and QCM is accomplished using the electrical circuit detailed in Ref [15]. The amplitude of vibration is measured by observing the lateral smearing of features along the shear direction as the drive voltage of the QCM is increased.

Figure 4 displays a STM image of the QCM surface while moving and stationary. The surface is that of a copper electrode deposited in situ in high vacuum.

Lubricated Contact

We now study the case of lubricated contact between the tip and surface, employing the (macroscopic) lubricant and anti-wear additive TBPP, which consists of a blend of tertiary-butyl phenyl phosphate (TBPP) molecules, whose atomic constituents are carbon, hydrogen, oxygen and phosphorus. It demonstrates high quality performance at elevated temperatures and exhibits oxidation inhibiting characteristics as well as a number of other desirable tribological properties, such as the reduction of wear. This case is particularly relevant to the possibility of vapor phase lubrication of MEMS devices. The QCM was exposed to TBPP vapor, registering an uptake of approximately 1 monolayer. The tip is expected to have adsorbed a comparable amount. The electrode and tip surfaces were at room temperature during deposition.

Figure 5 shows a 350 nm x 350 nm STM scan of the surface immediately after exposure to the lubricant. We find that in order to obtain an image, it is necessary to run the QCM while scanning. No stable image is obtained when the QCM is off. We understand this result by considering the following: When the QCM is off, the tip-surface junction is quite insulating. The "Z" voltage, which controls the vertical position of the tip, is unstable while a constant tunneling current "I,' is maintained through feedback. The so-called I-Z dependence is as follows: A change in voltage corresponding to a deflection of 100 to 300 nm into the surface is required to raise the tunneling current by 10 nA! Most likely, increases in the normal force and contact area are responsible for the increased current, not an actual change in tip-surface separation of such a large magnitude. (In contrast, for a clean metal-vacuum-metal tunneling junction, a change in Z voltage corresponding to a deflection of less than 1 Å changes the tunneling current by 10 nA). When the QCM is turned on and the tip engaged at 10 nA, the junction becomes more conductive over time (a few seconds or minutes) until an I-Z dependence close to that of tunneling through vacuum is achieved.
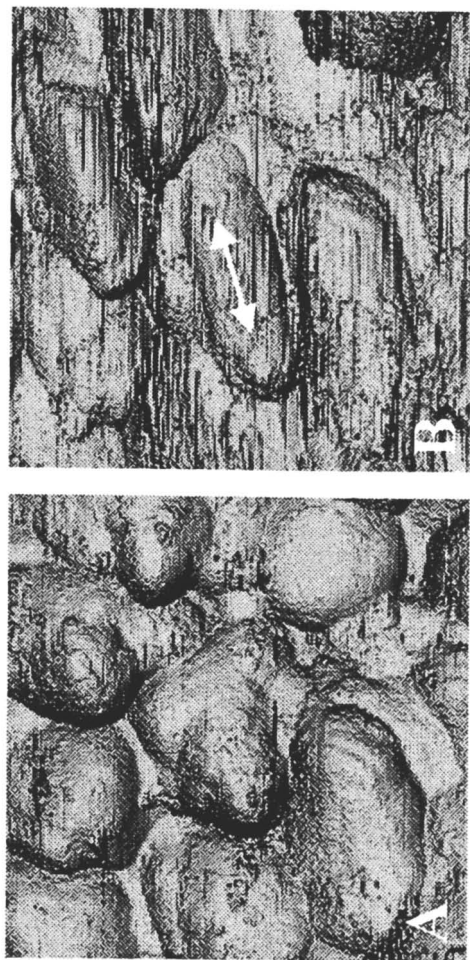
Figure 4 (top). Direct imaging of an oscillating quartz crystal by scanning tunneling microscopy. The surface (copper vacuum-deposited on quartz with preexisting metal electrodes) is shown both stationary (A) and oscillating at 5 MHz (B) in 50 x 50 nm^2 images. Since the scan rate is much less than the oscillation frequency, features in (B) appear elongated and blurred into one another along the direction of oscillation, indicated by the white arrows. The observed amplitude is about 5 nm, giving a maximum velocity of 0.2 m/s. These conditions of frequency and velocity approach those commonly realized in macroscopic media such as magnetic disk drives.
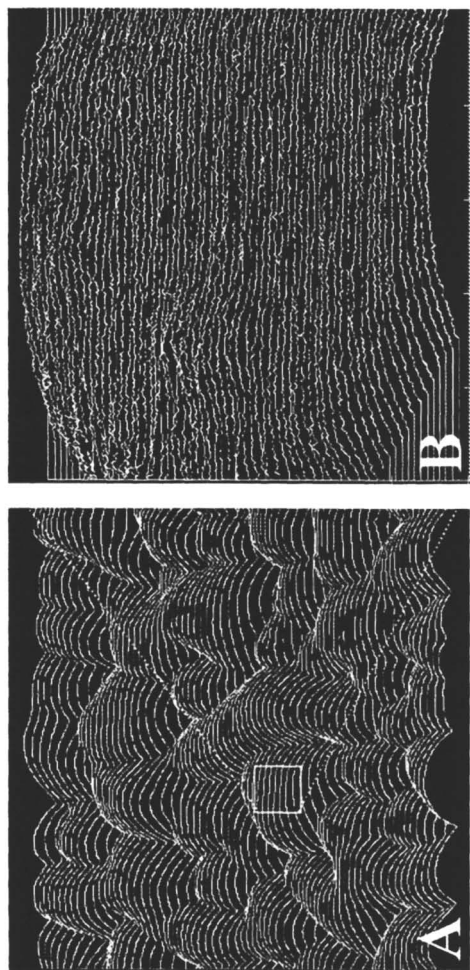
Figure 4 (bottom). The ability to deposit atomically flat metal surfaces on quartz is an important step towards well-controlled and quantifiable investigations of friction on nanometer length scales using QCM/STM. Here we show a pair of STM images in line plot mode of a copper surface deposited on quartz from an evaporative source. On a large scale, the surface consists of many separate grains, as shown in (A) (100 x 100 nm², total height range of 10 nm). However, zooming-in on the boxed region reveals a suitably large atomically flat region, as shown in (B) (10 x 10 nm², total height range of 0.5 nm, with less than 1 Å variation on top of plateau).
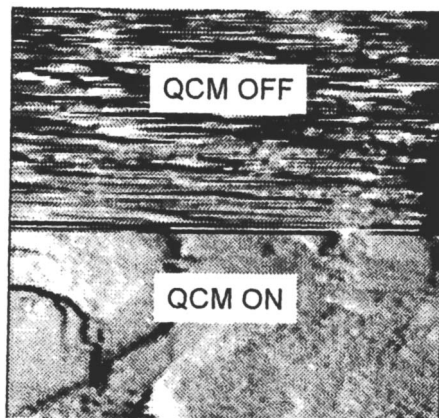
Figure 5. A 350 nm x 350 nm image of the TBPP-lubricated platinum surface at room temperature. The rubbing action of the vibrating QCM electrode against the STM tip is required to produce a stable image. The rubbing appears to clear away the lubricant, producing localized holes in which the surface may be imaged. These holes fill-in with additional lubricant once the QCM is turned off or the tip is moved away from the region, indicating that the TBPP film is mobile at room temperature.

This applies only to the region in close proximity to the tip. Changes in the Z voltage and QCM frequency indicate a decreasing normal load as the junction becomes more conductive. Under these conditions a recognizable image of the surface may be obtained. However, the junction returns to insulating as soon as the QCM is shut off, or if the tip is moved away from the region or raised up from the surface.

Our interpretation of these observations is that the rubbing action of the vibrating QCM electrode against the STM tip effectively brushes the insulating lubricant layer aside to allow imaging of the underlying surface, similar to a windshield wiper except that the vibration of the QCM surface is critical in the process. Holes or clear areas produced in this way are not permanent, however, and readily fill in with additional lubricant once the QCM is turned off or the tip is moved to a different position. We therefore conclude that there is a high degree of mobility associated with the TBPP layer at room temperature. This corresponds to the results of adsorption studies with QCM alone discussed earlier, in which the observed change in amplitude of the QCM during adsorption of the closely related material, TCP, indicated either wholesale slippage of the film layer. The ability of a lubricating film to replenish its depleted areas is indeed a known requirement for good lubrication.

Thus far, our studies of the lubricated interface have been performed exclusively at room temperature. TBPP is known to undergo a chemical reaction above 100^0C which renders the film more conductive. In view of this, we have

investigated the lubricated interface after annealing for several hours near 100^0C. (The entire vacuum system was raised to elevated temperature). Indeed, we find that the TBPP-lubricated platinum surface is much more readily imaged after annealing. The tip-surface junction is conductive enough to maintain a stable tunneling signal with or without the QCM in operation. The magnitude of the positive QCM frequency shift over the full range of normal load is significantly reduced. This suggests a reduction in sliding friction at the interface. Moreover, STM images of the annealed surface help identify a more subtle rubbing-induced response, which may provide evidence for a tribochemical reaction.

Figure 6 displays a pair of images of the lubricated surface after annealing. Image (a) shows a non-rubbed 70 nm x 70 nm region, for which the QCM has not yet been operated with the tip engaged. The image has a fringed appearance. (Due to the presence of the lubricant film, the appearance of the surface in these constant-current images is not to be interpreted literally as the topography of the surface. The imaging mechanism is unknown, and electronic effects are clearly present). Image (b) shows the same region after the QCM was operated for a few minutes with the STM tip held in tunneling contact at 2 nA. This short
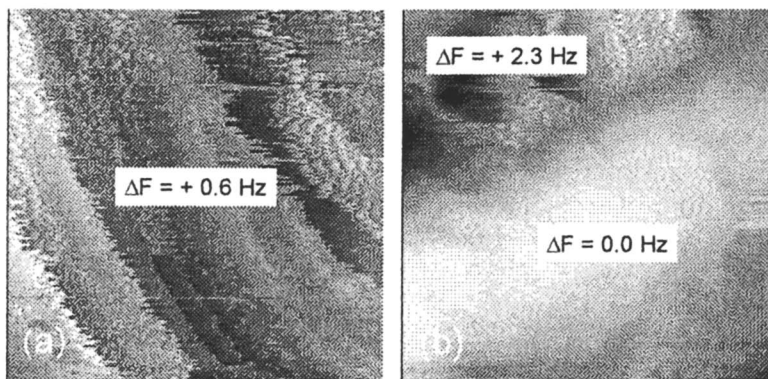

Figure 6. A pair of 70 nm x 70 nm images of the TBPP-lubricated platinum surface after annealing for several hours near 100 ^{0}C. QCM frequency shifts upon establishing tunneling contact at different places are shown in boxes. Image (a) shows a non-rubbed region. Image (b) shows the same region after a rubbing period of a few minutes, during which the QCM was vibrating with the tip engaged in tunneling contact. Two regions may be distinguished: non-rubbed regions have a fringed appearance and are accompanied by a small positive frequency shift when the tip is first engaged in tunneling. Rubbed regions have a more uniform appearance and exhibit no frequency shift when tunneling. The electrical properties of the tunneling junction suggest that the lubricant film is not simply worn away by rubbing. These results suggest a possible tribochemical reaction associated with the interfacial sliding conditions achieved by the STM-QCM.

rubbing experiment produced two distinct regions in the vicinity of the tip. The majority of image (b) has a uniform appearance, but a region in the upper left remains which bears the fringed appearance of image (a). Interestingly, the two regions are accompanied by different QCM frequency responses. In both (a) and (b), the fringed region registers a small positive frequency shift when the tip is briefly engaged in tunneling (at 2 nA). The uniform region in (b) registers no frequency shift. In general, we find that if the tip is held in tunneling contact at a fringed region while the QCM is operated, a small positive frequency shift appears and decays over a period of a minute or so, leaving a uniform region with no frequency shift for the same tunneling conditions.

This rubbing-induced effect is both localized to the region of rubbing and permanent. The uniform regions do not revert to fringed, and fringed regions are only converted to uniform by rubbing the tip against the vibrating QCM. The ability to distinguish rubbed and non-rubbed regions on the nanometer scale by both appearance and corresponding frequency response is intriguing, since improvements in the protective properties of lubricant films after interfacial sliding are well-known, yet poorly understood, on the macroscopic scale. [21] While the mechanism responsible for the change in frequency response observed here is unknown, we find that the tunneling junction never regains the conductivity (I-Z dependence) of a clean metal-vacuum-metal junction. This suggests that the film is not simply worn away by rubbing. Together these results provide evidence for a potential tribochemical reaction triggered by the interfacial sliding conditions attained with the STM-QCM.

Conclusion

In conclusion, we have combined a Scanning Tunneling Microscope (STM) with a Quartz Crystal Microbalance (QCM) with the intent of studying both applied and fundamental lubricant films. The STM-QCM allows unique and detailed investigations of the simple nanomechanical system formed by a contacting tip and surface. We have discussed our results obtained with STM-QCM in three situations: (1) measurements of the amplitude of a vibrating QCM electrode in the absence of the STM tip, and (2) in the presence of a tunneling contact with the QCM, (2) as well (3) lubricated contact (before and after annealing) using a vapor phase lubricant which is known to reduce wear in macroscopic applications. Application of molecularly thin quantities of lubricant to the same contact dramatically alters both the STM and QCM responses in a manner which is highly suggestive of the lubricant's known friction and wear reducing properties at the macroscopic scale. Our measurements also reveal a potential tribochemical reaction that is highly localized at the point of contact and is associated with the realistic rubbing conditions provided by the STM-QCM apparatus.

Acknowledgments

References

1. Krim, J., "Friction at the atomic scale," Scientific American, 275, 74-80 (1996).

2. Cieplak, M., Smith, E.D., and Robbins, M.O., "Molecular origins of friction: The force on adsorbed layers", Science, 265, 1209-1212 (1994); Robbins, M.O. and Krim, J., "Energy Dissipation in Interfacial Friction," MRS Bulletin, 23, 23 (1998).

3. Duncan-Hewitt, W.C. and Thompson, M., "Four-layer theory for the acoustic shear wave sensor in liquids incorporating interfacial slip and liquid structure," Anal. Chem., 64, 94-105 (1992).

4. Yang, M., Thompson, M., and Duncan-Hewitt, W.C., "Interfacial properties and the response of the thickness-shear-mode acoustic wave sensor in liquids," Langmuir, 9, 802-811 (1993).

5. Maboudian. R. and Howe, R.T., "Stiction reduction processes for surface micromachines," Tribology Letters, 3, 215-222 (1997).

6. Maboudian. R. and Howe, R.T., "Critical Review: Adhesion in Surface Micro-Mechanical Structures," J. Vac. Sci. and Tech., 15, 1-20 (1997).

7. Zavracky. P.M., Majumder, S., amid McGruer, N.E., "Micromechanical switches fabricated using nickel surface micromachining," J. Electromech. Sys., 6, 3 (1997).

8. Scanning Tunneling Microscope Measurements of the Amplitude of Vibration of a Quartz Crystal Oscillator, B. Borovsky, B. L. Mason and J. Krim, J. Appl. Phys. 88, 4017-4021 (2000).

9. Measuring Nanomechanical Properties of a Dynamic Contact Using an Indenter Probe and Quartz Crystal Microbalance, B. Borovsky, J. Krim, S.A.S. Asif and K.J. Wahl, J. Appl. Phys., 90, 6391-6396 (2001).

10. Applications of the Piezoelectric Quartz Crystal Microbalance for Microdevice Development, J.W. Bender and J. Krim, in Microdiagnostics, K. Breuer ed. (Springer, New York, 2003).

11. Applications of Piezoelectric Quartz Crystal Microbalances C. Lu and A. Czanderna, eds. (Elsevier, Amsterdam, 1984)

12. Damping of a crystal oscillator by an adsorbed monolayer and its relation to interfacial viscosity, J. Krim and A. Widom, Phys. Rev. B 38 (1988) 12184; Q factors of quartz oscillator modes as a probe of submonolayer dynamics, A. Widom and J. Krim, Phys. Rev. B 34 (1986) R3.

13. Experimental observation of interfacial slippage at the boundary of molecularly thin films with gold substrates, E.T. Watts, J. Krim and A. Widom, Phys. Rev. B 41(1990) 3466.

14. On the Limit of Compression in a Physisorbed Monolayer, L.W. Bruch, J.M. Gay and J. Krim, de Phys. (Paris) 46. 425 (1984).

15. Quartz Monitors and Microbalances, J. Krim and C. Daly, in Handbook of Thin Film Process Technology, D. Glocker and I. Shah, Eds. (IOP Publishing, Philadelphia, 1995) pp. D4.0:1-6

16. Nanotribology of a Kr Monolayer: A Quartz-Crystal Microbalance Study of Atomic-Scale Friction, J. Krim, D.H. Solina and R. Chiarello, Phys. Rev. Lett. 66, 181 (1991).

17. Measure of Au(111) Surface phonons by Low Energy Helium Scattering, M. Cates and D.R. Miller, J. Elec. Spec. Relat. Phenom. 30, 157 (1983).

18. Physics at Surfaces, Zangwill, (Cambridge University Press, Cambridge, 1988), p. 328

19. Surface Resistivity and Vibrational Damping in Adsorbed Layers. B.N.J. Persson, Phys. Rev. B 44, 3277-3296 (1991).

20. Physics of Sliding Friction, B.N.J. Persson and E. Tosatti, eds., (Kluwer, Dordrecht, 1996): Sliding Friction, B.N.J. Persson, (Springer, New York, 1997); Sliding friction, B.N.J. Persson, Surf. Sci. Rep. 33: (3) 85-119, (1999).

21. Linear Sliding Friction: On the origin of the microscopic friction for Xe on silver, B.N.J. Persson and A. Nitzan, Surf. Sci. 367: (3) 261-275, (1996).

22. Electronic versus Phononic Friction of Xenon on Silver, A. Liebsch, S. Goncalves and M. Kiwi, Physical Review B, 60, 5034 (1999).

23. Friction on adsorbed monolayers, E.D. Smith, M.O. Robbins, and M. Cieplak, Phys. Rev. B 54: (11) 8252-8260, (1996).

24. D.G. Placek and T. Freiheit, Trib. Trans. Of the ASME, 115, 700-705 (1993).

25 A.M N. Rao, Lubrication Engineering, 52, No.12, 856-862 (1996).

26. Forster, N.H. and Trivedi, H.K., "Rolling contact testing of vapor phase lubricants - part I: material evaluation," Trib. Trans., 40, 421-428 (1997).

27. Faut, O.D. and Wheeler, D.R., "On the mechanism of lubrication by Tricresylphosphate (TCP)-The coefficient of friction as a function of temperature for TCP on M-50 steal," A.S.L.E. Trans., 26, 344-350 (1983).

28. M.P. Marino and D.G. Placek, CRC Handbook of Lubrication and Tribology, Vol. III, R.R. Booser, ed. (CRC Press, Boca Raton, 1994), pp 269-286

29. Nanotribology of a Vapor-Phase Lubricant: A Quartz Crystal Microbalance Study of Tricresylphosphate (TCP) uptake on Iron and Chromium, M. Abdelmaksoud, J. Bender and J. Krim, Tribology Letters, 13, 179-186 (2002), and references therein.

30. STM-QCM studies of Vapor Phase Lubricants, B. Borovsky, M. Abdelmaksoud and J. Krim, "Nanotribology: Critical Assessment and Research Needs", S. M. Hsu and Z.C. Ying. eds. (Kluwer, Boston. 2002) (invited) pp. 361-375

31. Nanotribology of a Vapor Phase Lubricant: A Quartz Crystal Microbalance Study of Tricresylphosphate (TCP) Uptake on Iron and Chromium, M. Abdelmaksoud, Ph.D. Dissertation, North Carolina State University (2001)

32. C.S. Saba and N.H. Forster, Trib. Lett. 12, 135, (2002)

Chapter 2

Cold Welding and the Origins of Stick–Slip Friction

Seth J. Putterman and Raffi Budakian

Physics Department, University of California, Los Angeles, CA 90095

Abstract

Measurements of the conductance, charge transfer and forces between surfaces in contact suggest that stick-slip friction is due to the formation of bonds and junctions.

Introduction

Friction and static electricity are everyday characteristics of surfaces in contact. Despite early phenomenological pictures by Coulomb and Da Vinci [1] a description of friction in terms of surface physics is still a matter of debate [2], and despite its numerous applications [3] an understanding of contact electrification has "eluded researchers since the time of the ancient Greeks." [4,5]

It has been proposed [6] that a route to the explanation of friction lies in the discovery of the microscopic origins of stick-slip motion. Here we present a picture of friction based upon the formation of bonded regions between surfaces in contact. These spot welds spontaneously form even between surfaces comprised of different materials. Furthermore, friction between macroscopic bodies is accounted for by individual welds whose size is delineated in nanometers. Measurements of the physical properties of the cold welds such as force, stress, conductivity, indicate the operation of quantum mechanics in macroscopic friction.

19

Friction Between Metallic Surfaces

Figure 1 shows the time development of a weld that forms between two macroscopic gold spheres that are brought into contact. The spheres have radii 1mm and .1mm and the radius r_c of the cold weld is determined by a measurement of the conductivity G_s of the junction [7] and Sharvin's formula:

$$G_s = r_c^2 k_F^2 G_0 / 4$$

where k_F is the bulk metal Fermi wave number and $G_0 = 2e^2/h$ is the quantum of conductance.

As can be seen from this figure the radius of the junction which forms between the gold balls grows from angstroms to nanometers in about a second and then continues to grow on a long time scale extending past a minute. A positive displacement indicates that the balls are "sucking in", i.e. that the distance between their centers is decreasing. The longer the surfaces are in contact the bigger is the junction that forms and the greater is the force that is required to rupture the junction. This rupture force will be identified with the force of stick slip friction.

After a junction forms the gold balls can be pulled apart until the junction ruptures. The stress at the moment of rupture is shown in Figure 2. It can be seen that for smaller junctions the tensile strength approaches the ideal value of the
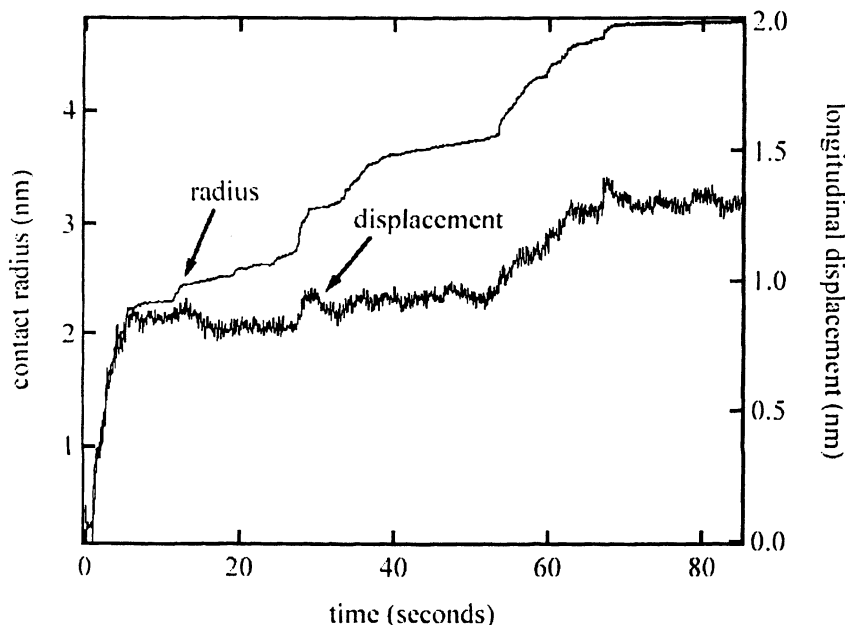
Figure 1. Weld development vs. time between gold spheres.
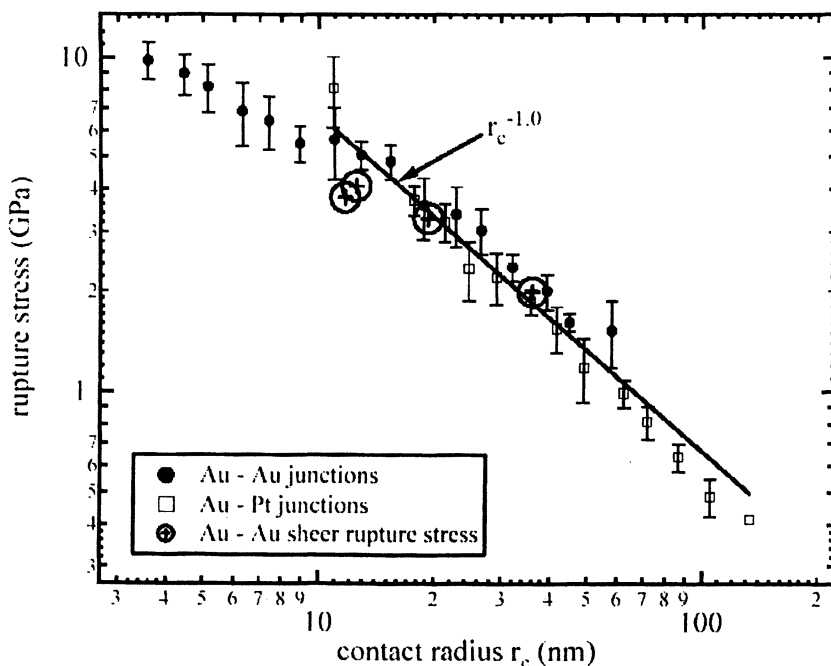
Figure 2. Rupture stress of junctions vs. contact radius.

Young's modulus for gold $E_g = 8 \times 10^{10}$ *Pa*. For larger junctions the rupture stress decreases by about a factor of 30 to the value characteristic of macroscopic specimens. Displayed as circles on the graph are the forces that must be supplied to overcome stick-slip friction when the two gold balls are forced to slide relative to each other. We note that these stresses are consistent with the measured rupture stresses of the junction. So we conclude that the stick in stick-slip friction is due to the spontaneous formation of cold welds. These experiments have also been performed with a gold ball sliding relative to a platinum ball. In this case the formation of cold welds also occurs even though the surfaces are incommensurate.

Friction Between A Metal And A Dielectric

An extreme example of incommensurate surfaces is realized when a metal slides relative to a dielectric, such as when gold slides on PMMA [polymethylmethacrylate]. In this case it is impractical to measure the conductivity, but instead one can measure the charge exchanged between the differing materials, as is shown in Figure 3: The figure displays the force required to scan the gold ball over the surface as well as the integrated charge
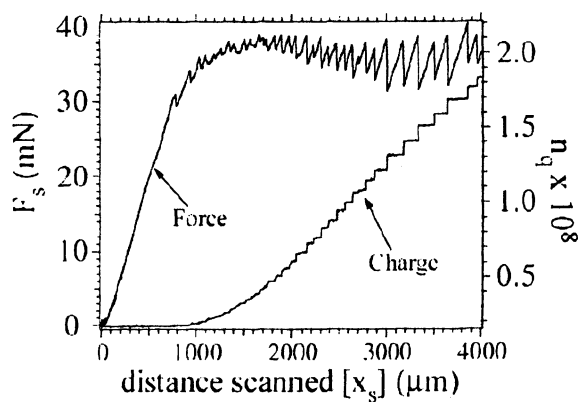
Figure 3. Friction and charge exchange between gold and PMMA.

remaining on the PMMA as a result of the stick slip events. Each slip event is accompanied by a step in the charge. The bigger the slip event the bigger is the amount of [positive] charge left on the surface. In fact if one assumes that each charge corresponds to a force of .4eV/A then the force and charge graphs collapse onto one curve as can he seen from Figure 4.

This observation suggests that when the gold and PMMA come into contact a region of bonds forms between them. The size of this region as well as the force of friction varies from event to event. The bond [for this system] redistributes the electrons into the potential well of the gold so that when a bond ruptures the electrons end up in the gold leaving the PMMA positively charged. Most importantly each bond contributes a precise force [here .4eV/A] to the overall force of friction.
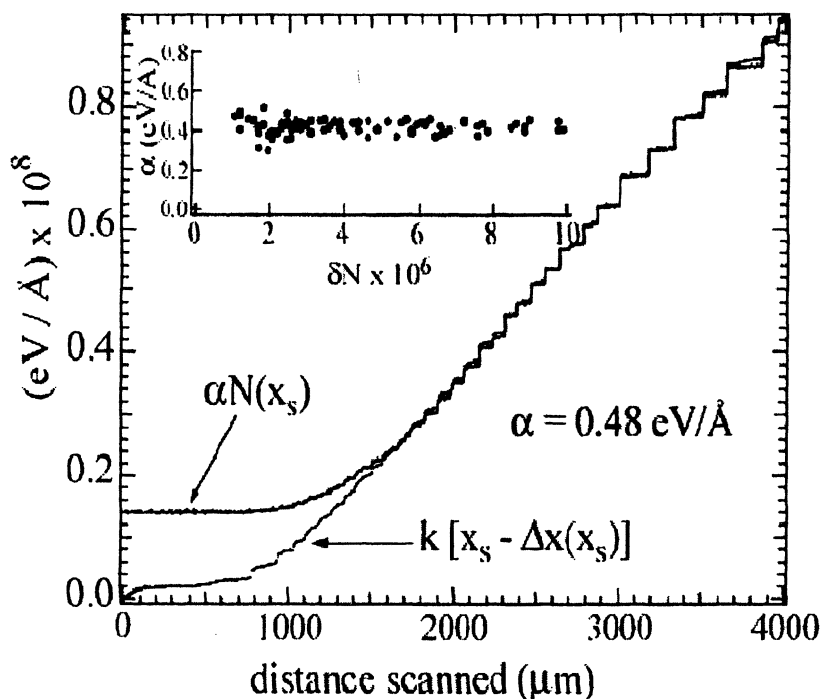
Figure 4. Force and charge curves collapsing to one curve.

Role of Quantum Mechanics in Friction

This force [.4eV/A] that each bond contributes to the total friction is characteristic of the quantum mechanically determined properties of the atomic domain yet its value can be obtained from the measurement of friction between

macroscopic bodies. The role of quantum mechanics in friction can also be seen in the response of metals brought into contact. As shown in Figure 5, the conductance shows clear quantum steps as a junction develops in time. These steps are still present at high values of the quantum number where the responses are macroscopic. The device, which enables one to measure the force exerted on the junction, also is capable of measuring the resonant frequency of the junction and therefore its stiffness. As we can see in Figure 5 this mechanical quantity is also changing in quantum jumps.
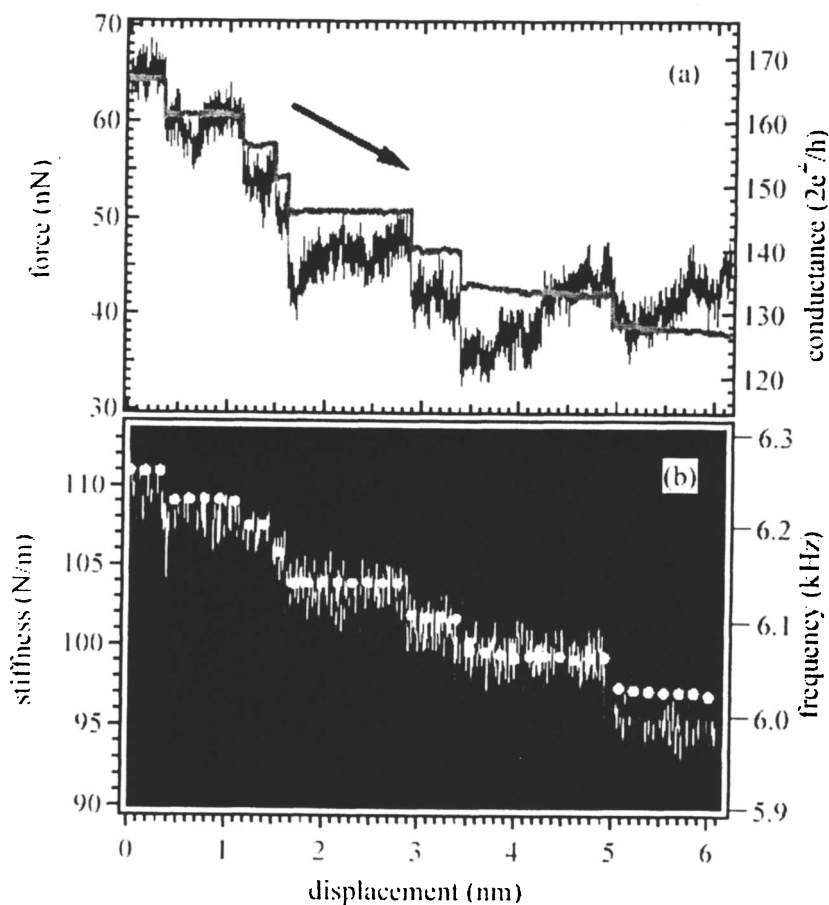
Figure 5. Characteristics of junction development.

Experimental Techniques

The data in Figures 1,2,5 were taken with a fiber optic cantilever, Figure 6, that was used both as a support and a detector for the motion. The spring constant of the fiber provided for the stiffness relative to which the forces of friction were measured, according to the displacements they induced. The displacement was measured according to the signal received on a quadrant detector due to the light from a superluminescing diode [SLD] that propagated down the fiber.

The gold ball attached to the fiber is made by taking a segment of 10 μm diameter 99.99 % gold wire and bending it in half. The bent section is then melted using a torch and forms a ball approximately 200 μm in diameter. The two halves of the gold wire that are naturally fused to the ball, are used in the 4-wire conductance measurement. A 250 μm gold or platinum wire is heated at one end and forms the larger 2 mm diameter ball that is attached to piezo stage. The vector g is drawn to show the orientation of the apparatus with respect to gravity.
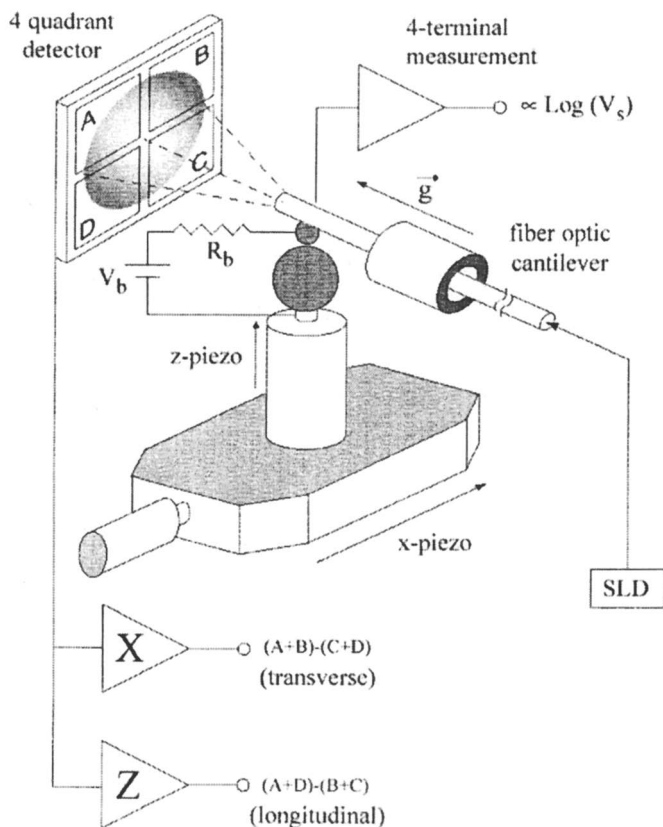
Figure 6. Fiber optic cantilever.

Figure 7 shows the apparatus that was used to measure the charge transfer and forces characteristic of stick-slip friction. The apparatus consists of a metal tip mounted on the end of an xz cantilever. It is scanned over the dielectric surface with a three axis translation stage. The vertical-z- displacement is used to apply a normal force while the lateral-x- deflection measures the frictional force. These deflections are measured independently using an ac capacitance bridge. In order to measure the integrated charge on the surface a grounded metal chopper is placed between the back of the dielectric sample and a metal plate. The rotating slots on the chopper produce a time varying current on the metal plate where the amplitude of the induced current is proportional to the integrated charge on the surface.
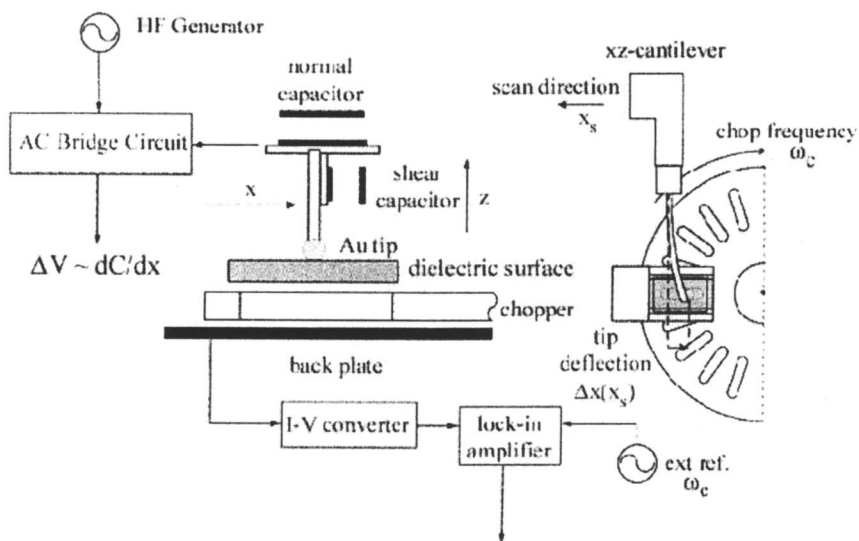
Figure 7. Apparatus for charge transfer and force measurement.

Conclusion

A long standing picture of the origins of friction relates it to the interaction of asperities at the interface of to bodies. The measurements reported here suggest that another key source of friction is due to the spontaneous formation of spot welds and bonds at the interface[10]. When extrapolated to MEMS and nanoscale devices these welds can be a significant source of interaction.

Acknowledgment

References

1. F.P. Bowden and D. Tabor, *The Friction and Lubrication of Solids* (Clarendon Press, Oxford, 1986).

2. J. Krim, *Scientific American* **275**, 74, (1996).

3. B. Maurer, *Chem. Ing. Tech.* **51,** 98, (1979); C. Holt, *Scientific American* **275**, 128, (1996).

4. B.D. Terris, J.E. Stern, D. Rugar and H.J. Mamin, *Phys. Rev. Lett.* **63**, 2669 (1989).

5. A.D. Moore, *Electrostatics* (Doubleday, New York 1968).

6. B.N.J. Persson, *Sliding Friction* (Springer, Berlin 1998).

7. R. Budakian and S. Putterman, Time Scales For Cold Welding and the Origins of Stick-Slip Friction, Phys. Rev B 65, 235429 (2002)

8. R. Budakian and S. Putterman, Correlation Between Charge Transfer and Stick-Slip Friction at a Metal Insulator Interface, Phys. Rev Lett. 85, 1000 (2000).

9. R. Budakian and S. Putterman, Force Detection Using A Fiber Optic Cantilever, preprint [xxx.lanl.gov/cond-mat/0203073]; Applied Physics Letters 81, 2100 (2002).

10. Phill Ball, Spot Welds Stick Sliding Metals, Nature Science Update, March 15, 2002.

Chapter 3

Dynamic Force Spectroscopy: Effect of Thermal Fluctuations on Friction and Adhesion

O. K. Dudko[1], A. E. Filippov[2], J. Klafter[1], and M. Urbakh[1]

[1]School of Chemistry, Tel Aviv University, 69978 Tel Aviv, Israel
[2]Donetsk Institute for Physics and Engineering, 83144 Donetsk, Ukraine

In this paper we propose a model which allows to describe the effect of thermal fluctuations on atomic scale friction and dynamical response of adhesion complexes. In the case of friction the model presents a generalization of Tomlinson model which includes the contribution of an external noise. We demonstrate that important information on friction and adhesion can be obtained from measurements of distribution functions for the maximal spring force which quantifies static friction and rupture forces. We derive relationships between equilibrium potentials and the forces measured under nonequilibrium conditions.

Experiments that probe mechanical forces on small scales provide a versatile tool for studying molecular adhesion and friction through the response to mechanical stress of single molecules or of nanoscale tips. The probing techniques include atomic force microscopy (AFM) (*1,2*), biomembrane force probe microscopy (*3*) and optical tweezers (*4*). Examples for processes which are investigated are friction on atomic scale (*1,2*), specific binding of ligand-receptor (*5*), protein unfolding (*6*), and mechanical properties of single polymer molecules such as DNA (*7*). In these experiments one probes forces along a reaction coordinate. Recent theoretical studies (*8-10*) suggest that microscopic

information on the potential and dissipative interactions, which a probe (a molecule or tip) experiences, can be obtained from dynamic force spectroscopy (DFS) by investigating the velocity dependence of the mechanical forces.

Here we introduce a model to describe the dynamical response of a probe subject to an external drive in the context of DFS. The response is governed by the Langevin equation (12,13)

$$M\ddot{x}(t) = -\eta\dot{x}(t) - \frac{\partial U(x)}{\partial x} - K(x - Vt) + \Gamma(t).$$ (1)

Here the probe of mass M is pulled by a linker of a spring constant K connected to a support moving with a velocity V. In the context of friction the probe (tip) is pulled along the surface and $U(x)$ is the periodic potential $U(x)=U_0\cos(2\pi x/b)$. In this case eq 1 presents a generalization of Tomlinson model (14) which includes thermal fluctuations. In studies of adhesion the probe (molecule) is pulled in the direction perpendicular to the surface and $U(x)$ presents the adhesion potential. η is a dissipation constant and the effect of thermal fluctuations is given by a random force $\Gamma(t)$, which is δ-correlated $<\Gamma(t)\Gamma(0)>= 2k_B T\eta\delta(t)$.

Below we start with a discussion of the effect of thermal fluctuations on friction and continue with the dynamical response of adhesion complexes. It is convenient to introduce the dimensionless space and time coordinates, $y=2\pi x/b$ and $\tau=t\omega$, where $\omega=(2\pi/b)(U_0/M)^{1/2}$ is the frequency of the small oscillations of the tip in the minima of the periodic potential. The dynamical behavior of the system is determined by the following dimensionless parameters: $\alpha = (\Omega/\omega)^2$ is the square of the ratio of the frequency of the free oscillations of the tip $\Omega = \sqrt{K/M}$ to ω, $\tilde{\eta} = \eta/(M\omega)$, $\sigma^2=\Delta^2/(U_0\eta)$, and $\tilde{V} = 2\pi V/(\omega b)$ are respectively the dimensionless dissipation constant, intensity of the noise, and stage velocity. Eq 1 describes also the response of macromolecules subject to an external drive provided for instance by optical tweezers.

The observable in DFS is the spring (or frictional) force, in particular its time series and dependencies on external parameters such as driving velocity, spring constant, temperature and normal load. The main result reported in DFS is $F(V)$, the velocity-dependent force, either maximal or time averaged. In order to understand the nature of the force and to establish relationships between the measured forces and the microscopic parameters of the system we apply two approaches: (a) direct integration of the Langevin eq 1, and (b) reconstruction of the force from the density of states, which is accumulated from the corresponding Fokker-Planck eqeation (15). In the Fokker-Planck approach the average friction force can be written as

$$F = \iint_{x,v} \rho(x,v;V,\sigma)\big(\sin(2\pi x/b)+\eta v\big)dxdv, \qquad (2)$$

where v is a tip velocity in response to V and $\rho(x,v,V,\sigma)$ is a time averaged density of states for the driven tip in phase space $\{x,v\}$. This equation explicitly demonstrates two contributions to the friction force: the potential given by the $\sin(2\pi x/b)$ term and the viscous one given by the $\eta\,v$ term.

Figure 1 shows the velocity dependence of the time-averaged forces found through direct numerical solution of eq 1 and by using eq 2, namely the Fokker-Planck approach. The time average forces in our periodic potential provide the same information as that of an ensemble pulled over a barrier.

All calculations have been done under the condition $\alpha < \hat{\eta}^2/4 < 1$, when the system is underdamped with respect to the periodic potential and overdamped with respect to the driven spring. Under these conditions we find that for low driving velocities the system exhibits well-defined stick-slip motion with a positive minimal spring force, that is usually observed in AFM measurements (1,2).

The Langevin and Fokker-Planck approaches should be equivalent when exact calculations are possible, however as approximations they can provide complimentary information on the dynamics of the system. Here we concentrate on averaged forces, however more information can be obtained from detailed analysis of the time series which characterizes the response of the system (16,17).

At low temperatures the velocity dependence of the averaged force clearly exhibits the existence of two different regimes of motion: at low driving velocities $F(V)$ depends only slightly on V, while for higher velocities $F(V)$ approaches ηV. The first regime corresponds to stick-slip motion in the time series and the second one to sliding. Increasing the temperature leads to an irregular motion of the tip and smears out the difference between these regimes. It should be noted that for relatively strong spring constants K, when α is of the order of η^2, spikes are observed in the averaged force for a weak noise, see Figure 1a. These spikes correspond to parametric resonances which arise under oscillating driving forces (18). They are smoothed out for weaker springs and/or stronger fluctuations.

The thermal fluctuations contribute to the response of the tip in two opposite directions: (a) they help in getting out of locked states at the minima of the total potential $\Phi(X,t) = U_0\cos(\dfrac{2\pi}{b}x) + \dfrac{K}{2}(x-Vt)^2$, and (b) they can make a sliding tip return back to a locked state. Therefore the fluctuation assisted motion is expected to cause a decrease in the mean frictional force at low velocities, when the activation over the potential dominates. At high velocities the second

effect becomes relevant and causes the observed enhancement of the friction in the sliding regime. These behaviors have been actually found in our simulations (see Figure 1a).
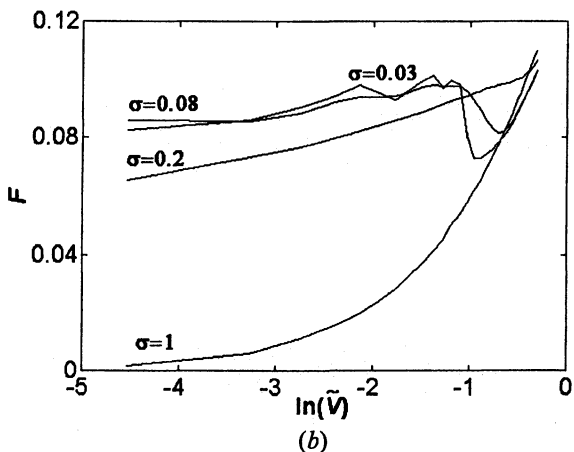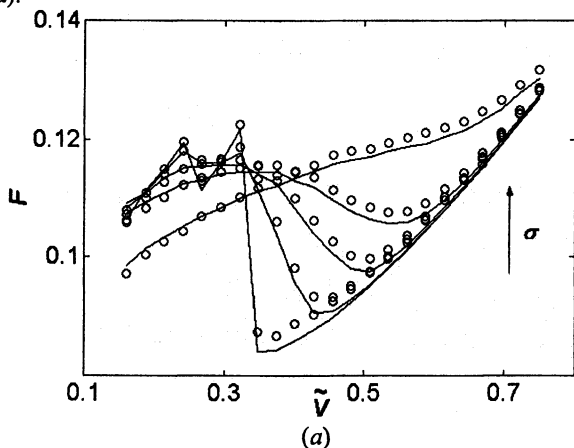

(a)

(b)

Figure 1. An average frictional force as a function of driving velocity (a), and of the logarithm of the driving velocity (b) in dimensionless units. Solid lines and circles show the forces found by using eqs 1 and 2, respectively. The arrow indicates growing intensity of noise. Parameter values: $\sigma = 0, 0.05, 0.08, 0.1, 0.2$; $\alpha = 7 \cdot 10^{-3}$, $\tilde{\eta} = .2$.

Both effects of the fluctuations are clearly reflected in the projections of the time-averaged density of states $\rho(x,v;V,\sigma)$ on x and v, which are shown in the

Figure 2. The density ρ has been accumulated over long periods of time, and in order to improve the averaging process we considered an ensemble of tips. In the stick-slip regime (low driving velocities V) $\rho(x,v;V,\sigma)$ exhibits two maxima as a function of v, a sharp one at $v=0$, and a less pronounced one at $v \neq 0$ (see Figure 2 a). These maxima reflect the existence of two well-defined states, locked and sliding states. Increasing the intensity σ^2 of the noise leads to a decrease in the density of locked states at the cost of an increase of the sliding states. This is reflected in the temperature dependence of the friction force described above. In the sliding regime (high driving velocities) the density of states is localized around $v=V$, and the contribution of the locked state is small. Figure 2b shows that the density as a function of the coordinate for the locked states is concentrated near the minimum of the potential, while for the sliding state it is approximately uniform along the space coordinate. Using eq 2 and the phase space properties of the density of states we conclude that locked states contribute mostly to the *potential* component of the friction force that dominates at low driving velocities, and sliding states contribute to *viscous* friction dominating at high driving velocities.
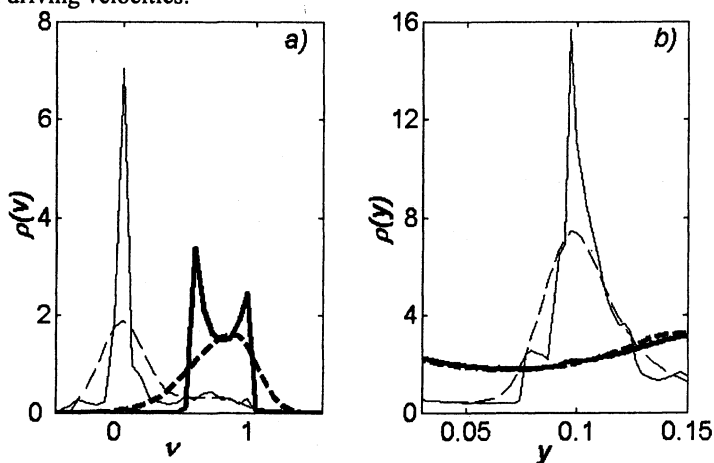
Figure 2. Projections of the time-averaged density of states on the velocity (a) and coordinate (b) of the tip for the driving velocities $\tilde{V} = 0.15$ (thin lines) and $\tilde{V} = 0.7$ (bold lines) and noise amplitudes $\sigma = 0.03$ (solid lines) and $\sigma = 0.2$ (dashed lines). Parameter values as in Figure 1.

The force $F(V)$ measured in DFS is usually plotted versus $\ln V$ based on the theoretical assumption and supported by experiments (2,10,11,19) that $F \propto k_B T \ln V$. In Figure 1b we test this assumption of the logarithmic dependence of the average force on V. Our results clearly show that the logarithmic variation

of $F(V)$ is certainly not universal. This behavior is valid here only over a limited range of the intensities σ^2. For weak and strong fluctuations the behavior of $F(V)$ deviates from the logarithmic one. For weak spring constants, $\alpha/\hat{\eta}^2 \ll 1$, the logarithmic behavior becomes more pronounced and holds over a wider range of parameters σ and V. The dependence of the averaged frictional forces on the driving velocity and noise intensity, as shown in Figure 1, agrees with what is found experimentally: logarithmic dependence on the external velocity and the dependence on the potential (2). The maximal friction force calculated for various values of σ^2 basically behaves the same way.

We suggest below a simple analytical model, which describes the influence of the fluctuations on the density of locked states. The locked states, as mentioned, determine the friction in the region of low driving velocities. In the absence of noise the driven tip leaves a locked state (a minimum of the total potential $\Phi(x,t)$) only when the potential barrier vanishes, i.e. at the instability point where $d^2\Phi/dx^2=0$. At this point the spring force reaches the maximum value of $F_c=2\pi U_0/b$. In the presence of noise the transition to sliding occurs earlier, and the probability $W(t)$ to find the tip in the locked state is given by the following kinetic equation

$$\frac{dW(t)}{dt} = -\frac{\Omega_1(t)\Omega_2(t)}{2\pi\eta/M}\exp[-\Delta E(t)/k_B T]W(t), \qquad (3)$$

where $\Delta E(t)$ is the instantaneous barrier height and $\Omega_{1,2}(t)$ are the effective oscillation frequencies at the bound minimum and maximum of the combined potential $\Phi(x,t)$. The experimentally measured distribution of the maximal spring forces, $P(F_{max})$, and the ensemble averaged maximal force, $<F_{max}>$ can be expressed in terms of W as

$$P(F_{max}) = -\frac{d}{dF_{max}}W(F_{max}), \langle F_{max}\rangle = -\int_0^{F_c}F'_{max}\left(\frac{d}{dF'_{max}}W(F'_{max})\right)dF'_{max} \quad (4)$$

Because of the exponential character of the transition rate we focus on values of F close to the critical field F_c at which the barrier disappears completely. Then the instantaneous barrier height and oscillation frequencies can be written in terms of the reduced bias, $\varepsilon = 1 - F_{max}/F_c$ as (20)

$$\Delta E(t) = U_c\varepsilon^{3/2}, \Omega_{1,2}(t) = \Omega_c\varepsilon^{1/4} \qquad (5)$$

where U_c and Ω_c are the parameters of the unbiased potential $U(x)$. In the case of periodic potential $F_c = 2\pi U_0/b$, $U_c = U_0$, $\Omega_c = 2\pi U_0^{1/2}/(bM^{1/2})$.

Solution of the kinetic eq 3 with $\Delta E(t)$ and $\Omega_{1,2}(t)$ given by eq 5 leads to the final expressions for $P(F_{max})$ and $<F_{max}>$

$$P(F_{\max}) = P_0\varepsilon^{1/2}\exp\left\{-\frac{U_c}{k_BT}\varepsilon^{3/2} - \frac{k_BT\Omega_c^2F_cM}{U_c3\pi\eta KV}e^{-\frac{U_c}{k_BT}\varepsilon^{3/2}}\right\}, \quad (6)$$

$$\left\langle F_{\max}\right\rangle \approx F_c\left\{1-\left(\frac{k_BT}{U_c}\right)^{2/3}\left[\ln\left(\frac{U_c3\pi\eta K}{k_BT\Omega_c^2F_cM}V\right)\right]^{2/3}\right\}, \quad (7)$$

where P_0 is a normalization constant.

The dependence of $<F_{max}>$ on V given by eq 7 is close to a logarithmic dependence for driving velocities $\tilde{V} > \alpha$. For $\tilde{V} < \alpha$ velocity dependence is $<F_{max}(V)> \propto (\ln V)^{2/3}$. This result differs from the previous phenomenological estimations of the maximal spring force that predicted only a logarithmic variation of $<F_{max}(V)>$. It should be noted that eq 7 includes explicitly the dependence of the force on the parameters of the microscopic underlying potential and the macroscopic spring constant K. This equation can be used also for the other types of underlying potentials, for instance for elastic contacts, where logarithmic-type behaviors were also observed (22).

Additional information on the effect of fluctuations on the dynamics of friction can be obtained from the analysis of other observables. Studying a random process it is natural to consider the time evolution of the variance of the displacement, ΔL, of the driven tip. In order to calculate these quantities we consider an ensemble of tips initially placed at the same point on the substrate. Figure 3 displays the time evolution of the size of the spatial "spot", S, which is the span of the ensemble of driven tips. At short times ΔL and S have maxima when most of the tips slide, and minima when they are locked. These limiting values come together as the time increases showing that at any given moment the two types of motion mix. Typical stages of the time evolution of the spot are presented in Figure 4 showing the density distribution in the phase space.

The time evolution of S demonstrates that after a few stick-slip periods the spot reaches its maximal size that equals to a length of sliding of the individual tip. The variance of the displacement shows however a long time redistribution of the density inside the spot. The bottom envelop of $\Delta L(t)$ follows the time

dependence of the mean square displacement for the Ornstein-Uhlenbeck process that describes diffusion in a harmonic potential, supplied here by the spring, $\Delta L(t) = [k_B T(1 - \exp(-2Kt/\eta_{eff}))/K]^{1/2}$ (15). This results from the fact that during sliding the tips diffuse in the combined potential $\Phi(x,t)$ which for a weak spring is harmonic with slight modulations due to the periodic potential of the substrate.
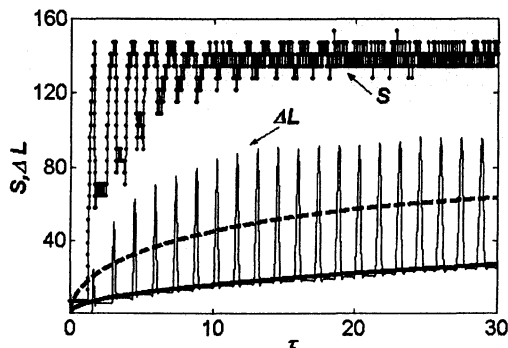
Figure 3. Time evolution of the size S of the spatial "spot" created by the ensemble of driven tips and of the variance of the displacement, ΔL. Solid and dashed lines show the envelops calculated according to the Ornstein-Uhlenbeck equation for the noise intensities σ=0.03 and σ=0.3. Parameter values: α = 3.2·10⁻³, η̃ = .2, Ṽ = .45.
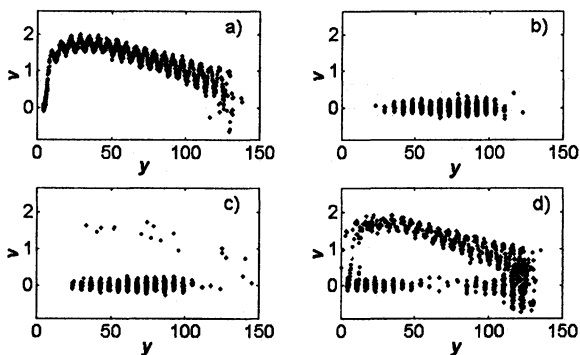
Figure 4. Time evolution of the density of states distribution in the phase space. Typical stages of the time evolution of the portrait are presented: (a) the first jump of the tip from the locked state, (b) the locked state at short times, (c) intermediate stage, (d) stationary shape of the phase portrait showing mixing of locked and sliding states. All portraits are shown within the same interval of the space coordinates. Parameter values as in Figure 3.

It should be noted that in order to fit the Ornstein-Uhlenbeck equation to the results of our calculations, the damping coefficient η_{eff} entered the equation should be considered as a fitting parameter that is inversely proportional to the intensity of the noise. This reflects the influence of the substrate potential that traps tips leading to an increase of the effective friction η_{eff}. This effect is most important at low intensities of the noise. Thus, envelopes of $\Delta L(t)$ and $S(t)$ becomes steeper as σ increases, and they approach asymptotic values at shorter times (see Figure 3).

Dynamic response of adhesion complexes can be also described by the Langevin equation 1 and the approximate kinetic model in eq 3. Here, for illustration the adhesion potential is presented by the Morse potential,

$$U(x) = U_0 \left\{ [1 - \exp(-2b(x - R_c)/R_c]^2 - 1 \right\}.$$ Then the distribution of the

maximal unbinding force and ensemble averaged inbinding force are given by

eqs 6,7 with $F_c = bU_0/R_c$, $U_c = U_0$, $\Omega_c = 2bU_0^{1/2}/(R_c M^{1/2})$.

Equation 7 predicts a universal scaling of $\left(F_c - \langle F_{max} \rangle \right)^{3/2} / T$ with

$\ln(V/T)$ which is independent of temperature. Figure 5 shows results of direct numerical calculations using Langeven equation 1 which confirm the prediction of analytical theory in eq 7.
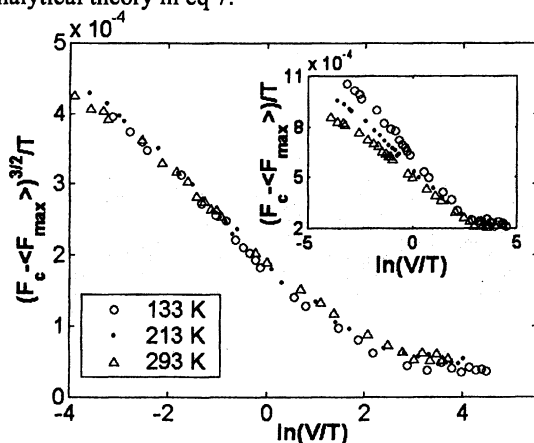
Figure 5. Results of numerical calculations supporting the scaling behavior of the ensemble averaged unbinding according eq 7. The inset shows significantly worse scaling for the traditional description $<F_{max}> \propto const - \ln(V/T)$. The units of velocity V are nm/sec, temperature is in degrees kelvin. Parameter values: $K=0.93$ N/m, $\eta=7.7\times10^{-6}$ sec^{-1} kg, $M = 8.7\times10^{-12}$ kg, $U_0 = 0.12$ nN $\times$ nm, $R_c=0.24$ nm, $b=1.5$.

In a wide range of driving velocities numerical data obtained for three different temperatures collapse to a single straight line in coordinates $\left(F_c - \langle F_{max} \rangle\right)^{3/2} / T$ vs $\ln\left(V/T\right)$. In contrast, the handling of numerical data according to the traditional description, $< F_{max} > \propto k_B T \ln(V/T)$, does not show a good scaling (see inset to Figure 5). Figure 6 presents numerical data and analytical results in eq 6 for a distribution function of rupture forces which have been calculated for a given driving velocity. There is a good agreement between numerical results and theoretical predictions. We note that the distribution function does not have a Gaussian form and it is asymmetric with respect to the maximal force, its width decreases with a decrease of V.
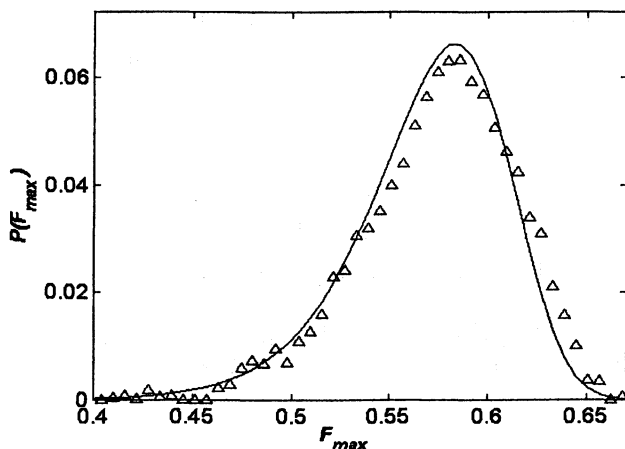
Figure 6. Normalized distribution of the unbinding force at temperature T=293K and velocity V=115 nm/sec. The result from the numerical simulation (solid line) is in a good agreement with the theoretical distribution, eq 6. Parameter values as in Figure 5.

Our results suggest that fitting experimental data on $<F_{max}>$ vs $\ln\left(V/T\right)$ and $P(F_{max})$ to eqs 7 and 6 one can determine three microscopic parameters of adhesive potential: F_c, U_c and $(U_c 3\pi\eta K)/(\Omega_c^2 F_c M)$. Analizing the numerical data presented in Figures 5,6 by this strategy gave values of F_c=0.77 nN, U_c=0.12 nN nm, and $(U_c 3\pi\eta K)/(\Omega_c^2 F_c M)$=7.1×10^{-7} nN sec. This compares well to the corresponding values of F_c=0.75 nN, U_c=0.12

nN nm, and $\left(U_c 3\pi\eta K\right)/\left(\Omega_c^2 F_c M\right)$=6.8 ×10⁻⁷ nN sec used in the numerical calculations. Thus, DFS experiments can provide a new complementary information on adhesive potentials as compared to equilibrium measurements which offer a spontaneous rate of bond dissociation.

Numerical data presented in Figure 5 deviate from the predicted straight line, $\left(F_c - \left\langle F_{max}\right\rangle\right)^{3/2}/T$ vs $\ln\left(V/T\right)$, in the regions of very law and very high driving velocities. The deviation at high driving velocities results from the effect of viscous dissipation given by the term $\eta\dot{x}$ in eq 1, which is not included into the kinetic model 3. In the region where dissipation contributes essentially to the unbinding force the latter grows linearly with the driving velocity and it is only slightly sensitive to the properties of adhesion potential. The deviation of the unbinding force from the analytical form 7 at low driving velocities is a direct result of rebinding events which are clearly seen in time series of the spring force shown in Figure 7.
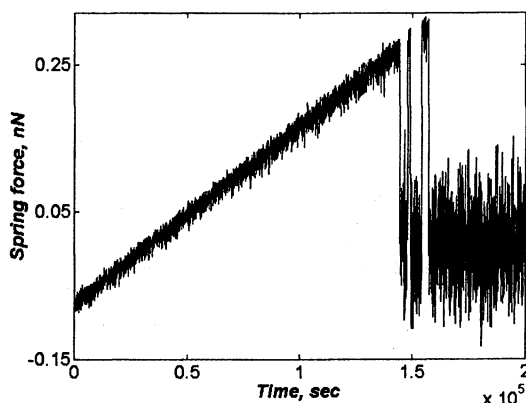
Figure7. Time series of the spring force showing the rebinding events. Parameter values: T=293K, V=115 nm/sec, other as in Figure 4.

In conclusion, DFS results depend not only on the underlying potential and dissipative interaction but also on the intensity of external noise and on the driven spring constant. Tuning these parameters allows to separate the potential and dissipative contributions to the force and to extract desirable information on the microscopic properties of the system. Relationships between equilibrium potentials and the forces measured under nonequilibrium conditions is derived. Increasing the intensity of the noise makes the dissipative component of friction ηV dominate already at low driving velocities and enable to obtain η experimentally.

References

1. Overney, R.M. *et al. Phys. Rev. Lett.* **1996**, *76*, 1272.
2. Gnecco, E. *et al. Phys. Rev. Lett.* **2000**, *84*, 1172.
3. Merkel, R. *et al. Nature* (London) **1999**, *397*, 50.
4. Mehta, A.D. *et al. Science* **1999**, *283*, 1689.
5. Florin, E.-L.; Moy, V.T.; Gaub, H. E. *Science* **1994**, *264*, 415.
6. Rief, M. *et al. Science* 276, 1109 (1997);
7. Oberhauser, A.F. *et. al. Nature* (London) **1998**, *393*, 181.
8. Lee, G.U.; Chrisey, L.A.; Colton, R.J. *Science* **1994**, *266*, 771.
9. Shillcock, J.; Seifert, U. *Phys. Rev. E* **1998**, *57*, 7301.
10. Heymann, B.; Grubmüller, H. *Phys. Rev. Lett.* **2000**, *84*, 6126.
11. Galligan, E. *et al. J. Chem. Phys.* **2001**, *114*, 3208.
12. Dudko, O.K.; Filippov, A.E.; Klafter, J.; Urbakh, M. *Chem. Phys. Lett.* **2002**, *352*, 499.
13. Sang, Y.; Dube, M.; Grant, M. *Phys. Rev. Lett.*, **2001**, *87*, 174301.
14. Tomlinson, G.A.; *Philos. Mag.* **1929**, *7*, 905.
15. Risken, H. *The Fokker-Planck Equation*; Springer, Berlin, 1996.
16. Rozman, M.G.; Urbakh, M.; Klafter, J. *Phys. Rev. Lett.* **1996**, *77*, 683.
17. Rozman, M.G.; Urbakh M.; Klafter, J.; Elmer, F.-J. *J. Phys. Chem.* **1998**, *102*, 7924.
18. Helman, J.S.; Baltensperger, W.; Hołist, J.A. *Phys. Rev. B* **1994**, *49*, 3831.
19. Bouhacina, T. *et al. Phys. Rev. B* **1997**, *56*, 7694.
20. Garg, A. *Phys. Rev. B* **1995**, *51*, 15592.
21. Gradshtein, I.S. and Ryzhik, I.M. *Table of Integrals, Series, and Products*; Academic Press, New York, 1980.
22. Heslot, F. *et al. Phys.Rev. E* **1994**, *49*, 4973.

Chapter 4

Non-Lipshitzian Control of Friction

Y. Braiman, J. Barhen, and V. Protopopescu

**Center for Engineering Science Advanced Research Computing
and Computational Sciences Directorate, Oak Ridge National Laboratory,
Oak Ridge, TN 37831**

Abstract

Recently, we proposed a new algorithm to control frictional dynamics of an array of particles towards pre-assigned values of the average sliding velocity [1]. The algorithm is based on the concepts of terminal attractor and global targeting, which endow the control with robust efficiency. In this paper, we focus on the transient times needed to reach the prescribed behavior and their dependence on the control parameters.

Despite great progress made during the past half century, many issues in fundamental tribology, such as the origin of friction and failure of lubrication, have remained unsolved. Moreover, the current reliable knowledge related to friction and lubrication is mainly applicable to the macroscopic systems and machinery and, most likely, will be only of limited use for micro- and nano-systems. Indeed, when the thickness of the lubricant film is comparable to the molecular or atomic size, its behavior becomes significantly different from the behavior of macroscopic (bulk) lubricant [2]. Better understanding of the intimate mechanisms of friction, lubrication, and other interfacial phenomena at the atomic and molecular scales is expected to provide designers and engineers with the required tools and capabilities to monitor and control friction, reduce unnecessary wear, and predict mechanical faults and failure of lubrication in MEMS and nano-devices [3].

The ability to control and manipulate friction during sliding is extremely important for a large variety of technological applications. The outstanding difficulties in realizing efficient friction control are related to the complexity of the task, namely dealing with systems with many degrees of freedom, under strict size confinement, and only very limited control access. Moreover, a nonlinear system driven far from equilibrium can exhibit a variety of complex spatial and temporal behaviors, each resulting in different patterns of motion and corresponding to different friction coefficient [4].

Friction can be manipulated by applying small perturbations to accessible elements and parameters of the sliding system. This operation requires a-priori knowledge of the strength and timing of the perturbations. Recently, the groups of J. Israelachvili [5] (experimental) and U. Landman [6] (full-scale molecular dynamics computer simulation) showed that friction in thin-film boundary lubricated junctions can be reduced by coupling the small amplitude (of the order of 1 Å) directional mechanical oscillations of the confining boundaries to the molecular degree of freedom of the sheared interfacial lubricating fluid. Using a surface force apparatus, modified for measuring friction forces while simultaneously inducing normal (out-of-plane) vibrations between two boundary-lubricated sliding surfaces, load- and frequency-dependent transitions between a number of "dynamical friction" states have been observed [5]. In particular, regimes of vanishingly small friction at interfacial oscillations were found. Extensive grand-canonical molecular dynamics simulations [6] revealed the nature of the dynamical states of confined sheared molecular films, their structural mechanisms, and the molecular scale mechanisms underlying transitions between them. Significant changes in frictional responses were observed in the two-plate model [7] by modulating the normal response to lateral motion [8]. In addition, surface roughness and thermal noise are expected to play a significant role in deciding upon control strategies at the micro and the nano-scale [9,10]. These results point to a completely new direction for realizing ultra-low friction in mechanical devices.

In a previous paper [1], we proposed a global feedback control scheme, based on the properties of terminal attractors [11, 12]. The main advantage of terminal attractor algorithms consists in their robustness and efficiency [1]. In this paper, we continue the study of the non-Lipschitzian control algorithms for friction, by focusing on the dependence of the transient times on the parameters of the control.

We illustrate the proposed control strategy on a phenomenological model of friction [7,13-16]. Despite their relative simplicity, phenomenological models [10,13-16] show a fair agreement with many experimental results using the friction force apparatus [7,18,19] and quartz microbalance experiments [9,17,20]. The basic equations for the driven dynamics of a one dimensional particle array of N identical particles moving on a surface are given by a set of coupled nonlinear equations of the form [16]:

$$m\ddot{x}_n + \gamma\dot{x}_n = -\partial U / \partial x_n - \partial V / \partial x_n + f_n + \eta(t), \quad n=1,...N \qquad (1)$$

where x_n, is the coordinate of the *nth* particle, m is its mass, γ is the linear friction coefficient representing the single particle energy exchange with the substrate, f_n is the applied external force, and $\eta(t)$ is Gaussian noise. The particles in the array are subjected to a periodic potential, $U(x_n + a) = U(x_n)$, and interact with each other via a pair-wise potential $V(x_n - x_j)$, n, $j = 1,2,...N$. The system (1) provides a general framework of modeling friction although the amount of details and complexity varies in different studies from simplified 1D models [15,16,21,22] through 2D and 3D models [17,23-25] to a full set of molecular dynamics simulations [25].

To better present our ideas, we make the following simplifications, namely: (i) the substrate potential has a simple periodic form, (ii) there is a zero misfit length between the array and the substrate, (iii) the same force f is applied to each particle, and (iv) the interparticle coupling is linear. The coupling with the substrate is, however, strongly nonlinear. For this case, using the dimensionless phase variables $\phi_n = 2\pi x_n / a$, the equations of motion reduce to the dynamic Frenkel-Kontorova model [16]

$$\ddot{\phi}_n + \gamma\dot{\phi}_n + \sin(\phi_n) = f + \kappa(\phi_{n+1} - 2\phi_n + \phi_{n-1}), \quad n = 1, 2, ... N \quad (2)$$

Throughout this paper, we shall use an array with $N=25$ particles. We performed extensive numerical simulations for other arrays sizes ($3 < N < 40$) to verify that we indeed present a typical example. Without control, we observed four co-existing different regimes: periodic sliding, periodic stick-slip, chaotic stick-slip, and rest (no motion). All motion types are obtained by only changing the initial conditions of the particle's positions and velocities, but not the system's parameters. The average (center of mass) velocity for the "natural" (i.e.. uncontrolled) motion may take only a limited range of values, namely: (i) $v = f / \gamma$ for periodic sliding motion, (ii) $v = nv_0$, where n is an integer, and $v_0 =$

$$\frac{2\pi}{nN\gamma} \sqrt{\frac{\pi - \cos^{-1} f}{\pi}} (\kappa - \kappa_c)^{1/2} \quad , \text{ for periodic stick-slip motion, (iii) } v = 0$$

for rest (no sliding). [16]. In the range of parameters under consideration, we observed only one single value of the average velocity for chaotic stick-slip.

To better illustrate the dynamics of the uncontrolled system, we display the time series of the average velocity and the velocity of the first particle in the array for different sets of initial positions and initial velocities.

Our objectives are to: (i) achieve any targeted value of the average sliding velocity using only small values of the control and (ii) significantly reduce the transient time needed to reach the desired behavior. To that effect, we propose the following control algorithm:

$$C(t) = \alpha(v_{t\arg et} - v_{cm})^\beta \quad (3)$$

where $v_{cm} = (1/N) \cdot \sum_{n=1}^{N} \dot{\phi}_n$ is the average (center of mass) velocity, v_{target} is a
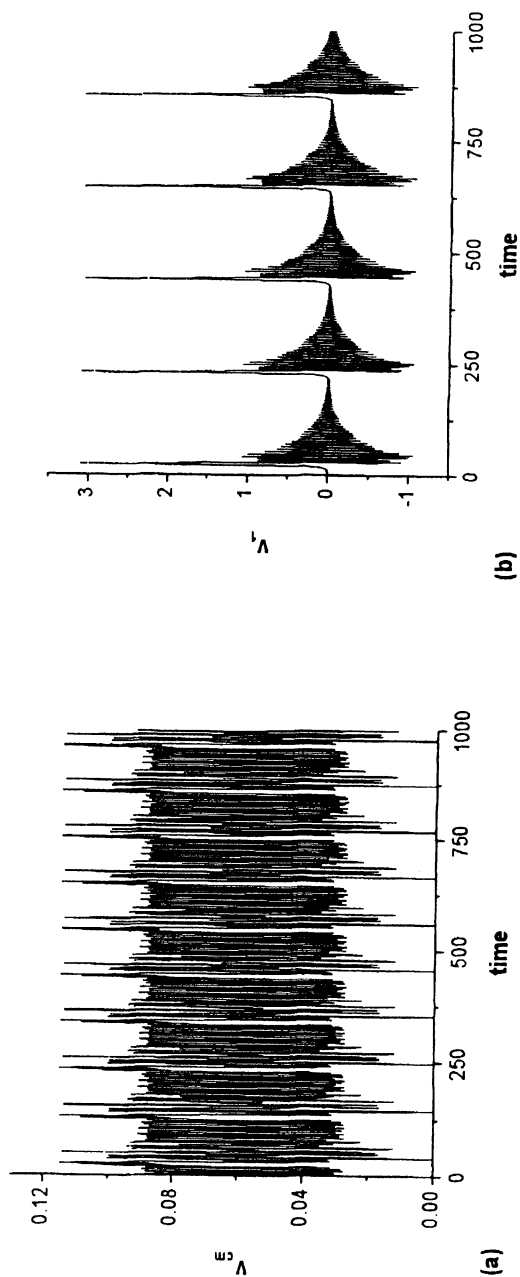
Figure 1a-b: (a) Time series of the average velocity and (b) time series of the first particle in the array with no control. The average velocity is 0.0625. The other parameters are: $N = 25$; $f = 0.3$; $\gamma = 0.1$; $\kappa = 0.26$.
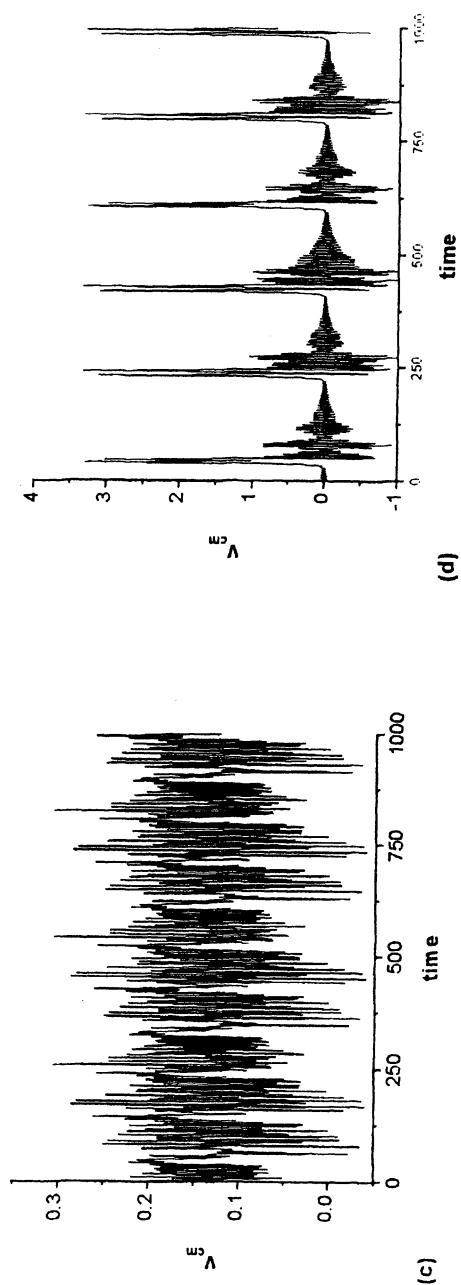
Figure 1c-d: (c) Time series of the average velocity and (d) the time series of the first particle in the array with no control. The average velocity is 0.13. The other parameters are: $N = 25$; $f = 0.3$; $\gamma = 0.1$; $\kappa = 0.26$.
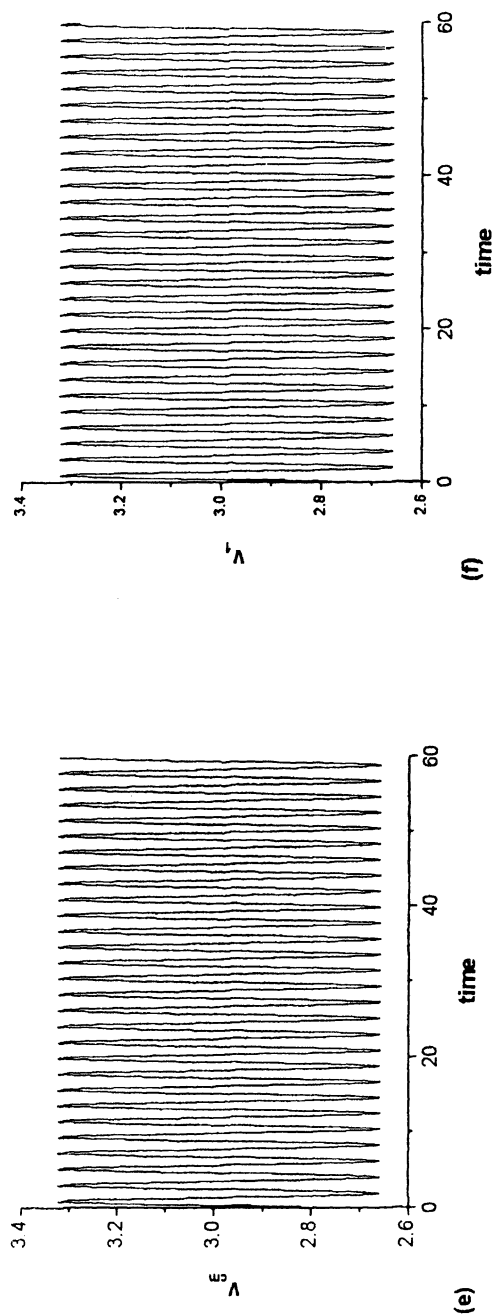
Figure 1 e-f: (e) Time series of the average velocity and (f) time series of the first particle in the array with no control. The average velocity is 3.0. The other parameters are: $N = 25$; $f = 0.3$; $\gamma = 0.1$; $\kappa = 0.26$.
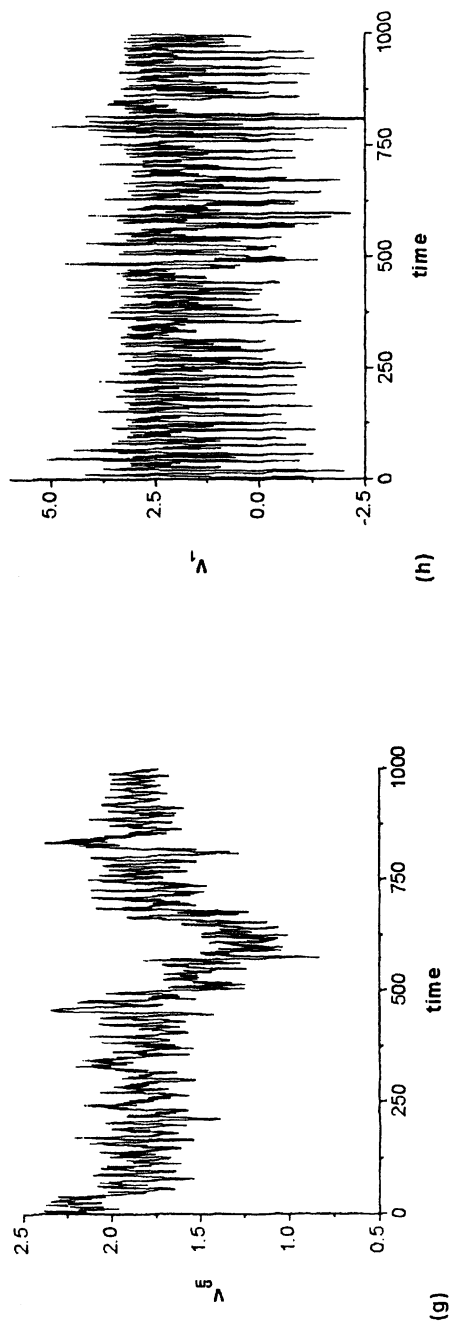
Figure 1g-h: (g) Time series of the average velocity and (h) time series of the first particle in the array with no control. The average velocity is 1.81. The other parameters are: $N = 25$; $f = 0.3$; $\gamma = 0.1$; $\kappa = 0.26$.

constant targeted velocity for the center of mass, $\beta = 1 /(2n +1)$, and $n = 1, 2, 3....$ Note that the control term is identical for all the particles in the array and requires only the knowledge of the average velocity of the array. This control utilizes the concept of "terminal attractors" [11,12] whose relevance for the dynamics is explained below.

The equations of motion (Equation 2) in the presence of the control term $C(t)$ (Equation 3) reads:

$$\ddot{\phi}_n + \gamma\dot{\phi}_n + \sin(\phi_n) = f + \kappa(\phi_{n+1} - 2\phi_n + \phi_{n-1}) + C(t) \qquad (4)$$

System (4) can be written as a 2N-dimensional first order system:

$$\dot{\phi}_n - F_n(\phi_1, \phi_2, \ldots \phi_{2N}) = 0, \quad n = 1, 2, 3, \ldots, 2N \qquad (5)$$

where, for simplicity, we maintain the same notation for the (now different) unknown functions. The fixed points of this *2N*-dimensional, dissipative dynamical system are obtained by solving the stationary version of Eq. (5). If the real parts of the eigenvalues μ_e of the Jacobian matrix, *M*, $M_{nm} = \partial F_n/\partial \phi_m$, at a fixed point are all negative (that is $Re\mu_e < 0$) then this point is locally asymptotically stable and constitutes a local attractor of the dynamics.

When a nonlinear dynamical system satisfies the Lipschitz condition, namely $|\partial F_n /\partial \phi_m | \leq K < \infty$, there is a unique solution for each initial configuration. Moreover, the time spent by each trajectory to reach an attractor is, in principle, infinite. Therefore, the time needed to reach the desired target within the needed precision may become unacceptably large.

In contrast, the terminal attractor dynamics that we are utilizing violates *by construction* the Lipschitz condition. As a result, trajectories reach the terminal attractor in finite time. To illustrate this point, consider one of the simplest systems with terminal attractor [11], i.e. the equation $\dot{\phi} = -\phi^{1/3}$. At the equilibrium point, $\phi = 0$, the Lipschitz condition is violated, since $\partial\dot{\phi} / \partial\phi = -(1 / 3)\phi^{-2/3}$ tends to minus infinity as ϕ tends to zero. Also, one can easily check that the trajectory started at the initial point ϕ_0 reaches the terminal attractor in a finite time, $\tau = \dfrac{3}{2}\phi_0^{2/3}$.

This is precisely the effect realized by the non-Lipschitzian control term, $C(t)$. The "infinite attraction power" of the "terminal" (non-Lipschitzian) attractor endows the proposed algorithm with excellent efficiency and robustness, as illustrated in Figure 2 for the target velocity of: $v_{target} = 1$. Red color lines indicate the time series of the control (Equation 3), while the blue lines show the time series of the velocity of the center of mass. In all cases, we reached and sustained the (arbitrarily chosen) target value for rather small values of the control.
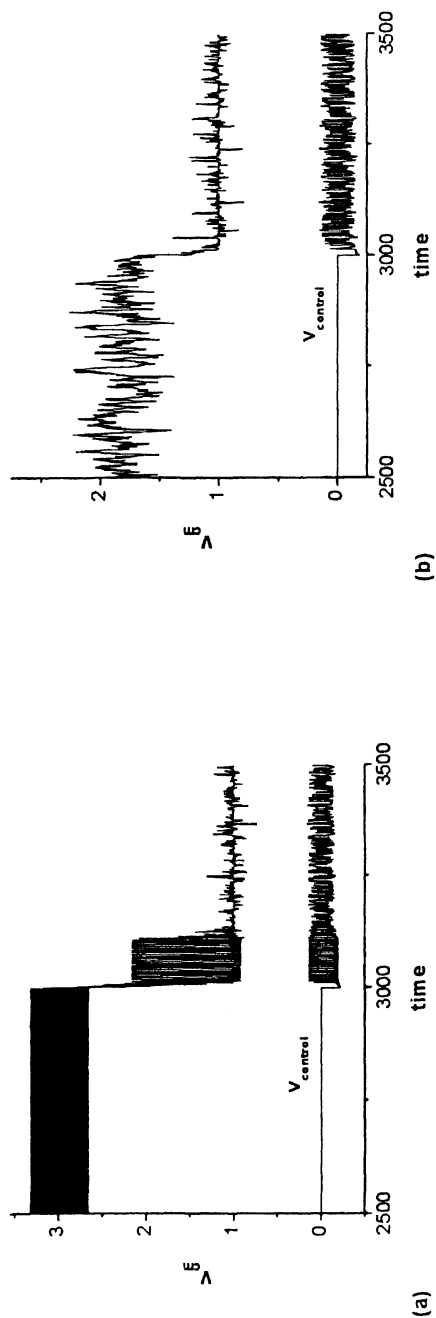
Figure 2a-d. Time series of the average velocities and of the control. In all cases, the targeted velocity is equal to 1.0, while the initial uncontrolled velocities are: 3, 1.81, 0.0625, and 0. The other parameters are the same as in Figure 1, and the control parameters are: $\alpha = 0.15$, and $\beta = 1/7$. The control is applied at time $t = 3000$.
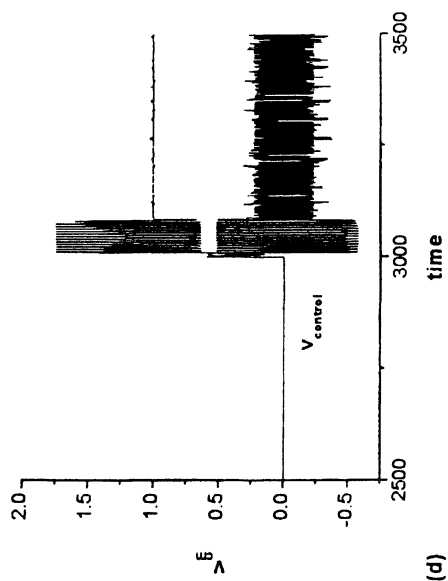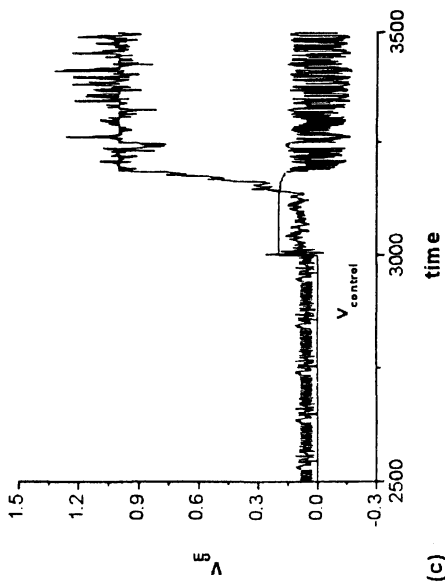
Figure 2. *Continued.*

We performed extensive testing of the proposed algorithm (Eqs.3-4) by choosing numerous values of the target velocity [1]. For some values of v_{target}, the dependence of the average velocity, v_{cm} on α appears to be irregular. In all cases, however, we succeeded to identify a specific value of control α to reach the desired value of the average velocity. We also studied the convergence process, i.e. the dependence of the average velocity of the center of mass as a function of the control amplitude α. Figures 3a-b illustrate this dependence.

Figure 3a illustrates that the convergence to the targeted value is faster for smaller values of the exponent. The reason for this behavior is the fact that smaller exponents correspond to larger average controls in the vicinity of the target (Fig. 3b).

In summary, we proposed a new type of algorithm to control friction of sliding nano-arrays. This algorithm is based on the concepts of "terminal attractor" and global targeting and requires only the knowledge of the velocity of the center of mass of the array. We demonstrated the ability to control the array towards the desired sliding velocity and this control was achieved in a short transient time. Finally, we studied the dependence of the transient time on the parameters of the control.
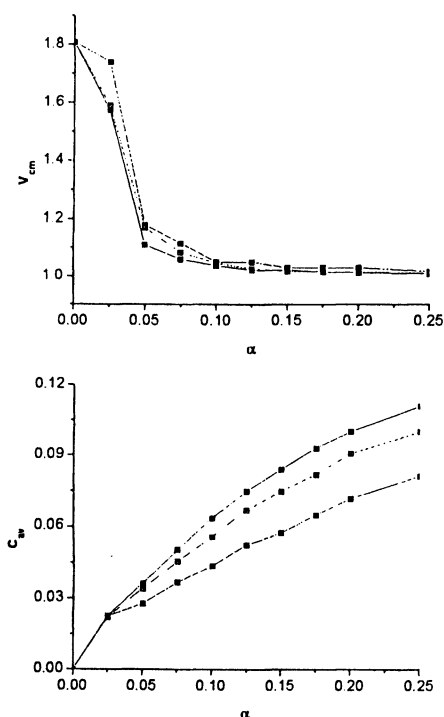
Figures 3a-b. (a) Dependence of the average velocity on the control amplitude α; (b) dependence of the time averaged control on the control amplitude. The exponent values are: $\beta = 1/7$ (dashed line), $\beta = 1/5$ (dotted line), and $\beta = 1/3$ (solid line), and all the other parameters are as in Figure 1.

Acknowledgment

References

1. Y. Braiman, J. Barhen, and V. Protopopescu, Phys. Rev. Lett. **83**, 094301 (2003).
2. Y. Z. Hu and S. Granick, Tribol. Lett., **5**, 81 (1998). Fujita in Proceedings IEEE, Tenth Annual International Workshop on Micro Electro Mechanical Systems, Published by: IEEE Robotics and Control Division Div., New York, NY (1997). Brushan, in Proceedings IEEE, The Ninth Annual International Workshop in Micro Electro Mechanical Systems, Published by: IEEE Robotics & Autom. Soc. IEEE, New York, NY (1996).
3. H. G. E. Hentschel, F. Family, and Y. Braiman, Phys. Rev. Lett.. **83**, 104 (1999).
4. M. Heuberger, C. Drummond, and J. Israelachvili, J. Phys. Chem. B, **102**, 5038 (1998).
5. J. P. Gao, W. D. Luedtke, and U. Landman, J. Phys. Chem. B, **102**, 5033 (1998).
6. M. G. Rozman, M. Urbakh, and J. Klafter, Phys. Rev. Lett., **77**, 683 (1996), and Phys. Rev. E **54**, 6485 (1996).
7. V. Zaloj, M. Urbakh, and J. Klafter, Phys. Rev. Lett., 82, 4823 (1999).
8. Y. Braiman, F. Family, H. 6. E. Hentschel, C. Mak, and J. Krim, Phys. Rev. E, **59**, R4737 (1999).
9. J. P. Gao, W. D. Luedtke, and U. Landman, Tribol.Lett., **9**, 3 (2000).
10. J. Barhen, S. Gulati, and M. Zak, IEEE Computer, **22(6)**, 67 (1989).
11. M. Zak, J. Zbilut, and R Meyers, *From Instability to Intelligence,* Springer (1997).
12. J. M. Carlson and A. A. Batista, Phys. Rev. E, **53**, 4153 (1996).
13. A. A. Batista and J. M. Carlson, Phys. Rev. E, **57**, 4986 (1998).
14. B. N. J. Persson, Phys. Rev. B, 55, 8004 (1997).
15. Y. Braiman, F. Family, and H. G. E. Hentschel, Phys. Rev. B, **55**, 5491 (1997), and Phys. Rev. E, **53**, R3005 (1996).
16. B. N. J. Persson and A. Nitzan, Surface Science **367**, 261 (1996).
17. G. Reiter, A. L. Demirel, and S. Granick, Science **263**, 1741 (1994);
18. A. L. Demirel and S. Granick, Phys. Rev. Lett., **77**, 4330 (1996).
19. H. Yoshizava, P. McGuiggan, and J. Israelachvili, Science, **259**, 1305 (1993); H. Yoshizava and J. Israelachvili, J. Phys. Chem. **97**, 11300 (1993).
20. C. Daly and J. Krim, Phys. Rev. Lett., **76**, 803 (1996); C. Mak and J. Krim, Phys Rev. B, **58**, 5157 (1998).

21. B. N. J. Persson, Phys. Rev. B, **48**, 18140 (1995), and J. Chem. Phys., **103**, 3849 (1997).
22. F.-J. Elmer, J. Phys. A, **30,** 6057 (1997), M. Weiss and F.-J. Elmer, Z. Phys. B, **104**, 55(1997), and Phys. Rev. B, **53**, 7539 (1996).
23. E. D. Smith, M. O. Robbins, and M. Cieplak, Phys. Rev. B, **54,** 8252 (1996).
24. B. J. Sokoloff, Phys. Rev. B, **52**, 5318 (1995).
25. B. Brushan, J. Israelachvili, and U. Landman, Nature, **374**, 607 (1995), U. Landman, W. D. Luedtke, and J. P. Gao, Langmuir, **12**, 4514 (1996).

Chapter 5

Nature of Instabilities in Boundary Lubricants and Their Effect on Kinetic Friction

Martin H. Müser[1,2] and Martin Aichele[2]

[1]Department of Applied Mathematics, University of Western Ontario, London, Ontario N6A 5B7, Canada
[2]Institut für Physik, Universität Mainz, 50099 Mainz, Germany

While boundary lubricants automatically lead to static friction between two crystalline walls, it is shown that the persistence of finite *kinetic* friction $F_k(v)$ at small sliding velocities v depends on the qualitative features of the system such as dimensionality of the interface, symmetry, and also details of the lubricant-wall interactions. This observation can be understood from an analysis of the instabilities that occur in the boundary lubricant. These differ qualitatively from elastic instabilities. As a result, corrections to the $F_k(v)$ law due to thermal noise in boundary lubricants are of order $T\ln v$ instead of order $(T\ln v)^{2/3}$ as for elastic instabilities. While most of the analysis is based on idealized assumptions, some predictions are tested by large-scale molecular dynamics simulations.

The atomistic origin of wear less finite friction F between two solids in slow relative sliding motion has remained a controversial issue. It has long been recognized that solid friction must be due to instabilities (*1*), unlike Stokes or viscous friction, for which F is linear in sliding velocity v_0. Linear friction laws can be explained in terms of equilibrium statistical mechanics (*2*). The condition

for linear friction to occur is the (anharmonic) coupling of the central degree of freedom to (infinitely) many other degrees of freedom. The damped motion of a Brownian particle in solution and phonon damping are two examples for linear friction. However, solid friction is typically almost independent of v_0, in many cases there is only a weak logarithmic dependence on v_0. A v_0 independent friction law can be understood from the following picture: When a solid slider is moved laterally with velocity v_0 relative to a substrate, `pops´ (instabilities) of certain microscopic degrees of freedom become inevitable, even if v_0 is extremely small. The microscopic peak velocities during these sudden pops are almost independent of v_0. Consequently, the energy dissipated via a Stokes-type mechanism also becomes independent of v_0 and $F(v_0)$ remains finite as v_0 tends to zero. The question is what are the relevant microscopic instabilities and how does the motion of the associated degrees of freedom change when the boundary conditions (temperature, pressure, humidity,...) change?

The prototypical instability leading to solid friction was first proposed by Prandtl in 1928 (3) and then suggested again one year later by Tomlinson (4). In their one-dimensional model, a surface atom in the slider is coupled to its ideal lattice site with a spring of stiffness k. The lattice site moves at constant velocity v_0. Interactions with the rigid substrate are modeled with a potential energy surface V that is periodic in the substrate's lattice constant plus some drag force linear in the atom's velocity v. If k is smaller than some threshold value, pops become unavoidable and kinetic friction F_k remains finite as v_0 goes to zero. Instabilities in more complex elastic systems have been investigated since the Prandtl Tomlinson (PT) model was introduced. Examples are the motion of elastic manifolds on disordered substrates (5) and jump to contact instabilities of microasperities (6). In the absence of thermal excitations, the friction velocity relationship is given by:

$$F_k(v_0) = F_k(0) + c \, v_0^{\beta} \tag{1}$$

In principle, elastic instabilities are a legitimate scenario for solid friction to occur. However, they do not seem to be the most generic mechanism. Detailed calculations and atomistic computer simulations show that *atomic-scale* elastic instabilities as suggested in the PT model should be almost impossible (7). Incorporating larger length scales can change the picture. For instance, an AFM tip may interlock geometrically with the substrate on a nanometer scale without elastic instabilities (8). Those instabilities that do occur involve larger length scales, because they arise as a consequence of the large compliance of the cantilever. Yet, for multi-asperity contacts, where the long-range elastic interactions may play a role, the net friction coefficient would be remain small if geometric interlocking of surface corrugations on a local scale was the main friction mechanism (9).

It has been suggested that weakly adsorbed atoms and molecules, for instance a boundary lubricant, may be a more likely source for the commonly observed solid friction *(10)-(12)*. A simple argument shows why such particles lead to *static* friction. Molecules that are only weakly bound to either surface can accommodate the surface corrugation of both walls simultaneously. This will lock the walls together even if they are incommensurate. However, the argument is insufficient to explain kinetic friction, which requires – as argued above - the occurrence of instabilities. One could envision a situation where a boundary-lubricated system shows finite static friction but zero kinetic friction in the small-velocity limit. This phenomenon occurs, for instance, in the (athermal) commensurate Prandtl-Tomlinson model for sufficiently strong spring stiffness k.

Here, it will be discussed in some more detail than in a previous work *(13)*, what the features of the atomic scale instabilities are in the case of boundary lubricants and how they relate to the `pops´occuring in the Prandtl-Tomlinson model. The main focus will be on a rather simplifying picture, namely the neglection of interactions between adsorbed atoms. Some of the predictions will be tested in terms of molecular-dynamics simulations.

Prandtl-Tomlinson model revisited

The basic idea of the Prandtl-Tomlinson (PT) model is described in the introductory remarks to this chapter. The equation of motion for atom n of mass m in the slider can be written as:

$$m \, a_n + m \, \gamma v_n = -k(x_n - x_n^0) + f \sin(x_n / b), \qquad (2)$$

where the atom's equilibrium lattice site $x_n^0 = v_0 t$ moves at a velocity of v_0. The maximum force exerted from the substrate on an atom is f, the substrate's lattice constant is $b/2\pi$, and γ is a damping term, which reflects the interaction with phonon bath which is not treated explicitly.

Let us discuss the motion of atom n qualitatively for large and small values of k. If k is larger than f/b, then it is easy to see that each atom has only one well-defined mechanical equilibrium site, irrespective of the value of x_n^0. When the upper solid is moved at a constant, small velocity v_0, each atom will always be close to its unique equilibrium position. This equilibrium position moves at a velocity v that is in the order of v_0. Hence the dissipated friction force is of the order of $m\gamma v_0$ and consequently F_k vanishes linearly with v_0 as v_0 tends to zero. The situation becomes different for $k < f/b$. Atoms with more than one stable equilibrium position will now pop from one stable position to another one when the slider is moved laterally. For small pulling velocities v_0, such a process

occurs when an atom does not have a mechanically stable position at time $t+\delta t$ in the vicinity of the old stable position near which it was located at time t. Such a situation is discussed in Fig. 1 in terms of the time-dependent potential energy $V(x)$ associated with the conservative forces, namely

$$V(x) = fb \cos(x/b) + \frac{1}{2} k (x_n - x_n^0)^2 \qquad (3)$$

In the ``popping'' processes (indicated by the thick solid line in Fig. 1), the velocities v_n will exceed v_0 by orders of magnitudes for $v_0 \to 0$. At small v_0, the dynamics along most of the sinusoidal line is rather independent of the precise value of v_0 and the dissipated energy $\int dx \gamma m v_n$ has a well-defined positive limit $F_k(v_0=0)$. Hence in the absence of thermal fluctuations that have been disregarded in this discussion so far, F_k remains finite even in the limit of infinitesimally small v_0.
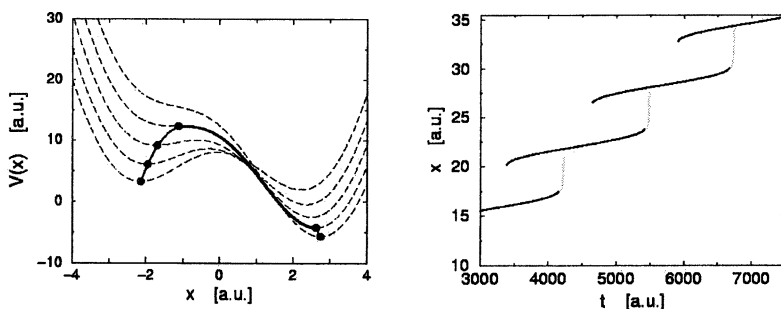
Figure 1: Left: Schematic representation of the time evolution of the potential energy in the Prandtl model (dashed lines), see Eq. (3). All curves are equidistant in time, separated by a constant time interval Δt. The circles denote mechanically stable positions and the solid line connects mechanically stable points, indicating the motion of a damped point atom. Right: Schematic representation of the time evolution of the trajectories in the Prandtl model. The thin, black lines show the mechanically stable positions, the gray line the adiabatic trajectory of the damped particle.

The time evolution of the trajectories is shown in Fig. 1. It can be seen that the (damped) dynamics of the atoms follows essentially the stable position until no stable mechanical position is available any longer in the immediate vicinity of the old stable position. In this case a pop occurs which leads to energy dissipation and hence to finite friction. The time evolution of mechanically stable positions is thus essential to understand low-velocity kinetic friction. From this analysis, one can see that solid friction arises from instabilities. Prandtl formulated the condition for finite F_k in the limit of small sliding velocities: *If the elastic coupling of the mass points is chosen such that at every instance of*

time a fraction of the mass points possesses several stable equilibrium positions, then the system shows hysteresis.... In the context of friction, hysteresis translates to finite static friction or to a finite kinetic friction that does not vanish in the limit of small sliding velocities. It is not necessary for instabilities to be mechanical in nature. During the ACS 2002 meeting in Orlando, Putterman presented an analysis of electronic instabilities and concluded that these contribute to the tribological features of his system.

Thermal effects in the Prandtl-Tomlinson model

Thermal effects can be incorporated into the Prandtl-Tomlinson model in terms of Langevin dynamics as discussed by Sang et al (*14*) and Dedkov et al (*15*). Sang et al. exploit the analogy of the elastic instability to temperature driven spinodal decomposition. They analyze the effect of thermal fluctuation by considering the time dependence of the energy barrier that an atom has to overcome to escape into the energetically more favorable well. In the regime in which we are interested (small sliding velocities but still far from thermal equilibrium), the friction force varies even slower than logarithmically with v, namely with $(T \ \ln v)^{2/3}$. In his pioneering paper, Prandtl obtained velocity corrections due to thermal fluctuations in the order of $\ln v$ (like many others after him), but he neglected the effect that the potential barrier is continuously ramped. One may note that static friction can only be observed if there is a meaningful time scale separation between experimental times and the *relevant* relaxation time of the system.

Extension of analysis to boundary lubricants

Prandtl's condition for friction does not require the instabilities to be elastic. One may apply a similar analysis as that presented in the previous discussion to a lubricant confined between two walls, in which the substrate is considered fixed and the slider moves at constant sliding velocity v_0. In a first approximation, one may assume that the lubricant atoms move along the adiabatic solution, which means that the forces at every point always balance exactly. Then one may consider damped dynamics, and in a third step include thermal fluctuations.

In the following qualitative discussion, we neglect interactions between lubricant atoms. The top wall is moved at constant velocity v_0 with respect to the bottom wall. While the confining solids are considered to be rigid, dissipation is included just like in Eq. (2), thus

$$ma_n = -m\gamma_b v_n - m\gamma_t (v_n - v_0) + f_b(x_n) + f_t(x_n - v_0 t) \quad (4)$$

where f_b and f_t are the forces that the bottom wall and the top wall exert on the lubricant atom n, respectively. $\gamma_{b,t}$ is the drag friction coefficient from the bottom/top wall. We now turn to a discussion of the motion of the adiabatic and damped solution as a function of symmetry and surface potential in one-dimensional systems.

Commensurate walls

Let us first consider the case in which the lubricant-substrate and the lubricant-slider interaction is described with one single harmonic, i.e. $f_b(x_n) = f_0 \cos(x/b)$ and $f_t(x_n) = f_0 \cos[(x-v_0 t)/b]$. The net time-dependent potential that the lubricant experience is then simply given by:

$$V(x,t) = 2f_0 \cos\left(\frac{1}{2b}v_0 t\right)\cos\left(\frac{1}{b}\left[x - v_0 t / 2\right]\right), \quad (5)$$

moreover one should assume symmetry concerning γ_t and γ_b.

As we will discuss below in some more detail, the athermal, completely symmetric description of the walls without higher harmonics in the potential $V(x)$ is a complicated (multi)critical point with respect to many variables. Here the term *critical point* is meant within Morse theory (*16*), although we will use the language usually employed in the context of phase transitions. Note that Landau's theory of phase transition is a special case of Morse theory. A critical point within Morse theory is a point in parameter space, where mathematical solutions change their behavior qualitatively when one or more parameters are infinitesimally varied. In the present case, the adiabatic solution moves at velocity $v_0 t/2$ as can be seen from Eq. (5). Although half of the time, the solution corresponds to the maximum of $V(x,t)$. There is no symmetry-breaking element making the atom slide 'downhill'. The solution will automatically be qualitatively different in that it requires non-trivial functions periodic in time if one of the following conditions is no longer satisfied: $\gamma_t - \gamma_b = 0$, $b_t - b_b = 0$, $V_t - V_b = 0$, and $f_{n>0} = 0$, where $f_{n>0}$ denotes higher harmonics in the potential. Furthermore thermal fluctuations and round-off errors in numerical treatments can prevent the atom from following the constant velocity solution. All these perturbations to the completely symmetric case will ultimately lead to a *qualitatively* altered dependence of friction on velocity.

In the following, we will introduce ad-hoc a symmetry-breaking element by using $\gamma_t = 0$. This choice is a matter of convenience, which cannot be justified from symmetry arguments, but it allows us to break symmetry in a well-controlled way. For incommensurate walls, this choice is unproblematic, as there is no reason for γ_t to equal γ_b. Despite this symmetry breaking, the commensurate case without higher harmonics remains a multicritical point.

Effect of higher harmonics

We will now be concerned with an analysis of the adiabatic motion, similar to the analysis shown on the right-hand side of Fig. 1. In addition to the term $f_0 b \cos(2\pi x/b)$ in the lubricant wall potential, the first higher harmonic is considered, namely $f_1 b \cos(\pi x/b)$. As shown in Fig. 2, it turns out that the qualitative features of the adiabatic solution depend only on the sign of f_1.
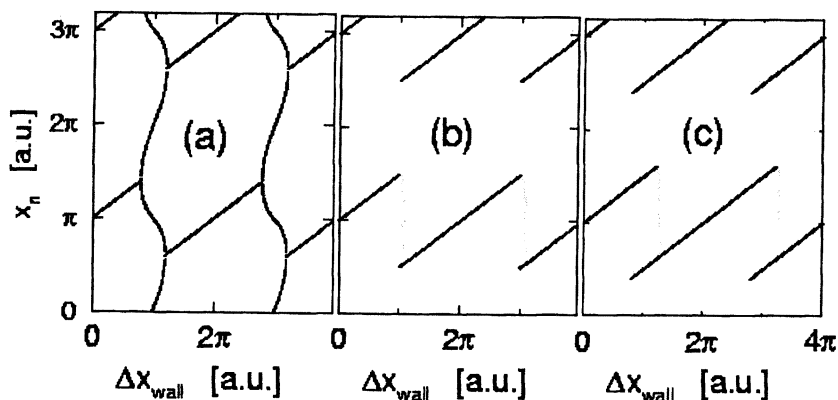
Figure 2: Mechanical equilibrium positions (black lines) of a particle physisorbed between two commensurate walls with various first higher harmonics f_1 as a function of relative, lateral displacement Δx_{walls} between the walls. The thick gray line indicates the damped motion of an atom. (a) $f_1 > 0$: Mechanically stable positions are connected. (b) $f_1 = 0$. Jumps of atoms occur between symmetrically equivalent positions. (c) $f_1 > 0$. Pops occur between inequivalent positions

The differences in the motion of the atoms discussed in the caption of Fig. 2, can be expected to result in different friction-velocity relationships. Only if jumps occur between symmetrically inequivalent positions, can we expect F_k. to remain finite, when v_0 tends to zero. For the cases shown in Fig. 2 (a) and (b), F_k. will tend to zero, however, this will not happen linearly, as the ratio of the atomic (peak) velocities v and the relative wall velocity v_0 will diverge as v_0 approaches zero. In Fig. 3, numerical results for the friction force are shown that confirm this behavior. The F_k (v_0) relationship can be fit well using Eq. (1).
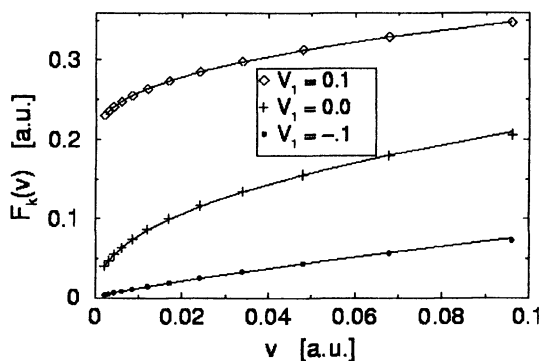
Figure 3. Kinetic friction force F_k (v_0) as a function of sliding velocity v_0 for commensurate walls with different first higher harmonics. Straight lines are fits according to Eq. (1). Only positive values of f_1 lead to finite F_k (0). The apparent exponents β turns out to be: (i) $\beta=0.29$ for $f_1>0$. (ii) $\beta=0.41$ for $f_1=0$. (iii) $\beta=0.74$ for $f_1<0$. A finite $F_k(0)$ is only assumed .

Incommensurate walls

If we consider two walls with $b_t \neq b_b$ where each wall is described by one single harmonic, then the two surfaces do not share a single periodicity and therefore will behave in many aspects as if they were incommensurate. This concerns in particular the F_k (v_0) relationship, where it is not relevant whether the ratio of b_t and b_b is rational or irrational as long as it differs from unity. The situation is similar to the Prandtl-Tomlinson model, where the kinetic friction does not depend on the degree of commensurability, while static friction is indeed a function of commensurability (7).

If higher-order harmonics are absent in the lubricant-wall potential, then one wall has the larger maximum force that it can exert on the confined atom and the atom will always be dragged with that wall. The peak velocities of the adsorbed atom will be in the order of the relative wall velocity and as a consequence, kinetic friction will be similar to Stokes friction. The friction-velocity

relationship can only change when higher harmonics are considered. We find again a critical first higher harmonic f_1^*, which for incommensurate walls, however, is positive. In order to minimize numerical errors for the calculation of the friction force, it is appropriate to chose b_t / b_b rational and to average the friction force over an integer multiple of the common period. Results for the adiabatic solution and the kinetic friction in the incommensurate case are shown in Fig. 4. The results for $F_k(v_0)$ can again be fitted with Eq. (1).
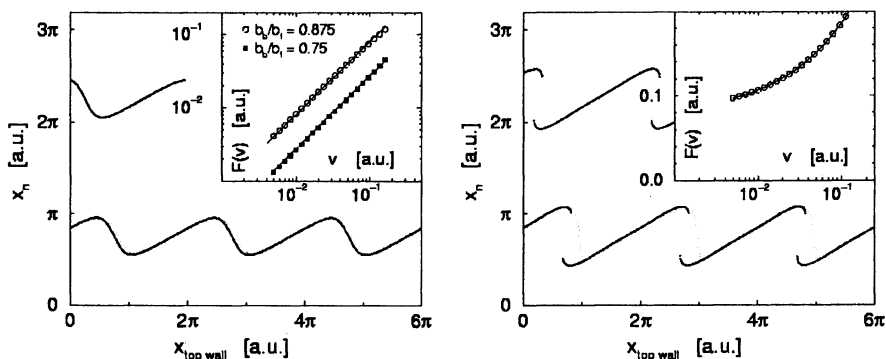
Figure 4. Adiabatic positions of an atom confined between two walls, with similar notations as in Fig. 2. Here, however, walls are incomensurate. The insets show the kinetic friction force F_k (v_0) as a function of sliding velocity v_0. Left: incommensurate walls with first higher harmonic $f_1 < f_1^*$. Right: $f_1 > f_1^*$.

Incorporation of thermal noise

Up to this point, the effect of thermal noise has been neglected in this study. The effect of such fluctuations can be incorporated into the description in terms of a Langevin thermostat. This is done by adding a random force $\Gamma(t)$ to the equation of motion, Eq. (4), such that $\Gamma(t)$ satisfies the fluctuation-dissipation theorem.

Let us discuss the implications of non-zero temperature qualitatively. The random forces will assist the atoms to overcome the barriers. If v_0 is sufficiently small, the atoms will be able to equilibrate. The distribution of positions and velocities will be close to the distribution in thermal equilibrium and the shear force can be calculated from linear response theory. This implies that friction must be linear at small sliding velocities. At large v_0, however, thermal activation is less efficient and the friction-velocity dependence will be altered barely due to thermal noise. Figure 5 shows the friction velocity dependence for the critical case of commensurate walls in a broad range of velocities.
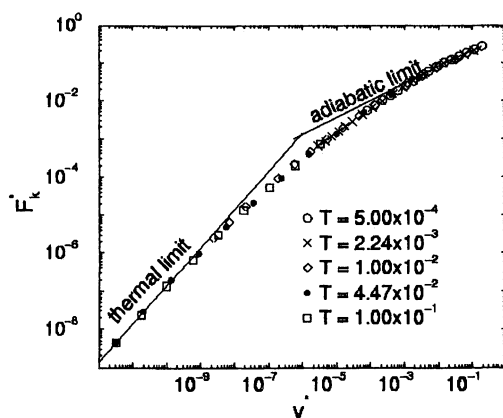
Figure 5. Friction velocity dependence for boundary-lubricated, commensurate walls in the impurity limit at different temperatures T in case of zero higher harmonic included. The reference temperature is T = 5·10⁻⁴. Scaled data from additional temperatures assuming Arrhenius activation are included.

It can be seen that the predicted behavior is found for the multicritical case, namely large velocities are in agreement with the critical behavior, while small velocities exhibit the linear friction known from equilibrium statistical mechanics. A similar analysis can be done if first-order instabilities are present, which means that athermal kinetic friction would remain finite. While this is not shown here explicitly, we would like to mention nevertheless that at small velocities friction is linear before it increases proportional to ln$v$ as discussed elsewhere (*13*).

Two-dimensional surfaces

Qualitative discussion of impurity limit in 2d

Real surfaces are two-dimensional and it is necessary to address the question in how far this alters the present discussion. As far as commensurate surfaces with negligible higher harmonics are concerned, no qualitative difference can be expected, because similar interference of upper and lower wall registry will occur in 2 dimensions just like in 1 dimension. In both cases, the atoms `jump' between symmetrically equivalent positions and essentially no energy is dissipated when the relative, lateral motion of the walls is slow. For incommensurate surfaces, however, one must expect qualitatively different behavior in 1*d* and 2*d*. The reason is that in 2 dimensions, atoms can circumnavigate the points of maximum lateral force through transverse motion. Instabilities must then occur even without higher harmonics.

Thus in *2d*, kinetic friction between boundary-lubricated, commensurate surfaces should be much smaller than between incommensurate walls, while the opposite is true for static friction. Static friction is (almost) always larger between commensurate walls than between incommensurate walls, because commensurate surfaces interlock geometrically.

This discussion explains large-scale molecular dynamics simulations by one of the present authors, in which the transition from stick-slip to smooth sliding was investigated. The simulations revealed that kinetic friction was large for commensurate walls in the stick-slip regime, in which friction is dominated by the static contribution. In the smooth sliding regime, however, friction is larger for *incommensurate* surfaces for the above-mentioned reasons. A more detailed discussion of this phenomenon, which could also be tested experimentally, is given elsewhere.

2d boundary lubrication beyond the impurity limit

The discussion left out effects that are due to the interaction between the confined atoms, which might turn out as an oversimplification. It is thus necessary to address the question, to what extent the arguments stated above remain relevant, if less idealized conditions are encountered. It is obvious that the above-made symmetry arguments are less rigorous if the interactions between lubricant atoms are considered. We therefore extend our numerical treatment to a model system that has been used extensively to study static friction due to boundary lubricants (*10-12*). The model consists of two *2d* surfaces of trigonal symmetry. Atoms or molecules that are inserted into the interface interact with each other and with the wall atoms in terms of Lennard Jones potentials. The substrate is fixed in space and the upper wall is driven, in our case, at constant normal load and constant lateral sliding velocity. Two types of boundary lubricants are considered: Simple atoms and bead-spring chains, so-called *n*-mers, which are meant to mimic short carbohydrate chains. One *n*-mer reflects a chain of about *n* Kuhn's segments. For more details on the model, we refer to the original literature.

Fig. 6 shows the results of the simulations. The amount of surface contamination corresponds to a quarter layer. Simple point particles show the expected behavior. Kinetic friction between commensurate surfaces rapidly decreases as v_0 tends to zero. A fit that is not shown in the figure agrees almost perfectly with a description $F \sim v_0^\beta$ for the commensurate system with $\beta \approx 0.84$ up to velocities 0.01. The incommensurate system shows an exponent close to zero.

Of course, the effect of commensurability on static and kinetic friction, becomes less important as the normal separation between the surfaces increases. It can only remain relevant as long as the imprint of the wall's corrugation does not decay completely within the confined lubricant. The characteristic length scale L_c, on which this imprint decays, will depend on the system of consideration. Experimental results reported recently can lead one to conclude that L_c may extend up to length scales of a few nanometers:
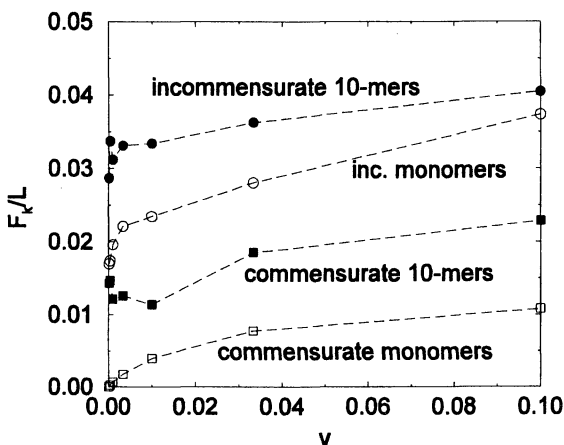
Figure 6. Friction velocity dependence for boundary-lubricated, 2d walls at finite but small temperature T. Commensurate and incommensurate, confining walls are considered as well as different types of lubricants, namely point atoms (monomers) and short chains consisting of 10 connected Lennard Jones units. The contamination of the surfaces corresponds to a quarter layer in all cases.

Conclusions

In this chapter, we have discussed a classification scheme for mechanical instabilities that occur in boundary lubricants when two solids are in relative sliding motion. Two types of instabilities are discussed: Jumps of atoms between symmetrically inequivalent positions, termed first-order instabilities in Ref. (*13*), and jumps between symmetrically equivalent positions, called continuous instabilities. If thermal fluctuations can be neglected, first-order instabilities lead to finite friction at zero sliding velocities while continuous instabilities lead to a law $F(v) \sim v^{\beta}$ with a non-universal exponent β. Thermal fluctuations and the absence of instabilities lead to linear friction-velocity dependence at extremely small velocities, however, depending on the actual model parameters, the relevance of thermal relaxation becomes smaller as the sliding speed increases and one crosses over to the athermal behavior at larger sliding speeds. This cross over happens with the typical ln$v$ behavior in the case of first-order instabilities.

Symmetry and dimensionality are crucial for the nature of the instability. In 1*d*, incommensurate surfaces typically do not show any instabilities, leading to drag friction within the current model. The reason is that the lubricant atoms are dragged with the wall that exerts the larger maximum lateral force and thus no pops occur. The situation changes if higher harmonics are included and if their magnitude exceeds a certain critical value, which depends among other things on the lattice misfit. In 2*d*, pops also occur between incommensurate surfaces

without higher harmonics in the lubricant wall interaction. The reason is that atoms can now circumnavigate the points of maximum lateral force through transverse motion. One of the implication of this result is that kinetic friction could be largely reduced if it was possible to confine the lubricant motion into one-dimensional channels. At the same time, static friction would nevertheless persist due to arguments stated in more detail in Ref. (*12*). For commensurate surfaces, kinetic friction should be small in both 1*d* and 2*d* interfaces, because the lubricant atoms jump between symmetrically equivalent states unless the first leading higher harmonics has a positive sign. But even in the latter case, the absolute value of the kinetic friction will remain small.

While the above discussion neglects the interaction between lubricant particles, we extended our analysis to cases, where they are taken explicitly into account. This was done for a quarter layer of simple spherical particles and for a quarter layer of bead-spring polymers, each containing 10 atoms. The simplistic picture is found to explain rather well the trends for this more realistic case, in particular for the non-bonded monomers, i.e., kinetic friction is small between commensurate walls, while it is relatively large between incommensurate plates. This trend is opposite to what is found for static friction, which is large between commensurate walls and small between incommensurate walls.

References

1. *Notice sur les travaux scientifique;* Brillouin M.; Gauthiers-Vilars: Paris, 1909.
2. *Theory of simple liquids;* Hansen J. P. and McDonald I. R.; Academic Press: London 1986.
3. Prandtl L., *ZS f. angew. Math. U. Mech.* **1928,** 8, 85.
4. Tomlinson G. A. ; *Phil. Mag. Series* **1929,** 7 905.
5. Fisher D. S.; *Phys. Rep.* **1998,** 301, 113.
6. Caroli C. and Nozieres Ph.; *Eur. Phys. J. B* **1998,** 4, 233.
7. *Modern Tribology Handbook;* Robbins M. O., Müser M. H., Ed. B. Bhushan; CRC Press: Boca Raton 2001.
8. Wenning L., Müser M. H., *Europhys. Lett.* **2001,** 54, 693.
9. Sokoloff J. B.; *Phys. Rev. B* **2002,** 65, 115415.
10. He G., Müser M.H. Robbins M. O.; *Science* **1999,** 284, 1650.

11. Müser M. H., Robbins M. O.; *Phys. Rev. B* **2000,** 64, 2335.
12. Müser M. H., Wenning L., Robbins M. O., *Phys. Rev. Lett.* **2001,** 86, 1295.
13. Müser M. H., submitted.
14. Sang Y., Dube M., Grant M.; *Phys. Rev. Lett.* **2001,** 87, 174301.
15. Dudko O. K., Filippov A. E., Klafter J., Urbakh M., *Chem. Phys. Lett.* **2002,** 352, 499.
16. *Morse Theory;* Milnor J.; Princeton University Press: Princeton, 1970.

Chapter 6

Effects on Friction of Adsorbed Molecules: How They Modify Dry Friction

C. Daly, J. Zhang, and J. B. Sokoloff

Physics Department and Center for Interdisciplinary Research on Complex Systems, Northeastern University, Boston, MA 02115

Recently, Muser and Robbins have argued that static friction for two weakly interacting flat atomically smooth clean non-metallic solid surfaces should be extremely small, unless there are mobile molecules adsorbed at an interface. Here we will consider "dry friction" (i.e., kinetic friction in the slow sliding speed limit). We will argue that mobile adsorbed molecules at an interface undergo Tomlinson model-like instabilities, which were shown by Caroli and Nozieres to be necessary for "dry friction" to occur.

Recently, Muser, Robbins, et. al., argued that static friction between two atomically smooth surfaces is only possible if the contacting surfaces are coated by a thin

layer of mobile molecules. A natural consequence of their result is that if one could remove these molecules from the interface one could eliminate static friction. Recently, it has been shown that if one considers the fact that when viewed on the many micron length scale, since virtually all contacting surfaces are only in contact at micron size regions of contact of micron length spacing, known as asperities, which are randomly distributed over the interface, one learns that there will always be static friction[2]. A more complete treatment of this problem [3], however, shows that although the Muser-Robbins idea, that the static friction between clean solid surfaces (i.e., there are no "third bodies" present at the interface) is negligible is not strictly correct, as noted above, their idea does result in the static friction for clean surfaces being noticeably smaller than what it would be for "dirty" surfaces.

It was argued by Caroli and co-workers [4] that without multistability there is no static or dry friction. Their work dealt with micron scale phenomena, but their ideas apply equally well to the smaller length scales that we are dealing with. On the basis of this idea, I suggest that it is the existence of multistability for the case in which there are mobile molecules between the two surfaces which leads to the friction found by Muser, et. al. In contrast, when the molecules are so strongly connected with one surface, so that they essentially can be considered part of that surface, the multistability will disappear, and as a consequence, so will the static friction. This opens the exciting possibility that the relative strengths of the bonding to each of the surfaces of molecules trapped at an interface can be responsible for whether the molecules reduce or increase friction. We have done calculations which demonstrate that when the interaction of a molecule with the two surfaces are of equal strength, the system exhibits multistability (i.e., the molecule can have two or more possible equilibrium positions for a given relative displacement of the two walls, one of which becomes unstable).

Let us consider two surfaces sliding relative to each other with a submono-layer of molecules present at the interface, which keeps the surfaces apart. In our initial treatment of this problem, molecules were assumed to be spherical and non-interacting. They are each subject to a potential from each surface. Initially, we assume that the temperature is very low, but still non-zero, so that the molecules will diffuse to minima of the potential due to the two surfaces. Now, let us slide one surface relative to the second at speeds which are sufficiently slow so that the adiabatic approximation can be used. Then the potential due to the two surfaces at the location of each interface lubricant molecule will no longer be minimum. If the lubricant molecules are initially placed at randomly chosen potential minima on the interface, the possibility exists that the potential at the location of some of these molecules will become unstable, allowing the molecule to drop down into a lower potential minimum. This is illustrated in figure 1 for a model consisting of a single lubricant particle acted on by two circularly symmetric Gaussian shaped attractive potentials of unequal strengths and widths.

$$V(r) = -V_1 e^{\alpha r^2} - V_2 e^{\beta(r-r_0)^2}, \tag{1}$$

where V_1 and V_2 are positive constants giving the potential strengths, α and β determine the widths of the wells, r_0 is the separation of the well centers and r represents the distance along the line joining the well centers. Imagine there to be many such potentials distributed over the each surface. Each potential can represent the potential acting on a lubricant molecule due to an atom one of two surfaces which are sliding relative to each other. We see that the net potential acting on the lubricant molecule (i.e., the sum of the two potentials) will have two minima until the two wells become fairly close together. We see in the figure that at a certain separation, one of the minima will become unstable, in the sense that the barrier between the wells disappears. At this point, if the lubricant molecule is initially at the minimum which becomes unstable, it will drop into the other (the lower) minimum. This will result in the molecule being given an amount of kinetic energy equal to the energy difference between the two potential well minima.
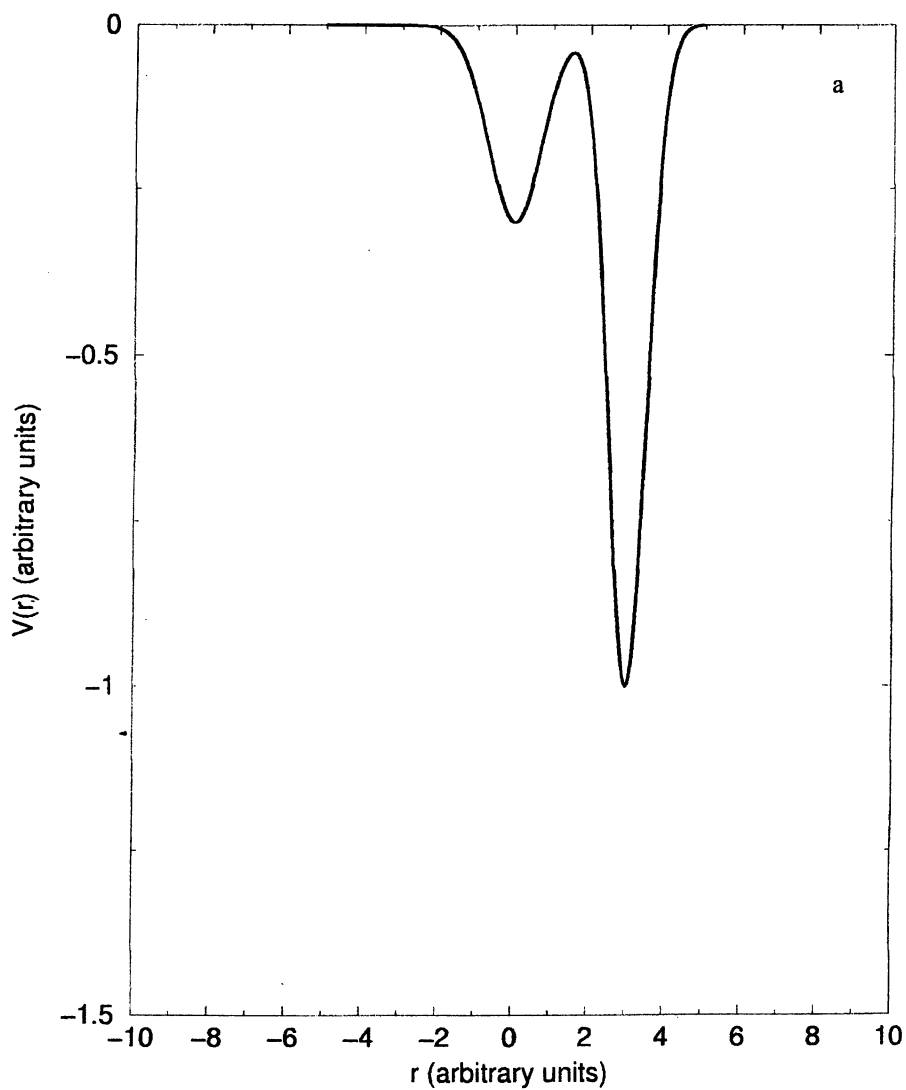
1. A plot of the model potential of Eq. (1) versus r with $V_1 = 0.3$, $v_2 = 1$, $\alpha = 1.0$ and $\beta = 2.0$ for a. $r_0 = 3.0$, b. $r_0 = 1.5$ and $r_0 = 3.0$.
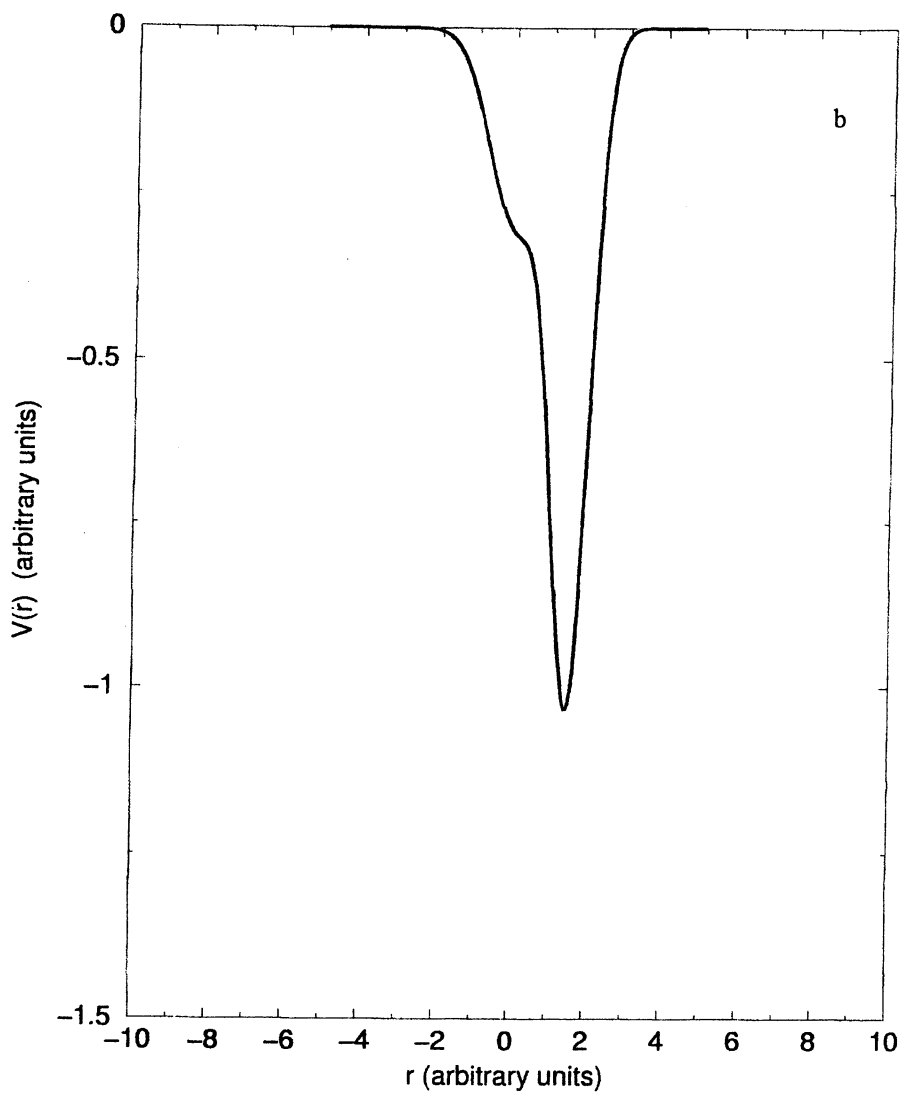
Figure 1. *Continued.*
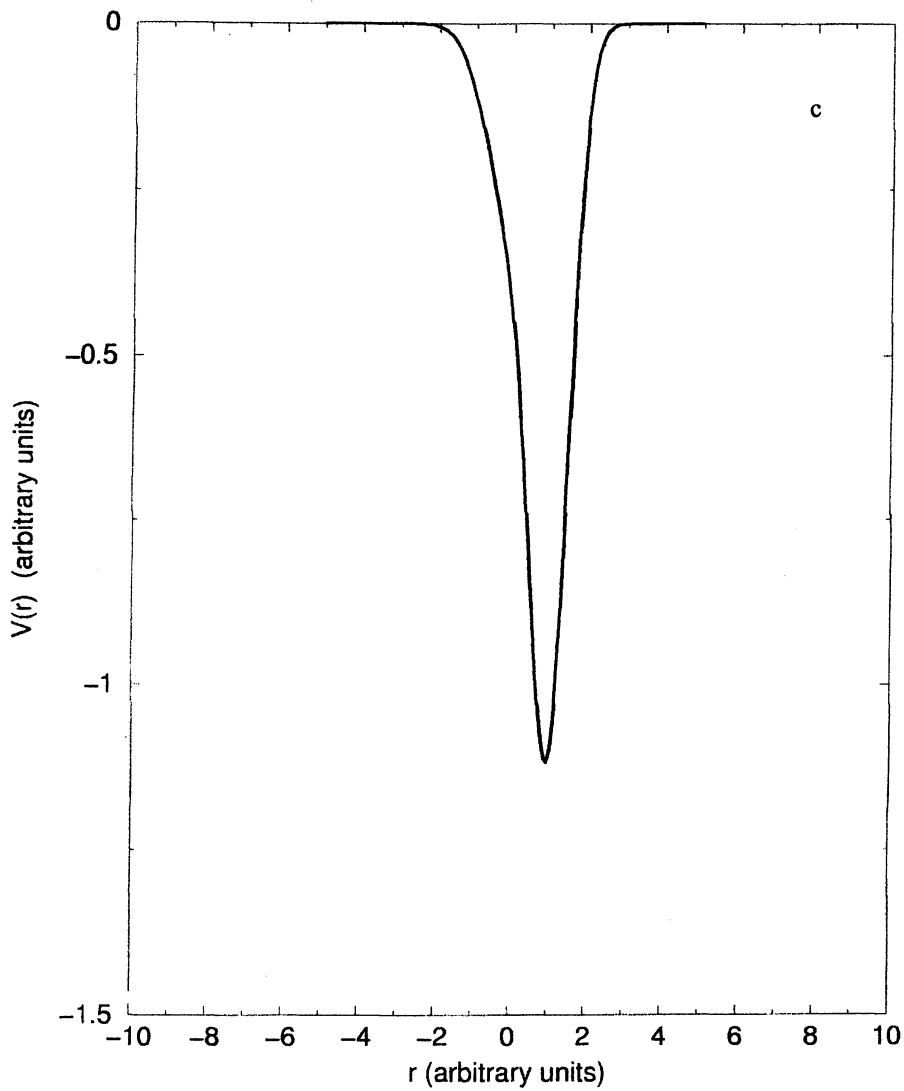
Figure 1. *Continued.*

In order to determine whether such a model can account for the almost universal occurrence of dry friction between solid surfaces, we must consider the question of how likely the potential due to two such potential wells acting on a molecule at the interface is to become unstable, which we have argued to be a necessary condition for the occurrence of dry friction. An extremum of $V(r)$ (i.e., maximum, minimum or saddle point) will occur when $dV(r)/dr$ is zero, which occurs when the derivative of the first potential in Eq. (1) is equal to the negative of the derivative of the second potential. Thus in order to study the occurrence of such extrema, we have plotted these quantities in figure 2 for the same values of V_1, V_2, α, β and r_0 used in Fig. 1. The instability found in Fig. 1b clearly occurs when the curves in Fig. 2, which in 2a intersected at three points, intersect at at one point and are tangent at a second point as in Fig. 2b. In Fig. 2c, there is just one intersection, which corresponds to the occurrence of the single minimum seen in Fig. 2c. It is easy to see from Fig. 2 that because both curves plotted in these figures go to zero at large distances, at sufficiently large values of r_0 there will be three intersections of the curves, implying two potential minima, which at smaller values of r_0 reduce to two. Changing the the values of the parameters V_1, V_2, α and β will change the heights and widths of the loops of the curves in Fig. 2, but will not change the conclusion that at sufficiently large values of r_0 there will always be three solutions, two of which disappear at smaller values. This can be seen because even if the the curve of $dV(r)/dr$ versus r for the potential of lower strength can be made to only intersect the $dV(r)/dr$ versus r curve for the higher strength potential at only one point for a particular value of r_0, it can always be made to intersect at three points again by shifting the this curve relative to the second curve to a place where the value of dV/dr is smaller on the second curve by increasing r_0. Thus if each surface consists of a collection of such potential wells distributed randomly or periodically over the surfaces, multistability will always occur for each such pair of potentials, provided that during sliding of the two surfaces they get close enough for one of the
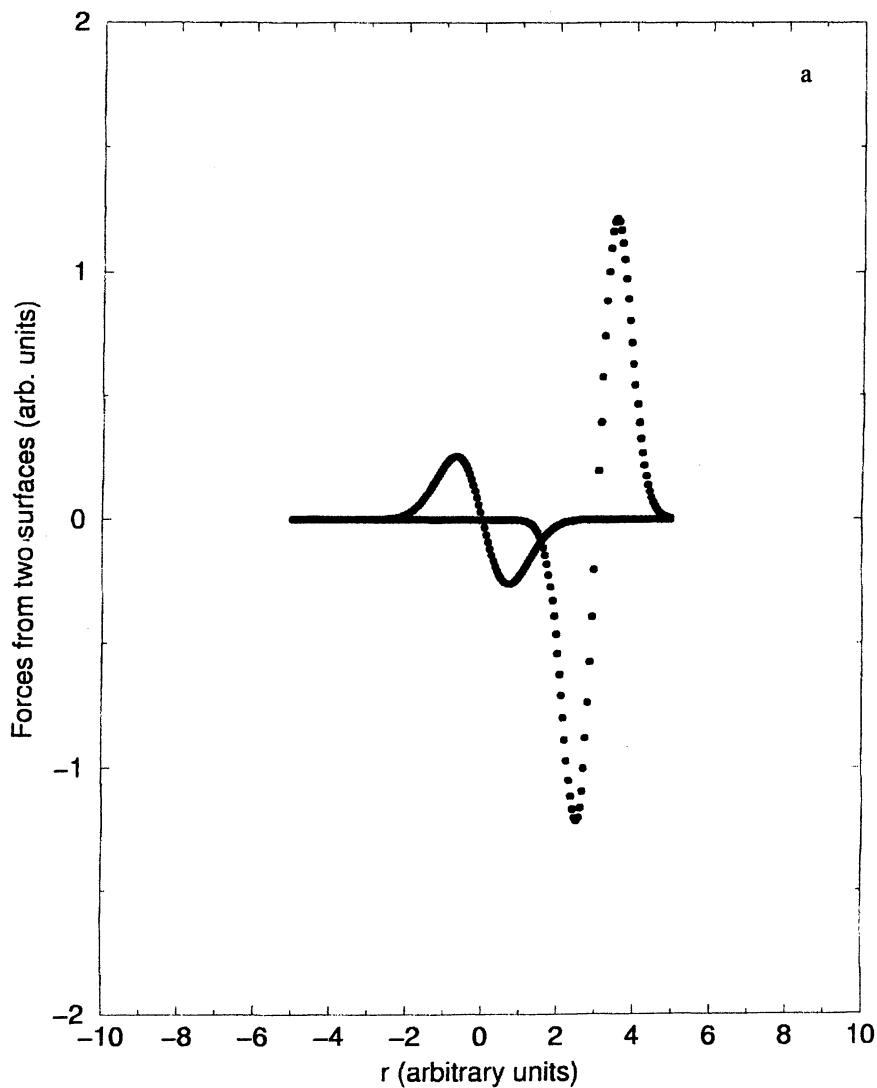
2. A plot of the the derivative with respect to r of the first and second terms of the model potential of Eq. (1) versus r with $V_1 = 0.3$, $v_2 = 1$, $\alpha = 1.0$ and $\beta = 2.0$ for a. $r_0 = 3.0$, b. $r_0 = 1.5$ and $r_0 = 3.0$.
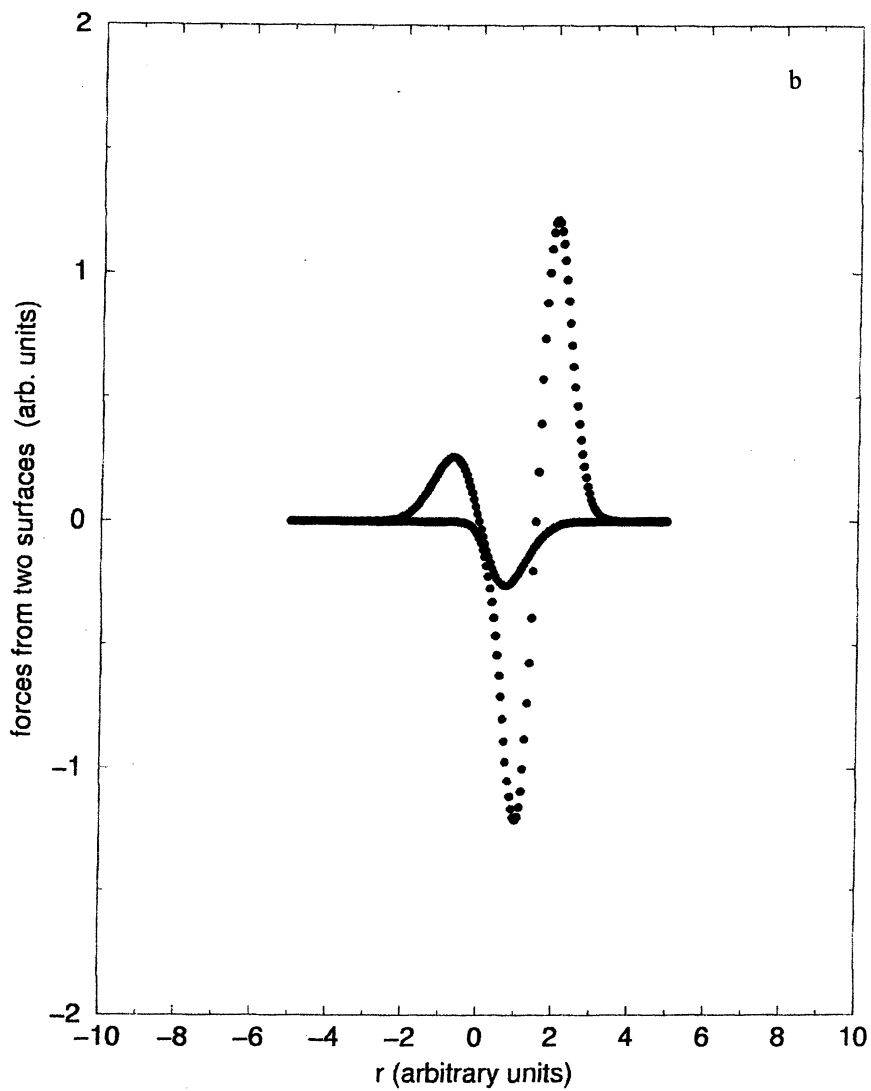
Figure 2. *Continued.*
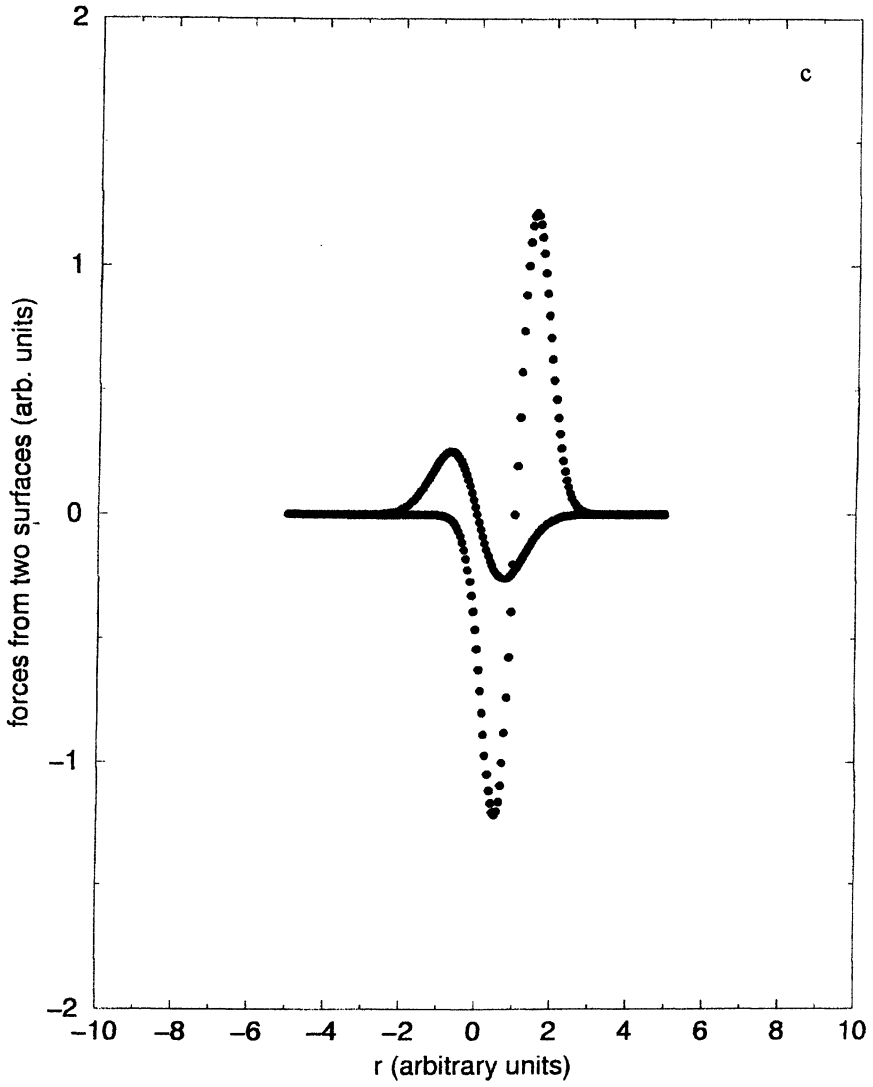
Figure 2. *Continued.*

two minima to become unstable and then disappear.

If one well is deeper than the other, which signifies that the molecule is more strongly attracted to one surface than the other, one of the two well minima in the sum of the two potentials will be higher than the other when they are far apart. As the wells overlap, it is always this minimum which becomes unstable. Since at temperatures low compared to the difference between the two potential minima, the molecule will always initially reside in the deeper well, which does not become unstable, there will be no energy loss and hence there is no dry friction. The picture that we propose is the following: Each surface possesses many of these potential wells, and there are many lubricant molecules present at the interface. If the lubricant molecules are more strongly attracted to one surface than the other and enough time is allowed initially for these molecules to diffuse to their absolute potential minima before sliding of the two surfaces begins, since as argued above the lower minima will never be the ones to become unstable, the molecules will remain in these minima and we will never have the instabilities that result in dry friction (i.e., kinetic friction in the slow sliding regime). In contrast, when the potentials on each of the surfaces are equally strong, the minima are initially of equal strength, when the potential wells are far from overlapping. As they overlap, however, one well will move up in energy relative to the second, and that well will become unstable at some point. The molecule will now drop from that well into the lower one, and in so doing, it will pick up some kinetic energy, which is assumed to be rapidly dissipated. If the sliding velocity is sufficiently low, the energy will be dissipated before the surfaces move a significant distance relative to each other. It is this dissipation which results in dry friction. This one dimensional model implies that in the low temperature limit, there will only be dry friction when the lubricant molecules interact almost equally strongly with the two surfaces. We certainly expect that when the interaction with one surface is much stronger than that with the other surface, the lubricant molecules can be thought of as being part of that

surface. In that case, our model reduces to the case of two relatively rigid surfaces, without "third bodies" between them, in Refs. 2 and 3. In such a case, we found that there was neither static nor slow speed kinetic (or dry) friction, as discussed in the last paragraph.

Although these conclusions were drawn for the special case of circularly symmetric Gaussian potential wells, all that is required is that we have potential wells with a minimum at one point and for which the potential goes to zero at large distances from the center of the well. It is quite likely that quite general surfaces will possess such wells due to various defects. Thus we would expect on the basis of this model for it to be the norm to have instabilities, which lead to dry friction, as argued above. For defect-free periodic surfaces, however, the wells due to the atoms on the surfaces might not fall to zero rapidly enough as we move away from the well center to justify the present picture. Therefore, we will now consider a more realistic model for two crystalline surfaces.

In more detailed two and three-dimensional models of an interface, the idea that lubricant molecules much more strongly coupled to one surface than the other result in no static or dry friction must certainly be true, but when the potential strengths of the two surfaces do not differ too much, we might expect that it is possible for static and dry friction to persist, even if one surface potential is stronger than the other on average. The reason for expecting this is that there is a good deal of variation in the depths of the potential wells of a two or three dimensional surface. In order to do model studies of this situation, we have studied the following model: The two surfaces are taken to have hexagonal symmetry, and the potential of each surface is well represented by a potential of the form

$$V_0 \sum_{\vec{G}} e^{i\vec{G}\cdot\vec{r}},$$

where $\vec{G}$ denotes the six smallest reciprocal lattice vectors of a triangular lattice[5].

The crystallographic lattices are taken to be rotated at an arbitrary angle with respect to each other, making the two potentials incommensurate with each other. This is a more realistic model for molecules trapped between two surfaces than two commensurate surfaces with their crystallographic axes lined up, which is often studied in molecular dynamic simulations of such problems[6]. In order to determine whether there will be static and dry friction, we initially deposit a sub-monolayer of lubricant molecules at random on the surface, and move these molecules to the nearest absolute minimum of the net potential of the two surfaces. Then, we slide one surface by a small amount relative to the second. We determine the shift in the positions of the minima of the potential felt by the lubricant molecules resulting from this sliding. Clearly the molecules are no longer in potential minima. We expand the new potential to first order in the shift of the surfaces relative to each other, and we use this expansion to estimate the location the molecules' new potential minima. We then try to find more accurate locations of the minima by expanding the potential to second order in a Taylor series around these approximate locations for the new potential minima to calculate the forces on the molecules resulting from the fact that these are not the correct minima and solve for the displacement of the molecules which makes these forces vanish. In this procedure, the vanishing of the determinant of the matrix whose elements are the second derivatives of the potential signifies the existence of a minimum which has become unstable. We used this criterion to locate such unstable minima, which according to the arguments given above, will result in static and dry friction. From the locations of the unstable minima, we can locate the nearby stable minima Figure 3 illustrates how a potential minimum becomes unstable as the surfaces slide relative to each other. This search method can also be used to locate the minimum that the molecule will slide into from a minimum that becomes unstable. This allows us to estimate $< \Delta E >$, the mean value of the drop in the molecule's potential energy when it makes such a drop from a minimum that becomes unstable to a stable minimum of lower energy.
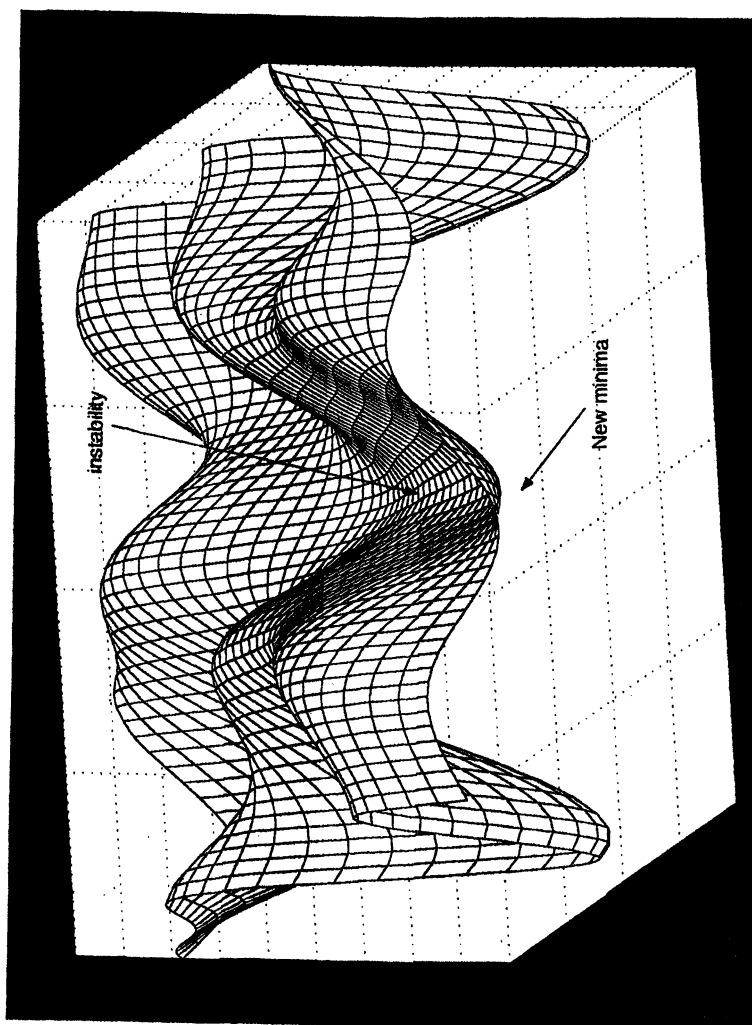
3. A plot of one minimum of the potential of the two dimensional potential model illustrating how a minimum becomes unstable. In a the minimum is still stable. In b, it has become unstable.

A typical value is about 0.06 eV. More details of this procedure will be reported in a future publication[7].

The mean value of the force of friction is given by the $< \Delta E > / < \Delta x >$, were $< \Delta x >$ denotes the mean distance that the two surfaces must be slid in order to find an instability. Since $< \Delta x >$ is of the order of a lattice spacing, which is of the order of $3 \times 10^{-8} cm$, we obtain a force of friction per molecule at the interface of the order of $5.4 \times 10^{-8} dyn$. If a unit cell area of a surface is of the order of $10^{-15} cm^2$ and there is a concentration of molecules (i.e. the number of molecules per unit cell) of 0.01, we obtain a frictional stress (i.e., the force of friction per cm^2 of contact area) of $5.4 \times 10^5 dyn/cm^2$. Then an interface of total area $1 cm^2$ with an area of contact (at asperities) which is 2 percent of this value, will exhibit a force of friction of $0.02 cm^2$ times the frictional stress, or about $10^4 dyn$ or about 0.1 N, which is a reasonable value.

We have repeated our procedure for the case in which the strengths of the potentials of the two surfaces, denoted above by V_0 differ. We find that once the strengths of the two surface potentials differ by only a few percent, instabilities are no longer found. This implies that at least at zero temperature, there will be no kinetic friction at slow sliding speeds. For large differences in potential strengths this is not an unexpected result because in that case the mobile molecules at the interface are much more strongly attached to one surface than the other. This is essentially the case of two surfaces in contact at randomly placed points of contact, which was considered in Refs. 2 and 3. There it was found that there is no static friction. Since the existence of static and kinetic friction require that there be instabilities, and since it was shown in Refs. 2 and 3 that there is no static friction, it is also likely that there will be no slow speed kinetic friction in this case. The lack of instabilities, and hence slow speed kinetic friction comes as a surprise. Since we did find near instabilities (i.e., a potential wells bounded by a very low ridge in one direction) for case of surfaces whose potential strengths differ by only a few

percent, the possibility still exists that there will still be friction once Boltzmann's constant times the temperature becomes comparable to these low potential ridges bounding nearly unstable potential wells.

References

1. G. He, M. H. Muser and M. O. Robbins, Science **1999**, 284, 1650; M. H. Muser and M. O. Robbins, Physical Review **2000**, B 61, 2335; M. H. Muser, L. Wenning and M. O. Robbins, Physical Review Letters **2001**, 86, 1295.

2. J. B. Sokoloff, "Static Friction between Elastic Solids due to Random Asperities," Phys. Rev Letters **2001**, 86, 3312.

3. J. B. Sokoloff, "A Possible Explanation if the Virtual Universal Occurrence of Static Friction," Physical Review **2002**, B 65, 115415-115424.

4. C. Caroli and Ph. Nozieres, European Physical Journal **1998**, B4, 233; Physics of Sliding Friction, edited by B. N. J. Persson and E. Tosatti, NATO ASI Series E: Applied Sciences, **1996**,Vol. 311 (Kluwer Academic Publishing, Dordrecht).

5. W. Steele, Surface Science **1973**, 36, 317.

6. P. A. Thompson and M. O. Robbins, Science **1990**, 250, 792; M. O. Robbins and P. A. Thompson, Science **1991**, 253, 916; P. A. Thompson and M. O. Robbins, Physical Review Letters **1992**, 68, 3448; B. N. J. Persson, Physical Review **1995**, B 51, 13568.

7. C. Daly, J. Zhang and J. B. Sokoloff, unpublished.

Chapter 7

Iterated Conformal Maps and Pinning of Stick–Slip Laplacian Flows

H. G. E. Hentschel[1], M. N. Popescu[2,3], and F. Family[1]

[1]Department of Physics, Emory University, Atlanta, GA 30322
[2]MPI für Metallforschung, Stuttgart, Germany
[3]ITAP Universität Stuttgart, Stuttgart, Germany

During the motion of the interface of thin fluid films pinning may be expected in the presence of stick slip boundary conditions, while thermal noise will lead to depinning, and this results in nontrivial flow patterns for the contact line on a surface. Both are mechanisms which can be expected to influence friction and lubrication at the nanoscale. Using a method recently proposed by Hastings and Levitov, the size of the pinned pattern is shown to scale with the yield stress for slip to occur. These pinned patterns have a lower effective fractal dimension than diffusion-limited aggregation due to the enhancement of growth at the "hot" tips of the developing pattern. At finite temperature, thermal noise leads to depinning and growth of patterns with a shape and dimensionality dependent on both the yield stress and the thermal noise. Using multifractal analysis, scaling expressions are established for this dependency.

85

Stick Slip Laplacian Flow

The importance of diffusion limited aggregation (DLA) as a paradigm for nonequilibrium growth and pattern formation (*1*) is due both to the fact that it is a self-organized growth process leading naturally to fractal structures; and because it has been identified as a stripped down model for several physical processes including two-fluid laplacian flow (*2*). Although we have gained a great deal of understanding of DLA and two-fluid laplacian flows during this period, many important questions remain open. One such issue is the influence, on the type of pattern formed, of a yield stress E_c for stick-slip flow to occur as the fluid interface wanders over a two-dimensional substrate.

A Saffmann-Taylor instability is known to exist (*3*) and DLA has been identified as the appropriate universality class for the fractal structure formed by the interface in two-fluid laplacian flow (*2*). Here we consider the influence of a yield stress in the pressure gradient $|\nabla p| > E_c$ for stick-slip flow to occur. In this work we show that such a threshold for grow has remarkable consequences: its influence is crucial to both growth — the patterns ultimately all become pinned — and to form — the rich branched stucture of DLA is replaced by a much lower dimensional shape consisting of a few surviving branches which are the last to be pinned.

Since in this study we are addressing laplacian flows, we will make use of a powerful tool recently proposed by Hastings and Levitov (*4,5*), namely iterated conformal mapping. It has been already shown that DLA in two dimensions can be grown by iterating stochastic conformal maps and studied in great detail using such methods (*6*), and we will show that a simple variant of this method allows us to study the patterns generated by stick-slip laplacian growth.

A simple physical model for studying the time development of pinning in stick-slip laplacian growth is to assume that the pressure gradient $\nabla p(s)$ should be greater than a certain yield stress E_c in order for motion of the interface to occur at a point s on the interface. Thus, the normal velocity $v(s)$ of the interface will be given by

$$v(s) = \begin{cases} \kappa \, \nabla p(s), & \text{if } |\nabla p| > E_c \\ 0, & \text{otherwise} \end{cases} \tag{1}$$

If the flows are incompressible, then the pressure field outside the developing pattern will still obey Laplace's equation $\nabla^2 p = 0$, and, consequently, the extremely difficult problem of calculating the pressure field in

the presence of the constant pressure boundary conditions on the freely evolving interface can be handled by using conformal mapping techniques.

Iterated Conformal Maps

The basic idea is to follow the evolution of the conformal mapping $z = \Phi^{(n)}(\omega)$ which maps the exterior of the unit circle in a mathematical ω-plane onto the complement of the cluster of n particles in the physical z-plane. $\Phi^{(n)}(\omega)$ is unique by the Riemann mapping theorem, given that it satisfies the boundary condition $\Phi^{(n)}(\omega) \sim F_1^{(n)}\omega$ as $\omega \to \infty$ where $F_1^{(n)}$ is the first Laurent coefficient in the expansion of the mapping (a real, positive coefficient, fixing the argument of $\Phi^{(n)}(\omega)$ to be zero at infinity).

As the complex pressure in the mathematical plane obeys $\Psi(\omega) = p + i\,\psi = \ln(\omega)$ (we assume the pressure on the free boundary $\omega = e^{i\theta}$ of the flow to obey $p = 0$), the complex pressure $\Psi^{(n)}(z)$ in the physical plane is given by

$$\Psi^{(n)}(z) = \ln \Phi^{(n)-1}(z) \qquad (2)$$

where $\Phi^{(n)-1}(z)$ is the inverse mapping and automatically satisfies $p(s) = 0$ on the free boundary of the flow.

The equation of motion for $\Phi^{(n)}(\omega)$ is determined recursively (see Figure 1). The choice of the initial map $\Phi^{(0)}(\omega)$ is rather flexible, and in this paper we select (arbitrarily) an initial condition $\Phi^{(0)}(\omega) = \omega$ since we expect the asymptotic cluster to be independent of this choice. Assuming that $\Phi^{(n-1)}(\omega)$ is given, then the cluster of n "particles" is created by adding a new "particle" of constant shape and linear scale $\sqrt{\lambda_0}$ to the cluster of $n-1$ "particles" at a position which is chosen randomly according to the harmonic measure, provided the pressure gradient is greater than the yield stress $|\nabla p| > E_c$. How is this constraint achieved?

Consider a point $z(s)$ on the boundary of the cluster, with s an arc-length parametrization. Eq.(2) implies $|\nabla p| = |d\Psi^{(n)}/ds| = 1/|d\Phi^{(n)}/d\omega|$, and therefore the probability to add a particle on an infinitesimal arc ds centered at the point $z(s)$ on the cluster boundary is $P(s, ds) = |d\Psi^{(n)}/ds|\,ds$. The pre-

images of $z(s)$ and ds in the ω-plane being $e^{i\theta}$ and $d\theta$ respectively, it follows that $ds = \left| d\Phi^{(n)}(e^{i\theta})/d\theta \right| d\theta$, and we therefore conclude that for a harmonic measure $P(s, ds) = d\theta$.
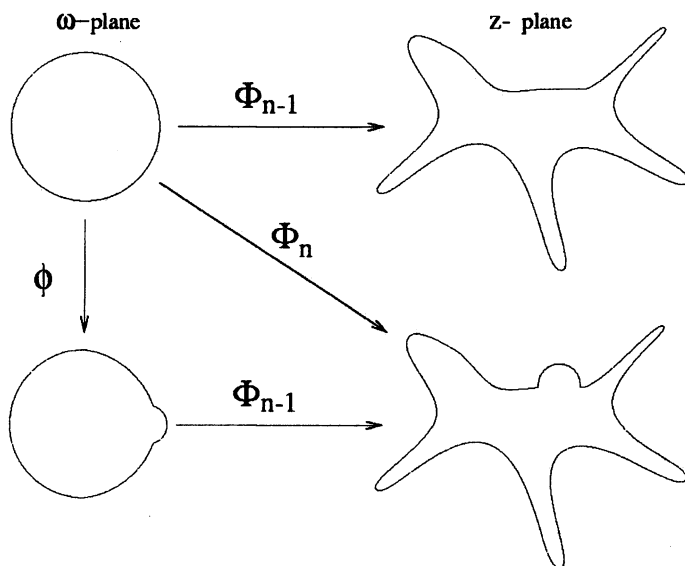
Figure 1. Diagramatic representation of the recursive evolution of the mapping Φ using the elementary mapping ϕ.

Thus, the harmonic measure on the real cluster translates to a uniform measure on the unit circle in the mathematical plane, and all we need for fulfilling the constraint is to grow only at values of θ which obey

$$1/\left| d\Phi^{(n)}(e^{i\theta})/d\theta \right| > E_c. \tag{3}$$

Let us define now a new function $\phi_{\lambda_n, \theta_n}(\omega)$. This function maps the unit circle to the unit circle with a bump of linear scale $\sqrt{\lambda_n}$ around the point $e^{i\theta_n}$. For $\omega \to \infty$, $\phi_{\lambda_n, \theta_n}(\omega) \sim \omega$ (with positive real proportionality coefficient). Using $\phi_{\lambda_n, \theta_n}(\omega)$, the recursion relation for $\Phi^{(n)}(\omega)$ is given by (see Figure 1):

$$\Phi^{(n)}(\omega) = \Phi^{(n-1)}(\phi_{\lambda_n,\theta_n}(\omega)). \tag{4}$$

and Eq.(4) induces the recursive dynamics of $\Phi^{(n)}(\omega)$. Finally to close the set of equations λ_n must be chosen to obey

$$\lambda_n = \lambda_0 / |d\Phi^{(n)}(e^{i\theta})/d\theta|^2 \tag{5}$$

in order to ensure that a bump of area λ_0 is added in the physical z plane. This is simply the result of the Jacobean of the transformation between the mathematical and physical planes.

The recursive dynamics can be represented as iterations of the elementary bump map $\phi_{\lambda_n,\theta_n}(\omega)$,

$$\Phi^{(n)}(\omega) = \phi_{\lambda_1,\theta_1} \circ \phi_{\lambda_2,\theta_2} \circ \circ \circ \phi_{\lambda_n,\theta_n}(\omega) \tag{6}$$

Although this composition appears at first sight to be a standard iteration of stochastic maps, this is not so because the order of iterations is inverted — the last point of the trajectory is the inner argument in this iteration. As a result, the transition from $\Phi^{(n-1)}(\omega)$ to $\Phi^{(n)}(\omega)$ is not achieved by one additional iteration, but by composing the $n-1$ former maps in Eq.(6) starting from a different seed which is no longer ω but $\phi_{\lambda_n,\theta_n}(\omega)$.

Conformal Map Algorithm

The algorithm simulating the growth of the cluster is based on Ref. (6). The n "particle" cluster is encoded by the series of pairs $(\lambda_i,\theta_i)_{i=1}^{n}$. Having the first $n-1$ pairs, the nth pair is found as follows. Choose θ_n from a uniform distribution in $[0,2\pi]$, independent of previous history; if it obeys the constraint given by Eq.(3), accept this value of θ_n, otherwise repeat until the constraint is obeyed. If no acceptable value of θ_n is found after n attempts the cluster is pinned; otherwise, we compute λ_n from Eq.(5), where the derivative of the iterated function $\Phi^{(n-1)}(\omega)$

$$d\Phi^{(n-1)}(e^{i\theta})/de^{i\theta} = \prod_{i=1}^{n-1} d\phi_{\lambda_i,a}(\omega_{n,i})/d\omega \tag{7}$$

is the product of the derivatives of the elementary maps computed respectively at the points $\omega_{n,n-1} = e^{i\theta_n}$, $\omega_{n,n-2} = \phi_{\lambda_{n-1},\theta_{n-1}}(e^{i\theta_n})$, etc. Note that the evaluation of both $d\phi/d\omega$ and ϕ after the addition of one particle involves $O(n)$ operations since the seed changes at every n, and this translates into $O(n^3)$ time complexity for the growth of an n-particle cluster.

Extracting Physical Properties

Once the mapping $\Phi^{(n)}(\omega)$ has been found, essentially all questions of physical interest can be addressed. For example, the local pressure gradient is given by the derivative of the mapping: $|\nabla p(s)| = 1/|d\Phi^{(n-1)}(e^{i\theta_n})/d\theta|$, while the radius of the developing pattern can be extracted from the first Laurent coefficient $F_1^{(n)}$ of the mapping. To see how this occurs we start with the observation that since the functions $\Phi^{(n)}(\omega)$ and $\phi_{\lambda,\theta}(\omega)$ are required to be linear in ω at infinity, they can be expanded in a Laurent series in which the highest power is ω:

$$\Phi^{(n)}(\omega) = F_1^{(n)}\omega + F_0^{(n)} + F_{-1}^{(n)}/\omega + \dots$$
$$\phi_{\lambda,\theta}(\omega) = f_1\omega + f_0 + f_{-1}/\omega + \dots \qquad (8)$$

where the Laurent coefficients depend on the details of the elementary maps. For example, for semicircular bumps $f_1 = \sqrt{(1+\lambda)}$.

Thus, the recursion equations for the Laurent coefficients of $\Phi^{(n)}(\omega)$ can be obtained by substituting the series of $\Phi^{(n)}(\omega)$ and $\phi_{\lambda,\theta}(\omega)$ into the recursion formula Eq.(4). Specifically,

$$F_1^{(n)} = F_1^{(n-1)}f_1^n = \prod_{i=1}^n \sqrt{(1+\lambda_i)} \qquad (9)$$

and therefore given the set of λ_i we can calculate $F_1^{(n)}$. Furthermore, from the one-fourth theorem (see Ref. 6), which states that the interior of the curve $z(\theta) = \Phi(e^{i\theta})$ is contained in a circle of radius $4F_1^{(n)}$, follows that the first Laurent coefficient $F_1^{(n)}$ is a typical length-scale of the cluster and thus a natural choice for the radius of the cluster is $R \sim F_1^{(n)}$. As any typical radius of the

cluster should scale like $n^{1/D}\sqrt{\lambda_0}$, where D is the dimension of the cluster, we can thus expect $F_1^{(n)}$ to scale as

$$F_1^{(n)} \sim n^{1/D}\sqrt{\lambda_0}. \qquad (10)$$

We note in passing that this scaling law was used in (6) as a very convenient way to measure the fractal dimension of the growing cluster.

The Pinning Transition in Laplacian Growth

The existence of a yield stress E_c for flow automatically means that all growth patterns will ultimately become pinned (see also Figure 3a) in the absence of noise because the pressure gradients diminish in a power law multifractal fashion as the cluster grows (7-9). For example, for a two-dimensional compact flow we would expect $|\nabla p| \sim 1/R$, where R is the radius of the growing cluster, while for a fractal shape multifractal theory shows that even the strongest gradients scale as $|\nabla p| \sim 1/R^{D_\infty}$ which also tends asymptotically to zero.

Summarizing the results of our simulations, we note that the pinned cluster radius and size both scale with E_c as shown in Figure 2. The maximal radius of the pattern scales as $R_c \sim E_c^{-\alpha}$ with $1.6 < \alpha < 1.8$, while the maximal size of the pattern scales as $N_c \sim E_c^{-\beta}$ with $\beta \approx 2.25$. In consequence, the pinned pattern retains mass-radius scaling $N_c \sim R_c^{d_f}$ with $1.25 < d_f = \beta/\alpha < 1.4$, although the resulting pattern no longer possesses local self-similarity, and thus is not a fractal.

How can we understand these results? From multifractal scaling (7-9) we know that the interface of the cluster consists of sets of $N_\alpha \sim (R/\sqrt{\lambda_0})^{f(\alpha)}$ sites with pressure gradients $|\nabla p| \sim (R/\sqrt{\lambda_0})^{-\alpha}$. Thus, we would expect that the weakest gradients, normally deep in the fjords, would be pinned first, with the hot tips surviving longest, and indeed this is what is observed in simulations, as shown in Figure 3a. The two clusters correspond to DLA with $E_c = 0$, and to a cluster grown with a pinning gradient $E_c = .002$, and one can see that deep inside the cluster the DLA grows further than the pinned cluster, while the hot tips of the pinned cluster are more likely to grow.
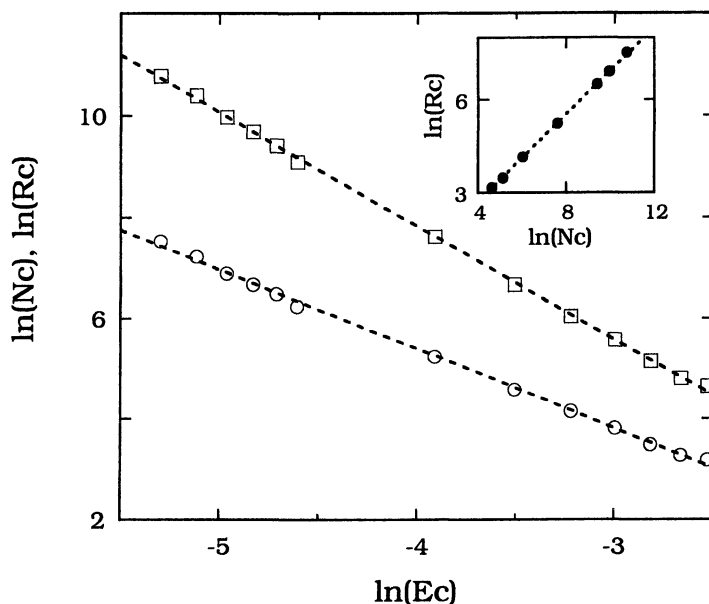
Figure 2. Scaling of radius R_c (○) and size N_c(□) with the yield stress for flow E_c.; inset shows scaling of radius with size. Lines are linear fits to data.

In order to understand these results theoretically let us begin with a simple argument which will help to set the stage for a better estimate later. As we mentioned, one would expect the hot tips have the maximal growing probability and thus to be pinned last. These maximal growth probabilities in DLA scale as $D_\infty = D - 1$ (where $D \approx 1.713$ is the fractal dimension for DLA, and we have assumed the Sher-Turkovitch identity (10) to be valid). Therefore, as a first estimate we assume the clusters are pinned when $P_{max} \sim (\sqrt{\lambda_0} / R)^{D_\infty} \sim E_c$. Before pinning we shall assume that the cluster scales like DLA and therefore $N_{max} \sim R_{max}^{D}$. If both these assumptions were correct we would then find that

$$\alpha = 1/D_\infty \approx 1.4, \quad \beta = D/D_\infty \approx 2.4, \quad d_f = D \approx 1.7$$

But we know that the argument above is not quite correct because the growing prepinned cluster is not in the same universality class as DLA, and

probably it is not even a fractal object. This can be seen by studying the first Laurent coefficient which shows that there is a breakdown in scaling after an initial period when DLA scaling $F_1^{(n)} \sim n^{1/D}$ applies. A better estimate therefore is to start with the question about when will the influence of E_c make itself felt and cause crossover to a new growth mode.
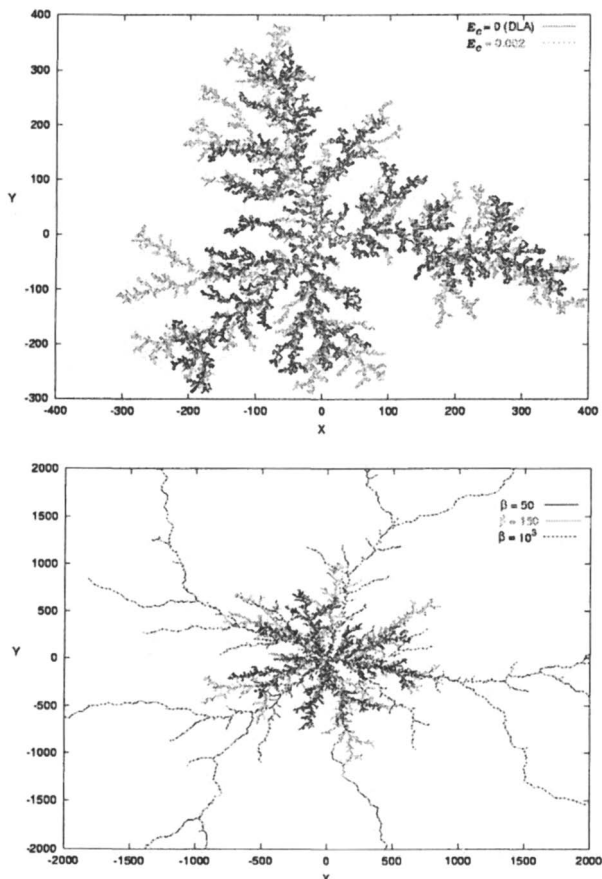
Figure 3. (a) Two clusters grown with different E_c values. Note both the pinned regions deep in the cluster and hot tips which grow preferentially compared to DLA; (b) Cluster growth in the presence of noise. All have $E_c = .01$. The values $\beta = 1/T$ are, respectively, i)$\beta = 50$; ii)$\beta = 150$; iii)$\beta = 1000$.

Based on the fact that essentially all the measure in a harmonic fractal (the integral over the electric field in the case of dielectric breakdown, or the pressure gradient in the case of two-fluid flow) lies on a one dimensional interface, one would expect crossover at scales l when $P_{inf ormation} \sim (\sqrt{\lambda_0} / l) \sim E_c$. Thus, instead of a DLA-like structure on all scales, a description of the cluster more likely to be correct is that it remains fractal on scales $r << l$ but becomes linear on scales $r >> l$. If this description of the growing pattern is valid, then

$$\beta = \alpha + D - 1 \tag{11}$$

Retaining our estimate of β (which was based on the fact that pinning can be expected when the hot tips can no longer grow), we find

$$\alpha = D / D_\infty - D + 1 \approx 1.7$$
$$\beta = D / D_\infty \approx 2.4 \tag{12}$$
$$d_f = \beta / \alpha \approx 1.3,$$

in good agreement with simulations.

The Influence of Noise on Depinning

So far we have assumed that the only relevant parameter is the yield stress E_c and therefore all patterns are ultimately pinned. In the presence of thermal noise, as will be the case in most physical situations, depinning can occur and thus the pinned patterns will represent the $T = 0$ limit of a finite temperature phase diagram, while DLA will be the $T \to \infty$ limit. To generate non-zero temperature patterns we can use a variation of a Monte Carlo algorithm in which the probability for growth at a site s is $P(s) = \min\{1, \exp[\beta(|\nabla p| - E_c)]\}$, where $\beta = 1/T$. In the conformal mapping approach, this translates to a variation of Eq.(3), i.e. the probability of grow at the randomly choosen point θ on the unit circle will be given by

$$P(\theta) = \min\{1, \exp[\beta(|d\Phi^{(n-1)}(e^{i\theta}) / d\theta| - E_c)]\} \tag{13}$$

The types of clusters corresponding to this type of growth can be seen in Figure 3(b).

Numerical simulations with fixed critical E_c and increasing temperature (decreasing $\beta = 1/T$) reveal that the fractal dimension of the resulting clusters appear to depend continuously on βE_c. This scaling behavior $F_1^{(n)} \sim n^{1/D(\beta E_c)}$ is illustrated in Figure 4. We would like to emphasise two points. First, as must be the case for high temperature, DLA patterns appear and therefore $D(\beta E_c \gg 1) \to D_{DLA}$. Second, the fractal dimension reduces continuously, apparently reaching $D = 1$ for a finite value of $\beta E_c \approx 3.5$, thus implying a transition to pure one-dimensional grow at finite, non-zero temperature. This last result is tentative but suggests that the fractal dimension depends only on the product βE_c.
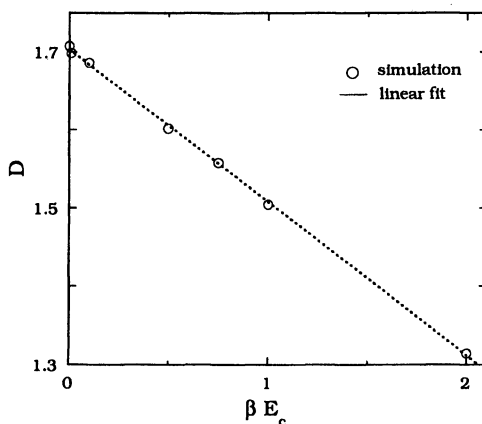
Figure 4. Scaling exponent D as a function of βE_c at $E_c = .01$.

Discussion

In this work we have shown numerical evidence that a threshold for growth dramatically influences both the growth pattern and the form of laplacian growth patterns with its resulting influence on the pinning and wetting properties of nanoscale stick slip thin film flows. Scaling relations for the pinned patterns have been proposed based on numerical evidence, and the scaling exponents of the pinned cluster have been derived as well as the form of the mass-radius scaling in the pre-pinning regime.

We expect that simple extentions of this model may be important for nanoscale lubrication. For example, in the presence of applied shear, viscoelastic behavior is exhibited by thin films, an initial elastic behavior being followed, at a well defined yield stress, by shear melting and ductile flow (11,12). This observed stick-slip behavior is not only due to the ordered state of the thin film of fluid but also to the presence of velocity weakening boundary conditions at the nanoscale. These significantly modify the lubricating properties of thin films creating localized mesoscopic regions of stick and slip in the sheared film (13), and how the flow patterns change due to such stick-slip boundary conditions can be studied using an approach like the one presented here.

Acknowledgments

References

1. Witten, T.A. Jr.; Sander, L.M. *Phys. Rev. Lett.* **1981**, 47, 1400.
2. Paterson, L. *Phys. Rev. Lett.* **1984**, *52*, 1621.
3. Saffman, P.G.; Taylor, G.I. *Proc. Roy. Soc. Lond.* **1958**, *A245*, 312.
4. Hastings, M. B.; Levitov, L. S. *Physica D* **1998**, *116*, 244.
5. Hastings, M. B. *Phys.Rev.E* **1997**, *55*, 135.
6. Davidovitch, B.; Hentschel, H.G.E.; Olami, Z.; Procaccia, I.; Sander, L. M.; Somfai, E. *Phys. Rev. E* **1999**, *59*, 1368.
7. Hentschel, H.G.E.; Procaccia I. *Physica D* **1983**, *8*, 435.
8. Halsey, T.C.; Meakin, P.; Procaccia, I. *Phys. Rev. Lett.* **1986**, *56*, 854.
9. Halsey, T.C. ; Jensen, M.H. ; Kadanoff, L.P. ; Procaccia I.; Shraiman, B.I. *Phys. Rev. A* **1986**, *33*, 1141.
10. Turkevich, L.A.; Scher, H. *Phys. Rev. Lett.* **1985**, *55*, 1026 .
11. Klein, J. ; Kumacheva, E. *J. Chem. Phys.* **1998**, *108*, 6996.
12. Kumacheva, E;. Klein, J. *J. Chem. Phys.* **1998**, *108*, 7010.
13. Tovstopyat-Nelip, I.; Hentschel, H.G.E. *Phys. Rev.E.* **2000**, *61*, 3318.

Chapter 8

Dynamics of Nanomechanical Devices

Donald W. Noid[1], Bobby G. Sumpter[1], and Robert E. Tuzun[2]

[1]**Computational Science and Mathematics Division, Oak Ridge National Laboratory, Oak Ridge, TN 37831–6197**
[2]**Department of Computational Science, State University of New York at Brockport, Brockport, NY 14420**

Abstract: Classical and quantum molecular simulation methods have proven an invaluable tool in the development of nano-materials and in feasibility studies of nanotechnology designs. This paper chronicles several classical and quantum simulation studies of model nano-bearings and nano-motors composed of concentric carbon nanotubes. While classical simulations show strong effects of internal mode coupling on key aspects of the performance of the motor and bearings, quantum mechanical results and studies of classical chaos indicate that classical simulation may overestimate these effects. Rigid body models or models with a reduced number of internal degrees of freedom have been explored as possible ways to address these issues.

I. Introduction

Nanotechnology, which can be broadly defined as the control of matter in three dimensions at the nanometer size scale, is beginning to gradually emerge past the conceptual level into the realm of technological application(1). The first and most obvious stage of the

97

evolution of nanotechnology is the development of nanomaterials. Significant strides have been made in such areas as nano-photonics(2) and nano-electronics(3) (with applications in computing) and nano-fluidics(4) (which will prove important in hydrogen storage and other important applications with significant environmental impact). Later stages of nanotechnology development, some of which at this time are more speculative, would use controlled motion at the nanometer scale. One important recent advance is the development of molecular motors(5). Advancing nanotechnology, whether in the development of nanomaterials or in later stages, will require a more complete understanding of the chemistry and physics of nanometer scale systems through computer simulation. The capabilities and results of computer simulation on nano-mechanical devices, as well as issues that need further study, are the subject of this paper.

Over the last several years, we (and others) have made preliminary investigations into the performance of nano-bearings(6-9) and motors(10-14). Various types of molecular bearings and other mechanical devices have recently been proposed in the growing nanotechnology literature. The simplest of the proposed bearings consisted of two concentric single-walled carbon nanotubes. Initial studies by Merkle(15) used molecular mechanics to explore the smoothness of the potential surface with respect to relative rotation of the two nanotubes. The smoothness of the resulting energy profile, as well as the low barriers to internal rotation, suggested that carbon nanotubes were indeed suitable components for a nano-bearing. However, since these studies did not explicitly address wobbling between the two nanotubes or the internal motion of the nanotubes themselves, we decided to explore the rotational friction between concentric carbon nanotubes using fully dynamical (molecular dynamics, or MD) simulation.

One desired capability of later stages of nanotechnology development, and an interesting scientific problem in its own right, is the introduction of controlled motion at the nanometer size scale. Closely related to the molecular bearings, we have simulated several model graphite nanometer scale laser-driven motors. The motors

consisted of two concentric graphite cylinders (shaft and sleeve) with one positive and one negative electric charge attached to opposite ends of one of the end rings of the shaft. Rotational motion of the shaft was induced by applying one or sometimes two oscillating laser fields. The shaft cycled between periods of rotational pendulum-like behavior and unidirectional rotation (motor-like behavior). Motor performance was mapped as a function of size, field strength and frequency, and relative location of the attached positive and negative charges. Drawing on observations of multi-laser enhanced energy absorption in small molecular systems, the motor performance was also mapped as a function of one- versus two-laser excitation.

One possible issue in classical simulations is the flow of zero-point energy(16). Classically, energy can flow between vibrational modes subject only to the restriction of constant total energy. Quantum mechanically, however, a certain amount of energy is restricted to each vibrational mode. This suggests that energy may flow too freely in some classical simulations and that the level of classical chaos can be misleading in regards to the performance of nano-mechanical devices. In this paper we will summarize our work in this area, especially regarding the issue of classical/quantum correspondence, and present results based on rigid body and continuum approaches.

II. Classical Molecular Simulation Methods

Since MD techniques are well-known and well-reviewed(17) we will present only a minimum of detail here. Basically, one needs to integrate Hamilton's equations

$$\partial H / \partial p = \dot{q}, \ \partial H / \partial q = -\dot{p}$$

or some other formulation of the classical equations of motion, starting with some initial conditions (positions and momenta). These

positions and momenta may be made to correspond to a desired temperature, initial rotational velocity, or other conditions. External forces and/or torques may also be applied. The Hamiltonian used in the studies discussed here was:

$$H = T \; + \Sigma \; V_{2b} \quad + \Sigma \; V_{3b} \quad + \Sigma \; V_{NB} \quad + \quad \Sigma \; V_{NB} \quad + \; H_{external}$$

	bonded	bend	nonbonded	nonbonded	
	two	three	for dynamic	for dynamic-	
	body	body	atoms	static interactions	

where T is the kinetic energy operator in Cartesian coordinates and momenta and V_{2b}, V_{3b} and V_{NB} are the bonded two-body and three-body terms and non-bonded interactions, respectively.
The potential energy functional forms were

$$V_{2b}(r_{ij}) = D[1 - \exp(-\alpha(r_{ij} - r_e))]^2$$

for CC bond interactions,

$$V_{NB}(r_{ij}) = 4\varepsilon[(\sigma/r_{ij})^{12} - (\sigma/r_{ij})^6]$$

for non-bonded interactions between atoms in the two different nanotubes, and

$$V_{3b}(\theta_{ijk}) = (\gamma/2)(\cos \theta_{ijk} - \cos \theta_o)^2$$

for CCC bend interactions. The potential parameters were D = 114.3776 kcal/mol (794.7168 maJ), α = 2.18676 Å^{-1}, r_e = 1.418 Å, ε = 0.0692 kcal/mol (0.4808 maJ), σ = 3.805 Å, γ = 33.56915 kcal/mol (233.2447 maJ), and cos θ_o = -0.5, which corresponds to a bond angle of 120 degrees. For more details of the simulations see reference 18 and for the sympletic integration of Hamilton's equations(19). In the case where a motor was simulated the external interaction term was that of a charge with one or more external (laser) electric fields:

$$H_{laser} = q_x(E_1 cos\omega_1 t + E_2 cos\omega_2 t)$$

where q_x is the appropriate charge and E and ω are the field strengths and frequencies.

Figure 1 shows the basic construction of a nanobearing/motor at the beginning of a simulation. Both the shaft (inner cylinder) and sleeve (outer cylinder) are centered about a common rotational axis, denoted the z axis, and the shaft extends symmetrically out of the sleeve. The number of atoms per ring and number of rings for the shaft are denoted n and n_r, respectively; for the sleeve, these quantities are denoted m and m_r. Bond distances and bend angles were initially approximately at their equilibrium values. Trajectory calculations of these bearings with no added momentum, angular momentum or torque yield an average temperature of about 5° K, which demonstrates no large mismatch in atom positions or strain energy release.

Shaft and sleeve radii, which greatly affect bearing performance, were calculated as follows. From the equilibrium bond distance and bend angle, the distance between the end atoms in a bend interaction is 2.46

Å. The shaft radius is the radius of a regular polygon with n/2 sides of length 2.46 Å. From simple trigonometric identities and the approximation $sin\theta \approx \theta$ (an approximation accurate to within less than
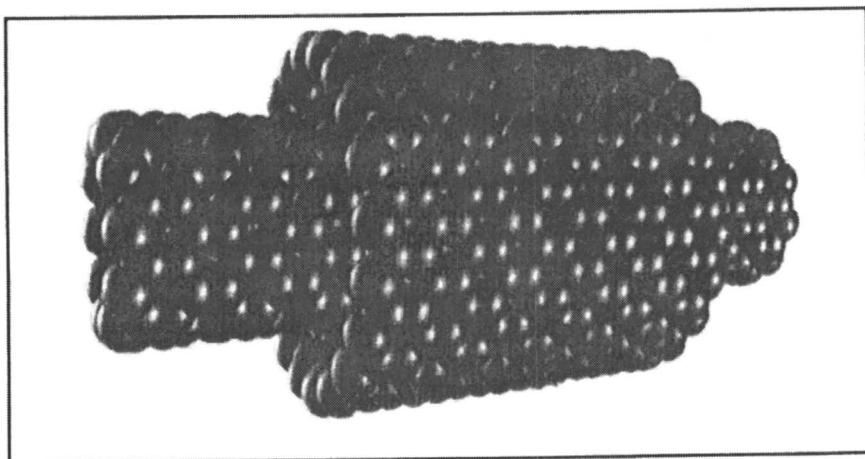
Figure 1

1% even for the worst case, n = 10), this radius is about $(1.23/2\pi)$ n Å. Thus, the bearing clearance is approximately $(1.23/2\pi)(m - n)$ Å. In some simulations a random amount of momentum was added to create a desired temperature and in other simulations a torque was added to simulate the startup process in the shaft and sleeve. The external torque was applied to the first ring of the shaft and the first and last ring of the sleeve. In a few other simulations, an external load was applied in either the x or z direction to the first and last rings of the shaft and sleeve. For the laser motor project we attempted to model a startup process the shaft was initially motionless. The sleeve was frozen throughout the simulation. Calculations were performed for several bearing sizes and field strengths and frequencies(see reference 6). Electric fields are given in reduced units; laser intensities are related to these E's by $I = 2.49 \cdot 10^{10} E^2$ W/cm^2 and ranged from 0.249 GW/cm^2 to 6.24 TW/cm^2. Typical simulations ran for several hundred ps.

III. Classical Simulations of Bearings and Motors

Using our novel MD methods (involving symplectic integration of Hamilton's equation written in geometric statement functions), we have simulated several model graphite bearings and laser driven motors. The bearings varied in size from an inner shaft of between 4 and 16 Å in diameter and up to 120 Å in length and an outer cylinder of between 10 and 23 Å in diameter and up to 40 Å in length. The symbols n and n_r refer to the number of atoms per ring and number of rings in the shaft; m and m_r refer to the number of atoms per ring and number of rings in the sleeve. The turning shaft was either instantaneously started or was torqued up to the desired rotational speeds. Frictional properties were size-, temperature-, and velocity-dependent. The presence of more than one bearing vibrational mode in some simulations created beats that could possibly adversely affect bearing performance; placing a stretching tension on the bearing suppressed one of the modes and therefore the beats.

All calculations were performed in double precision on an IBM RS6000 model 580 cluster with 4 CPUs. To illustrate the type of data available in our simulations we will focus on a few simulations of a small bearing which all run about 12 ps. Typical profiles of shaft angular momentum L_z, and shaft-sleeve non-bonded interaction energy are shown in Figure 2. The shaft (n=10, n_r=21) was given an initial clockwise angular momentum of 10^4 ℏ with a rotational period of about 1 ps (1×10^{12} Hz). The sleeve (m=30, m_r=11) rotated counterclockwise with an initial angular momentum of -10^4 ℏ but with a period of about 15ps (6.67×10^{10} Hz). At the beginning of simulations, the moment of inertia is $I=NMr^2$, where N, M, and r are number of atoms, mass of atoms, and radius of either the shaft or sleeve. This can change during simulation if there is significant
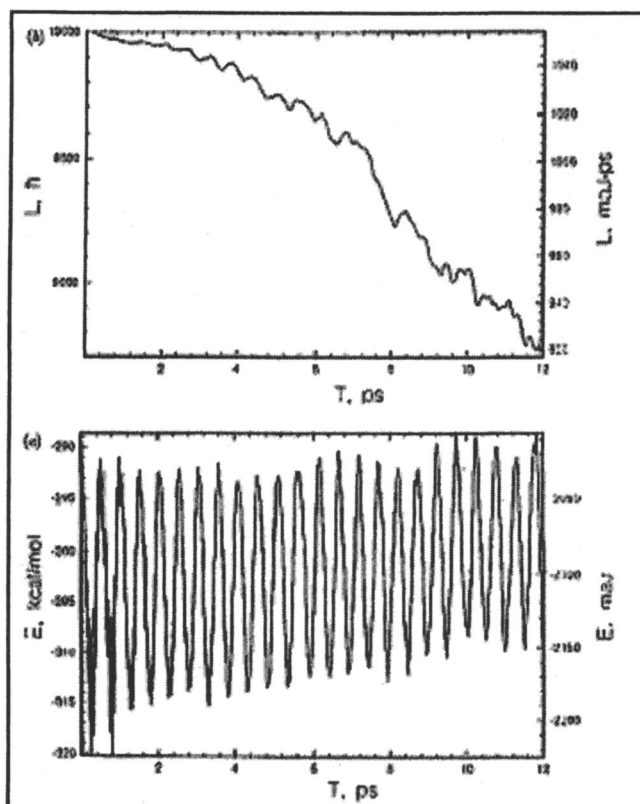
Figure 2

vibration-rotation coupling, especially with the low-frequency, large-amplitude vibrations or centrifugal distortion (which in this study proved insignificant). The strength of this dynamical coupling would depend on the rotational velocity, initial temperature, and the sizes of the shaft and sleeve. One revealing way to examine the frictional drag on the rotating shaft is to plot the shaft-sleeve non-bonded interaction energy as a function of time.

However, more significant is the large peaks which probably correspond to a vibration of the bearing as a whole or wobbling of the shaft. The drag coefficients showed distinct size, velocity, and temperature dependence. As the bearing grew tighter (smaller m - n) or the temperature rose, the drag coefficient increased. In addition, the coefficients were small if the sleeve was frozen during simulation, because no energy could be dissipated into sleeve internal modes. The bearing frictional losses after 2 ps often followed the trends of the drag coefficients for the first 2 ps. The results of one particularly interesting simulation, are shown in Figure 3.

Initially, the shaft and sleeve are rotated in opposite directions with a rotational velocity corresponding to 10000 $\hbar$ (1054 maJ·ps); no external torque is applied. From the shaft angular momentum in
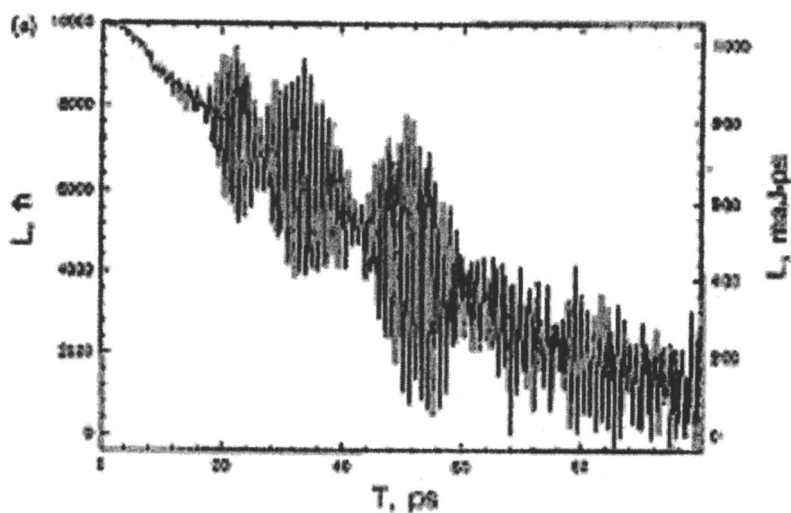
Figure 3.

Figure 3, the first 15 ps of the simulation are similar to those of most of the other simulations in this study: slow, steady loss of angular momentum with fairly small oscillations. Between about 15 ps and about 60 ps, however, there are three beats with oscillations of several thousand ℏ (several hundred maJ·ps). After 60 ps, the shaft once again steadily loses angular momentum; however, the oscillations are much larger than in the first 15 ps. At times, the shaft (and therefore the sleeve, since in this case the total angular momentum is zero) briefly reverse direction. To understand this behavior, it is helpful to visualize the trajectory and we found that the shaft and sleeve slide over one another. This simultaneous sliding and flexing motion gives rise to the beats. After 60 ps, the shaft and sleeve no longer slide across one another, and so the beats disappear. An ideal bearing would not exhibit beats; it would exhibit a slow, steady loss of angular momentum or no loss.

In the laser driven molecular motor simulations we attempted to model a startup process the shaft was initially motionless. The sleeve was frozen throughout the simulation. Calculations were performed for several bearing sizes and field strengths and frequencies, typical simulations ran for several hundred ps. Figures 4 shows a typical profile of shaft angular momentum L_z and the total system energy for several runs for one configuration of the motor. Both angular momentum and energy show strong beat patterns; in many cases, it cycles between rotational pendulum-like behavior (angular momentum oscillations between positive and negative values) and unidirectional motion (motor-like behavior) in which the oscillations die down and then build up again. The beat patterns tend to be fairly symmetrical. The runs show an initial lag time of pendulum-like behavior; this lag time can run up to about half the time for a full cycle of pendulum-like behavior. The performance of motors with the same size and excited with the same frequency varies greatly with the field strength. The best frequency ranges for operation clearly depend on size (axial moment of inertia). Several
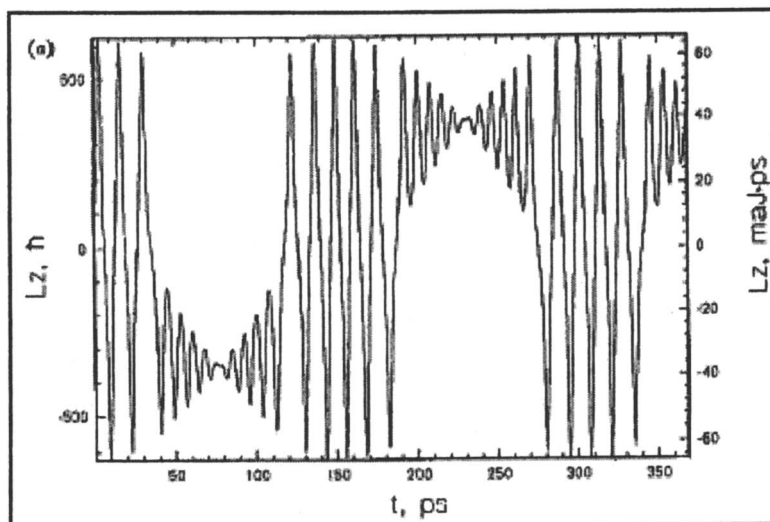
Figure 4

low-frequency simulations showed only pendulum-like motion; it is probable that if some of these simulations were allowed to run several nanoseconds, they would show comparatively long on and off times. In previous laser chemistry applications, it has been found that two lasers are more efficient for creating vibrational and rotational excitations than a single laser (20). For this reason and because of the surprising on/off behavior of the one-laser excitations, we have performed several two-laser runs. Figure 5 shows a run for which the second laser field is an overtone of the first and has the same intensity; other than the second laser field.

We find not only a greatly enhanced on/off time ratio, but much weaker oscillations in both angular momentum and total energy, i.e., more ideal motor performance. If the two lasers are slightly detuned from each other, we obtain even better performance. To find the most optimal operating conditions will require a more extensive search of parameter space, perhaps with the aid of neural network methods.
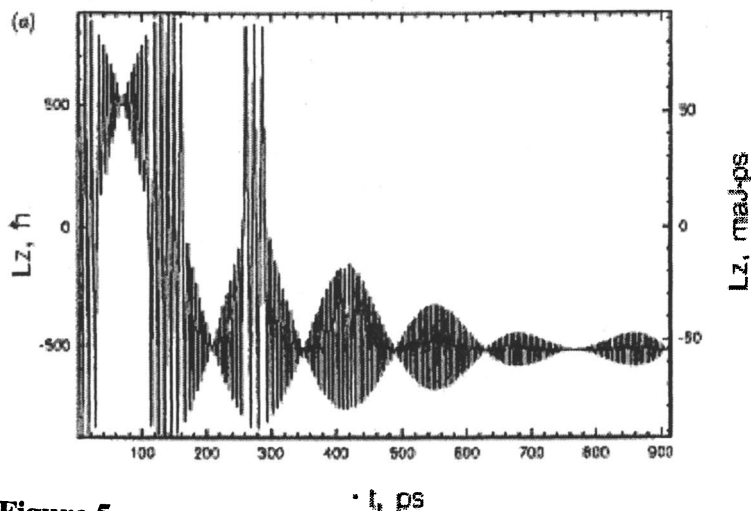
Figure 5

IV. Classical Conclusions

We have found from the completely classical mechanics models that the performance of the nano bearing is temperature-, velocity-, and size-dependent. Bearing clearances must fall in an intermediate range in order to obtain a smooth fit and smooth rotation. Frictional behavior follows expected trends in temperature and rotational velocity. The key bearing shaft interaction appears to be a vibrational effect rather than the coherent crossing of atomic barriers. **Small departures from equilibrium bond distances and angles rapidly destroy the coherence of angular potential energy barriers crossed during rotation.** A bearing can behave poorly if it has more than one type of vibrational motion; this may give rise to beats. Transverse loads can significantly degrade bearing performance if the bearing deforms under shear. However, it seems safe to say that bearing components should either be stiff or should be constrained so as to not allow extraneous vibrational effects.

The use of one- or two-laser excitation of nanometer scale components may prove to be a practical method for introducing controlled motion into nanomachines. With sufficient shaft-sleeve clearance and in the proper regimes of laser field strength and frequency, stable rotational motion was introduced into a model

nanometer scale motor at speeds up to about 10^{12} Hz. The shaft of the motor did not significantly distort during simulation, except at the end with attached charges. The induced motion appeared to be almost purely rotational, except at the most intense laser fields. For simulation purposes, we have used fairly high laser powers in order to fairly quickly excite rotational motion. Similar results could perhaps be obtained with lower powers but for much longer simulation times.

We would expect weaker beat patterns and slower induced rotations. The rotational excitation of a "doped" nanotube is quite complex. The use of two lasers appears to enhance the transfer of laser energy into rotational motion and to induce more stable motion than using one laser. In the two-laser excitation of HF, chaotic motion was proposed to be the mechanism for this enhanced excitation.

The role of chaos in our model graphite motors and in other nanosystems needs to be studied further. In the next section, we examine the static properties of these nano-devices and the important issue of chaos and the partitioning of zero point energy. At this point an important question to ask is whether a purely quantum calcuation would the performance characteristics and optimum operational regimes be significantly different.

V   Importance of Quantum Mechanics for Nanotechnology

Recently we have begun to initiate research in the quantum/classical correspondence for polymer dynamics/nanotechnology and found that for a reasonable model of polyethylene that the dynamics are almost completely chaotic at temperatures as low as 2K(21). Similar conclusions were also reached for carbon nanotubes (a two dimensional arrangement of carbon atoms on the surface of a cylinder) and it is expected that diamondoid materials (which have a fully three dimensional bond network) may behave similarly. In this section it is argued that while classical MD studies of nano-machines are useful they may not give an accurate representation of their performance. Fortunately a new method,

Internal Coordinate Quantum Monte Carlo, an improved technique for computing quantum mechanical ground state energies and wavefunctions, has the potential capability for modeling these systems.

Although space limitations do not permit a complete discussion of the the Internal Coordinate Quantum Monte Carlo method(22), a brief description is included here for the sake of clarity and completeness in the nanotechnology literature. The Schrodinger equation for a system of n particles is

$$-\frac{\hbar}{i}\frac{\partial \Psi}{\partial t} = \left\{ -\sum_{i=1}^{n} \frac{\hbar^2}{2m_i}\nabla_i^2 + V \right\}\Psi$$

Defining $\tau = it/\hbar$, this can be rewritten in the form

$$\frac{\partial \Psi}{\partial \tau} = \left\{ \sum_{i=1}^{n} \frac{\hbar^2}{2m_i}\nabla_i^2 - V \right\}\Psi$$

which has the form of the diffusion equation with diffusion constants

$$D_i = \frac{\hbar^2}{2m_i}$$

plus a first order term with a rate constant V. The formal solution is

$$\Psi(q,\tau) = \sum_{k} a_k \Phi_k(q)\exp(-E_k\tau)$$

which reaches the ground state in the steady state limit. One way to solve this equation is to generate a random set of "psi particles", or psips, which are diffused according to the diffusion constants and created or annihilated according to the first order rate constant. An

especially useful method for improving the convergence of QMC calculations is to incorporate importance sampling (23). Defining the guiding function ψ_0 (also called the trial or sampling function) and ψ according to $\Phi = \psi/\psi_0$ and substituting into the Schrodinger equation yields

$$\frac{\partial \psi}{\partial \tau} = \sum_i D_i [\nabla_i^2 \psi - \nabla_i \cdot (\psi \nabla_i \ln \psi_o)] - \left(\frac{\hat{H}\psi_o}{\psi_o}\right)\psi$$

The second term on the right hand side, which includes what is called the drift velocity, essentially guides the psips to the most probable coordinate regimes and thereby accelerates convergence. A very suitable choice which is the heart of the ICQMC method is to use a trial function as a product of functions of internal coordinates

$$\psi_0 = \prod_i \psi_i(r_i)\prod_j \psi_j(\cos\theta_j)\prod_k \psi_k(\cos\tau_k)$$

Using this method for the nanotube structure above we computed the ground state wave function and compared structural stability with a completely classical simulation.

The initial starting conditions (velocity and positions) for each MD simulation of both systems were generally chosen based on either a quasiclassical (state-to-state) or random (bulk) distribution of the energy. Quasiclassical initial conditions assign zero-point energy to each of the 3N-6 vibrational normal modes according to quantization rules for harmonic oscillators. It appeared that the expected instability in fullerene nanotubes was due to rapid energy transfer to low frequency modes which tend to retain the energy due to resonant transfer back and forth between the longitudinal and ring breathing modes, causing the onset of large-amplitude motion. MD studies of carbon-based nanostructures such as molecular bearings, shafts, pumps, and motors have all demonstrated the same phenomenon: large amplitude motion resulting from chaos and non-linear resonances leads to positional instability. The resulting microscopic motion correlates to the coupled longitudinal-ring breathing

vibrational modes and resembles an S-shape(24). Although the positional instability is easy to predict *a priori* using an empirical scaling law, other similar large amplitude vibrations could equally spoil nanotechnology designs. However, upon rigorous examination of the vibrational motion in macromolecular systems such as a single polyethylene chain, it became apparent that the overall motion was somehow overestimated: too much energy was transferred to low frequency modes. surface since it is based solely on geometrical measures of the nanotube.

For comparison of the classical instability discussed above to a corresponding quantum calculation, ICQMC calculations were performed on three different sizes of nanotube: 6/9, 6/27, and 6/49, where the first number is the number of atoms per ring and the second number is the number of rings. The nanotube discussed in the previous article had the size 6/99. Once again, the energies scaled approximately linearly with the number of atoms. Just as importantly, however, the ground state of even the longest nanotube studied was found to be extremely stiff. Figure 6 shows the distributions of psi
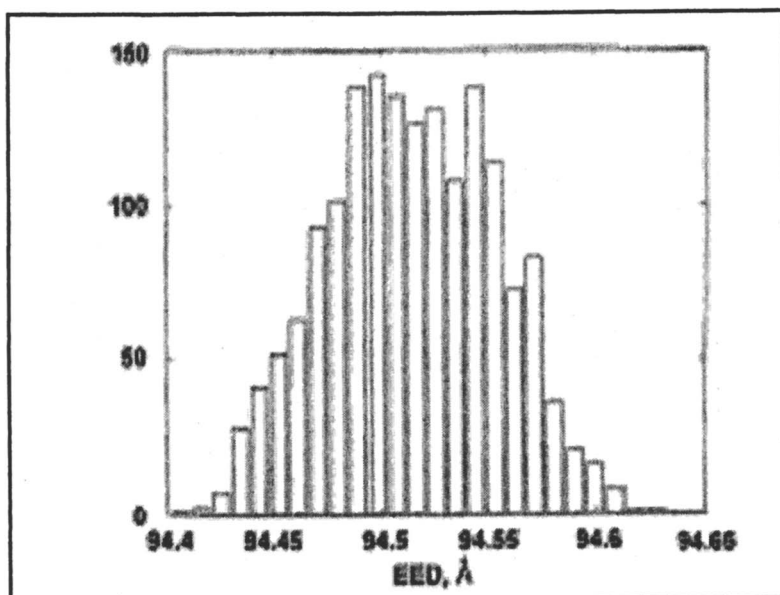
Figure 6

particle end to end distances for a typical 6/49 calculation, where the end to end distance is defined above. The distribution is approximately gaussian with a width on the order of 0.07 Å. Although the end to end distance as defined here would inevitably show some effects from ring breathing and other modes in addition to accordion modes which would lengthen the tube, the accordion modes would change this distance the most. Distances between other pairs of atoms (where the effects of breathing or S modes would predominate) show similar distributions. Results for 6/9 and 6/27 tubes are similar. In contrast, classical MD calculations had end to end distance distributions (over the entire simulation) with widths greater than 20 Å, which is in qualitative disagreement with the quantum results. In a similar way the nanotube also demonstrated the qualitative error of the classical molecular dynamics simulations. From semiclassical studies on few body models it has been shown that resonant coupling does not change the nature of ground eigenstate. Such resonances are responsible for the onset of chaos in these systems and therefore instabilities due to the facile sharing of the zero point energies. It is the tremendous amount of energy in the high frequency modes that can be used to generate the large amplitude motion in the low frequency modes. This behavior is seriously incorrect and represents a major challenge to the use of classical molecular dynamics for simulation of nano machines or components. It is especially ironic that a method based on using a random/chaotic propagation of a collection of particles to simulate the solution to the ground state wave function yields a perfectly stable solution and, being exact quantum mechanics, is correct, while a deterministic molecular dynamics calculation of the motion of atoms which therefore should be stable and quasiperiodic, is instead chaotic. It should be noted that from a statistical point of view (ensembles of objects) the concept of temperature in these calculations would require the generation of a large number of excited states. At T = 300K, the number of accessible states can be crudely approximated to be superexponential in N, the number of particles. These excited states would have to be weighted by $e^{-E/kT}$ and various observables

would be generated from the wavepacket. In this case the quantum reults would give larger fluctuations than we have presented here; however, variances in end to end distance would still be expected to small compared to MD results. We are currently pursuing this area of inquiry.

In summary, we have found that classical molecular dynamics simulations of many body systems may not accurately reflect the true stability, structure or dynamics of systems of interest to nanotechnology. The problem appears to be less severe for highly connected bond networks such as carbon nanotubes. The importance of this result is that current designs for various nano-components may actually perform better and be more stable than recent molecular dynamics simulations suggest. Hopefully this result will encourage further research on the construction of these new types of molecular structures. Specifically, classical MD simulations exhibit excessive vibrational motion. This results from pooling the quantum zero-point vibrational energy into low frequency modes (a process which is not allowed quantum mechanically) and, in the case of the graphite nanobearings, leads to an instability which tremendously degrades the performance of the bearing. Unfortunately, a complete model using time-dependent quantum mechanics is not currently feasible for the study of molecular bearings, although the recently developed internal coordinate quantum Monte Carlo (ICQMC) technique is making significant inroads into the quantum mechanical description of the vibrational ground state of nanoscale systems.

V Application of Semi-classical Rigid-body Dynamics for Nanotechnology

In this section, we demonstrate the utility of rigid-body dynamics and semiclassical mechanics for studying the dynamical properties of nano-bearings(25). This approach avoids the zero point energy problem of fully atomistic classical molecular dynamics simulations and has the added benefit of being tremendously more efficient, making simulations possible which are much longer in time. Two

different types of bearing models are considered in this study. This first is a rigorously planar model which consists of a single atomic layer (slice perpendicular to the z-axis) from a pair of nested graphitic nano-tubes somewhat similar in spirit to figure 1. This model, while synthetically unachievable, contains the essentials of the dynamics of a nano-bearing, and its simplicity makes it a useful model for understanding the dynamics of such systems. In this model the n=2 carbon atoms of the inner ring are fixed with respect to each other as are the m=2 carbon atoms of the outer ring. The outer ring or sleeve is then held in place and the inner ring or shaft is allowed to vibrate and spin in the x-y plane. The configuration of the system is completely described with three independent variables, the x and y positions of the center of mass (COM) of the shaft, and the angular orientation of the shaft in the x-y plane, denoted.

The second type of rigid body bearing model studied here is less restricted than the previous model and has three-dimensional motion. It also consists of a pair of nested carbon nanotubes as depicted in Figure 1 with the sleeve held in place but the shaft held in position only in the longitudinal z-direction. In this model, the shaft is free to translate and rotate in the x-y plane, but is restricted to maintain its z-position. Such a model is both chemically reasonable and representative of an actual bearing in application where the bearing shaft is fixed in its longitudinal position by the construction of the machine. Any dynamics or friction introduced by the components restricting the z-position of the shaft is neglected in this work. The orientation of the system is fully described by the same three independent variables which are used in the rigorously planar model, but the mass and moment of inertia of the shaft, as well as the interaction potential between the shaft and the sleeve, are dependent on the full three-dimensional nature of the system. In the present work, we employ the rigid-body approximation in which the entire body (bearing shaft in the present case) is allowed to translate and rotate, but all of its internal coordinates are frozen in their equilibrium positions.

The methods of constraint dynamics, while well known in other fields (26), have been used relatively little in computational chemistry. As noted in the introduction, however, it is now clear that the vibrational motion of nanosystems modeled with fully atomistic simulations is overestimated. Accurate quantum calculations have shown these structures to be essentially rigid in the ground state (16,27). In light of these developments we have concluded that nanosystems operating at low temperatures will, in many cases, be more accurately modeled with rigid-body dynamics.

The calculation of quantum eigenstates with semiclassical methods is based on the correspondence of quantum eigenstates to classical invariant tori, a concept discussed in more detail elsewhere(28). The semiclassical quantization condition for a one-dimensional bound system is well known and given by the WKB formula which can be found in any standard quantum mechanics text (29),

$$J = \int p.(q) \, dq = (n + \tfrac{1}{2})\hbar$$

Here J is the action, q is the coordinate variable with conjugate momentum p, h is Planck's constant, and n is a non-negative integer index, the quantum number for the state. The integral (called the phase integral) is over a complete cycle of the motion, i.e. one oscillation. The N-dimensional analog of the WKB quantization condition is really a generalization of the Bohr-Sommerfeld quantization rules.

Consider a bearing consisting of a sleeve composed of 30-membered rings (m = 30) and a shaft composed of 10-membered rings (n = 10). The rigorously planar model based on such a bearing has five atoms in the inner ring at the corners of a rigid regular pentagon with sides of length 2.46 Å, and 15 atoms in the fixed outer ring at the corners of a regular pentadecagon with sides of length 2.46 Å. For brevity, this will be termed the planar 10- 30 model. It is enlightening to consider the shape of the potential energy surface which is felt by the shaft due to the presence of the sleeve and which

controls the dynamics of the bearing. The potential felt by the inner ring produces hindered rotation of order 15 as demonstrated by Merkle(15). Also as predicted by Merkle (15), the rotational barriers are very small when the inner ring is centered, on the order of a small fraction of a kcal mol-1. The rotational potential for R = 0 is shown in Figure 3 of reference (25), along with that for a 10-32 planar model and a 10-40 planar model. (Cuts at other values of _ behave similarly.) Note that the planar 10-32 and 10-40 models exhibit off-center minima in the potential. This means that the energetically favored position for the inner ring is slightly off-center. The minima in the radial potential for the planar 10-30 model is at R = 0, favoring a centered position for the inner ring. The minimum in the potential is determined by the relative values of the separation of the inner and outer rings, and the equilibrium separation in the site-site interaction potential. The bearing clearance is approximately 1.23(m-n) (30), which gives the 10-30 system a clearance of about 3.91 Å and the 10-32 system a clearance of about 4.31 Å. These values compare with an equilibrium separation of re $_D$ = 4.27 Å. It will be seen that optimizing this 'fit' is the key to optimizing bearing performance. Dynamical simulations have been run for the three planar models using the techniques of rigid-body dynamics as described above. A typical trajectory is shown in figure 7, which displays the x and y positions of the COM of the inner ring as a function of time for the planar 10-30 model. For an N-degree-of-freedom model, the classical trajectory is characterized by 2N phase-space variables: N independent coordinates and their conjugate momenta. These are the variables which are solved for in the numerical integration. Such trajectories can be classified as either quasiperiodic, or chaotic. If there exist N integrals of motion, the trajectory will be restricted to develop on the surface of an N-dimensional torus (invariant torus) embedded in the full 2N-dimensional phase space. Such a trajectory will be quasiperiodic or 'regular' in nature, developing in an orderly fashion over time. In the absence of at least N isolating integrals of motion, some of the phase space will be filled with chaotic trajectories. One signature of chaotic behavior is that neighboring trajectories separate
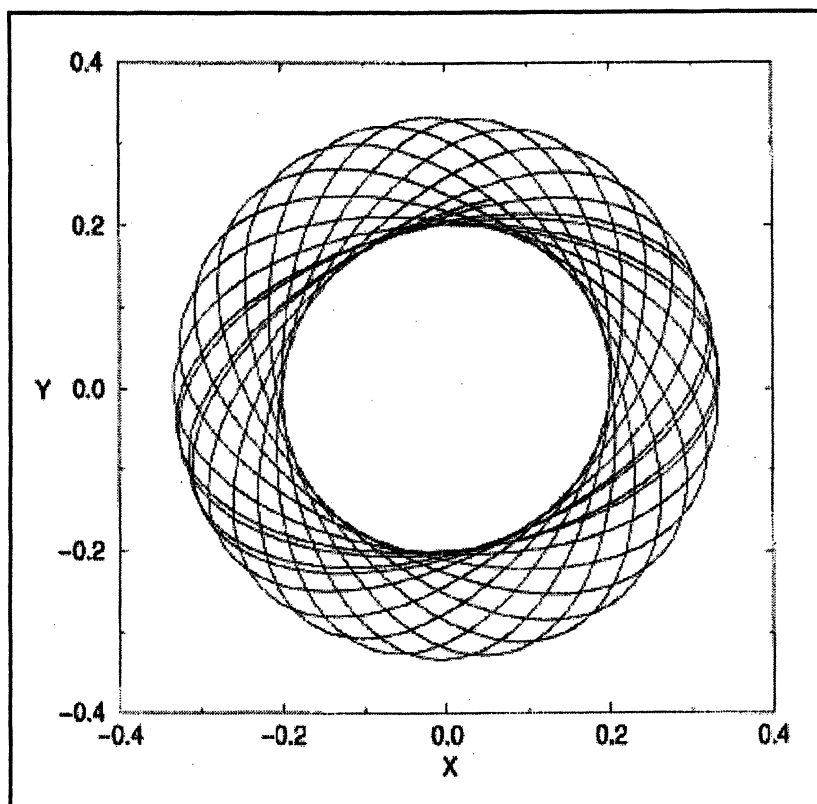
Figure 7

exponentially (31,32). Since quasiperiodic trajectories are restricted to a N-dimensional torus embedded in the 2N-dimensional phase space, the set of points where a quasiperiodic trajectory passes through a plane in phase space will lie on simple closed curves. Such a figure, termed a Poincare surface of section (SOS), is an important analysis tool from the field of nonlinear dynamics. Composite SOS plots (SOS plots generated with multiple trajectories of the same total energy) for the planar 10-30 model are shown in figure 8a. The three trajectories used to generate figure 8a are quasiperiodic. Note that the SOS points lie on simple closed curves. In contrast, the three trajectories used to generate Figure 8b are chaotic. In this case the SOS points do not lie on simple closed curves, indicating that the trajectory is not confined to a three-dimensional invariant torus in the six-dimensional phase space.
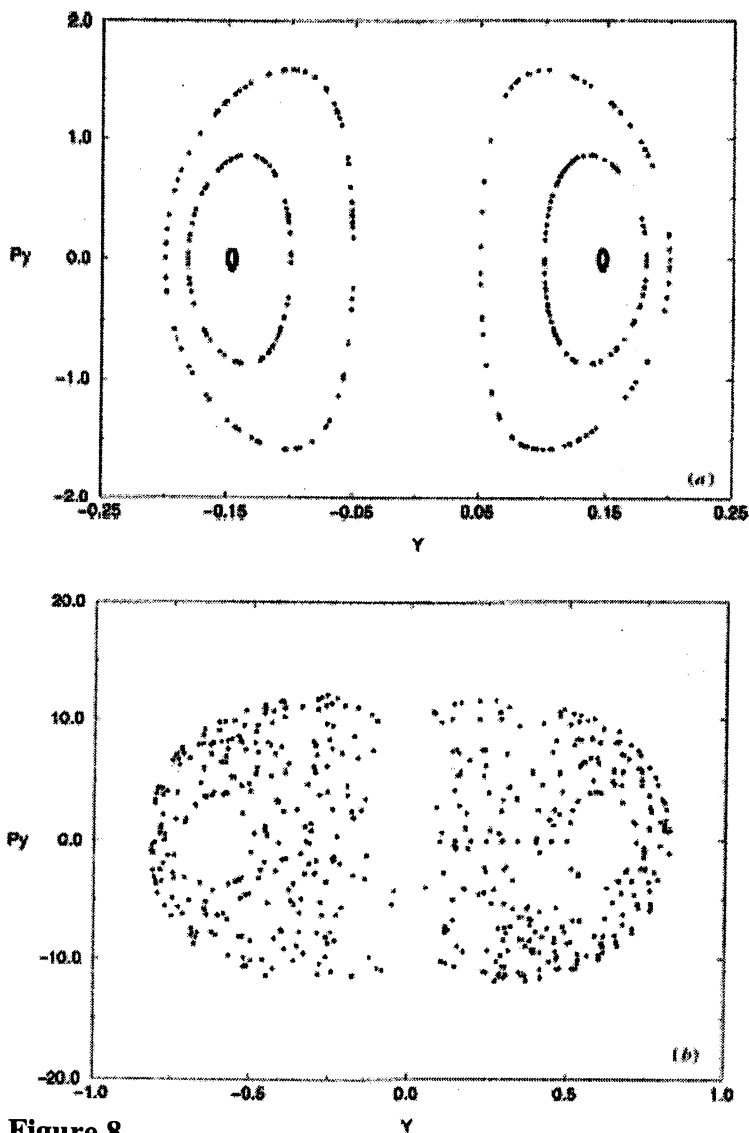
Figure 8

Quasiperiodic trajectories are dynamically important because they correspond to frictionless motion. The system is multiply periodic and will continue to develop in time without loss of energy from spin to other modes. While the spin rate changes with time, it does so in an oscillatory fashion, maintaining a fixed long-term average. In contrast for a chaotic trajectory the spin rate changes over time in an irregular way. In the chaotic case, energy can be lost from spin into other

modes while in the quasiperiodic case, the bearing will continue to spin indefinitely, a behavior we term super-rotary. This will allow atomically precise nanobearings to be run dry as suggested by Feynman (33). It is clear that one important design consideration in the development of nanobearings will be delimiting the quasiperiodic regime. In any actual nanobearing application, it is likely that the bearing will support some load. It is therefore important to ascertain the dynamics of the bearing under load. To elucidate the nature of nanobearing performance under load(25), we repeated the chaos analysis of the planar 10- 30 bearing with a constant force of 70 pN exerted on the center of mass of the ring perpendicular to the axis of rotation. This force is similar in magnitude to the weakest tip-sample interactions in scanning force microscopy (SFM) (34). It was found that the regions of superrotary motion are much more restricted under load (25), suggesting that nanobearings must be very carefully designed for optimum performance. Again, high speed rotation favors superrotary dynamics. With the dynamical parameters chosen to mimic those used in the fully atomistic simulations, the bearings are all superrotary, in contrast with the results of the fully atomistic simulations where unphysically large amplitude vibrations severely deteriorated the performance of the bearing. Such unphysical vibrations are avoided in the rigid-body approximation as shown here. While regions of chaotic motion exist, there are also regimes of quasiperiodicity where the rotation is frictionless as alluded to by Feynman (33). In the present model, the motion involves three independent degrees of freedom. While the system is not analytically separable, the existence of smooth SOS curves indicates that the motion is, at least in some regimes, quasiperiodic. In addition, we have seen that in cases of high spin, the spin of the bearing shaft is essentially decoupled from the motion of its center of mass.

VI Final Conclusion

By using the tools of rigid-body dynamics and semi-classical mechanics we have investigated the performance of graphitic nano-

bearings. A rigorously planar model exhibits the essentials of the dynamics which are confirmed with restricted three-dimensional simulations. It was found, as intimated by Feynman (33), that under the right conditions nano-bearings are super-rotary. Such super-rotary motion is manifest by quasi-periodicity in the classical trajectories and is more prevalent under conditions of fast rotational speed, where most of the total energy available to the bearing is tied up in the spin of the shaft. It was also found that the regime of super-rotary motion is more restricted when the bearing is under load, suggesting that a very careful design of a nano-bearing is needed to ensure optimum performance. In light of the fact that the present methods exhibit dynamics in agreement with earlier predictions about the dynamics of atomically precise bearings (33), and the fact that fully atomistic simulations exhibit unphysical dynamics, we believe that the present rigid-body dynamics approximation represents a more accurate method for the simulation of nano-systems at low temperatures. Fully atomistic classical dynamics simulations allow leakage of the quantum zero-point vibrational energy leading to excessively large amplitude vibrational motions. The rigid-body treatment avoids this unphysical effect. Finally, it is fortunately unnecessary to completely forfeit all knowledge of the quantum mechanical properties of the system when the rigid-body approximation is made. Quite detailed information about the quantum mechanics of the system can be obtained through the application of semi-classical methods which dovetail perfectly with rigid body dynamics.

Acknowledgements

References

1] K. E. Drexler, *Nanosystems: Molecular Machinery, Manufacturing, and Computation*, John Wiley, New York, NY, 1992.

2] M.D. Barnes, K. Runge, B. Hathorn, S. Mahurin, B.G. Sumpter, D.W. Noid, Materials Today **5**, 20-25 (2002).

3] D.Y. Kim, H.N. Cho, C.Y. Kim, Prog. Polym. Sci. **25**, 1089-1139 (2000).

4] R. E. Tuzun, D. W. Noid, B. G. Sumpter and R. C. Merkle , **7** , 241-246 (1996); R. E. Tuzun, D. W. Noid, B. G. Sumpter and R. C. Merkle, Nanotechnology **8** , 112-118 (1997).

5] Henningsen U, Schliwa M NATURE **389** (6646): 93-96 SEP 4 1997

6] R. E. Tuzun, D. W. Noid and B. G. Sumpter, Nanotechnology **6**, 64-74 (1995).

7] S. J. Sowerby, N. G. Holm and G. B. Petersen, Biosystems **61** (1): 69-78 JUN 2001

8] H Eda and J. Shimizu , J JPN SOC TRIBOLOGIS **45** (9): 661-666 2000

9] JK Gimzewski , C. Joachim, RR. Schlittler RR, et al.SCIENCE **281** (5376): 531-533 JUL 24 1998

10] R. E. Tuzun, D. W. Noid and B. G. Sumpter, Nanotechnology **6**, 52-63 (1995).

11] D. Srivastava, Nanotechnology 8 (4): 186-192 DEC 1997

12] K. Fukui, JH Frederick and JI Cline, Phys Rev A **58** (2): 929-934 AUG 1998

13] A. Globus, CW. Bauschlicher, J Han, et al, Nanotechnology **9** (3): 192-199 SEP 1998

14] J. Vacek and J. Michl, P Natl Acad Sci USA **98** (10): 5481-5486 MAY 8 2001

15] R. C. Merkle, Nanotechnology **4**, 86 (1993).

16] D. W. Noid, R. E. Tuzun and B. G. Sumpter, Nanotechnology **8** , 119-125 (1997) .

17] M. L. Klein, Ann. Rev. Phys. Chem. **36**, 525 (1985); W. G. Hoover, Ann. Rev. Phys. Chem. **34**, 103 (1983)

18] R. E. Tuzun, D. W. Noid, B. G. Sumpter and C. E. Wozny, - Die Makromolekulare Chemie: Theory and Simulation **6** , 855-880 (1997)

19] S. K. Gray, D. W. Noid and B. G. Sumpter , J. Chem. Phys., **101**, 4062-4072 (1994).

20] Stine JR, Noid DW. 1981, Chem. Phys. Lett. **77**:287.

21]D. E. Newman, C. Watts, B. G. Sumpter and D. W. Noid, Die Makromolekulare Chemie: Theory and Simulation , **6** , 577-590 (1997) .

22] R. E. Tuzun, D. W. Noid and B. G. Sumpter, J. Chem. Phys. **105** , 5494-5502 (1996).

23] D. Ceperly 1983 J. Comp. Phys. **51** 404

24] B. G. Sumpter and D. W. Noid, J. Chem. Phys. 102, 6619-6622 (1995).

25] K Sohlberg, R. E. Tuzun, B. G. Sumpter. and D. W. Noid, Nanotechnology **8** , 103-108 (1997).

26] Goldstein H 1980 *Classical Mechanics* (Reading, MA: Addison-Wesley)

27] R. E. Tuzun, D. W. Noid and B. G. Sumpter, Die Makromolekulare Chemie: Theory and Simulation, 7 , 203- 209 (1998)

28] Noid D W and Marcus R A 1975 *J. Chem. Phys.* **62** 2119; D. W. Noid, M. L. Koszykowski, and R. A. Marcus, Ann. Rev. Phys. Chem. 32, 267-309 (1981).

29] Merzbacher E 1970 *Quantum Mechanics* (New York: Wiley)

30] Tuzun R E, Noid D W and Sumpter B G 1995 *Nanotechnology* **6** 64.

31] Gustavson F G 1966 *Astron. J.* **71** 670

32] Ford J 1973 *Adv. in Chem. Phys.* **24** 155

33] Feynman R P 1960 *Eng. Sci.* **23** 22

34] Spatz J P, Sheiko S, M"oller M, Winkler R G, Reineker P and Marti O 1995 *Nanotechnology* **6** 40

Chapter 9

Wetting, Confinement, and Drainage of Liquids

Miquel Salmeron[1], Frieder Mugele[2], and Lei Xu[1]

[1]Materials Science Division, Lawrence Berkeley Laboratory, University
of California, Berkeley, CA 94720
[2]Universität Ulm, Abteilung Angewandte Physik, Ulm, Germany

Abstract

Using proximal probe tools such as the Surface Forces
Apparatus (SFA) and the Atomic Force Microscope (AFM), as
well as spectroscopic tools such as Sum Frequency Generation
(SFG), we have studied the welling, spreading and drainage of
liquids at the nanometer scale. Two examples will be
discussed here. The first involves the layering and drainage of
long alkyl-chain alcohols octanol and undecanol. The second
example involves the drainage of perfluoropolyether
lubricants.

I. Drainage and Viscous properties of long alkyl-chain alcohols

On mica, the main substrate used in these investigations, long alkyl-chain
alcohols form autophobic monolayers made of densely packed, self-assembled
molecules with the alcohol end groups bound to the substrate and the alkyl
chains arranged in a straight nearly vertical position. The SFG spectra
corresponding to an undecanol monolayer is shown in the figure 1. The sharp
intense peaks at the position of the symmetric CH_3 stretch modes and the lack of
intensity at the position of the CH_2 stretch modes inside the chain indicate that
the alkyl chains are indeed straight and packed tightly, as shown schematically
at the bottom of the figure. Above this monolayer, the rest of the molecules form

123

a partially welling droplet, with contact angle of 50°, similar to that formed on a silanated surface[1].

When the alcohols are compressed between the flat mica surfaces of the SFA, drainage takes place under very small pressure until the wall separation is equal to a few nanometers. At this point, structural or solvation forces become important and increase rapidly in strength and in an oscillatory' form, with a period of twice the molecular length in the case of octanol. This indicates that the liquid is expelled in bi-layers units. In these units pairs of molecules bind to each other through H-bonds or their alcohol ends. In addition the bilayers are quite flexible and a substantial compressibility is observed. We interpret this compressibility as arising from the rigid tilt of the alkyl chains from vertical to a nearly horizontal position before being expelled. Figure 2 illustrates these results.

In the case of undecanol the period of the oscillatory solvation forces is close to 5 Å, the diameter of the alkyl chain. We thus believe that the longer molecules lie flat instead of normal to the wall surface. This does not apply to the first strongly bound layer, where the molecules are nearly vertical to the mica surface. In both alcohols the surface-bound monolayers could not be expelled from the SFA at the highest pressures applied, around 10-20 MPa.

The next phenomenon that we observed is the dynamics of the process of the layering transition. i.e., the expulsion of a molecular layer. By using monochromatic light instead of white light in the SFA, and by choosing the wavelength close to a sharp transmission peak, we could monitor the variation of transmitted light intensity across the gap with a spatial resolution of a few micrometers in the plane, and of a few angstroms in the perpendicular or z-direction. In this manner changes in wall-to-wall separation of less than a molecular diameter could be discerned. In the present experiment the walls of the two mica surfaces were approached fast enough to trap a metastable last layer of molecules (in addition to the two monolayers strongly bound to the mica substrates). The drainage of this metastably trapped layer (the 4 -> 2 transition in figure 2) was then imaged with a CCD camera and stored in video format. A few snapshots of the process, lasting less than one second, are shown in figure 3. The images show the nucleation of an initial hole (dark patch near the left edge), and the advance of its boundaries until the whole contact area, which has a diameter of about 40 micrometers, is covered and the layer completely expelled. As the images show, a few residual pockets of molecules remain trapped[2].

The viscoelastic properties of the films were studied by oscillating laterally one of the mica wallsand measuring the decrease in oscillation amplitude caused by the viscous drag as the two mica surfaces approach each other[3]. This is shown schematically by the drawings at the top of figure 4. The
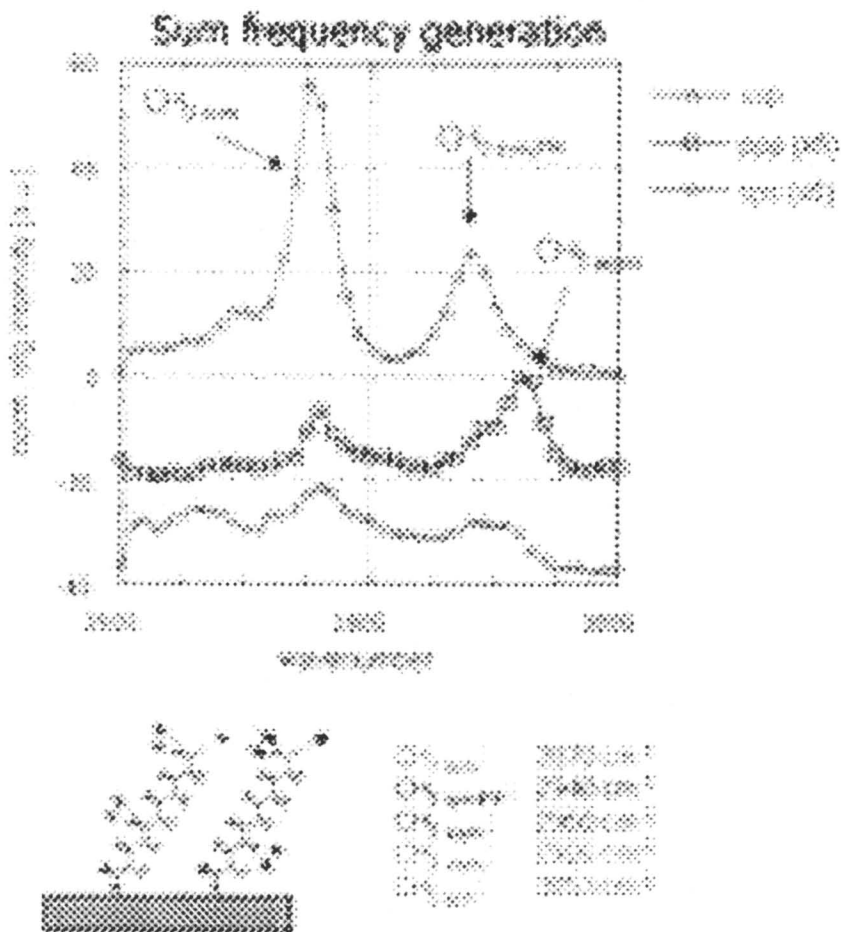
Figure 1.
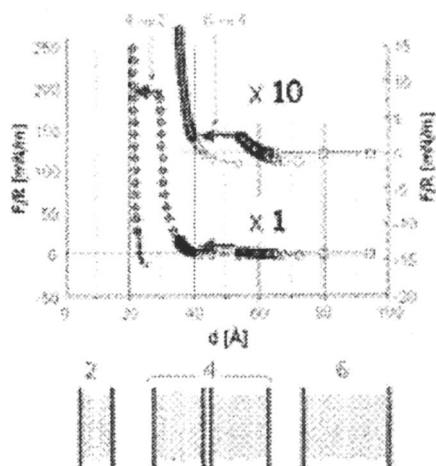
Figure 2.

Hole nucleation and growth in the layering transition of last *mobile* undecanol layer
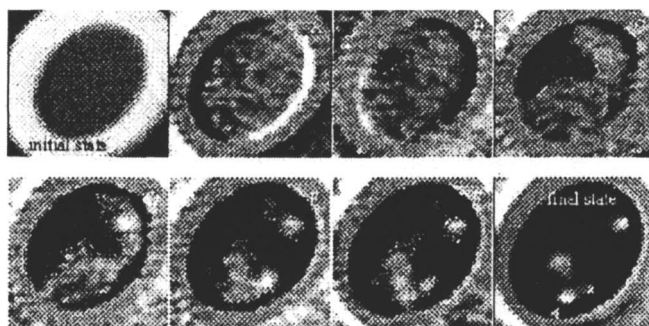
Residual trapped pockets

Figure 3.

left ordinate scale shows the decreasing separation of the gap between the two mica walls and the abrupt jump at point A corresponding to the 6 -> 4 transition in figure 2. In the right ordinate we plot the viscosity. As can be seen the viscosity remains equal to the bulk value of octanol until the last bi-layer that can be expelled (point A of the figure). At this point only a modest increase of viscosity of about 5% was detected. The two cylindrical mica surfaces start to flatten now by elastic deformation due to the applied pressure. The increase in viscosity between this point A and the final point B, where the last bilayer is finally removed (end point of figure 3) is simply due to the increasing contact area. At point B the surfaces become stuck to each other and large forces, leading to boundary friction and stick-slip phenomena, appear. This example is interesting because unlike many other cases, the viscosity of molecularly thin film remains bulk-like until the very last layers[4].
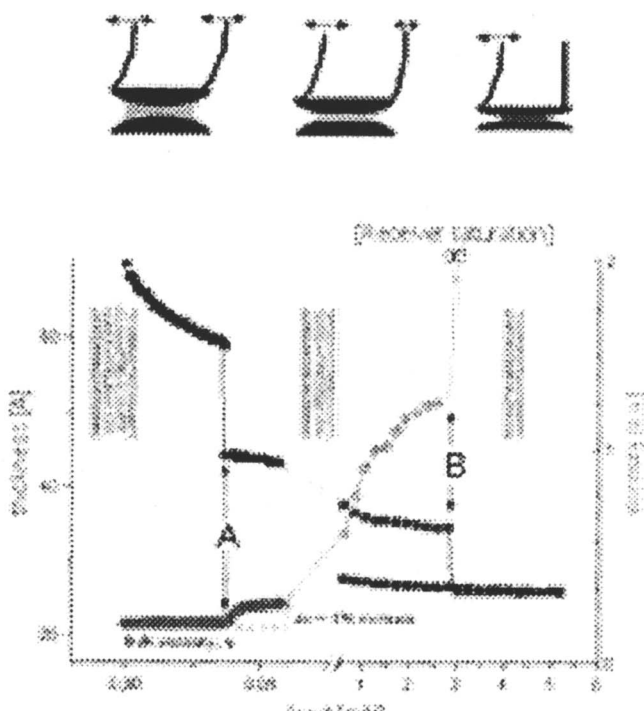
Figure 4.

II. Drainage of perfluoropolyethers

Our final example concerns the drainage of perfluoropolyethers, long chain lubricants used in hard disk drives to protect the recorded media from wear and stiction of the write-read head. These lubricants are made with a

variety of different end groups, from inert terminations like CF_3 to single or double alcohols in one or the two ends. A common double-ended alcohol termination is that of ZDOL, while Demnum has only one alcohol termination. When these molecules are squeezed between the two mica surfaces they are expelled with little applied force[5]. In a slow approach of a few Å/min, viscous forces are observed to increase when the separation becomes equal to two equivalent gyration diameters R_G, which for the ZDOL used in this study (molecular weight 5600) is 37 Å, and for Demnum (MW = 6524) is 52 Å. As shown in figure 5, the force to drain the lubricants increases rapidly under slow approach below $2R_G$ separation until finally the approach stops when a film of lubricant one molecule thick remains in the gap, with a total separation of 1 R_G.
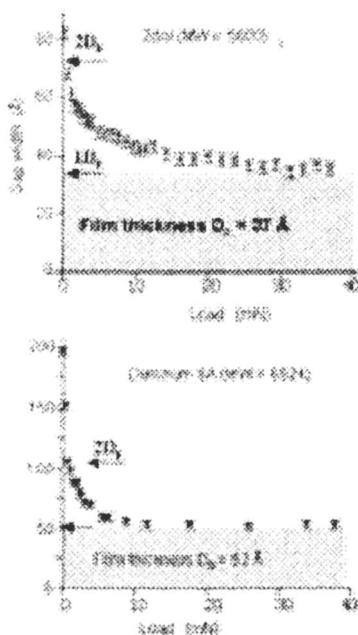
Figure 5.

If instead of a slow approach the confining walls are approached fast, like in the case of alcohols, excess liquid is trapped in a metastable state that drains at a rate dictated by its viscosity. In our experiment we trapped the equivalent of 4 R_G of ZDOL after increasing the pressure from near zero to close to 10 MPa in a few milliseconds, from an initial separation of a few micrometers. The time evolution of the gap separation due to the drainage is shown in the graphs of figure 6. From this data and the Navier-Stokes equation that relates thickness and time (shown at the bottom of the figure), we obtained a viscosity value that is more than 10 times larger than the bulk value of 2 Poise.
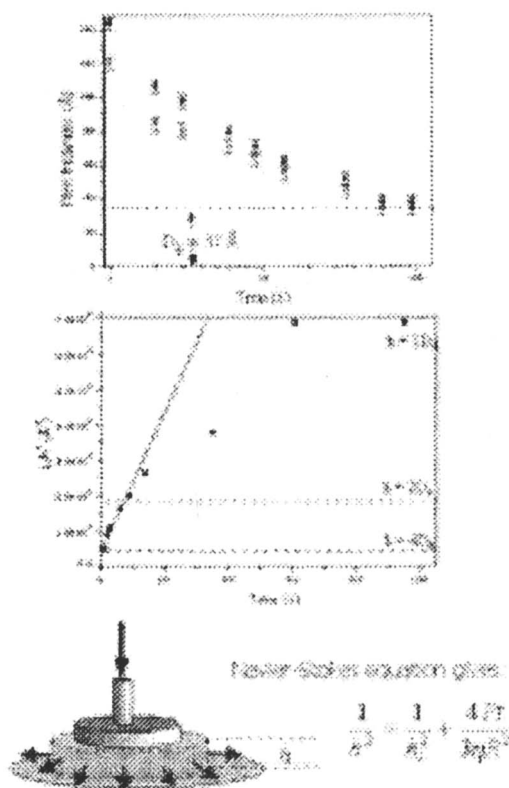
Figure 6.

In summary, we have shown that the drainage of liquids from narrow cavities of molecular size can be studied in a quantitatively using a combination of techniques. These techniques provide force and gap separations that permit the determination of the viscous properties of liquid films of nanometer thickness. In the two examples examined here have found that alcohols with long alkyl chains tend to organize under confinement in bi-layers bound through their OH group ends. They are expelled in pairs for the octanol case. The last layer in direct contact with the mica walls cannot be expelled. The alcohols retain the bulk viscosity down to the last layer expelled. We have also shown how the dynamics of layer expulsion, by nucleation of holes can be studied quantitatively to obtain information on the friction and viscous properties of at the molecular scale. We have shown that in the case of the much more viscous perfluoropolyethers, ZDOL and Demnum, the viscosity increases by approximately one order of magnitude when the trapped film has a thickness of less than four gyration diameters.

Acknowledgment

References

1. F. Mugele, S. Baldelli. G.A. Somorjai and M. Salmeron. *J. Phys. Chem.* **104**, 3140 (2000).
2. F. Mugele and M. Salmeron. *Phys. Rev. Lett.* **84**, 5796 (2000).
3. F. Mugele and M. Salmeron. *J. Chem. Phys.* **114**, 1831 (2001).
4. J. Klein and E. Kumacheva. *Science* **269**, 816 (1995).
5. L. Xu, D.F. Ogletree, M. Salmeron, H. Tang and J. Gui. *J. Chem. Phys.* **114**, (23). 10504 (2001).

Chapter 10

The Implication of "Jump-In" for the Shear Viscosity of Ultra Thin Liquid Films

Uri Raviv[1], Nir Kampf[1], and Jacob Klein[2]

[1]Department of Materials and Interfaces, Weizmann Institute of Science, Rehovot 76100, Israel
[2]Physical and Theoretical Chemistry Laboratory, Oxford University, South Parks Road, Oxford OX1 3QZ, United Kingdom

A surface force balance has been used to investigate the shear behavior and to evaluate the viscosity of water-based solutions confined between smooth surfaces in various conditions. We examine the process of jump-in, across the last few nanometers of thin water films, to adhesive contact between the surfaces. Analysis of the jump behavior indicates that the effective viscosity of the films of the different solutions examined remains similar to its bulk value even when it is confined to sub-nanometer gaps. Independently, we find that the shear stress across the progressively thin films is immeasurably small (within our resolution) down to the adhesive contact. These findings lead us to conclude that the two observations are related to each other and that this should be a general phenomenon.

Introduction

The properties of water and salt solutions under confinement have been studied extensively because of their importance in colloidal dispersions, tribology, and particularly because of their relevance to a quantitative understanding of many processes in biological systems [1-9]. The fluidity of water in confined geometries and its molecular mobility in pores and slits has been extensively studied using a variety of methods [1,4,10-14].

We have shown that, in contrast to non-associating liquids [15], the effective viscosity, η_{eff}, of water remains close to its bulk value η_{bulk} even when it is confined between two (hydrophilic) mica surfaces to films in the thickness range 3.5±1 to 0.0±0.4 nm [16]. Two observations supported this conclusion. The first was that, when one of the surfaces is slid over the other across the confined liquid film, over the shear rates used, the shear stresses maintained by these films were immeasurably low (within our resolution). The second was obtained from the analysis of the time it takes for the two mica surfaces to jump from a separation distance D of 3.5±1 nm into a flat adhesive contact at $D = D_0 = 0.0±0.4$ nm due to the van der Waals attractive forces between the surfaces across water.

In this paper we show that the normal and shear forces measured across dilute acetic acid and salt solutions exhibit similar features. We then discuss and compare our results with other systems that show similar behavior and argue that the coupling between the jump-in and the shear forces is a general phenomenon.

Experimental

The normal $F_n(D)$ and shear $F_s(D)$ forces between two opposing curved mica surfaces (of mean radius R) as a function of their closest separation D, were directly measured using a surface force balance (SFB), for which detailed experimental procedures have been described elsewhere [17,18]. Multiple beam interference allows the distance between the mica surfaces, which are silvered on their backsides, to be measured with resolution of ± 0.2 - 0.3 nm and their contact geometry (including R) to be determined from the shape of the interference fringes. F_n is determined directly from the bending ΔD of the springs, as $F_n = K_n \Delta D$, where $K_n = 150 N/m$ is the normal spring constant. Lateral motion is applied to the top surface by applying suitable potentials to opposite sectors of a sectored piezo electric tube. and the shear forces transmitted to the lower surface are determined by measuring the deflection of the lateral spring ($K_s = 300$ N/m) using an air gap capacitor.

Water Purification: Tap water treated with activated charcoal was passed through a Millipore purification system (RiOs™ followed by a Milli-Q™ Gradient

stage), yielding water with specific resistivity greater than 18.2MΩ and total organic content less than 4 ppb. Acetic acid ('Suprapure', 99.9%) was purchased from Merck and used as received. The measured pH value of the acid solution was 3.5±0.3 prior introducing into the SFB. Sodium chloride, certified standard (99.886%) was supplied by Fluka (Berlin). The NaCl solution was prepared at a concentration of 1.0±0.1 mM.

Results

Pure (conductivity) water was introduced between curved mica surfaces in the SFB and normal and shear force were measured and were in agreement with earlier studies [16,19]. The conductivity water was then replaced by acid or salt solutions. $F_n(D)$ profiles measured during compression are shown in Fig. 1. The long-ranged repulsion measured is associated with double layer forces at the presence of charge on the mica surfaces. In agreement with earlier work [19], the surfaces jump from separations $D = D_j = 3\pm1$ nm into flat adhesive contact, at $D = D_0 = 0.0 \pm 0.4$ nm. The spontaneous inward motion occurs in a single monotonic jump from D_j to D_0 and its duration is estimated as less than 0.5 sec. It is driven by van der Waals (vdW) attraction between the surfaces overcoming the double-layer and is due to an instability expected whenever $|(\partial F_n/\partial D)| > K_n$. This behavior is reproduced on subsequent separation and approach cycles. However, the long-ranged repulsive forces in the acid solution are somewhat weaker than expected from DLVO theory for the ion concentration corresponding to pH = 3.5±0.3. This may be related to the fact the $F_n(D)$ was not measured on first approach. On second approach, in conductivity water, it has been found that there is an energy barrier for the release of surface H_3O^+ ions from the mica surfaces [20] that leads to weaker and time dependent normal forces. A solid-liquid surface tension of -1.5 ± 0.5 mN/m was deduced from the force required for pull-off from adhesive contact in the case of the acid solution. This value is lower than found in conductivity water (-2.5 ± 0.7 mN/m). The surface tension in the salt solution, deduced from the pulloff force, was −9.8 ± 0.5 mNm[-1].

Shear forces were measured in both solutions as described in a recent study[16]. With the surfaces compressed down to separations of a few nanometers, the upper mica surface is made to move laterally back-and-forth exactly parallel to the lower one at velocity v_s (traces (a) and (c) in Fig. 2). The shear forces F_s transmitted across the intersurface gap are simultaneously recorded as the surfaces further approach under slow thermal drift (traces (b) and (e) in Fig. 2) and compared with the shear forces at large separation (trace (d) in Fig. 2B). No shear forces greater than the noise-limited sensitivity δF_s (±20 nN) are detected between the surfaces down to adhesive contact at $D = D_0$. The right inset in Fig. 2B shows the frequency (ν) dependence $F_s(\nu)$ of the shear force response, with the arrow showing the drive frequency of the upper mica surface. At this drive frequency the magnitude of F_s before the jump is within the noise level δF_s (±20 nN) of its magnitude at large separations.
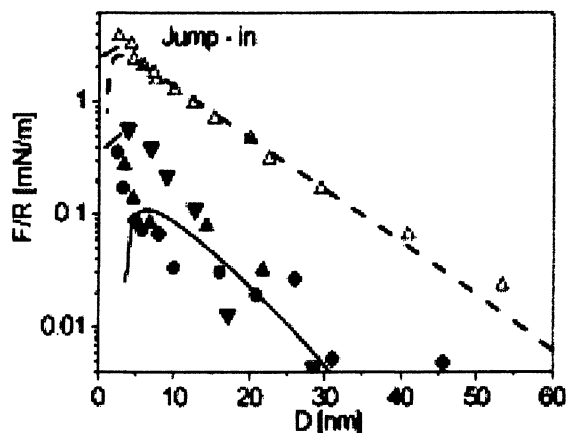
Figure 1. Normal force (F_n/R) vs. distance (D) profiles between curved mica surfaces (mean radius of curvature $R \approx 1cm$) across acetic acid solution (0.01% volume fraction) at $24\pm1°C$ measured during compression (solid symbols). The solid line corresponds to a DLVO expression, $F/R = 128\pi C k_B T \kappa^{-1} \tanh^2 (e\psi_0/4k_B T) \exp(-\kappa D) -A/6D^2$, with a Debye length κ^{-1} of 7.5 ± 0.5 nm, corresponding to $C=1.6\times10^{-3}M$ 1:1 ion concentration; an effective (large-separation) surface potential ψ_0 of 20 mV (Hamaker constant $A=2\times10^{-20}$ J). $F_n(D)/R$ profiles across 10^{-3} M NaCl solutions are indicated by open symbols and the broken line corresponds to the DLVO expression with $\kappa^{-1} =9.5$ nm and $\psi_0 = 78$ mV, $(A=2\times10^{-20}$ J).
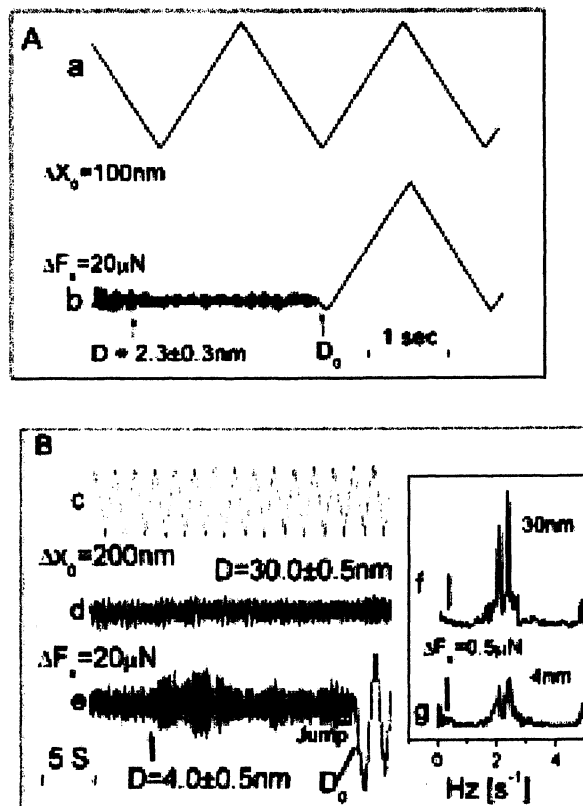
Figure 2. The shear force $F_S(D)$ [traces (b), (d) and (e)] as a result of the lateral motion of the top surface Δx_0 [traces (a) and (c)] for curved mica surfaces sliding past each other across the salt solution (A) and acid solution (B), at large separation [trace (d)] and as the surfaces approach each other under slow thermal drift before jumping (arrow) from $D = 2.3 \pm 0.3$ nm [in (A)] or from $D = 4.0 \pm 0.5$ nm [in (B)] into adhesive contact at D_0, following which they are rigidly adhered and move in tandem (all traces taken directly from the oscilloscope). The frequency components of the shear forces corresponding to traces (d) and (e) are shown in the inset [traces (f) and (g)], with the drive frequency of the top surface (0.5 Hz) indicated by arrows. The peaks around 2.4 Hz correspond to the flexural motion of the building.

Discussion and conclusions

The shear behavior and the total extrusion of the solution from between the adhering surfaces resemble that observed in pure water. We have discussed [16,21] the implication of these results on the effective viscosity η_{eff} of water at these small gaps. The underlying assumption in the analysis was that, as mica surfaces are hydrophilic - there is no slippage of liquid on the solid surfaces. Dynamic surface force investigations [13,14] and other studies [22] confirmed the validity of this assumption. A very recent study by Butt and co-workers[23] suggests that at high enough shear rates some slippage of water might occur even on wetted surfaces, including mica, characterised by a slip length of ca. 8 – 9 nm. We have therefore recently extended our analysis and checked the effect of slip boundary conditions[23] on the evaluation of η_{eff}. We found that this has only a small effect on the viscosity deduced from the jump time[24].

Similarly we have found that the viscosity of water confined to sub-nanometer gaps between two hydrophobic surfaces is comparable to that of bulk water, even when slippage of liquid at the hydrophobic surfaces is accounted for[24]. Here again the two features – jump-in from D = 11±2 nm to contact and immeasurably low shear stress, within our resolution, down to contact - were observed. We have also found [25] that dilute solutions of non-adsorbing polymers in conductivity water exhibit the same shear behavior as found with (polymer-free) conductivity water.

These different studies lead to the following conclusions:

1.) The effective viscosity of ultra-thin (nanometer and subnanometer) aqueous films is comparable to its bulk value, under different types of confining surfaces (hydrophilic or hydrophobic), at different pH values and ionic strength. Within the range of our parameters to date, this persistence of fluidity should therefore be attributed to the properties of water and not to the nature of the surfaces confining the water..

2.) The viscosity of the confined aqueous solutions is presumably the same whether the liquid is being sheared by the confining surfaces as they slide past each other or whether it is being sheared due to being squeezed out as the surfaces approach. Values of the viscosity evaluated from either of these approaches – shear stresses in one case and jump time to contact in the other – should therefore be consistent with each other. This implies that whenever – in the surface force balance - there is a jump–in to contact of the two surfaces (which, in order for it to be considered a 'jump', should occur over a time, τ, that is of order or less than a second) over a distance D_j of a few nanometers, water flows out of the gap and therefore its effective viscosity, η_{eff}, should be comparable to η_{bulk}, as discussed above. For

stick boundary conditions [16], [16a]: $\eta_{eff} = \tau A/18\pi R(D_j^2 - D_0^2)$, where A is Hamaker constant (ca. 2×10^{-20} J for mica across water). If there is slippage of liquid at the surface, then a similar analysis of the jump time suggests that η_{eff} might be as much as an order of magnitude larger[24]. (for a similar jump time). In all events, any shear stresses measured across such films[26] should reflect the low viscosity indicated by the jump of the surfaces into contact.

References

[1] M. C. Bellissent-Funel, J. Lal, and L. Bosio, *J.Chem. Phys.* **98**, 4246-4252 (1993).

[2] M.-C. Bellissent-Funel, S. H. Chen, and J. M. Zanotti, *Phys. Rev. E* **51**, 4558 (1995).

[3] S.-H. Chen and M.-C. Bellissent-Funel, in *Hydrogen Bond networks*, Vol. 435, edited by M.-C. Bellissent-Funel and J. C. Dore (Kluwer Academic Publishers, Dordrecht, 1994), pp. 307-336.

[4] J. Clifford, in *Water in Disperse Systems*, Vol. 5, edited by F. Franks (Plenum Press, New York and London, 1975), pp. 75-132.

[5] P. Pissis, J. Laudat, D. Daoukaki-Diamanti, and A. Kyritsis, in *Hydrogen Bond networks*, Vol. 435, edited by M.-C. Bellissent-Funel and J. C. Dore (Kluwer Academic Publishers, Dordrecht, 1994), pp. 425-432.

[6] M. A. Ricci, F. Bruni, P. Gallo, M. Rovere, and A. K. Soper, *J. Phys.: Condnes. Matter* **12**, A345-A350 (2000).

[7] P. J. Rossky, in *Hydrogen Bond networks*, Vol. 435, edited by M.-C. Bellissent-Funel and J. C. Dore (Kluwer Academic Publishers, Dordrecht, 1994), pp. 337-338.

[8] F. Bruni, M. A. Ricci, and A. K. Soper, *J. Chem. Phys.* **109**, 1478-1495 (1998).

[9] J. N. Israelachvili and H. Wennerstrom, *Nature* **379**, 219-225 (1996).

[10] X. Xia, L. Perera, U. Essmann, and M. L. Berkowitz, *surface science* **335**, 401-415 (1995).

[11] M. Meyer and H. E. Stanley, *J. Phys. Chem. B* **103**, 9728-9730 (1999).

[12] P. Gallo, M. Rovere, M. Ricci, C. Hartnig, and E. Spohr, *Europhys. lett.* **49**, 183-188 (2000).

[13] J. N. Israelachvili, *J. Colloid and Interface Sci.* **110**, 263-271 (1986).

[14] R. G. Horn, D. T. Smith, and W. Haller, *Chem. Phys. Lett.* **162**, 404-408 (1989).

[15] J. Klein and E. Kumacheva, *Science* **269**, 816-819 (1995).

[16] U. Raviv, P. Laurat, and J. Klein, *Nature* **413**, 51-54 (2001).

[16a] D. Y. C. Chan and R. G. Horn, *J. Chem. Phys.*, **83**, 5311-5324 (1985)

[17] J. Klein and E. Kumacheva, *J. Chem. Phys.* **108**, 6996-7009 (1998).

[18] J. Klein, *J. Chem. Soc., Faraday Trans. 1* **79**, 99-118 (1983).

19 R. M. Pashley, *J. Colloid and Interface Science* **80,** 153-162 (1981).

20 U. Raviv, P. Laurat, and J. Klein, *J. Chem. Phys.* **116,** 5167-5172 (2002).

21 U. Raviv and J. Klein, *Science* **297,** 1540-1543 (2002).

22 O. I. Vinogradova, *Langmuir* **11,** 2213-2220 (1995).

23 E. Bonaccurso, M. Kappl, and H. J. Butt, *Phys. Rev. Lett.* **88,** 076103-1 - 076103-4 (2002).

24 U. Raviv, S. Giasson, J. Frey, and J. Klein, *J. Phys. Cond. Matt.* **in press** (2002).

25 U. Raviv, J. Frey, R. Sak, P. Laurat, R. Tadmor, and J. Klein, *Langmuir* **in press** (2002).

26. Y. Zhu and S. Granick, Phys. Rev. Lett. **87,** 096104 (2001)

Chapter 11

Modeling Structure Property Relationships in Synthetic Basestocks

Peter A. Gordon

Corporate Strategic Research, ExxonMobil Research and Engineering Company, Annandale, NJ 08801

We employ equilibrium molecular dynamics to evaluate the potential of United-Atom models for isoparaffins to explore the relationship between molecular structure and viscosity. Calculations for viscosity show that the model captures the correct relative viscosity trends among groups of low molecular weight isomers at the same temperature and pressure. Despite the fact that the model generally underpredicts the viscosity, a single experimental datum for any one of the isomers allows the scaling of the relative viscosities to produce estimates of the viscosity of the real fluid. This approach has been shown to produce very satisfactory estimates for the viscosity of several C_{10} isomers, correctly exposing erroneous recommended viscosity values for fluids in the DETHERM database. In addition, data from extensive calculations on over 75 different isomer systems between C_6 and C_{16} show a strong correlation to a modified Stokes-Einstein relating self-diffusion to viscosity and simple descriptions of molecular size and shape.

139

Introduction

A good understanding of the relationship between molecular structure and performance attributes is becoming increasingly important in the area of lubricating oils. This is especially relevant in instances where minimum performance standards are increasing. For example, maximum allowable volatility levels expected of passenger vehicle engine oils, as defined by ILSAC and ACEA, have decreased markedly in recent years. The expectation of even lower volatility requirements in future engine oil specifications will continue to pressure base oil manufacturers to meet these demands. Meeting such stringent specifications economically certainly depends on the ability to efficiently process starting crude materials, but an improved understanding connecting final product composition and performance should aid in this effort.

Complicating molecular structure-property studies as applied to commercially available lubricants are the limitations in attainable compositional resolution. It is extremely difficult to characterize specific branching structure of molecules in mixtures of many thousands of components. Even for synthetic hydrocarbon fluids, where chemical composition is more uniform a wide range of isomeric structures hampers efforts to elucidate structure-property relationships. In addition, direct synthesis, characterization, and property measurement of individual components is an expensive and time-consuming process. Yet it has been observed that these sorts of molecular-level structural features can have a dramatic impact on properties such as volatility, low-temperature performance, traction behavior, and general rheological behavior with respect to changes in temperature, pressure, and shear rate.

Compared to thermodynamic property databases such as DIPPR[1], TRC[2], and DECHEMA[3], systematic characterization of basic transport properties such as viscosity, has received scant attention, particularly for low molecular weight species. The most notable compilation of viscosity data for individual components is API Project 42[4], which tabulates the viscosity of approximately 50 isoparaffins between C_{10} and C_{50}. This represents only a miniscule fraction of the possible isomers in this range. Furthermore, the range of structures contained in the report is not sufficiently broad to develop a relationship between structure and viscosity in a general way. Yet this sort of information is essential in attempting to develop an improved understanding of the structure property relationships in the area of lubrication science.

Molecular simulation has been a fruitful avenue of research in attempting to increase our understanding of the relationship between molecular structure and rheological properties. Over the past decade, a number of workers have employed equilibrium[5-8] and NEMD (non-equilibrium molecular dynamics)[9-17] to examine the bulk rheological properties of normal and isoparaffins. Much attention has been focused on assessment of computational methodology for

reliable viscosity prediction and comparison of intermolecular potentials for computation of viscosity. To date, studies that examine the influence of chain architecture on rheological properties have generally been restricted to a relatively small number of isomers.

In this work, we present extensive molecular dynamics simulation results aimed at generating a set of transport property data to be used for examining the impact of chain architecture on the shear viscosity of bulk fluids. Our initial focus is to assess the quality of refined intermolecular potentials for isoparaffins for transport property predictions in order to describe the *relative* differences between isomers of a given molecular weight. We demonstrate this with several examples of isomers of octane and decane.

In a broader sense, we seek to identify molecular features of isomers that appear to give rise to variations in viscosity. To this end, we have conducted extensive simulations on over 75 different isomer systems between C_6 and C_{16} at different temperatures to help identify the descriptors that clarify the relationship between molecular structure and viscosity.

Simulation Details

Isoparaffins were modeled using the TRAPPE-United Atom potential parameterized by Martin *et al*[18]. In this representation, hydrogen atoms are lumped with their bonded carbon neighbors to form an effective interaction site. This description significantly reduces the computational requirements necessary to compute interactions among neighboring molecules. The resulting united atom group interacts with a Lennard-Jones potential with all sites on neighboring molecules and with intramolecular sites separated by 3 or more bonds. Lorentz-Berthelot mixing rules are applied to cross interactions of Lennard-Jones parameters. We note that parameterization of this model was designed to reproduce thermodynamic properties such as vapor pressure and liquid density; thus transport property prediction represents a stern test of the transferability of the potential.

Intramolecular degrees of freedom are constrained by interaction potentials governing bond lengths, bond angle bending, dihedral rotation about bonds, and umbrella inversion of single branch points. With the exception of dihedral rotation, a harmonic potential is used to govern the geometry. The dihedral rotation is given by the OPLS potential[19].

All molecular dynamics simulations were performed using LAMMPS99, a parallelized molecular dynamics engine suitable for atomic and molecular systems.[20] A multiple time step algorithm was employed, separating the motion of bonded, 3/4 body intramolecular, and short range Lennard-Jones motions into separate timescales. The innermost timestep (corresponding to the integration

timestep for bond stretching) was set at 1 fs, and 3/4 body interactions set at 2fs. In most of the simulation results presented here, the outermost timestep was set at either 4 or 6fs. The corresponding propagator algorithm employed in integrating the equations of motion requires fewer force evaluations of the slower molecular modes, thus increasing the computational efficiency of the simulation.

Simulations performed in this work were generally conducted in two stages. The first stage consists of a 1 ns phase of temperature annealing at fixed volume, with the temperature scaled from a very high initial value to the target simulation temperature by the end. The system is then allowed to relax for 1 ns at the target pressure and temperature (NPT). A Nose Hoover thermostat and barostat were employed in this ensemble with associated relaxation time constants of 0.1 and 0.5 ps, respectively. Following this relaxation, additional NPT simulation of total time was conducted to compute the equilibrium density at the target pressure.

In the second stage, a longer simulation is performed in the microcanonical ensemble at the equilibrium density obtained from the first simulation stage. Atomic and molecular pressure tensor data is computed during the entire production trajectory, while center-of-mass positions and velocities, and molecular orientation data were computed for subsequent analysis over a subset of the total production run time. In general, atomic and molecular stress tensor data were saved every 8fs, center-of-mass positions and velocities every 40fs, and orientation and radius of gyration information every 100fs.

Unless otherwise noted, the viscosities reported below have been computed using the Green-Kubo formalism relating fluctuations in the symmetrized-traceless form of the *molecular* stress tensor to shear viscosity[6,21]. Simulation times were set to ensure that at least several hundred intervals of the rotational relaxation time were sampled, in order to achieve good statistics in the stress tensor autocorrelation function.

Simulation Results

In figure 1, we compare the dynamic viscosity of several n-alkanes at 293K and 373K to the corresponding experimental data. In all cases, the TRAPPE-UA model underpredicts the viscosity. The degree to which the viscosity is underpredicted for the homologous series increases somewhat with increasing carbon number and lower temperatures. Despite the obvious shortcomings of the predictions, we focus on sets of simulations of groups of isomers in the bulk at the same state point to compare the relative rheological properties of the species.
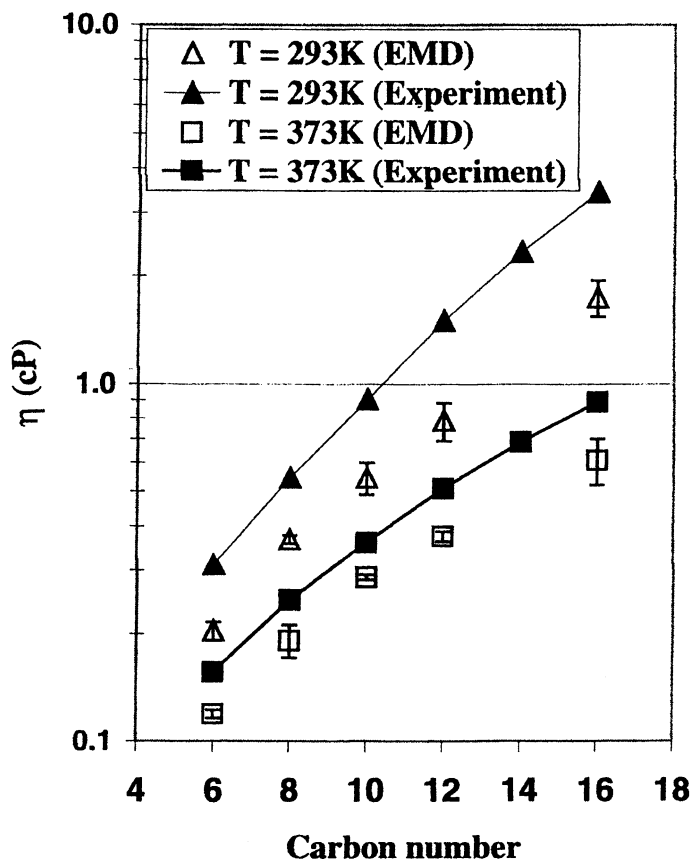
Figure 1. Dynamic viscosity of selected n-alkanes at several temperatures and atmospheric pressure computed through molecular dynamics simulations and from experiment[2].

Figure 2 shows the viscosity of various isomers of octane at 293K and atmospheric pressure, relative to the normal alkane at the same state point. This state point was chosen because of the availability of experimental data for a number of these isomers. Viscosities determined from both the atomic and molecular stress tensor formalism are in good agreement, as expected. The plot illustrates that, although quantitative agreement between model and experiment is not obtained, the trends in relative viscosity appear to agree quite well. For instance, moving a single methyl branch from the end to the middle of the chain in 2, 3, and 4-methylheptane produces a modest decrease in viscosity. The magnitude of this decrease is approximately the same in both experimental and simulation data. In both cases the relatively hindered 2,2,3-trimethylpentane has a viscosity higher than that of the normal alkane. In terms of the trends relating variations in molecular architecture to viscosity, the plot illustrates the utility of the approach in elucidating these relationships.

Given that relative viscosity trends seem well described by the TRAPPE-UA model, we have attempted to test predictions about viscosity of molecules for which data is not readily available. As a test case, we found several correlations[22] for viscosity of C_{10} isomers (3,3,4,4-tetramethylhexane, 2,2,5,5-tetramethylhexane, 4-n-propylheptane, and 3,3,5-trimethylheptane) in DETHERM[3], a thermophysical property database covering over 12,000 compounds of relevance to the chemical industry. Unfortunately, we could not obtain a description of the method by which the recommended values for viscosity were determined. Initial simulations of the relative viscosities of these species at T=293K produced values that differed by as much as 100% compared to the DETHERM correlations.

To resolve this discrepancy, 4 commercially available, highly purified (> 97-99%) isomers of the previously mentioned C_{10} isomers were obtained in 5g quantities and their kinematic viscosities measured in a capillary viscometer between 298-423K. The viscosity of n-decane was also measured as a check against the accuracy of the measurement. Additional simulations of the corresponding model fluids were conducted at atmospheric pressure and a range of temperatures. To test the assumption that ratios of viscosities obtained from simulation at the same state point mirror that of the real fluids, we compute the viscosity of isomer as

$$\left(\eta_{isoalkane}\right)_{\text{expt}} = \left(\eta_{n-alkane}\right)_{\text{expt}} \left(\frac{\eta_{isoalkane}}{\eta_{n-alkane}}\right)_{\text{EMD}} \qquad (1)$$

It is presumed that the viscosities in eq 1 refer to the same measurements or calculations at the same pressure and temperature. Although we have chosen the corresponding normal alkane as our reference with which to compare other isomers, any species for which experimental data is available could be used as a
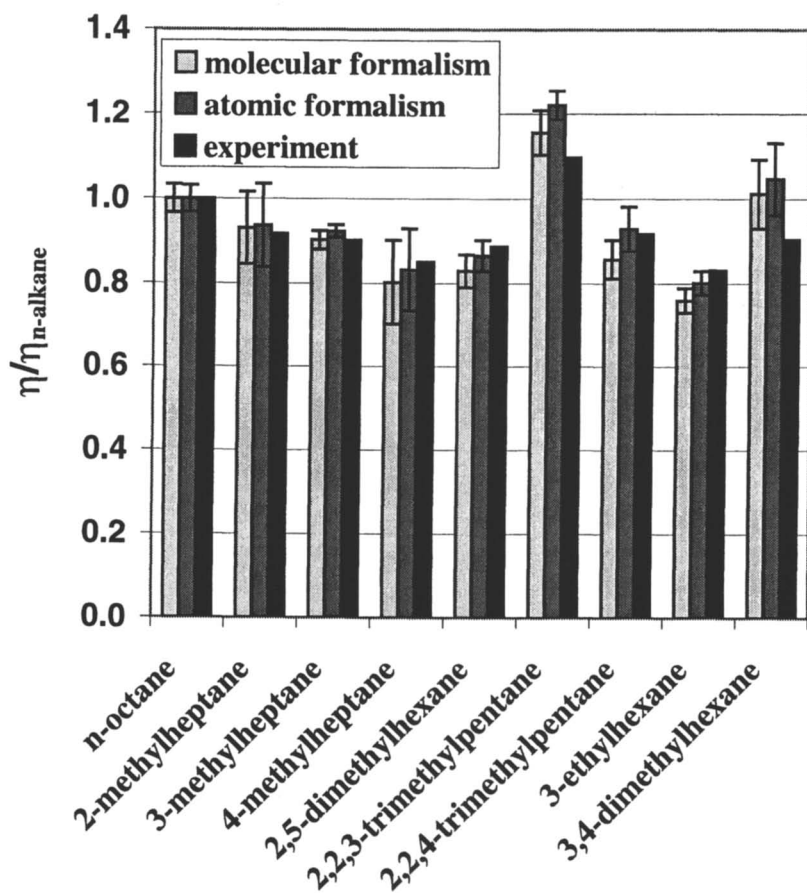
Figure 2. Relative viscosity computed through molecular and atomic stress tensor fluctuations for selected isomers of C_8 paraffins at $T=293K$ and atmospheric pressure. Experimental data derived from variety of sources [2,27,28]

reference for other isomers. This would be necessary, for example, when examining relative viscosities of higher molecular weight compounds at temperatures where the normal alkane is a solid.

The comparison of viscosity vs. temperature obtained for 3,3,4,4-tetramethylhexane is shown in figure 3. Error bars on molecular dynamics results were obtained from 3 subblock averages of the individual simulation runs, along with the propagation of relative error from eq 1. It is clear from the figure that the DETHERM values significantly underpredict the actual viscosities. In this instance, the DETHERM correlation looks almost identical to the viscosity curve of n-decane, which is plotted in the figure for comparison. Despite the larger error bars associated with the simulation results, the data appears to yield an improved representation of the actual viscosity.

Similar plots of viscosity vs. temperature for the 4-n-propylheptane and 2,2,5,5-tetramethylhexane are shown in figure 4. For these species as well, the simulation results appear to be as good as or better than the recommended DETHERM correlations. These examples appear to lend strong support in utilizing the TRAPPE-UA model for discriminating differences in bulk rheological behavior among paraffin isomers.

As another example of using these models to explore structure-property relationships, we have also examined the influence of chain branching on viscosity variation with pressure for a variety of C_{10} isomers at T=293K. Simulations at target pressures between atmospheric and 300MPa were conducted in a similar manner as described above, and results are shown in figure 5. The viscosity in all cases is found to follow a roughly exponential increase with pressure. An effective pressure-viscosity coefficient, α, can be found by fitting the data to the Barus equation,

$$\eta = \eta_0 \exp(\alpha P). \tag{2}$$

Parameters resulting from this fit are summarized in table 1. We find that the linear n-decane has the lowest pressure-viscosity coefficient, and increasing branching leads to larger values of α. The spread in pressure-viscosity coefficient is more dramatic than the corresponding atmospheric pressure Eyring activation energies characterizing viscosity-temperature behavior. Although we do not have experimental viscosity data over this pressure range with which to compare these results, the findings are qualitatively consistent with the observation that increased chain branching results in a higher pressure-viscosity coefficient. Obtaining high-pressure viscosity data for these isomers would be of particular use in verifying the accuracy of these predictions. We note that accurate pressure viscosity coefficients for 9-octylheptadecane and squalane have been determined using similar models through nonequilibrium molecular dynamics simulations at pressures in the Gigapascal range[23].
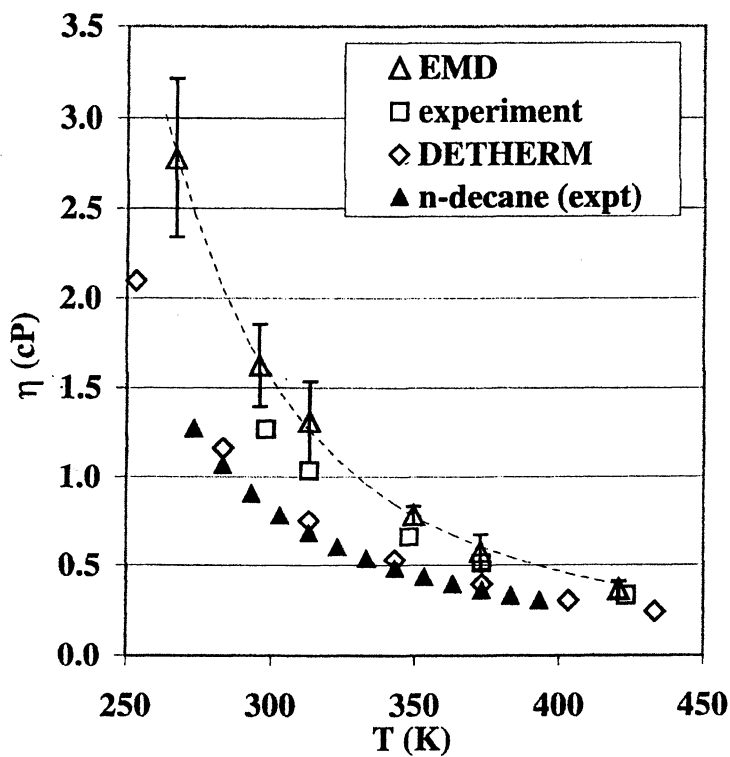
Figure 3. Viscosity of 3,3,4,4-tetramethylhexane over a range of temperatures at
P=0.1MPa from capillary viscometry (□), DETHERM recommended values
(◇), and molecular dynamics calculation (△). The viscosity of n-decane (▲)
is also shown for comparison.
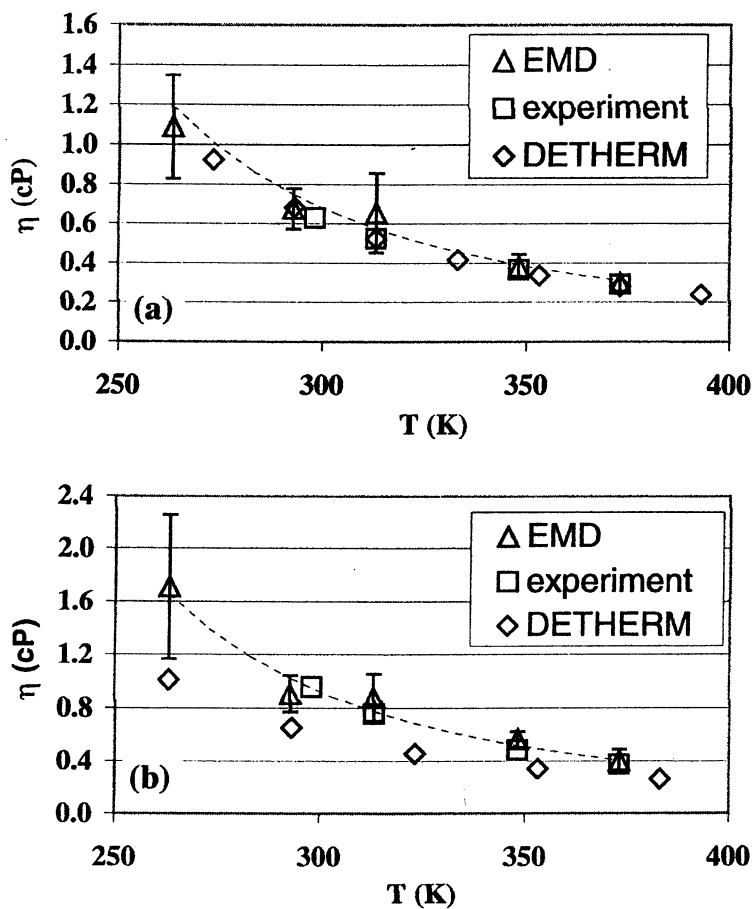
Figure 4. Viscosity of (a) 4-n-propylheptane and (b) 2,2,5,5-tetramethylhexane over a range of temperatures. Labels are as in figure 3.
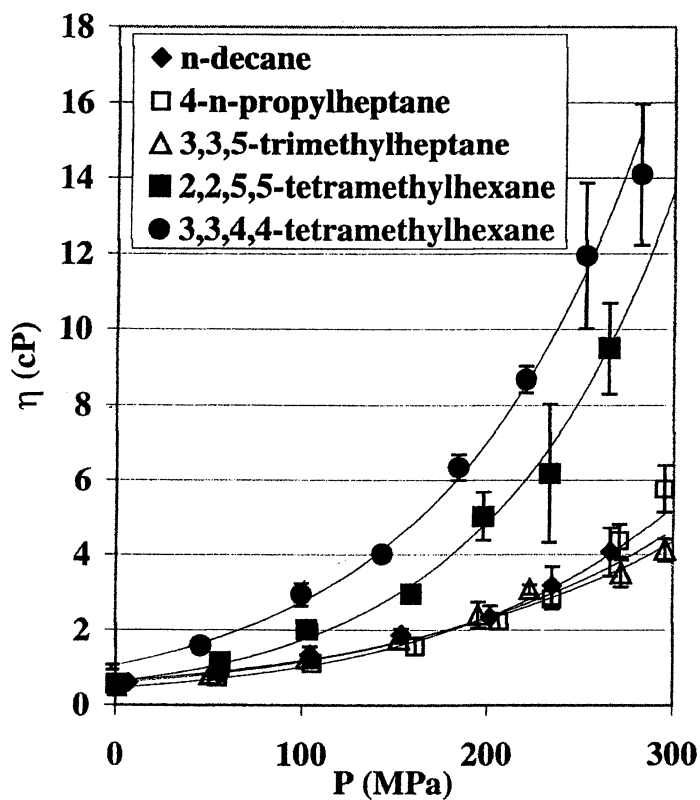
Figure 5. Viscosity as a function of pressure computed via molecular dynamics for several isomers of decane at T=293K.

Table 1. Barus equation parameters for viscosity as a function of pressure for isomers of decane at 293K. Results are for molecular dynamics simulations corresponding to figure 5.

species	η_0 (cP)	$\pm \sigma$	α (GPa^{-1})	$\pm \sigma$
n-decane	0.59	0.03	6.4	0.4
4-n-propylheptane	0.47	0.02	8.0	0.3
3,3,5-trimethylheptane	0.57	0.02	7.1	0.3
2,4,6-trimethylheptane	0.50	0.02	7.4	0.2
2,2,5,5-tetramethylhexane	0.59	0.03	10.4	0.3
3,3,4,4-tetramethylhexane	1.03	0.03	9.6	0.2

Relating viscosity, self-diffusivity and molecular geometry

Because of the computational requirements needed to obtain accurate estimates of the viscosity from Green-Kubo formulae, we have strong incentive to try to link viscosity to other more easily computed descriptors of the molecular dynamics. For example, Mondello *et al*[6] found that using the Rouse model applied to n-alkanes, viscosity estimated from τ_{rot} , the rotational relaxation time of the molecule, was accurate to within approximately 20% for low molecular weight alkanes. The Rouse model viscosity estimates were found to be within the statistical precision of NEMD calculations for C_{60} chains and higher[24]. When applied to branched alkanes, however, the connection between the rotational relaxation time and viscosity is no longer a simple function; for 3 isomers of C_{18} isoparaffins, Kioupis *et al* found that even the qualitative Rouse prediction of $\eta \propto \tau_{rot}$ and $D \propto 1/ \tau_{rot}$ was not satisfied for their systems [9]. This deviation is expected, as branching along a hydrocarbon chain greatly affects the

dihedral rotational dynamics, and hence the overall flexibility of the chain. A chain with increased chain branching has a slower rate of internal conformational changes along the chain backbone. Thus, instantaneous local stress inhomogeneities tend to be relieved by global rotation of the molecule, leading to a faster rotational relaxation time. This is exemplified in figure 6, which shows the orientational autocorrelation function of isomers of decane at 293K and atmospheric pressure. The instantaneous orientation is defined through the coordinate system defining the principle moments of inertia; the smallest eigenvalue that diagonalizes the moment of inertia tensor defines the longest axis of the molecule. Rotational relaxation times, fit to a Kohlraush-Williams-Watts expression reflects the faster global rotation of more highly branched, stiffer molecules.

Another possible approach to correlate viscosity to more easily computed properties lies in Stokes-Einstein relationships; the frictional drag force on a particle suspended in a viscous medium moving at (creeping) velocity U, coupled with Einstein's equation for the diffusion of a particle undergoing Brownian motion, yields an expression of the general form

$$D = \frac{kT}{C_{bc} f(shape)\eta} \tag{3}$$

where C_{bc} is a constant that depends on the boundary conditions employed in deriving the drag force (stick or slip), η is the viscosity of the fluid medium, and $f(shape)$ is a term that depends on the geometry of the particle. For example, the familiar expressions for flow past a spherical particle of radius R given stick or slip boundary conditions are

$$D_{stick} = \frac{kT}{6\pi R\eta}, \qquad D_{slip} = \frac{kT}{4\pi R\eta} \tag{4}$$

A number of expressions for translational and rotational diffusion have been developed for particles of differing shapes[25,26]. For example, for axisymmeric diffusion along the long axis of a prolate ellipsoid,

$$D_{trans,//} = \frac{kT}{C_{bc} b K_{tr,prolate}(\phi)\eta} \tag{5}$$
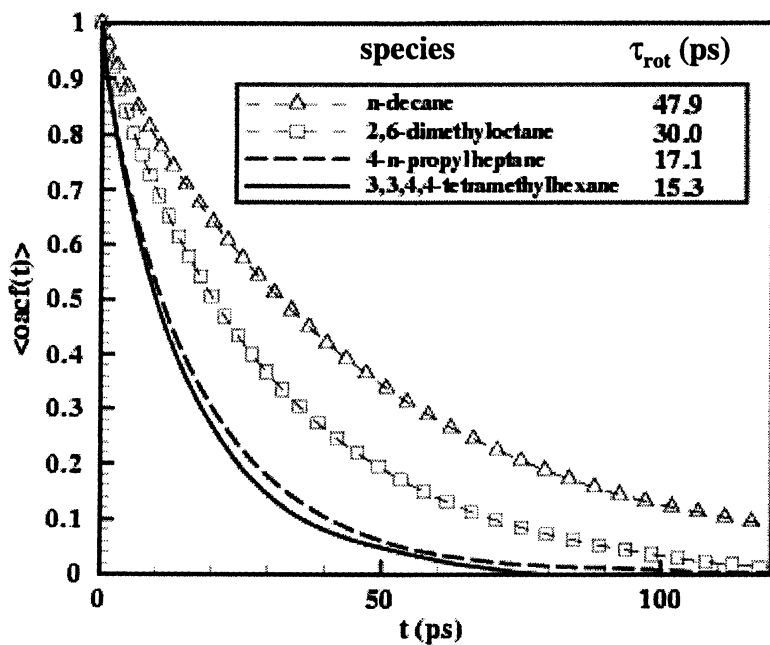
Figure 6. Orientational autocorrelation function and rotational relaxation time, τ_{rot} for several isomers of C10 paraffins at T=293K and P=1Atm.

$$K_{tr,prolate}(\phi) = \frac{4}{3}\left[-\frac{\phi}{\phi^2 - 1} + \left(\frac{2\phi^2 - 1}{\left(\phi^2 - 1\right)^{3/2}} \right)\coth^{-1}\left(\frac{\phi}{\sqrt{\phi^2 - 1}} \right)\right]^{-1} \quad (6)$$

where $\phi = a/b$, the ratio of the long to short axis of the prolate ellipsoid. The eigenvalues and principle axes of the moment of inertia tensor help characterize the molecular size (via the radius of gyration) and shape (through ellipsoidal semiaxes a, b, and c) of the molecule. The prolate ellipsoid closely approximates the shape of the isoparaffins we have considered in this study. We define the effective asphericity parameter κ_{eff}, as

$$\kappa_{eff} \approx \frac{1}{\phi} = \sqrt{\frac{bc}{a^2}} \quad (7)$$

which ranges from 0 (needle) to 1 (spherical).

Application of a modified form of eq (3), relating self-diffusion coefficient to viscosity, radius of gyration (used as an effective radius of the molecule), is shown in figure 7. Our dataset consists of over 70 different isomers between C_6 and C_{16} at T=293 and 373K. The figure shows that, for molecules of a given molecular shape, as characterized by the average asphericity parameter, the proportionality between self-diffusivity and the product of viscosity and the effective molecular size (given as the radius of gyration) is very nearly constant. This apparent relationship lends support to the idea that a simple modification of relationships such as eq (5) could describe the relationship between viscosity and more readily computed descriptors like self-diffusion, and molecular shape and size.

One shortcoming of this approach is that modified Stokes-Einstein equations for flow past particles are derived on the basis of a static particle shape; in our systems, the flexibility of the molecule has an important influence in governing the time-evolution of molecular shape in response to instantaneous local stresses. We are currently extending our work to try to capture this relationship on the basis of eqs (5)-(7), along with descriptors of molecular dynamics that capture the degree of molecular flexibility.

Conclusions

In this work, we have shown that United atom models such as TRAPPE-UA potential show promise in being able to quantitatively reproduce relative changes
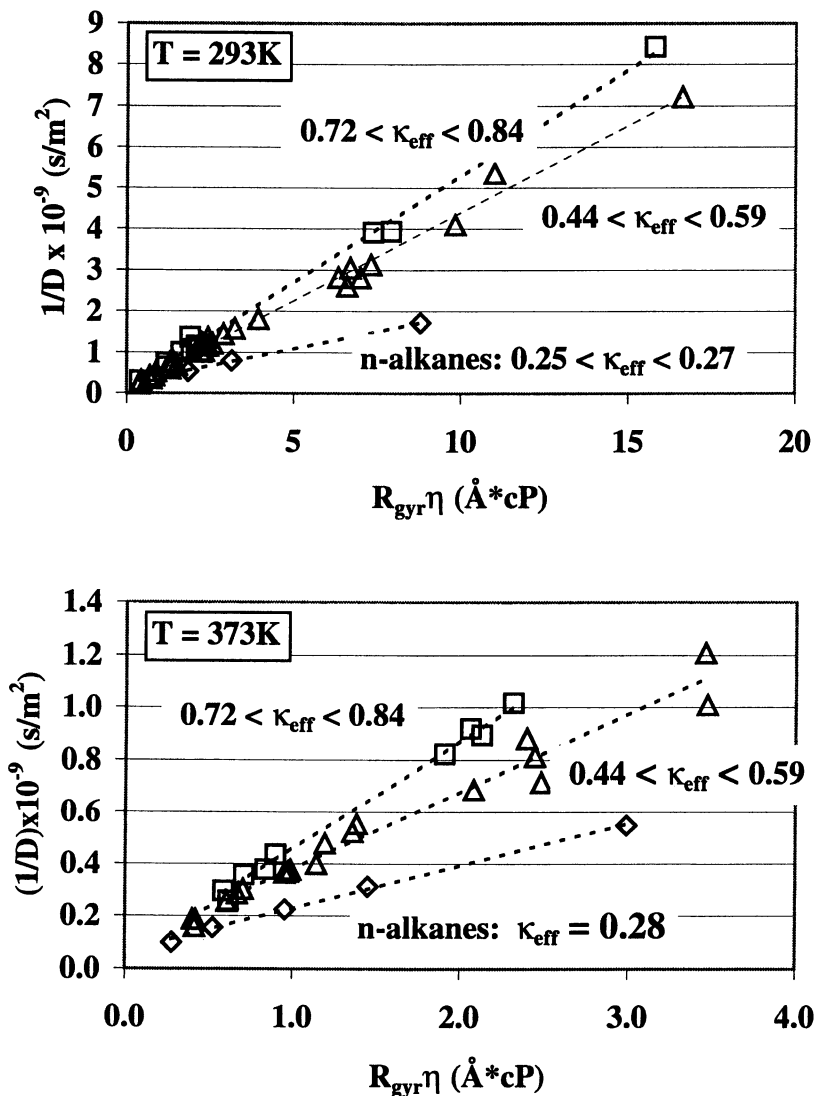
Figure 7. Relationship between self-diffusion, viscosity, molecular shape and size for various isoparaffins between C_6 and C_{16}. The different groupings of points correspond to molecules with approximately the same value of κ_{eff}, the asphericity parameter.

in viscosity among isomers of isoparaffins. The demonstration of satisfactory estimates of viscosity for which data was generally unavailable shows the potential for this approach to fill out gaps in the API-42 database for isoparaffin viscosity for structures of potential interest but for which data is unavailable. In addition, a strong link between viscosity, self-diffusion, molecular shape and size is apparent throughout a broad range of isomers between C_6 and C_{16}. Further work will focus on developing a more rigorous relationship based on modified Stokes-Einstein relationships.

Acknowledgments

References

(1)   Daubert, T. E.; Danner, R. P., Eds. Physical and Thermodynamic Properties of Pure Chemicals: Data Compilation; Hemisphere Publishing Corp.: New York, 1989; Vol. 3-5.

(2)   Selected Values of Properties of Hydrocarbons and Related Compounds. Research Project 44 of the American Petroleum Institute and the Thermodynamic Research Center; Thermodynamics Research Center: College Station, TX, 1985.

(3)   DECHEMA; DECHEMA e.V., 2001; Vol. 2001.

(4)   Dixon, J. A. "Properties of Hydrocarbons of High Molecular Weight," American Petroleum Institute, 1966.

(5)   Mundy, C. J.; Klein, M. L.; Siepmann, J. I. J. Phys. Chem. 1996, 100, 16779-16781.

(6)   Mondello, M.; Grest, G. S. J. Chem. Phys. 1997, 106, 9327-9336.

(7)   Mondello, M.; Grest, G. S. J. Chem. Phys. 1995, 103, 7156-7165.

(8)   Dysthe, D. K.; Fuchs, A. H.; Rousseau, B. J. Chem. Phys. 1999, 110, 4047-4059.

(9)   Kioupis, L. I.; Maginn, E. J. J. Phys. Chem. B 1999, 103, 10781-10790.

(10)   Kioupis, L. I.; Maginn, E. J. J. Phys. Chem. B 2000, 104, 7774-7783.

(11)   Lahtela, M.; Pakkanen, T. A.; Rowley, R. L. J. Phys. Chem. A 1997, 101, 3449-3453.

(12)   Lahtela, M.; Linnolahti, M.; Pakkanen, T. A.; Rowley, R. L. J. Chem. Phys. 1998, 108, 2626-2630.

(13)   Lee, S. H. Molecular Simulation 1999, 22, 271-284.

(14)   Moore, J. M.; Cui, S. T.; Cochran, H. D.; Cummings, P. T. J. Chem. Phys. 2000, 113, 8833-8840.

(15)   Cui, S. T.; Gupta, S. A.; Cummings, P. T. J. Chem. Phys. 1996, 105, 1214-1220.

(16)   Cui, S. T.; Cummings, P. T.; Cochran, H. D. J. Chem. Phys. 1996, 104, 255-262.

(17)   Allen, W.; Rowley, R. L. J. Chem. Phys. 1997, 106, 10273-10281.

(18)   Martin, M. G.; Siepmann, J. I. J. Phys. Chem. B 1999, 103, 4508-4517.

(19)   Jorgensen, W. L.; Madura, J. D.; Swenson, C. J. J. Am. Chem. Soc. 1984, 106, 6638-6646.

(20)   Plimpton, S. J.; Pollack, E. L.; Stevens, M. J.; Simon, E. J.; Carpenter, J. E.; Lustig, S. R.; Belak, J.; Stouch, T. R.; LAMMPS99 ed., 1999.

(21)   Daivis, P. J.; Evans, D. J. J. Chem. Phys. 1993, 100, 541-547.

(22)   Liessmann, G.; Schmidt, W.; Reiffarth, S. Recommended Thermophysical Data; Data compilation of the Saechsische Olefinwerke, 1995.

(23)   McCabe, C.; Cui, S.; Cummings, P. T.; Gordon, P. A.; Saeger, R. B. J. Chem. Phys. 2001, 114, 1887-1891.

(24)   Mondello, M.; Grest, G. S.; Webb, E. B.; Peczak, P. J. Chem. Phys. 1998, 109, 798-805.

(25)   Happel, J.; Brenner, H. Low Reynolds Number Hydrodynamics; Prentice-Hall, Inc.: Englewood Cliffs, NJ, 1965.

(26)   Lamb, H. Hydrodynamics; 6th ed.; Dover Publications, Inc.: New York, 1945.

(27)   Geist, J. M.; Cannon, M. R. Ind. Eng. Chem. 1946, 18, 611-613.(28)Evans, E. B. J. Inst. Pet. Techn. 1938, 24, 321-337.

Chapter 12

The Complex Behavior of Simple Fluids in Nanoscale Restricted Geometries

John H. Cushman[1] and Joan E. Curry[2]

[1]Center for Applied Mathematics, Math Sciences Building, Purdue University, West Lafayette, IN 47907
[2]Department of Soil, Water and Environmental Science, University of Arizona, Tucson, AZ 85721

On the nanoscale, fluids in restricted geometries exhibit complex and nonintuitive behavior. In many ways our classical interpretations of fluids at this scale can be tossed out the window. We illustrate this fact quite graphically with molecular scale simulations of simple fluids between nanoplatelets, nanowires and structured infinite flat surfaces. Specifically, we discuss layering, shear-induced liquifaction, anomalous dispersion, quantized imbibition, thermodynamic stability under shear, transiently coexisting nanophases for surfaces with asperities and their relation to molecular thrusters, nanochromatography, and finite size effects on capillary condensation.

157

Despite their importance in the sciences and technologies, the physical behavior of interfaces when bathed in a fluid and brought together to within molecular distances of one another, is not well understood. Our intuition, which is largely based on macroscale observations, often sends us down the wrong path when we try to interpret measurements of interfacial properties in nano sciences. This latter point is best illustrated with an example.

Consider two atomically flate, parallel surfaces which are immersed in a liquid. Further, suppose the surfaces are brought to within a few fluid molecular diameters of one another. This scenario is consistent with the surface forces apparatus (Israelachvili, et al. 1990; Granick, 1991) and the friction force microscope (Meyer and Amer, 1998) and many clays and polymeric systems. In such an environment, even a fluid as simple as a rare gas displays an extremely rich, anomalous behavior. The fluid's phase diagram is changed, its thermal transport coefficients are radically altered from that of the bulk, and it may become inhomogeneous and anisotropic. Its properties depend in a complex way on the initial structure of the fluid, the separation of the walls, the structure and commensurability of the confining surfaces, the wall-fluid interaction potential, and asperities within the walls. A vicinal fluid can exist as a gas, liquid or solid even though it is in equilibrium with its liquid state bulk phase counterpart. In some cases, the freezing or liquifaction of the vicinal fluid results from epitaxial arrangement with the surface atoms, which can be enhanced or destroyed by either moving the walls normally or laterally relative to one-another. In other cases freezing is not epitaxial. These observations suggest we have a limited understanding of the behavior of an interfacial-fluid, or even how to define an interfacial-fluid. Many other examples illustrating the anomalous character of interface may be cited. For example, when modeling fluid flow around nanoscale features, the continuum Navier-Stokes equations, upon which much classical intuition is based, can become inaccurate. In this limit, the mean free path of the molecules is similar to the length scale of the interface itself (intermediate to large Knudsen number). The challenge is that while the system of interest may still contain a huge number of molecules, their behavior can no longer be emulated by the standard macroscopic state variables and new descriptions must be formulated.

Many studies focus upon interfacial effects for their own sake; as is indeed necessary for the development of nanotechnology. Often, however, the study of such nanoscale physical and chemical effects can have far reaching implications for the behavior of much larger systems. For example, while the behavior of a fluid several molecular layers thick needs to be understood in the context of delivery systems for nanotechnologies, it also has implications for such diverse fields as lubrication theory and the simulation of naturally occurring porous media systems (Rhykerd, et al. 1987; Sommers, et al. 1993). The study of nanoscale phenomena can give insight into effects which occasionally may be exploited at all scales.

Background

Since the advent of the surface forces apparatus and high speed computing in the late 1960's, researchers (cf. references in Israelachvili, 1991; Bhushan, et al. 1995; Cushman, 1997) have had a growing interest in studying various phenomena related to the interfaces on both the molecular- and nano-scales. A proper understanding of these interfaces and their manifestation on larger scales is of relevance to most aspects of life and many modern technologies. The P.I.'s group has been instrumental since the mid 1980's in using and developing computational statistical mechanical tools to study the interaction of fluids with surfaces on molecular, nano and higher scales (cf. Cushman, 1997). In the following paragraphs we outline several of the authors contributions to this area and their relevance for providing physical interpretations for experimental results, and for uncovering new physical phenomena. Unless otherwise mentioned, we restrict our attention to high surface area materials.

Layered Density Profiles

Early experiments with the surface forces device showed that when two flat, parallel surfaces in a fluid bath are brought to within a few molecular diameters of one another, the force exerted on one plate by the other oscillates with a period of roughly one molecular diameter (Figure 1a) and increases amplitude with decreasing separation of the surfaces (Israelichvili, 1991). These early experimenters hypothesized the oscillation was associated with quantized drainage of entire layers of fluid aligned parallel to the walls. This was confirmed via computational statistical mechanical experiment (c.f., Brushan, et al., 1995). One such result is presented in Figure 1b. We present this result because in addition to layering, it provides the first illustration, 1987, of strain-induced liquifaction. This is illustrated in panel (b) wherein the dashed line has the two surfaces aligned crystalligraphically (both surfaces consist of the (100)-plane of a fcc lattice), while the solid line has them exactly out of registry in say the x-direction. The dashed line corresponds to a two layered frozen fluid, while the solid line corresponds to a one-layer liquified fluid. The only state variable which differs between the two curves is their relative registry, i.e., the relative shear-strain between the two surface lattices.

Shear-Induced Liquefaction and Nanotribology

In the early 1990's the surface forces device was substantially modified to examine dynamic shear as well as normal stresses in this slit-pore environment.
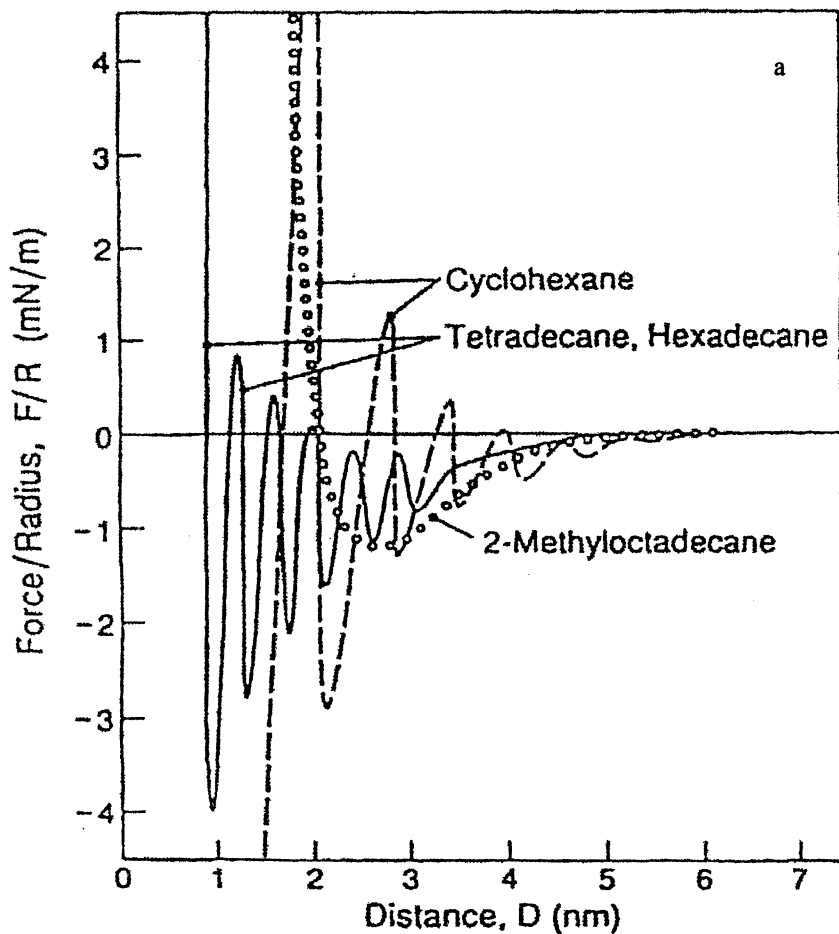
Figure 1. (a) Experimentally measured forces between mica surfaces for various organic vicinal phases. Adapted from Schoen (1993), Figure 3.1. (b) Local density profiles normal to the walls from grand-canonical MC calculations for surface separation (h*). Full lines have surface lattices in registry and dashed lines have them exactly out of registry. Adapted from Rhykerd et al. (1987), Figure 2.
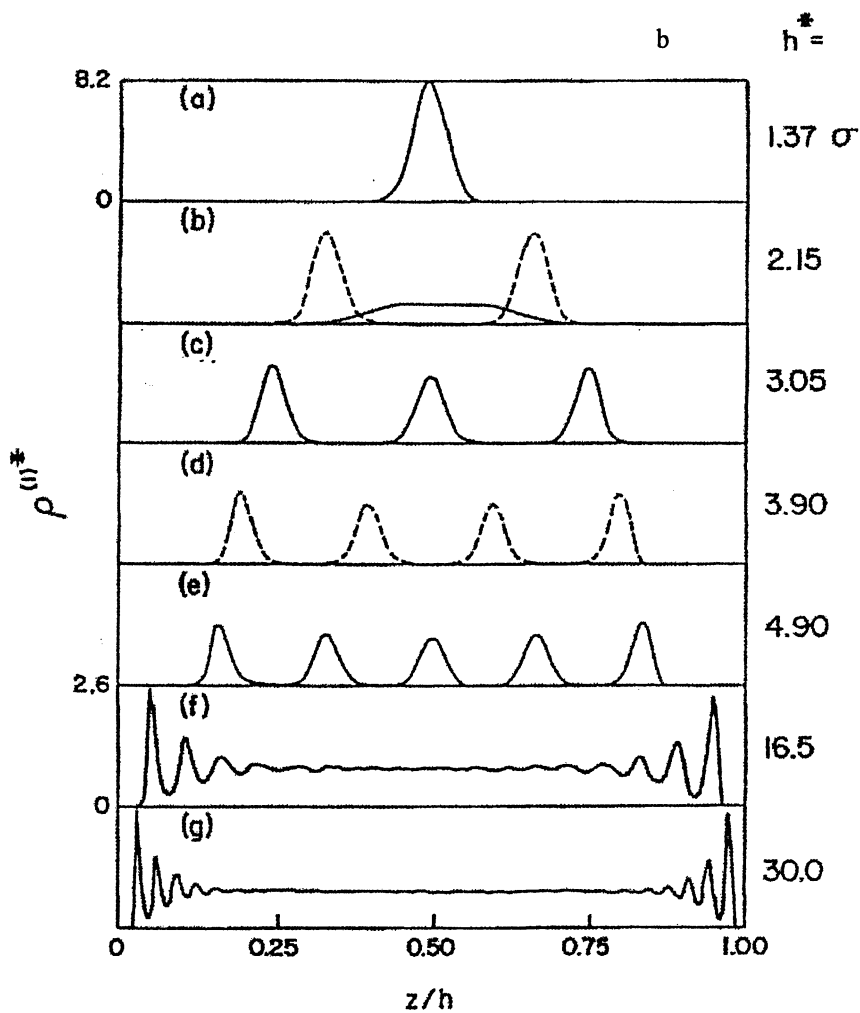
Figure 1. *Continued.*

This led to the birth of molecular (nano) tribology and an illustration of typical dynamic observations is presented in Figure 2a. A quasi-static computational experiment illustrating a possible explanation for the stick-slip behavior is presented in Figure 2b. The sawtooth shape is associated with periodic freezing and thawing. This computational experiment was performed in an isostrain-grand canonical ensemble, and the authors later carried out computational experiments in the isostress-isostrain canonical and isostress-isostrain grand canonical ensemble, producing similar results, but more consistent with experiment.

Anomalous Diffusion

When the mean-free-path of a molecule is on the same order as a characteristic dimension of the pore, the classical Fickian expression relating the diffusive flux to the activity gradient breaks down. That is, both diffusivity and the related viscosity become wave vector and frequency dependent. A Gedankin experiment for a fluid confined in a slit pore is illustrated in Figure 3a. Panel b is especially interesting as it gives rise to fractional Brown diffusion as illustrated by the computational results given in Figure 3b. Here the mean-square displacement scales as t^d with $d \approx 0.64$ as opposed to the Brownian limit of $d \approx 1$.

Quantized Imbibition and Interfacial Tension

As the aggregation and interaction of nanoscale particles and devices is strongly affected by the interfacial tension of fluids absorbed to surfaces (nanofilm), we illustrate the complexity of this effect next. As pointed our earlier, the imbibition and drainage of micro and nanopores is often quantized as a function of both slit pore width (h) and the relative strain between the atoms of the adjacent surfaces (α). (See Figure 4a). This gives rise to incredible complexity in the interfacial tension, γ, of the fluid between the surfaces as indicated in Figure 4b. The most important point here is the non-monotonic character of the tension for fixed α as a function of h.

Thermodynamic Stability Under Shear

When two flat-surfaces are brought together in a fluid bath the force normal to the surfaces oscillates as a function of distance (Figure 1a). As Figure 1b illustrates this oscillation is associated with quantized imbibition or drainage of

whole layers of fluid as h varies. That the isobars τ_{zz} = constant intersect the τ_{zz} versus h curve at several distinct values of h (Figure 5a) suggests that a number of different phases (corresponding to different numbers of layers) are possible for fixed chemical potential, temperature, normal force (τ_{zz}) and relative strain (α) between the atoms of adjacent surfaces (i.e. in the isostress-isostrain grand canonical ensemble). Only one of these states is globally stable, the remaining are metastable and will not persist in nature. The relative stability of a phase can be established by minimizing the potential (Φ), or more specifically the relative potential, for the isostress-isostrain grand canonical ensemble (care must be taken because $d\Phi$ is not homogeneous in area (A) and so can't be integrated analytically, i.e. $\Phi \neq \gamma A$). Globally stable states have been computed and are displayed in Figure 5b as a function of relative strain between the surfaces. Thinner films are in general more stable than thicker films, but in either case, stability is strongly affected by relative strain.

Transiently Coexisting Nanophases

All previous results are for the interaction of surfaces possessing lattices without defects. The addition of nanoscale defects in the crystal surfaces considerably increases the complexity of their interactions. A prototype of a system with molecular-scale crystal structure and nanoscale defects is depicted in Figure 6a. We label this system as a corrugated slit-pore.

Simulations of fluids in this corrugated pore have displayed for the first time transiently coexisting nanophases (Figure 6b), or if you will, the formation and destruction of oriented nanocapillaries as a function of relative strain between the surfaces. In the upper most panel of Figure 6b the fluid is liquidic over the entirety of the body, however as one surface is slid relative to the other the fluid gains structure until in the third panel from the top, the narrow region freezes while the wider region remains liquidic (forming a nanocapilary perpendicular to the page). Finally, as the walls continue to slide by one another, the entirety of fluid freezes, thus destroying the capillary. Continued sliding of the surface periodically creates and destroys the capillary.

By Newton's law, the expulsion of the atoms from the nanocapillary upon liquifaction would create a thrust. If the asperity has a V shape, then this becomes nanoscale thruster.

Nanochromatography

In this case the two surfaces are brought together while bathed in a binary mixture of "large" and "small" molecules. We are interested in species
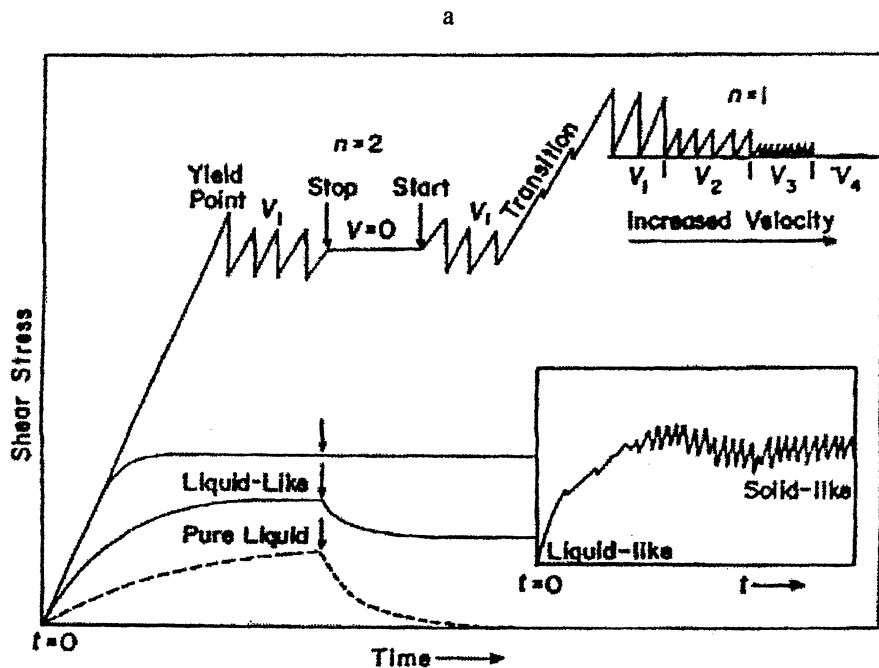
Figure 2. (a) Shear forces associated with different types of sliding modes as a function of elapsed time for constant load: v is the velocity of the translational stage and n is the number of layers in the film. Adapted from Gee et al. (1990), Figure 5. (b) Shear stress, τ_{xz} as a function of strain α for walls separated by h^* = 2.20(0), 3.10(∇), and 4.9 ($\square$). Adapted from Schoen et al. (1989), Figure 2.

b
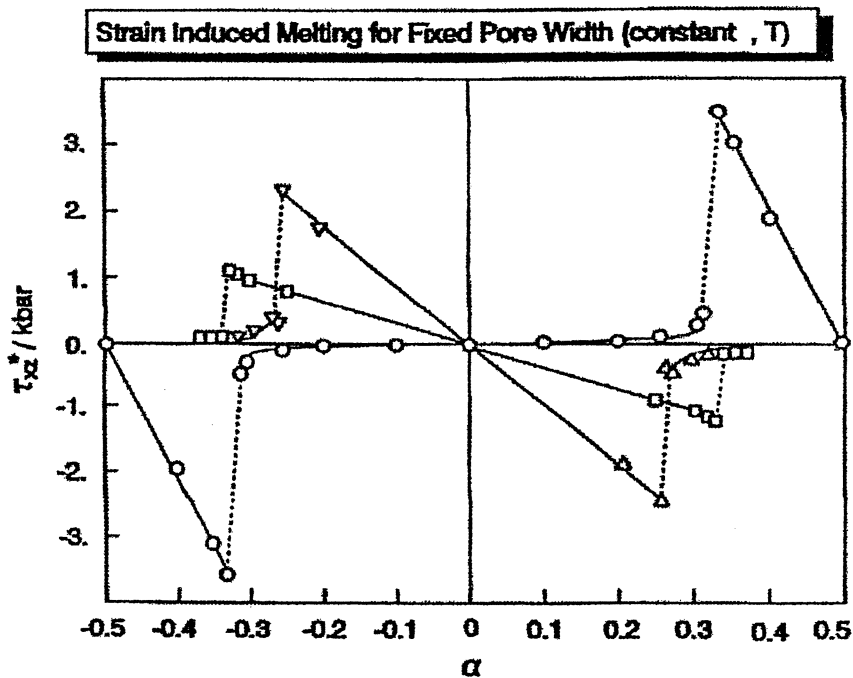
Figure 2. *Continued.*
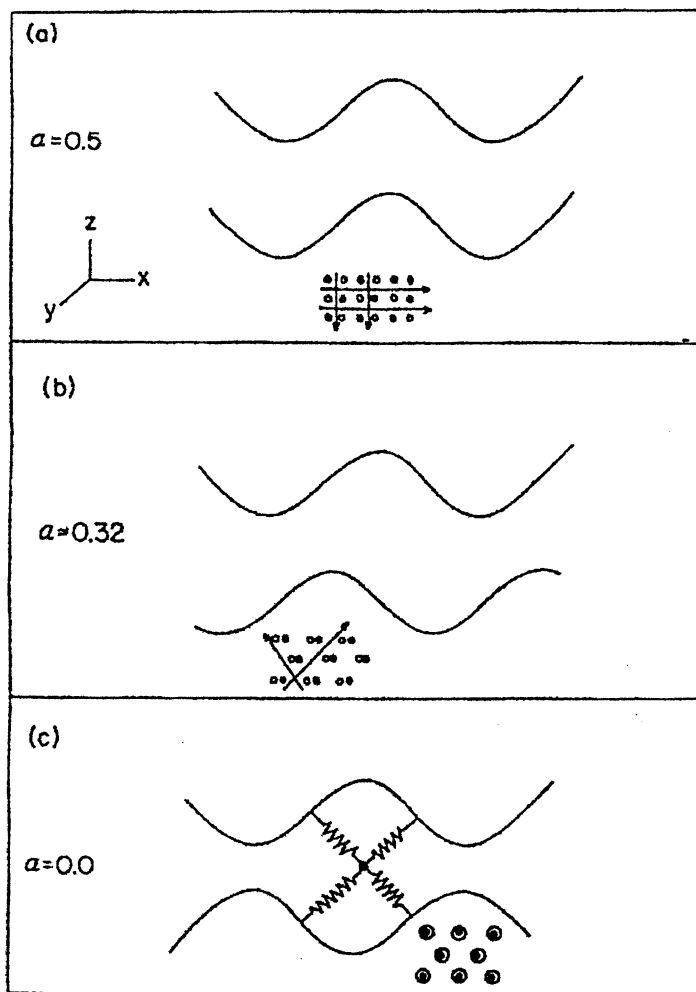
a

Figure 3. (a) Types of microstructures encountered by a vicinal atom diffusing in a prototypal slit pore. Atoms represented by open (upper wall) and filled (lower wall) circles. Arrows indicate paths of diffusing atoms and oscillatory curves projections of equipotential surfaces onto planes containing these paths. Adapted from Schoen et al. (1994), Figure 2. (b) Double-logarithmic plot of mean square displacement in the x-direction in unites of $10^{-20}m^2$ versus time at $\alpha = 0.35$, (V) MD (units $10^{-11}s$); ($\bullet$) MC (units of time: displacement/atom). Adapted from Schoen et al. (1994a), Figure 3.
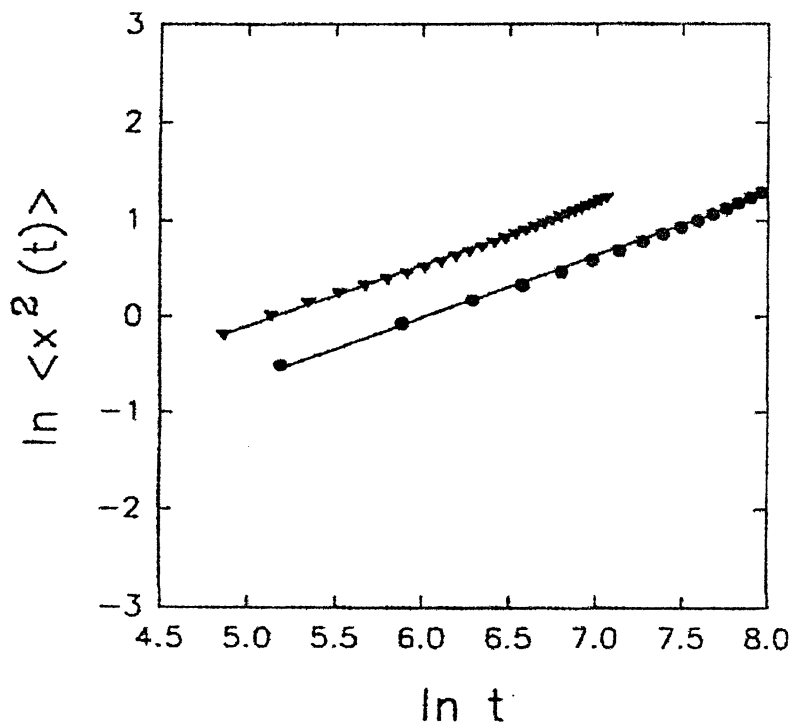
b

Figure 3. *Continued.*
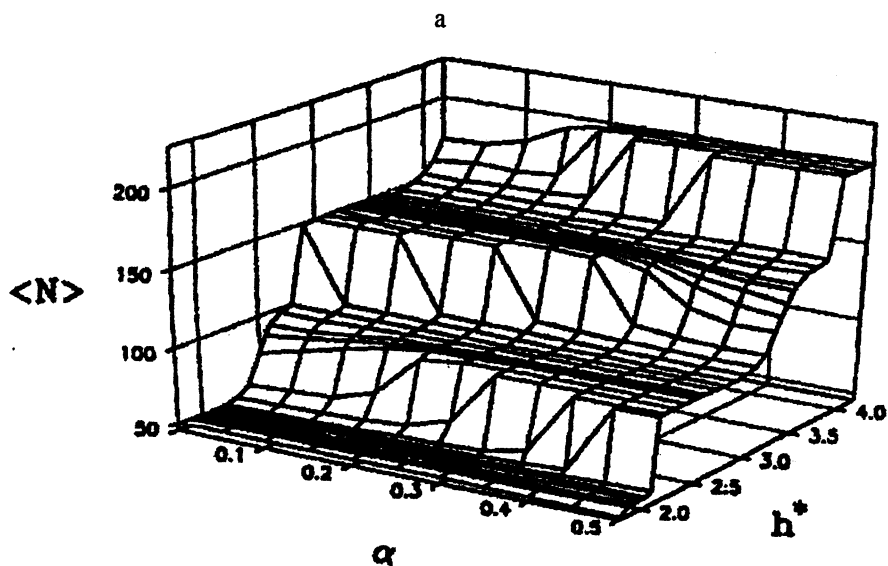
Figure 4. (a) Average number of atoms, <N>, as a function of registry, α, and pore width, h*. Adapted from Curry, et al. (1994), Figure 9. Interfacial tension, γ*, as a function of registry, α, and pore width, h*. Adapted from Curry, et al. (1994a), Figure 10.

b
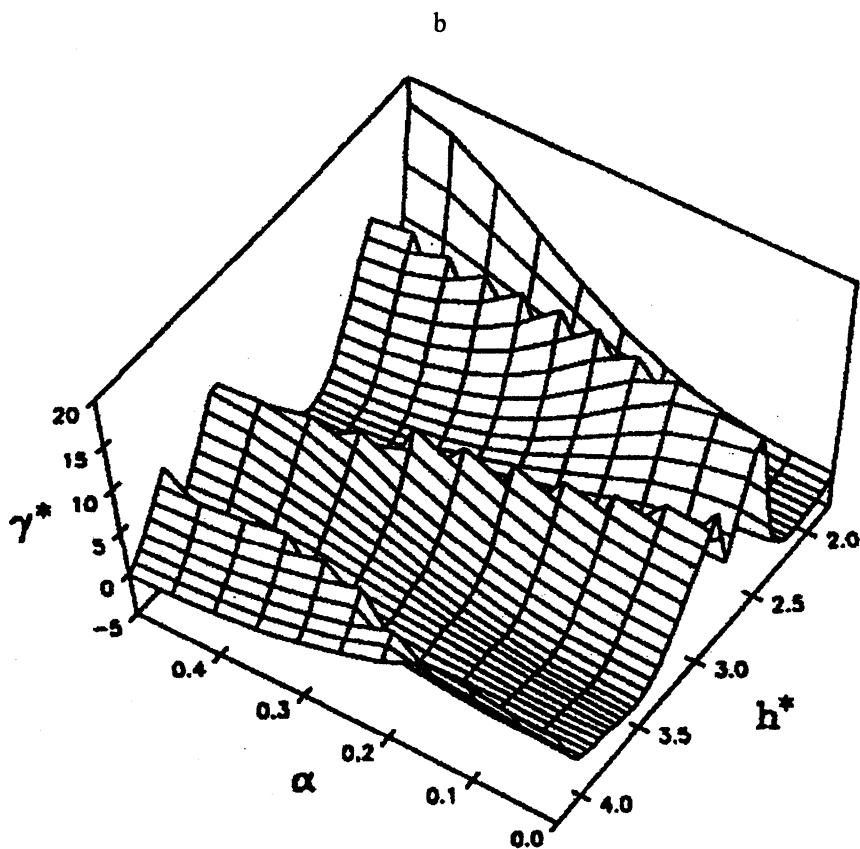
Figure 4. *Continued.*

a
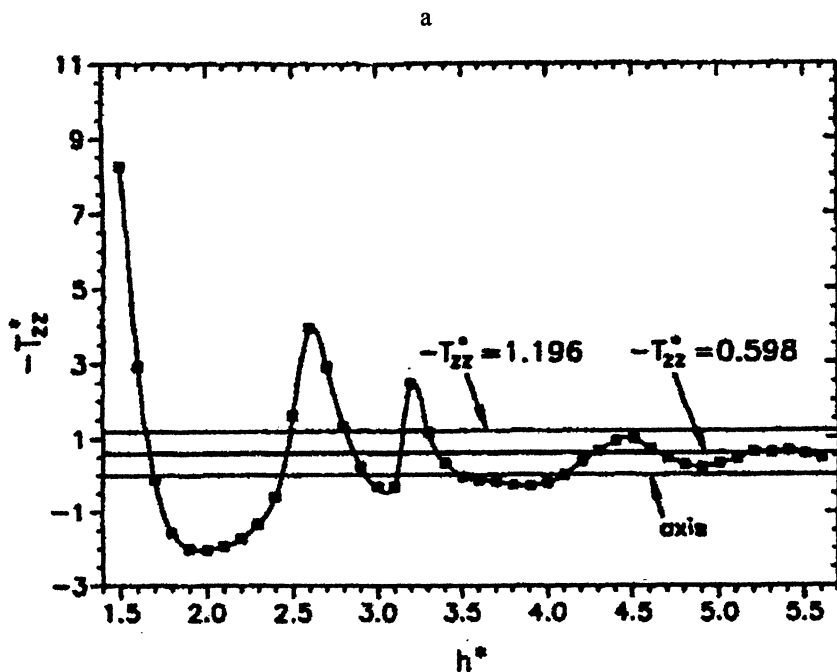
Figure 5. (a) Negative normal stress, τ_{zz}^{*}, as a function of wall separatio, h^{*}, from grand isostrain MC calculations, $\alpha = 0.0$ (■). Also shown are three isobars $-\tau_{zz} = 0.0, 0.598,$ and 1.196 indicated by the horizontal lines. Intersections between isobars and the curve $\tau_{zz}^{*}\left(h^{*}\right)$ correspond to metastable phases. Adapted from Schoen, et al. (1994b), Figure 2. (b) The change of the grand isostress potential $A^{*}\Delta\Phi^{*}$ as a function of shear strain α with $\tau_{zz}^{*} = -0.598$. One layer (●), two-layer (○), three-layer (■), and four-layer (□) phase. Average number of atoms in lower panel accommodated by the stable phase as a function of shear strain α; same symbols. Adapted from Schoen et al. (1994b), Figure 4.

b
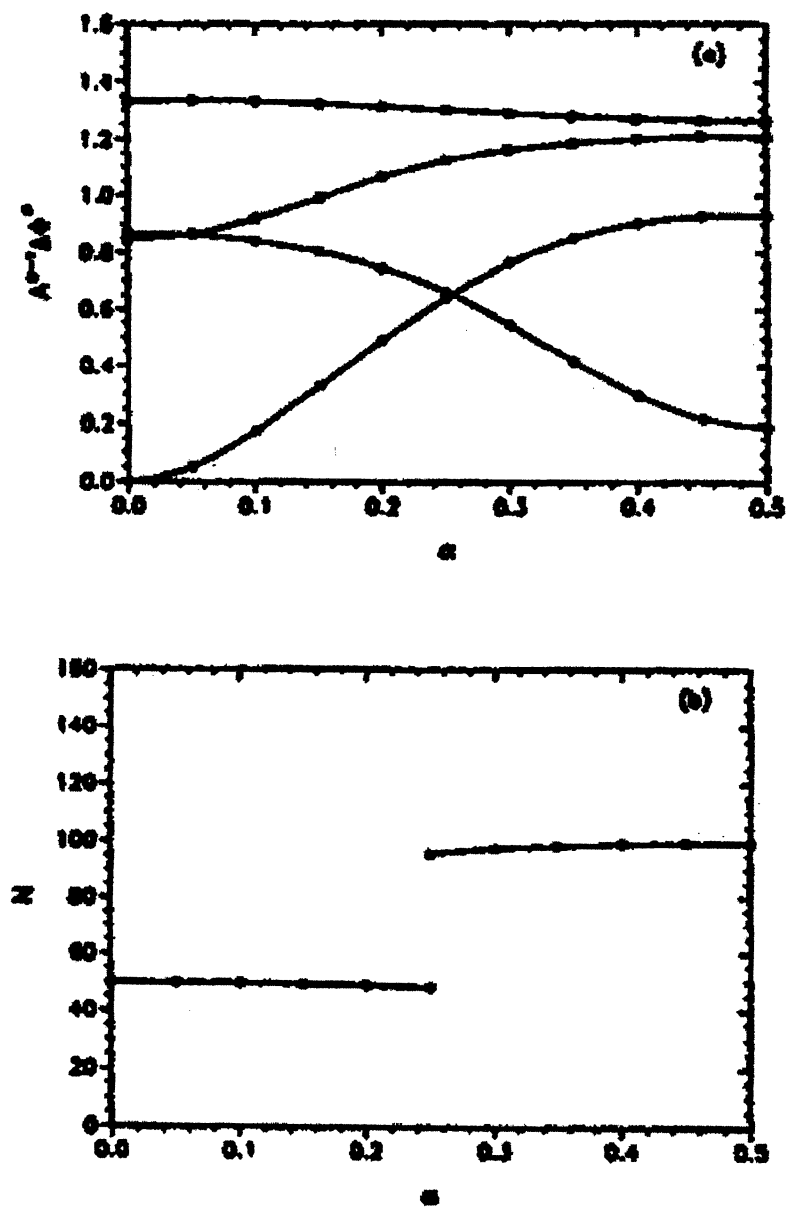
Figure 5. *Continued.*
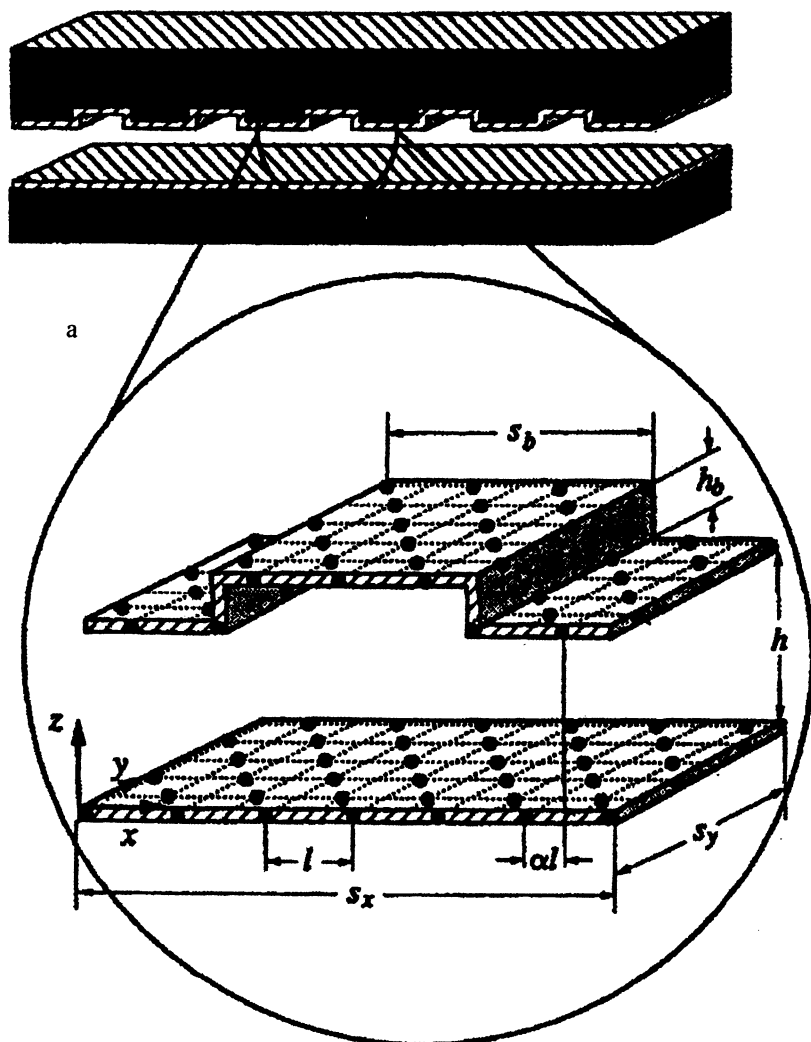
Figure 6. (a) Scheme of the corrugated slit-pore; inset details simulation cell. Adapted from Curry, et al. (1994b), Figure 1. (b) A. local density profiles $\rho^{(1)}$; C. in-plane pair correlation functions, $g^{(2)}$ calculated separately for the narrow (- - -) and wide (—) regions of the corrugated por; B. snapshots (looking down the y-axis) of the pore fluid for various registries α. Film atoms are represented by unshaded spheres. Adapted from Curry, et al. (1994b), Figure 3.

b
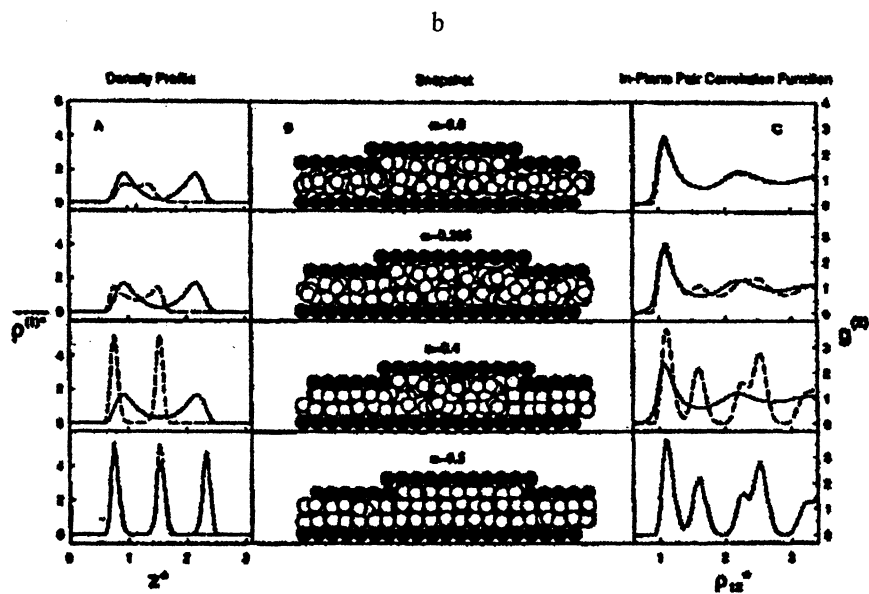
Figure 6. *Continued.*

174

separation as a function of wall separation and relative registry for both atomically flat walls, and walls with nanoscale corrugation. Figure 7a displays a typical result for atomically flat walls. As can be seen, the species separation process is immensely complex, and the complexity is significantly magnified by nanoscale defects (Figure 7b).

Nanowires and Finite Nanoplatelets, and Capillary Condensation

Here we briefly look at the affect of particle size and shape on capillary condensation and snapoff. Specifically we look at finite nanoplatelets (Figure 8a), nanowires (Figure 8b) and infinite slit-pores (Figure 8c). The fluid which bathes the particles is in the vapor region of its phase diagram (details of the simulations may be found in Stroud, et al., 2001). Figure 9 compares three types of particles; a five-wire, a ten-wire and the infinite slit-pore. By x-wire we mean an infinite rectilinear wire of x unit-cells wide in the lateral direction. Four panels are presented with interlayer separations ranging from 7.5 to 5.5 molecular diameters. This figure illustrates the role specific area plays in nanowire adsorption, narrower wires "snapoff" at shorter interlayer separations. In all cases a dense vapor forms prior to complete snapoff. Figure 10 is similar to Figure 9 except here we compared 3-wires to finite 3×3 particles. As is expected, the 3×3 particle snaps off prior to the 3-wire and in both cases, a dense gas forms before snapoff. In both Figures 9 and 10 the layered structure of the fluid is evident for all types of particles, irregardless of their shape. These observation contradict much earlier folklore in this area.

Conclusion

The authors have been simulating the behavior of simple fluids in restricted geometries for the better part of two decades. In this article we have provided a brief summary of several of the more interesting and unusual observations we have made. Amongst these observations are shear-induced liquifaction and its role in stick-slip behavior, non-Fickian diffusion, quantized imbibition and its' relation to the complex nature of surface tension, meta-stable states in the isostress-isostrain grand canonical ensemble and their relation to surface forces measurements, transiently coexisting nanophases in slit-pores with linear asperities and their relation to molecular thrusters, molecular sieving in binary mixtures and its' relation to nanochromatography, and the role finite-size effects have on capillary adsorption and snapoff. More detailed discussions of these phenomena, and many other anomalous behaviors as well, may be found in Chapters 3 and 4 of Cushman (1997) and Stroud et al. (2001).

a
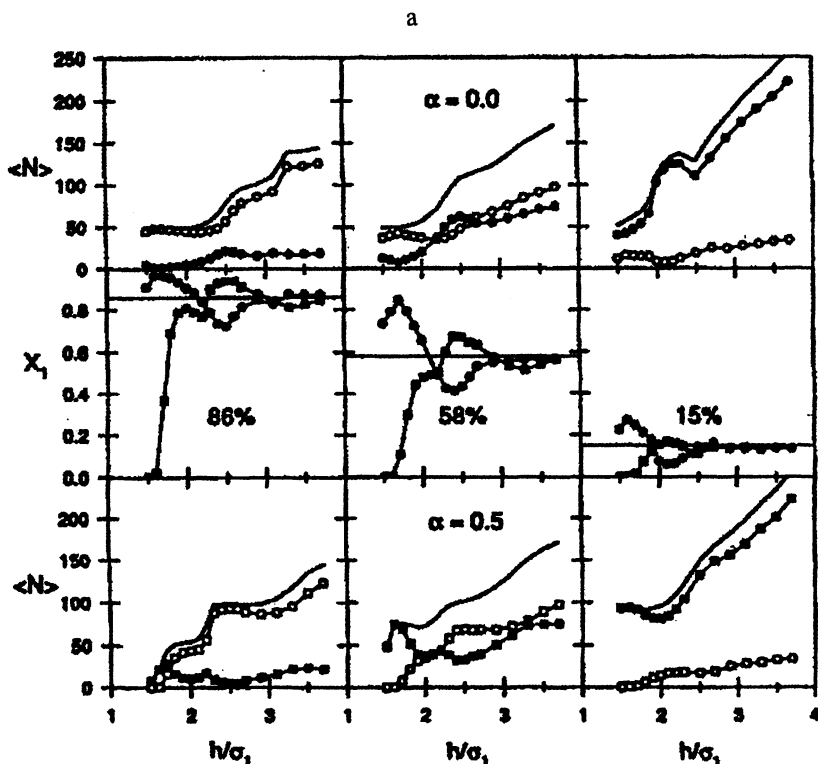
Figure 7. (a) Fraction of large X_l (center row) and average atom number <N> for $\alpha = 0.0$ (upper row), and $\alpha = 0.5$ (lower row) as a function of pore width. The left column, center column and right column are data for 86%, 58% and 15% large atoms in the bulk solution, respectively. Squares denote data for $\alpha = 0.5$ and circles for $\alpha = 0.0$. In the <N> plots open symbols represent the large component and filled symbols represent the small component. The solid curve is the average total number of atoms in the pore. Adapted from Curry and Cushman (1995), Figure 2. (b) Local density profiles, $\rho^{(l)}$, for large atoms (●) and small atoms (○) calculated separately for the narrow (left) and wide (right) regions for various registries for 86% large atom bulk mixture in the corrugated pore. Adapted from Curry and Cushman (1995), Figure 4.

b
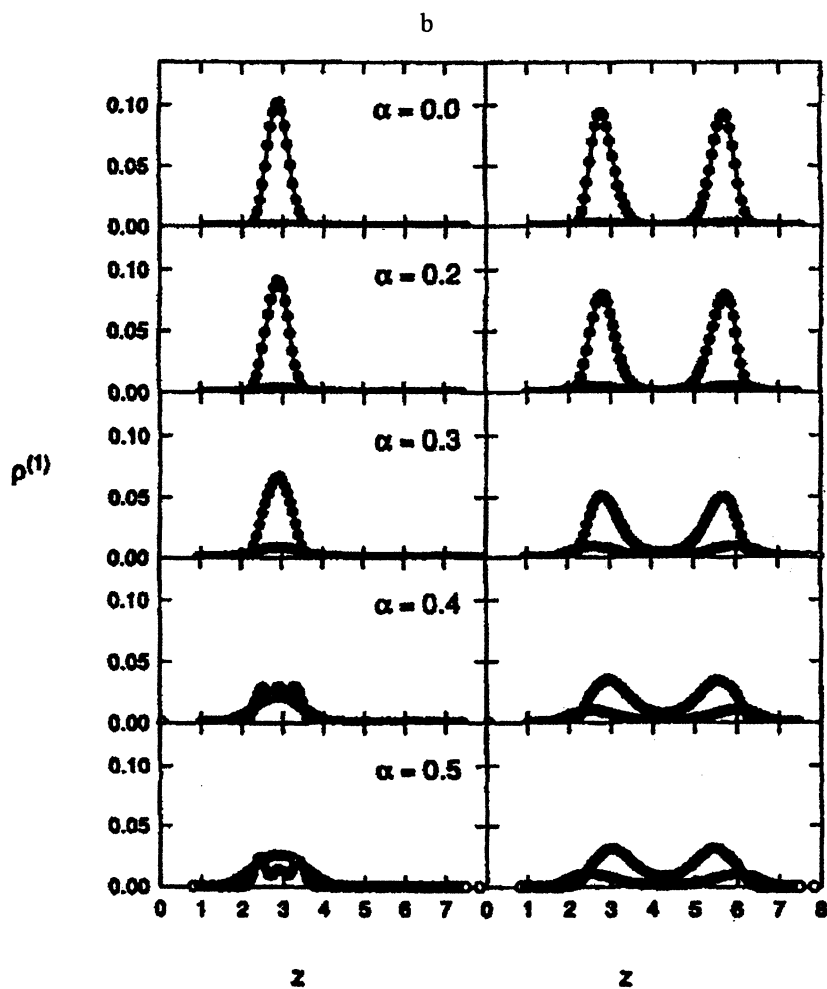
Figure 7. *Continued.*
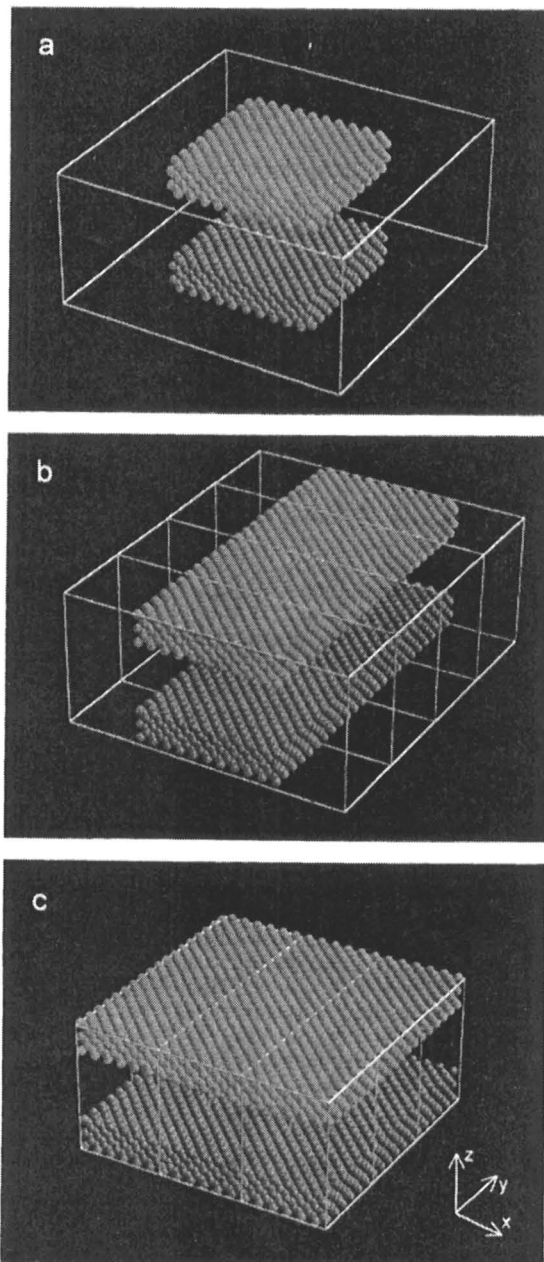
Figure 8. Schematic of the (a) nanoplatelet, (b) nanowire, and (c) infinite slit pore systems. The solid atoms are shown as spheres, and the solid white lines outline the simulation cell. The infinite slit pore is finite in the z direction only, the nanowires are finite in both the x and z directions, and the platelets are finite in all directions. Adapted from Stroud et al. (2001).

(See Page 1 of color insert.)
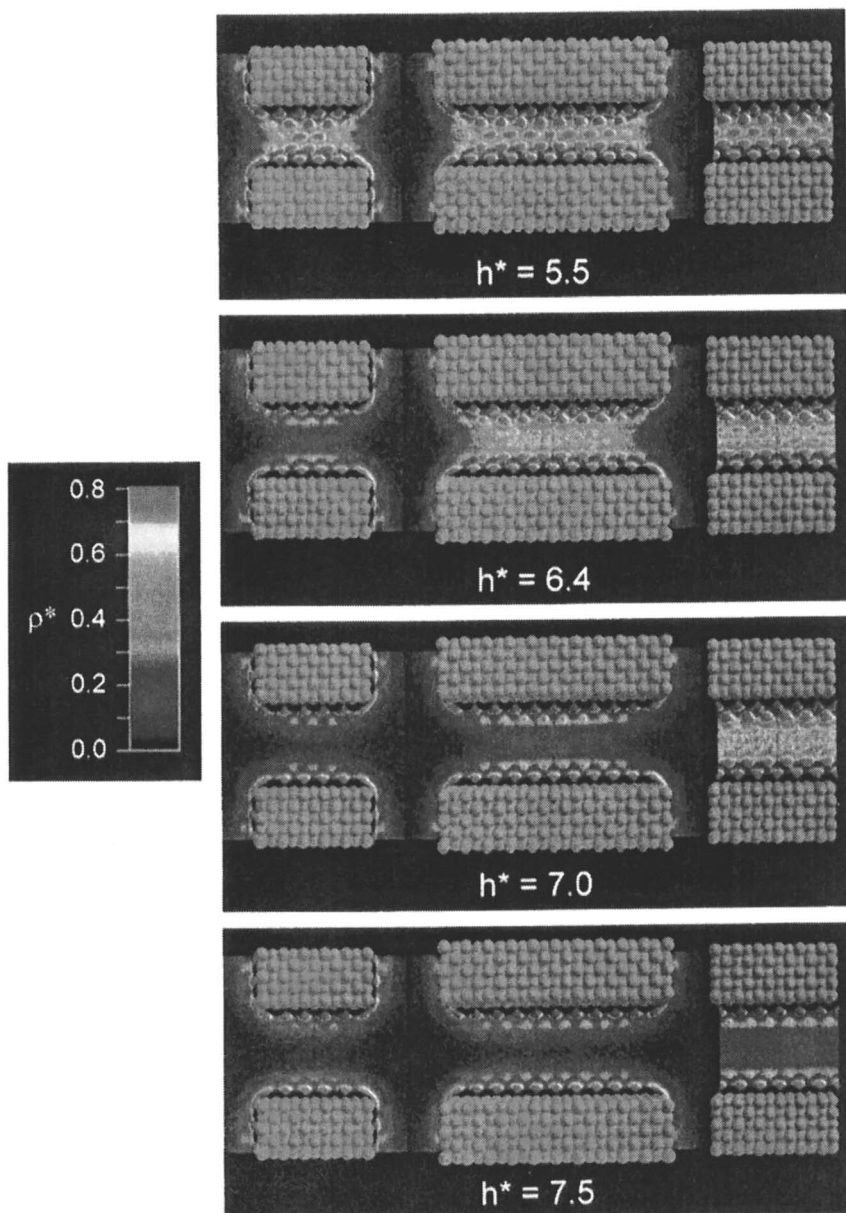
Figure 9. As for Figure 3 but for (from left to right) a 5-wire, 10-wire, and ∞-slit pore at h* = 5.5, 6.4, 7.0, and 7.5. Adapted from Stroud et al. (2001).

(See Page 2 of color insert.)
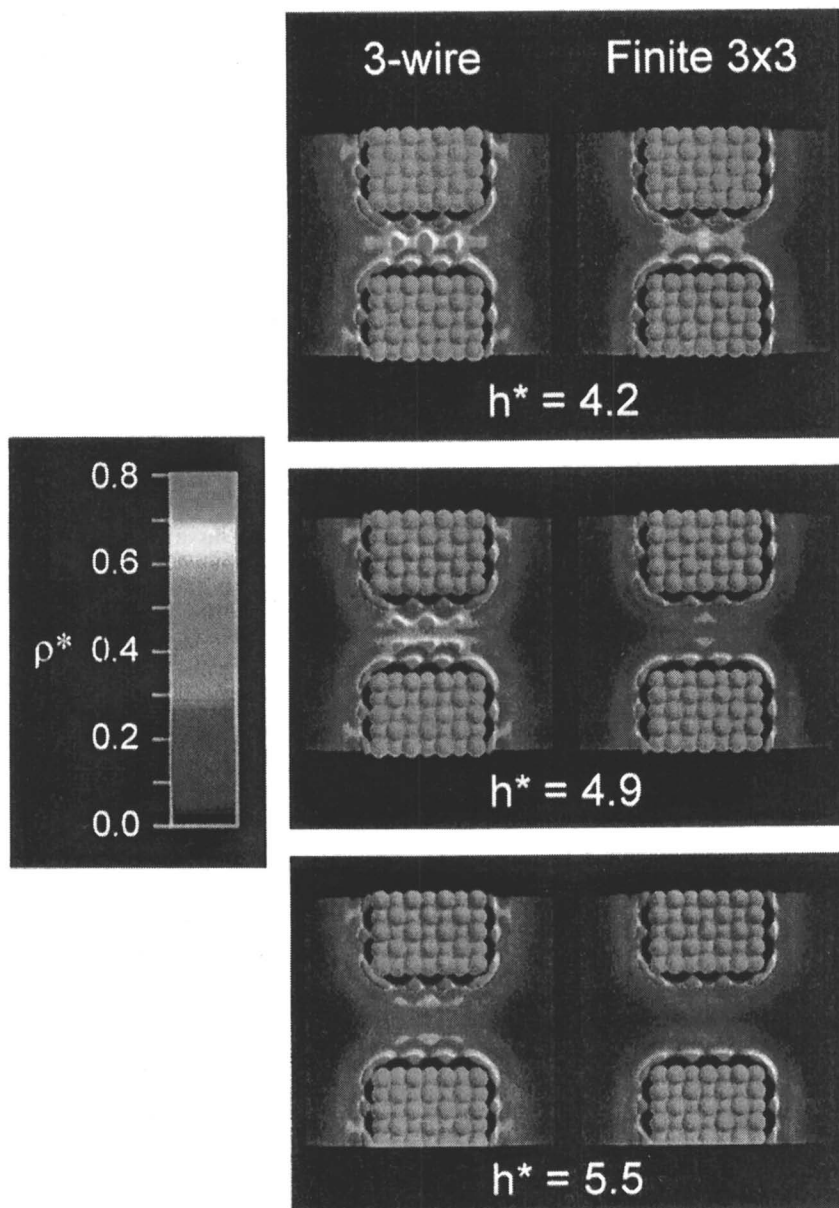
Figure 10. Maps of two-dimensional slices through the three-dimensional, ensemble-average particle density of the fluid condensed between nanowires three unit cells wide (left, slice taken at y = 0.0) and finite platelets with dimensions three unit cells in both the x and y directions (right, slice taken across the center of the contact at y = 0.5) for μ* = -11.7, T* = 1.0, α = 0.0, and h* = 4.2, 4.9, and 5.6. Adapted from Stroud et al. (2001).
(See Page 3 of color insert.)

References

1. Israelachvili, J. *Intermmolecular and Surface Forces*, Academic, NY, 1991.
2. Granick, S. Motions and relaxations of confined liquids. Science **1991**, 253, 1374-1379.
3. Meyer, G.; Amer, N. M. Simultaneous measurement of lateral and normal forces with an optical-beam-deflection atomic force microscope. Applied Physics Letters **1998**, 57, 2089-2091.
4. Rhykerd, C. L. Jr.; Schoen, M.; Diestler, D.J.; Cushman, J. H. Epitaxy in simple classical fluids in micropores and near surfaces. Nature **1987**, 330, 461-463.
5. Sommers, S. A.; McCormick, A. V.; Davis, H. T. Superselectivity and solution forces of a two component fluid adsorbed in a slite micropore. J. Chem. Phys. **1993**, 99, 9890-9898.
6. Bhushan, B.; Israelachvili, J. N.; Landman, U. Nanotribology: friction, wear and lubrication at the atomic scale. Nature **1995**, 13, 607-616.
7. Cushman, J. H. *The Physics of Fluids in Hierarchical Porous Media: Angstroms to Miles*, Kluwer Academic, MA, **1997**.
8. Stroud, W. J.; Curry, J. E.; Cushman, J. H. Capillary condensation and snapoff in nanoscale contacts. Langmuir **2001**, 17, 688-698.
9. Gee, M. L., McGuiggan, P. M., Israelachvili, J. N., Liquid to solid-like transitions of molecularly thin films under shear. J. Chem. Phys. **1990**, 93, 1895-1906.
10. Schoen, M. *Computer Simulation of Condensed Phases in Complex Geometries*, Springer-Verlag, **1993**.
11. Schoen, M., Cushman, J. H., Diestler, D. J. Anomalous diffusion in confined monolayer films. Mol. Phys. **1994**, 81, 475-490.
12. Curry, J. E., Cushman, J. H., Schoen, M., Diestler, D. J. Interfacial tension in confined molecularly-thin films. Mol. Phys. **1994a**, 81, 1059-1073.
13. Curry, J. E., Zhang, F., Cushman, J. H., Schoen, M., Diestler, D. J. Transiently coexisting nanophases in ultra thin films confined between corrugated walls. J. Chem. Phys. **1994b**, 100, 10824-10832.
14. Curry, J. E., Cushman, J. H. Nannophase coexistance and sieving in binary mixtures confined between corrugated walls. J. Chem. Phys. **1995**, 103, 2132-2139.

Chapter 13

Spatially Resolved Dynamics of Supercooled Liquids Confined in Porous Glasses: Importance of the Liquid–Glass Interface

Ranko Richert and Min Yang

Department of Chemistry and Biochemistry, Arizona State University, Tempe, AZ 85287–1604

The dynamics of liquids is notorious to be affected by geometrical confinement, provided that sufficiently small length scales of order several nanometers are involved. Regarding the viscous regime of glass-forming materials, the effects of confinement are often characterized by a glass transition shift relative to the bulk material. We discuss several problems associated with this approach and show evidence for the important role of interfacial dynamics. In particular, we assess the spatial dependence of relaxation times within pores of 7.5 nm diameter as measured by site selective triplet state solvation dynamics experiments.

Non-crystalline materials in confined spaces and near surfaces are encountered in many situations. Lubrication, oil in rocks, water in porous materials, biological cells and membranes are only a few examples. Here, we are concerned with the behavior of glass-forming viscous materials when restricted geometrically within porous glasses characterized by length scales of several nanometers.

181

Introduction

The properties of liquids subject to geometrical restrictions at the sub-micron level have been addressed in a variety of experimental approaches. Surface force microscopy has revealed that the viscosity of room temperature liquids changes dramatically within a few molecular layers near atomically smooth mica surfaces (*1,2*). Confinement effects have also been observed for liquids in porous materials with rougher surfaces and a distribution of surface curvatures, but the effects remained less pronounced (*3*). For instance, Warnock has observed an increase in the viscosity of a liquid by a factor of 3 near a silica interface using picosecond experiments (*4*).

Glass-forming materials are those which do not crystallize easily, such that the viscosity and relaxation time scale increases many orders of magnitude if the liquid is cooled below its melting point. In this supercooled regime, the time scales of molecular motions rapidly approach a value of 100 s, which marks the glass transition temperature T_g. The most prominent characteristics of the dynamics in the supercooled state are non-exponential relaxation patterns and pronounced deviations from an Arrhenius type temperature dependence of the transport coefficients (*5*). The concomitant curvature of a relaxation time constant versus temperature trace in an activation diagram is commonly described in terms of the empirical Vogel-Fulcher-Tammann (VET) law.

$$\log_{10}(\tau/s) = A + B/(T - T_0), \qquad (1)$$

It implies a relaxation time divergence at a finite temperature T_0, typically positioned some ten Kelvins below T_g. Although generally accepted theory of the glass transition is available, an increasing length scale of cooperative motion is often made responsible for the slowing down of the dynamics as the temperature approaches T_g. Originally introduced by Adam and Gibbs (*6*) as theory of 'cooperatively rearranging regions', this length scale ξ can be viewed as the distance required by two molecules in order to relax independently. Estimates of this length based on experimental approaches have reported values of $\xi \approx 3$ nm. Accordingly, geometrical restrictions of supercooled liquids on the spatial scales of a few nanometers are of particular interest, because confinement and cooperativity share similar spatial dimensions. In fact, experiments on viscous liquids in porous materials have been used for determining the length scales associated with the cooperative nature of molecular motion (*7*).

The first confinement induced shift of the glass transition has been reported for glass-forming organic molecular liquids by Jackson and McKenna using Differential Scanning Calorimetry (*8*). A reduction of T_g was observed in porous glasses, equivalent to faster dynamics if compared with the bulk behavior

at the same temperature. Subsequent measurements of geometrically confined materials near T_g arrived at both signs for the glass transition shift ΔT_g. Thus, accelerated as well as frustrated dynamics in confinement have been reported on the basis of a variety of liquids, polymers, and confining geometries with different physical and chemical surface properties (9). Various possibilities for explaining these apparent discrepancies have been discussed: Differences in the thermodynamics path used to prepare the viscous state, neglect of specific surface interactions, and disregarding the relaxation amplitudes and changes in the time dependence when comparing relaxation patterns (7).

In the following, we emphasize the problems encountered when the relaxation strength and patterns are not properly taken into account. Then, we briefly discuss the technique of triplet state solvation dynamics applied to confined systems and in particular present recent results on site-selective solvation studies of 3-methylpentane in porous silica, which demonstrate how the relaxation time or viscosity depends on the distance from the liquid/glass interface. In the absence of atomically smooth conditions and specific interactions with the surface, a surface induced increase of the viscosity by more than three orders of magnitude is being observed, which emphasizes the interfacial over pure finite size effects. Consistent with typical length scales of cooperativity in viscous liquids, these frustrated dynamics disappear for distances from the pore boundary of a few nanometers.

Relevance of Relaxation Amplitudes

Casting the impact of geometrical confinement on the dynamics into a glass transition shift ΔT_g is not always appropriate. In the context of restricted geometries, a common observation is a bifurcation of the relaxation into a slow and fast component, often associated with a distinct surface layer of highly reduced molecular mobility. Whenever the relaxation pattern or the observed correlation functions changes qualitatively, the differences between bulk and confined dynamics are only poorly represented by ΔT_g or by a change in time scale. Less obvious are the problems encountered when the shape of the relaxation trace is preserved to a good approximation but the amplitude is altered significantly (7). Such a situation is found frequently in dielectric relaxation studies of liquids and polymers confined to porous glasses.

Dielectric techniques have been applied to a number of porous materials, and the interpretation of the data is not entirely straightforward (10,11). One of the problems is that the dielectric results refer to a mixture of two different materials, the liquid (filler) under study and the confining material (matrix), e.g. porous glass. Unfortunately, the two distinct dielectric contributions from the filler and matrix do not simply add to the signal measured for the composite

material. Instead, theories of the electrostatics of heterogeneous dielectrics like those of Maxwell, Wagner, and Sillars have to be involved, unless the dielectric behavior of filler and matrix are similar (*12*). A prerequisite for successfully retrieving the dielectric function of the filler from the measurement of the composite is the knowledge of the filler volume fraction, the dielectric properties of the matrix material, and details regarding the confining geometry.

The source of ambiguity discussed in the following is not related to these electrostatic mixing effects, i.e., we now assume that they are negligible or have been solved. There are numerous examples of relaxation data obtained for liquids confined to porous media where the amplitude of the relaxation is significantly smaller than the bulk counterpart. Some examples clearly show that relaxation strength is not really lost, but shifted far away from the time or frequency range of the bulk relaxation (*13*). This is the situation shown schematically in Figure 1.
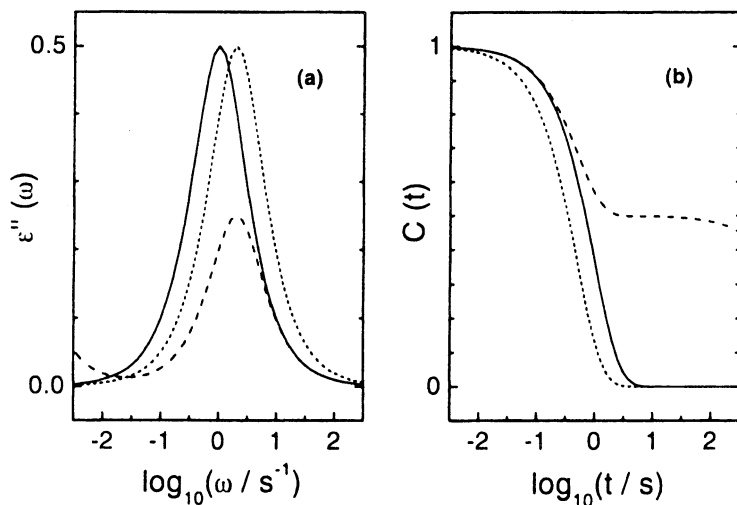
Figure 1. (a) Dielectric loss for a bulk and confined situation, assumed to separate the response into a contribution near the bulk peak frequency and a much slower one. Apparently, the relaxation under confinement is faster than in the bulk. (b) The same situation of (a) after transformation to the time domain. Comparing the bulk and confined results on an absolute amplitude scale indicates that there is no faster component in the confined case.

In Figure 1a the dielectric loss $\varepsilon''(\omega)$ is calculated for an exponential bulk relaxation with amplitude $a_{bulk} = 1$ and time constant $\tau_{bulk} = 1$ s (solid curve). The confined case is assumed a superposition of two exponentials with equal

weights, but differing in their time scale, $\tau_{fast} = 0.5$ s and $\tau_{slow} = 3000$ s (dashed curve). Without knowledge of the intensities, one would compare the loss peak positions after normalizing the peak heights, which leads to the amplitude $a_{norm} = 1$ and time constant $\tau_{fast} = 0.5$ s for the normalized fast component in confinement (dotted curve). Although such data are easily interpreted as a confinement induced acceleration of the dynamics, comparing the results on the correct ordinate scales demonstrates that no faster component exists in the confined case. Figure 1b reflects the identical situation but calculated as time domain signals. That the short time relaxation remained unchanged is particularly clear in the time domain representation, where the solid and dashed curves coincide for short times.

Intentionally, the above example has been selected such that the slope at time $t = 0$ remains constant, using

$$\frac{dC(t)}{dt}\bigg|_{t=0} = -\langle \tau^{-1} \rangle. \tag{2}$$

The example discussed here clearly shows that disregarding relaxation amplitudes can lead to erroneous interpretations of the relaxation time changes.

Triplet State Solvation Dynamics

Solvation dynamics experiments employing the long lived excited triplet states are particularly useful for assessing the dynamical behavior of molecules in the supercooled state close to the glass transition at T_g (14). The method is based upon the electronic excitation of a chromophore as dopant whose permanent dipole moment changes from the ground state value μ_G to that of the excited state μ_E. The $S_0 \leftarrow T_1$ (0-0) emission spectrum is recorded as a function of time and displays a shift towards lower energies whenever dielectric polarization is active within the phosphorescence lifetime τ_{ph}. The Stokes shift dynamics of the average emission energy thus reflects the orientational polarization of dipolar solvents (15). In the absence of dipolar interactions, solvation dynamics are also observed, but they reflect the local shear modulus relaxation in this case (16,17). This technique is advantageous for investigating the relaxation of viscous liquids in the optically clear porous silica glasses because the probe molecules are sensitive only to the local response without a significant spatial averaging. In liquid solvents, it has been shown that the coupling range inherent in the electrostatic interaction of this technique is characterized by spatial scales which hardly exceed the first solvent shell (14).

The porous glasses used here are Gelsil glasses (GelTech) of cylindrical shape (10mm $\varnothing$, 5 mm thick) with nominal pore diameters $\phi = 2.5$. 5.0, and 7.5

nm. The actual characteristics in the above order of ϕ are: pore diameters 2.6, 4.6, and 8.4 nm; pore volume fractions 0.39, 0.68, and 0.72; and surface areas 609, 594, and 342 m^2/g. Clean pore surfaces are obtained by washing with H_2O_2 and heating in vacuum to 400^0C for 24 hours. Silanized glasses have been prepared by exposing the dried porous glass to hexamethyldisilazane gas at ambient temperatures for 24 h. The glasses were filled with the solute/solvent mixture under dry N_2 atmosphere and placed into a vacuum sealed sample cell. Further details of the experimental setup have been reported previously (14).

The resulting $S_0 \leftarrow T_1$ (0-0) emission spectra are subject to a Gaussian analysis in order to determine the average emission energies $\langle v(t,T) \rangle$ as a function of time and temperature. For focusing on the dynamical aspect of the dipolar solvation process at a fixed temperature, the $\langle v(t) \rangle$ data are normalized according to the Stokes-shift correlation function

$$C(t) = \frac{\langle v(t) \rangle - \langle v(\infty) \rangle}{\langle v(0) \rangle - \langle v(\infty) \rangle}. \tag{3}$$

The total Stokes shift $\Delta v = \langle v(0) \rangle - \langle v(\infty) \rangle$ is a measure for the amplitude of the response, whereas the signal intensities remain irrelevant for the data analysis. Because the limiting values $\langle v(0) \rangle$ and $\langle v(\infty) \rangle$ are measured independently from a $\langle v(t) \rangle$ scan, the normalization of Equation (3) is unambiguous even if $\langle v(t) \rangle$ at a certain temperature does not attain the short or long time limit.

In many cases, the correlation decays $C(t)$ are well approximated by a stretched exponential or Kohlrausch-Williams-Watts (KWW) function of the form

$$C(t) = \exp\left[-\left(\frac{t}{\tau_{KWW}} \right)^{\beta_{KWW}} \right], \tag{4}$$

with a temperature invariant exponent β_{KWW} in the present temperature ranges. Thus, temperature variations affect $C(t)$ only in terms of the characteristic time $\tau_{KWW}(T)$ without changing the functional form.

Effect of Surface Chemistry

In Figure 2 we compare previous $C(t)$ results obtained for the solute quinoxaline in the glass-forming solvent 2-methyltetrahydrofuran (MTHF) in porous glasses subject to different surface treatments (18). In the case of silanized surfaces in Figure 2a, the silanol groups of a silica surface are passivated, which leads to more hydrophobic pore walls. Under these

conditions, the dynamics of MTHF remain unchanged compared with the bulk situation, even in the smallest pores of 2.5 nm diameter. For the clean but otherwise untreated and more hydrophilic pore boundary in Figure 2b, confinement does affect the dynamics significantly in the longer time range, while the short time relaxation remains that of the bulk case.
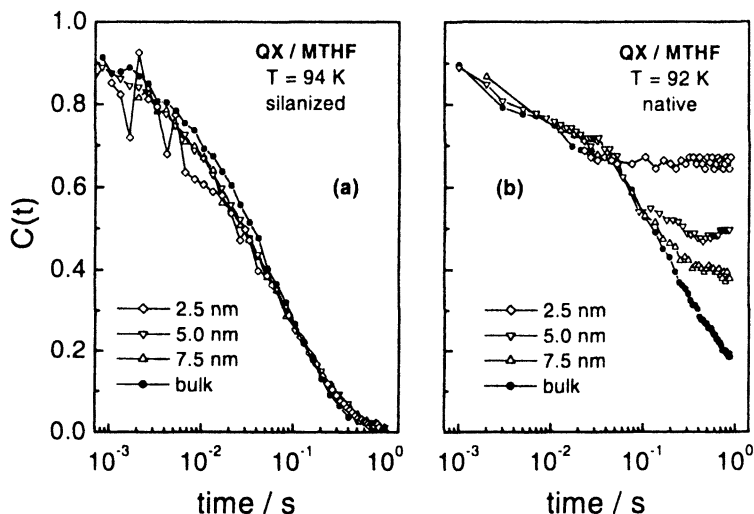
Figure 2. Stokes shift correlation function C(t) versus time for QX/MTHF in the bulk and confined to various pore sizes as indicated. (a) Results for a silanized glass surface, which leads to a hydrophobic interface. (b) Results for a clean but otherwise untreated glass surface.

These results clearly demonstrate that the boundary conditions constitute an important aspect of dynamics in confined geometries, because the two experiments confronted in Figure 2 differ only in the surface chemistry.

In these experiments, the progress of the solvent relaxation is monitored along the emission energy scale. Therefore, the result obtained for $C(t)$ is independent of the number of emitting chromophores. As a result, this technique does not involve ambiguities regarding the relaxation amplitudes, which are practically preserved for all pore sizes. Naturally, it is tempting to assign the very slow relaxation components observed for the native pore surface to more frustrated dynamics near the pore boundary. On the other hand, observing the interfacial dynamics selectively will provide a clearer picture of the importance of the liquid/glass boundary.

Observation of Interfacial Dynamics

In the following we exploit the different properties of the probe molecules quinoxaline (QX, polar) and naphthalene (NA, non-polar) regarding their affinity to populate the surface of porous glasses with 7.5 nm pore diameter (*19*). These experiments use the non-polar liquid 3-methylpentane (3MP), which exhibits a glass transition at $T_g = 77$ K. Figure 3a displays the average emission energies recorded at $t_0 = 100$ ms for bulk NA/3MP, bulk QX/3MP and confined QX/3MP. All three traces feature a step in $\langle v(t_0,T) \rangle$ near $T = 80 - 85$ K, which is the signature of solvation dynamics with comparable amplitudes. As has beemi observed previously, however, the energies of the QX/3MP experiment in pores are considerably below the bulk counterpart. This situation is preserved after removing the liquid from the porous glass and filling with Ar gas, as shown by the data labeled QX/Ar.

In Figure 3b, the emission energies of QX in the bulk and in pores are compared with the solvatochromism of QX observed in a series of bulk solvents which differ in their polarity on the E_T^N (*20*) scale. The graph shows that QX emitting as low as 20600 cm^{-1} implies its vicinity to a highly polar environment. In pure bulk solvents, it is only the case of alcohol which leads to such a pronounced red shift, and we conclude that QX is positioned at the silanol groups of the pore surface instead of remaining dissolved in 3MP. In contrast, NA is non-polar and not susceptible to hydrogen bonding and therefore not energetically favored near the silica surface. The distinct behavior of the two probes in confined 3MP allow us to observe the dynamics separately in the bulk, as the pore volume average, and at the liquid/silica interface (*21*).

The results for the different dynamics observed this way are compiled as $\tau_{KWW}(T)$ in Figure 4, after fitting the C(*t*) data to the KWW decay of Equation (4). The temperature dependence is well described by the VET law in each case. For the individual glass transition we obtain $T_{g,bulk} = 76.7$ K for the bulk liquid, $T_{g,conf} = 79.0$ K for 3MP confined to the 7.5 nm pores, and $T_{g,intf} = 81.9$ K for the interfacial 3MP. In terms of a glass transition shift relative to the bulk liquid, the above observations are summarized by $\Delta T_{g,conf} = +2.3$ K and $\Delta T_{g,intf} = +5.2$ K for the confined and interfacial liquid, respectively. However, the $\tau_{KWW}(T)$ traces of Figure 4 do not coincide after shifting by ΔT_g on the temperature scale, as indicated by the dashed curve which corresponds to the bulk VET fit shifted by $\Delta T_g = +5.2$ K. Instead, the three VFT fits indicate that the changes are accounted for by adjusting the preexponential parameter *A* only. Therefore, the effect of nanopores is more appropriately described by ΔA, or by a temperature invariant relaxation time ratio. Comparing the average time scale within the pore with that in the hulk leads to $\tau_{conf}/\tau_{bulk} = 40$, whereas the relaxation time within the interfacial layer is slower by a factor of $\tau_{intf}/\tau_{bulk} = 2000$.
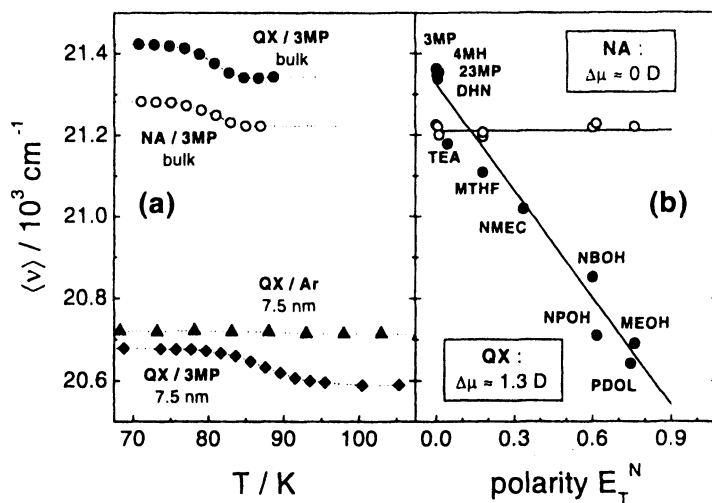
Figure 3. (a): Average emission energy at t = 100 ms versus temperature for various solute/solvent combinations in the bulk (circles) and in pores of 7.5 nm diameter (diamonds). Triangles are obtained after replacing the solvent by Argon gas. (b): Average steady state emission energy of quinoxaline (QX, solid circles) and naphthalene (NA, open circles) in various bulk solvents, sorted according to polarity. Comparing both sides demonstrates that QX in porous silica experiences the polarity of alcohol, implying its position at the interfacial OH groups.

An inspection of the probability densities $g(\ln \tau)$ based upon the stretching exponents β_{KWW} and time constants τ_{KWW} for the bulk, confined, and interfacial situations indicates the following. The interfacial and bulk relaxation time distributions are well separated, while the intermediate curve associated with the pore volume average covers both the fastest and slowest relaxation times. In particular, observing that 45 % of the $g(\ln \tau)$ area for the confined case overlaps with the range of τ values observed in the bulk suggests that a fraction of the liquid within the pore behaves bulk like, most likely originating from the pore center. As illustrated in Figure 5, we can now assign relative relaxation times as a function of the distance r ($0 \leq r \leq R$) from the center: $\tau(r = 0) = \tau_{bulk}$, $\tau(r = \langle r \rangle = R/4) = \tau_{conf} = 40 \times \tau_{bulk}$, and $\tau(r = R) = \tau_{intf} = 2000 \times \tau_{bulk}$, i.e., at the interface. It turns out that the random position of NA within the pore together with the $\tau(r)$ curve of Figure 5 are sufficient for rationalizing the broader and shifted probability density associated with the pore volume average.
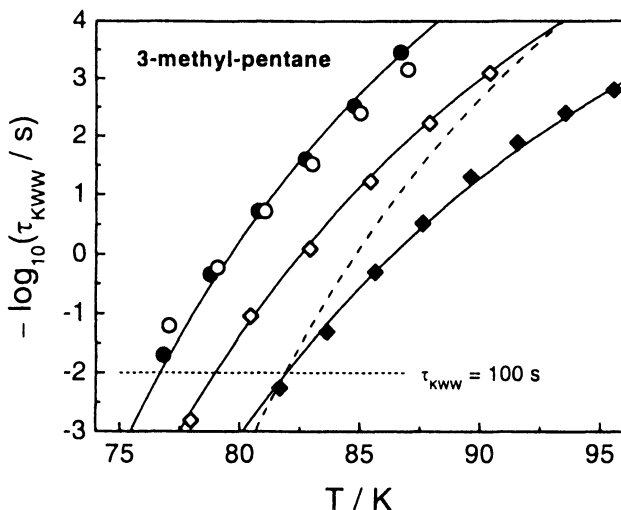
Figure 4. Temperature dependence of the solvent relaxation time in 3-methylpentane (3MP) for the bulk liquid (QX/3MP: solid circles, NA/3MP: open circles), for 3MP confined to 7.5 nm pores (NA/3MP: open diamonds), and for the interfacial layer of 3MP at time pore wall (QX/3MP: solid diamonds). The Solid lines are VFT curves with B = 464 K, T_0 = 52 K, and A = -16.8, -15.2, and -13.5, in time order from top to bottom curve. The dotted line indicates the τ = 100 s criterion for determining T_g. The dashed curve is obtained by shifting the VFT line for the bulk case by ΔT_g = +5.2 K.

The observation of a pronounced viscosity gradient in a simple liquid near a silica surface bears a series of implications. The behaviour of a wetting liquid acting as viscous lubricant changes dramatically within the first few nanometers distance from the surface, even in the absence of atomically smooth surface conditions, specific interactions with the surface, or external pressure. Such a spatial variation of viscosities implies the common observation that the distributions of relaxation times in confined systems are much broader than those of the bulk material. That the interfacial dynamics differ from the bulk case more drastically than that inside the pore suggests that the boundary effects dominate in altering the properties of the liquid, and that pure finite size effects are of minor importance. Within this picture, frustrated mobility of a wetting

liquid at the liquid/glass interface combined with the cooperative nature of molecular motion in viscous liquids are sufficient for explaining the distance dependence $\tau(d)$ of Figure 5. Particles at distances $d > 2$ - 3 nm away from the interface are no longer affected, consistent with typical length scales $\xi \approx 3$ nm reported for the cooperativity near T_g and with recent simulation results on a confined supercooled model liquid (22).
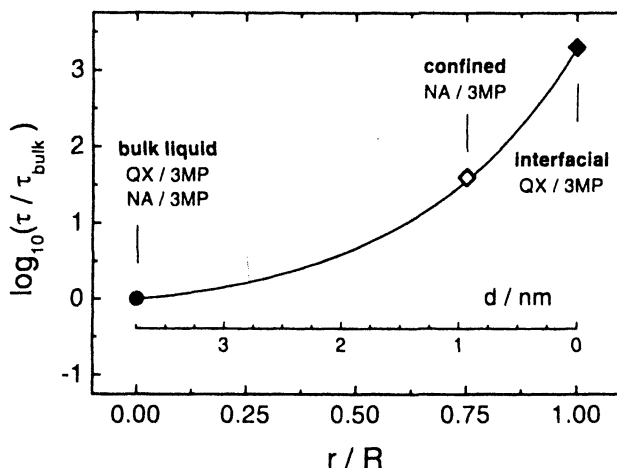
Figure 5. Suggested trend $\tau(r)/\tau_{bulk}$ based upon $\tau_{bulk}/\tau_{bulk} = 1$ for $r = 0$ (QX and NA in bulk 3MP), $\tau_{conf}/\tau_{bulk} = 40$ for $r = \langle r \rangle \approx R/4 = 0.94$ nm (NA/3MP in pores), and $\tau_{intf}/\tau_{bulk} = 2000$ for $r = R = 3.75$ nm (QX/3MP in pores). The line is an empirical interpolation only. The inner scale shows time distance d from the interface for a spherical geometry.

Cooling a liquid subject to geometrical confinement in order to form a glass will result in solidification which sets in at the interface, while lower temperatures are required to traverse the glass transition of the inner pore liquid. By the same token, the material near the interface is immobile on the time scale of viscous flow near the centre of the pore, thereby confining the liquid further. At the 'bottlenecks' which interconnect the pores, such immobile layers may eventually prohibit liquid flow among pores and create a crossover from an isobaric (constant pressure) to an isochoric (constant volume) path. This situation will occur when the spatial extent ξ of cooperativity competes with the smallest lengths scale of the confirming geometry, where ξ depends on the

material and temperature. Because T_g and the behaviour of the liquid near T_g depend on the thermodynamic path, a crossover to the isochoric condition is likely to play a role in the apparent inconsistency regarding confinement effects in supercooled liquids.

References

1. Israelachvili, J. N.; McGuiggan, P. M. *Science* **1988**, *241*, 795.
2. Granick, S. *Science* **1991**, *253*, 1374.
3. Drake, J. M.; Klafter, J. *Physics Today* **1990**, *43*, 46.
4. Warnock, J.; Awschalom, D. D.; Shafer, M. W. *Phys. Rev. B* **1986**, *34*, 475.
5. Ediger, M. D.; Angell, C. A.; Nagel. S. R. *J. Phys. Chem.* **1996**, *100*, 13200.
6. Adam, G.; Gibbs J. H. *J. Chem. Phys.* **1965**, *43*, 139.
7. Richert, R. *Phys. Rev. B* **1996**, *54*, 15762.
8. Jackson, C. L.; McKenna, G. B. *J. Non-Cryst. Solids* **1991**, *131-133*, 221.
9. McKenna, G. B. *J. Phys. IV France* **2000**, *10*, 53.
10. Daoukaki, D.; Barut, G.; Pelster, R.; Nimtz, G.; Kyritsis, A.; Pissis, P. *Phys. Rev. B* **1998**, *58*, 5336.
11. Pelster, R. *Phys. Rev. B* **1999**, *59*, 9214
12. Yan, X.; Streck, C.; Richert, R. *Mater. Res. Soc. Symp. Proc.* **1997**, *464*, 33.
13. Schüller, J.; Mel'nichenko, Yu. B.; Richert, R.; Fischer. E. W. *Phys. Rev. Lett.* **1994**, *73*, 2224.
14. Richert, R. *J. Chem. Phys.* **2000**, *113*, 8404.
15. Richert, R.; Wagener, A. *J. Phys. Chem.* **1991**, *95*, 10115.
16. Berg, M. *Chem. Phys. Lett.* **1994**, *228*, 317.
17. Wendt, H.; Richert, R. *J. Phys. Chem. A* **1998**, *102*, 5775.
18. Streck, C.; Mel'nichenko, Yu. B.; Richert, R. *Phys. Rev. B* **1996**, *53*, 5341.
19. Wendt, H.; Richert, R. *J. Phys.: Condens. Matter* **1999**, *11*, A199.
20. Reichardt, C. *Solvents and Solvent Effects in Organic Chemstry;* VCH:
21. Weinheim, 1988.
22. Richert, R.; Yang, M. *Phys. Rev. Lett.* (submitted).
23. Scheidler, P.; Kob. W.; Binder, K. *Europhys. Lett.* **2000**, *52*, 277.

Chapter 14

Reorientational Dynamics of Water Confined in Nanopores

Alessandra Scodinu and John T. Fourkas

Eugene F. Merkert Chemistry Center, Boston College,
Chestnut Hill, MA 02467

Ultrafast optical Kerr effect spectroscopy has been used to study the orientational dynamics of water confined in sol-gel glasses with hydrophilic and hydrophobic nanopores. Orientational relaxation is found to be significantly faster at hydrophobic surfaces than at hydrophilic surfaces, whereas the orientational relaxation of the liquid in the centers of the pores is independent of the chemical nature of the pore surfaces.

Introduction

Water is unquestionably one of the most important liquids in chemistry, biology, physics, and many other areas of science. In addition, its behavior puts it among the most anomalous liquids known. As such, the structure and dynamics of water have been the subject of intense scientific scrutiny for well over 100 years, and yet many of the mysteries of this liquid remain unresolved (*1*).

Many of the unique properties of water result from the extraordinary degree of hydrogen bonding in this liquid. For instance, the highly networked nature of

water makes its structural and dynamic properties extremely sensitive to the influences of solutes. As an example, so-called "structure-making" cations have low diffusion constants in water because they effectively carry a significant amount of the solvent along with them (2). Similarly, the properties of water near a surface are influenced strongly by the chemical nature of the surface, e.g. whether it is hydrophilic or hydrophobic (3,4). For instance, water at or near the surfaces of proteins is believed to have very different behavior from that of the bulk liquid (5).

Confinement can also exert a strong influence on the structural and dynamic properties of water (6,7), and as a result confined water plays as important a role in many areas of science as does the bulk liquid. For instance, in geology, understanding the behavior of in water in porous rocks is important in oil recovery and groundwater decontamination. In biology, confined water is also believed to play a key role in the structure and function of many proteins. In chemistry, confined water is an important element of many separations technologies and new synthetic methods.

There are many factors that can affect the behavior of water in confinement, including the dimensions, geometry, degree of saturation, and chemical nature of the surfaces of the confining region. The last of these is a particularly intriguing topic. For instance, when water is confined between two parallel hydrophobic surfaces, attractive forces between the plates can be observed at distances in the range of 10 nm (8), even though no such attractions are found when both surfaces are hydrophilic or when one is hydrophilic and one hydrophobic (9). A number of explanations have been proposed for this phenomenon, including long-range ordering of water (8) and the existence of phase instabilities near hydrophobic interfaces (10).

Nanoporous glasses (11) have proven to be highly useful media in which to study the behavior of confined liquids. These materials feature roughly cylindrical pores, the diameters of which are reasonably monodisperse. The average pore diameter of a sample can be controlled via the fabrication procedure, and can be as small as 20 Å. The surface chemistry of these materials is well known, and the interactions between the pores and confined liquids can thus be tuned using surface-modification chemistry.

Water confined in nanoporous glasses has been the subject of many studies over the past decades with techniques that include calorimetry (12), neutron scattering (13), X-ray diffraction (14), THz spectroscopy (15,16), Raman scattering (17), nuclear magnetic resonance (18) and simulations (19,20). However, because of the inherent difficulties associated with filling small hydrophobic pores with water, experimental studies have focused on the behavior of water in hydrophilic pores. We have developed a technique that allows us to introduce water into hydrophobic nanopores. This method has enabled us to make a comparative study of the orientational dynamics of water in hydrophilic and hydrophobic nanopores, a preliminary report of which

appears elsewhere (*21*). In this chapter we will discuss the results of this study in detail.

The experimental method that we used to probe the orientational dynamics of confined water ultrafast optical Kerr effect (OKE) spectroscopy (*22,23*). In OKE spectroscopy, an ultrafast laser pulse is used to create a small net alignment of the confined water molecules by taking advantage of their anisotropic polarizability. This net alignment in turn creates a transient birefringence in the liquid, the time-dependent behavior of which can be probed by a second laser pulse that arrives at a variable delay time, allowing the return of the liquid to its equilibrium orientational state to be observed. We have previously used OKE spectroscopy to study both wetting and non-wetting liquids confined in nanoporous sol-gel glasses (*24*). These studies demonstrated the ability of OKE spectroscopy to provide detailed, quantitative information about how confinement affects both the dynamics and structure of liquids. Water if the first networked liquid that we have studied, and by virtue of its small polarizability anisotropy it is more challenging to study with OKE spectroscopy than are the liquids we have looked at previously. Nevertheless, as we will show below, OKE spectroscopy has proven to be a valuable tool for studying the behavior of confined water as well.

Experimental

Our experimental apparatus has been described in detail elsewhere (*25*), and so we will describe it only briefly here. A modelocked Ti:sapphire laser was used to produce 60-fs pulses with a center wavelength of approximately 800 nm, a repetition rate of 76 MHz, and an average power of about 500 mW. The output of the laser is split into a strong pump beam and a weaker probe beam, each of which is chopped at a different rate. The beams are focused into the sample using an achromatic lens. The pump beam is made vertically polarized before the sample. The probe beam traverses an optical delay line to control its timing relative to the pump beam. Before reaching the achromatic lens, the probe beam passes through a polarizer set at 45° and then through a quarter-wave plate that is oriented so as to have one axis coincide with that of the polarizer. The two beams are aligned so that they cross only within the sample. After the sample, the probe beam is recollimated by a second lens and then is incident on the analyzer polarizer, which is set at -45°, such that it will only pass probe light that has been depolarized due to birefringence induced in the sample by the pump beam. In order to introduce a local oscillator, the input polarizer in the probe beam is rotated by a couple of degrees; the sense of this rotation is reversed on every scan so that the heterodyned component of the signal can be separated from the homodyned component. After the analyzer

polarizer, the signal beam is spatially filtered and then is directed into a low-noise amplified photodiode. A portion of the probe beam is picked off before the first polarizer and is directed into a matched photodiode. The outputs of the photodiodes are then sent to the differential inputs of a low-noise analog preamplifier, the output of which is sent to a digital lock-in amplifier that is synchronized to the sum of the chopping frequencies of the pump and probe beams. The pump beam is frequency doubled after the sample and is detected by a separate photodiode/lock-in amplifier pair in order to correct for any long-term drift in the laser power or pulse length.

Monolithic silicate sol-gel samples were prepared as described previously (*24*). Samples with average pore diameters of 25 Å, 59 Å, and 100 Å were used in this study. Disks with thicknesses of somewhat less than 2 mm were polished to optical quality. To study dynamics in the natural hydrophilic state of the pores, the disks were placed in a 2-mm-pathlength optical cell that was filled with ultrapure water and were allowed to fill before data were taken. Once data collection was completed, the samples were dried carefully and then were treated with chlorotrimethyl silane in order to make the pore surfaces hydrophobic (*26*). After silanization, the samples floated on water, and so could not be filled directly. In order to circumvent this problem, the hydrophobic pores were first filled with methanol, which was then displaced by soaking the samples in ultrapure water several times. In order to ensure that all of the methanol had been displaced from the samples, CD_3OH was employed so that the disappearance of the absorption bands involving the deuterium atoms on the methyl group could be monitored using infrared spectroscopy. Once the samples were filled with water, they were again immersed in ultrapure water in a sample cell. All experiments were performed at 293 K.

Results

Bulk water

Before presenting our results for nanoconfined water, it is useful to consider the OKE decay of bulk water. The reorientational portion of the OKE decay of bulk water has been studied by a number of different groups (*27-30*), and the reorientational times reported in these studies span a broad range of values. Much of the disparity in the reported reorientational times probably arises from the fact that the polarizability anisotropy of water is quite small. The OKE signal of bulk water is therefore weak, and it is can be difficult to collect data out to long enough times to determine the decay constant accurately.
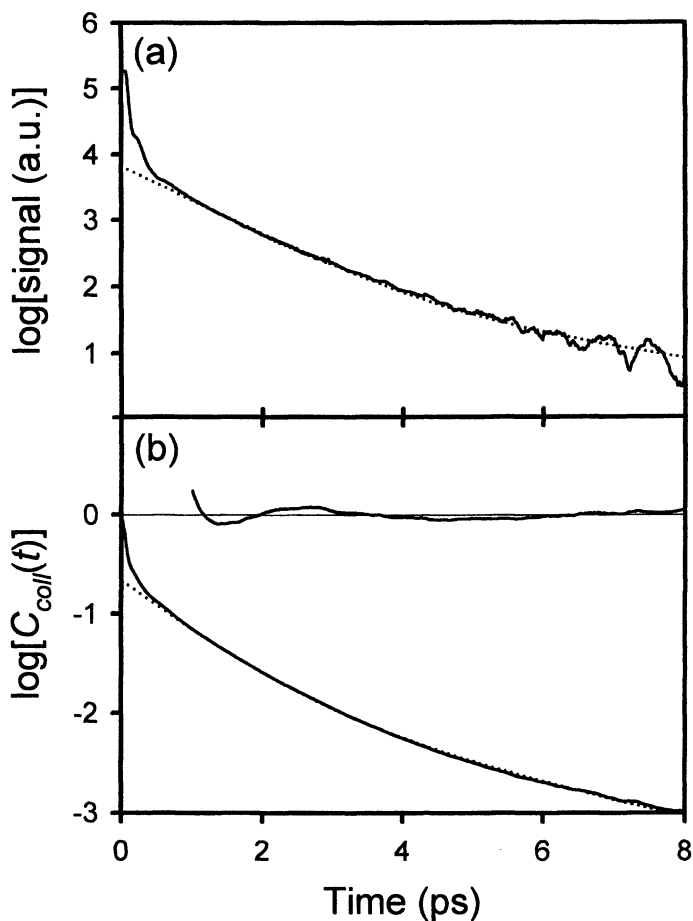
Figure 1. (a) OKE signal for bulk water at room temperature (solid line) and biexponential fit (dotted line). (b) Collective orientational correlation function (solid line), fit (dotted line), and magnified residuals on a linear scale (top).

Figure 1a shows smoothed raw data for bulk water. At times longer than 1 ps, the data can be fit reasonably well to the sum of two exponentials, one with a time constant of 2.7 ps and the other with a time constant of 0.81 ps. The former is presumably due to orientational diffusion and the latter to intermolecular dynamics. These numbers are in good agreement with those found by Winkler et al (29).

The OKE signal is proportional to the negative time derivative of the collective orientational correlation function, $C_{coll}(t)$ (31). Integration of the signal thus yields $C_{coll}(t)$, and simultaneously serves to smooth out high-

frequency noise in the data. This procedure does necessitate the determination of the constant of integration, in effect requiring that an additional fitting parameter be employed. However, for certain functional forms of the data, such as a multiexponential decay, the constant of integration can be determined readily and uniquely. Figure 1b shows $C_{coll}(t)$ for bulk water at 293 K along with a biexponential fit employing the above time constants. The residuals show that there are relatively small but systematic deviations between the data and the fit, which leads us to believe that the reorientational decay is not best described by an exponential function for this liquid.

Figure 2 shows a log-log plot of the OKE data for bulk water. This plot shows that the data can be represented reasonably well by a pair of power-law decays of the form t^{-b}. The first decay has an exponent of $b = 0.66$, and covers a range from about 100 fs to about 2 ps. The second decay has an exponent of $b = 2.0$, and covers times from 2 ps onward. The applicability of the power-law decay model to bulk water requires merits more detailed investigation, including obtaining data out to longer decay times and investigating different temperatures; however, it is apparent that this is a satisfactory empirical model for the current data, and we will use it to describe and compare the data in confinement as well.
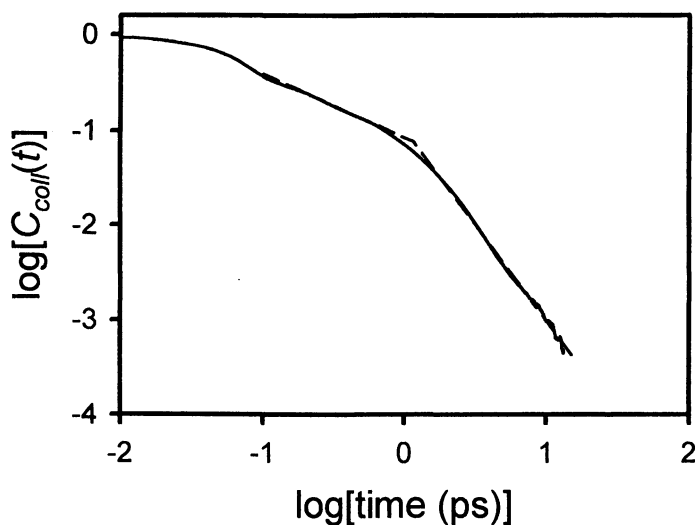
Figure 2. Log-log plot of the collective orientational correlation function of bulk water at room temperature (solid line) along with a fit to two power-law decays (dashed line).

Confined water

Figure 3 shows log-log plots of $C_{coll}(t)$ for water confined in hydrophilic and hydrophobic pores of different average sizes. In all cases power-law behavior is observed from times ranging from about 100 fs to greater than 10 ps, after which the decay is exponential. As was the case for bulk water, in the 59-Å and 100-Å pores two power-law decay regions are observed. The value of the power-law exponent in the short-time region (which we will denote b_1) is approximately 0.45 and depends only weakly on the nature and size of the pores, while the value in the long-time region (which we will denote b_2) is significantly greater than this and does depend on the nature and size of the pores). In the 25-Å pores only a single power-law decay is observed, with a value of b that is less than the 0.45 observed in the short-time power law decay in the larger pores. The power-law exponents and exponential decay constants (τ) for the various samples are given in Table I.
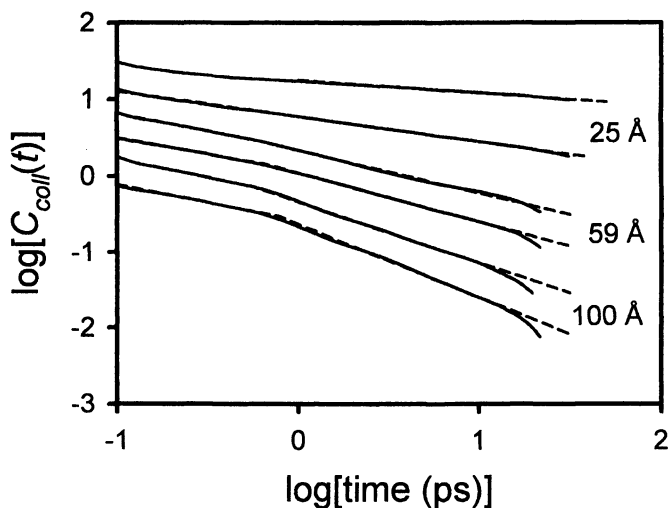
Figure 3. Log-log plot of the collective orientational correlation functions for water confined in pores of different diameters (solid lines) and power-law fits (dashed lines). The lower trace in each pair is for unmodified pores and the upper trace for modified pores.

Table I. Fitting Parameters for $C_{coll}(t)$

Sample	τ (ps)	b_1	b_2
Bulk water	--	0.66	2.0
100-Å pores, unmodified	20	0.46	0.97
100-Å pores, modified	18	0.49	0.80
59-Å pores, unmodified	31	0.42	0.64
59-Å pores, modified	25	0.45	0.56
25-Å pores, unmodified	36	--	0.33
25-Å pores, unmodified	29	--	0.07

NOTE: Uncertainties in τ are approximately ±2 ps and uncertainties in b_1 and b_2 are approximately ±0.03.

Discussion

We begin our discussion of the data for confined water with the exponential tails observed at long times, which we believe arise from the population of water molecules at or near the pore surfaces, in analogy with our previous findings for both wetting and non-wetting liquids (24). The data in Table I show that the surface relaxation slows down as the pore size decreases, in accord with our observations for other confined liquids. Based on a comparison of the exponential decay constants in hydrophobic and hydrophilic pores of the same size, orientational relaxation is roughly 25% slower near hydrophilic surfaces than near hydrophobic surfaces. The difference in surface relaxation times appears to be somewhat smaller in the largest pores, but these numbers also have the greatest uncertainty due to the smaller fraction of surface molecules in these pores. It is also possible that there is additional relaxation in these systems that is too slow for us to monitor. Nevertheless, the trend that the orientational relaxation of water is faster at hydrophobic surfaces than at hydrophilic surfaces is in qualitative agreement with the simulations of Lee and Rossky (3,4), although they observed a somewhat larger difference in reorientational times than we find here. We should also note that the procedure used for hydrophobization makes the pore diameters smaller (*vide infra*), thus slowing down the surface relaxation to some extent, so the actual increase in the surface relaxation time in going from a hydrophobic pore to a hydrophilic pore of the same radius is greater than the 25% seen in our data.

We now turn to the power-law portion of the relaxation, which we believe arises from the water molecules that are not at the pore surfaces. The short-time power-law decay with exponent b_1 probably arises from some sort of collective intermolecular relaxation. As mentioned above, in the two larger pore sizes, this exponent takes on values near 0.45. As can be seen in Table I, b_1 decreases

slightly as the pore size is decreased and increases slightly in going from hydrophilic to hydrophobic pores. The fact that this exponent differs significantly in confinement from the 0.66 observed in the bulk liquid suggests that there is an appreciable change in the intermolecular structure of water in confinement, even in pores with diameters as large as 100 Å. Significant changes in the pore diameter and the chemical nature of the pore surfaces have only a small influence on the value of b_1, which may indicate that the decrease of this exponent as compared to the bulk is related to the roughly cylindrical symmetry imposed on the confined liquid by the pores.

The values of b_2 observed in confinement are considerably smaller than the value of 2.0 seen in bulk water. In the confined liquids that we have studied previously we have always observed a relaxation component in the OKE signal that matches the orientational relaxation of the bulk liquid. This is not the case in confined water. Furthermore, as can be seen from Table I, b_2 depends strongly on the pore size. These two observations indicate that in liquid water the structure and dynamics of are affected more strongly by confinement than in the other liquids we have studied (24). None of the liquids that we have studied previously features a hydrogen-bond network, and so it is presumably this facet of water that distinguishes its behavior in confinement.

In Figure 4 we plot b_2 as a function of pore curvature for hydrophilic pores ( ), for hydrophobic pores ( ) and for the bulk liquid (Δ). The values of b_2 for the hydrophobic pores are smaller than those for hydrophilic pores of the same diameter, which might suggest that relaxation is slower in hydrophobic pores than in the hydrophilic pores, in apparent contradiction to the conclusions drawn for the surface population from the exponential tails of the orientational correlation functions. However, in calculating the pore curvature it is necessary to correct for the reduction of the radii in the hydrophobic pores arising from the addition of the trimethylsilyl groups at the pore surfaces. If we assume that the radii of the hydrophobic pores are 6 Å smaller than those of the corresponding hydrophilic pores, the values of b_2 for the hydrophobic pores in Figure 4 ( ) fall on the same curve with the bulk data and the data from the hydrophilic pores. This observation implies that the orientational relaxation of the water that is not at the pore walls depends solely on the pore size and not on the chemical nature of the pore surfaces. This further suggests that information about the chemical nature of the pore surfaces does not propagate any significant distance away from the surfaces. Our data therefore do not appear to be consistent with the idea that hydrophobic surfaces can impose long-range structural changes in liquid water.
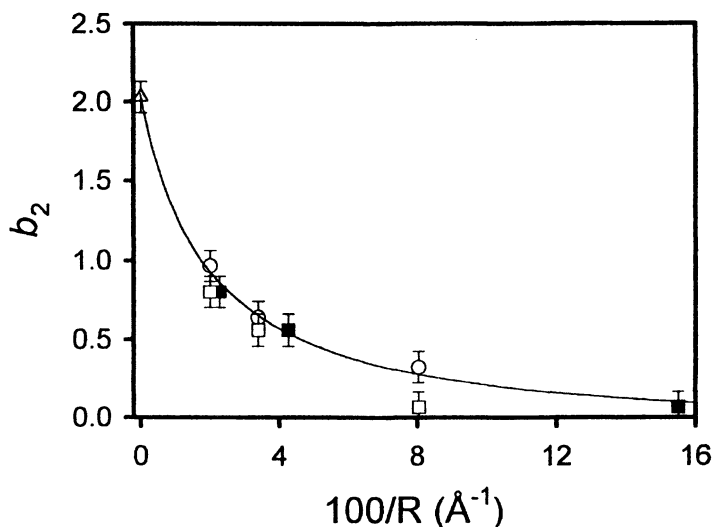
Figure 4. Second power-law exponent as a function of pore curvature for bulk water (Δ), hydrophilic pores (○), hydrophobic pores (■), and hydrophobic pores with a correction for the change in pore diameter after surface modification (□). The solid line is a guide for the eye.

Conclusions

We have studied the collective orientational relaxation of water confined in hydrophobic and hydrophilic nanopores at room temperature. In agreement with previous simulations, the orientational relaxation at hydrophobic surfaces is significantly faster than that at hydrophilic surfaces. However, the relaxation in the pore centers depends only on the pore size, and not on the chemical nature of the pore surfaces. These results imply that hydrophobic surfaces do not impart any long-range order to water, and so the long-range attractive interactions cannot be due to such ordering. Our data also have interesting implications for the understanding of the role of water in the structure and dynamics of biological systems. Future studies will examine the role of temperature and ionic solutes on the orientational dynamics of confined water.

Acknowledgments

References

1.   *Water: A Comprehensive Treatise*; Franks, F., Ed.; Plenum Press: New York, 1972; Vol. 1.
2.   Conway, B. E. *Ionic Hydration in Chemistry and Biophysics*; Elsevier: Amsterdam, 1981.
3.   Lee, C. Y.; McCammon, J. A.; Rossky, P. J. *J. Chem. Phys.* **1984**, *80*, 4448-4455.
4.   Lee, S. H.; Rossky, P. J. *J. Chem. Phys.* **1994**, *100*, 3334-3345.
5.   Nandi, N.; Bhattacharyya, K.; Bagchi, B. *Chem. Rev.* **2000**, *100*, 2013-2045.
6.   Bhattacharyya, K.; Bagchi, B. *J. Phys. Chem. A* **2000**, *104*, 10603-10613.
7.   Raviv, U.; Laurat, P.; Klein, J. *Nature* **2001**, *413*, 51-54.
8.   Pashley, R. M.; McGuiggan, P. M.; Ninham, B. W.; Evans, D. F. *Science* **1985**, *229*, 1088-1089.
9.   Zhang, X. Y.; Zhu, Y. X.; Granick, S. *Science* **2002**, *295*, 663-666.
10. Lum, K.; Chandler, D.; Weeks, J. D. *J. Phys. Chem. B* **1999**, *103*, 4570-4577.
11. Brinker, C. J.; Scherer, G. W. *Sol-Gel Science: The Physics and Chemistry of Sol-Gel Processing*; Academic Press: San Diego, CA, 1990.
12. Hodgson, C.; McIntosh, R. *Can. J. Chem.* **1960**, *38*, 958-971.
13. Swenson, J.; Bergman, R.; Longeville, S. *J. Chem. Phys.* **2001**, *115*, 11299-11305.
14. Fouzri, A.; Dorbez-Sridi, R.; Oumezzine, M. *J. Chem. Phys.* **2002**, *116*, 791-797.
15. Boyd, J. E.; Briskman, A.; Colvin, V. L.; Mittleman, D. M. *Phys. Rev. Lett.* **2001**, *8714*, art. no.-147401.
16. Venables, D. S.; Huang, K.; Schmuttenmaer, C. A. *J. Phys. Chem. B* **2001**, *105*, 9132-9138.
17. Venturini, F.; Gallo, P.; Ricci, M. A.; Bizzarri, A. R.; Cannistraro, S. *J. Chem. Phys.* **2001**, *114*, 10010-10014.
18. Akporiaye, D.; Hansen, E. W.; Schmidt, R.; Stocker, M. *J. Phys. Chem.* **1994**, *98*, 1926-1928.
19. Bellissent-Funel, M. C. *J. Phys.-Condes. Matter* **2001**, *13*, 9165-9177.
20. Gallo, P.; Ricci, M. A.; Rovere, M. *J. Chem. Phys.* **2002**, *116*, 342-346.

21. Scodinu, A.; Fourkas, J. T. *J. Phys. Chem.B* **2002**, *106,* 10292-10295.
22. Righini, R. *Science* **1993**, *262*, 1386-1390.
23. McMorrow, D.; Lotshaw, W. T. *J. Phys. Chem.* **1991**, *95*, 10395-10406.
24. Loughnane, B. J.; Farrer, R. A.; Scodinu, A.; Reilly, T.; Fourkas, J. T. *J. Phys. Chem. B* **2000**, *104*, 5421-5429.
25. Loughnane, B. J.; Scodinu, A.; Fourkas, J. T. *J. Phys. Chem. B* **1999**, *103*, 6061-6068.
26. Majors, R. E.; Hopper, M. J. *J. Chromat. Sci.* **1974**, *12*, 767.
27. Chang, Y. J.; Castner Jr., E. W. *J. Chem. Phys.* **1993**, *99*, 7289-7299.
28. Palese, S.; Mukamel, S.; Miller, R. J. D.; Lotshaw, W. T. *J. Phys. Chem.* **1996**, *100*, 10380-10388.
29. Winkler, K.; Lindner, J.; Bursing, H.; Vohringer, P. *J. Chem. Phys.* **2000**, *113*, 4674-4682.
30. Potma, E. O.; de Boeij, W. P.; Wiersma, D. A. *Biophys. J.* **2001**, *80*, 3019-3024.
31. Dhar, L.; Rogers, J. A.; Nelson, K. A. *Chem. Rev.* **1994**, *94*, 157-193.

Theory of Unimolecular Reactions in Confined Volumes

B. C. Hathorn, B. G. Sumpter, and D. W. Noid

Computer Science and Mathematics Division, Oak Ridge National Laboratory, Oak Ridge, TN 37831

A theory for treatment of reaction kinetics in confined spaces is developed using Transition State Theory as a guide. The technique employs modifying the partition functions for the reactant and transition state based on the geometric restrictions posed by the confining medium. The result of the calculation is a term which corresponds to an effective excluded volume for the reactants and transition state. Models for calculation of the restriction factor are proposed within two limiting cases which correspond to a "spherical" molecule and a "linear" molecule, where it is assumed that the potential can be treated as separable. The two limiting cases are related to possible reaction mechanisms.

Introduction

Recently, there has been much interest in the progress of reactions under novel experimental conditions. A particular example of this is a reaction which occurs in a nanostructure, for example the unimolecular decomposition of a hydrocarbon chain which is enclosed in a restricted volume, or a reaction which occurs inside a zeolite crystal. The *a priori* prediction of the enhancement or retardation of the reaction rate can be used to stimulate the design of additional experimental systems with desirable chemical reactivity. Although the reaction rate can be affected by a number of influences, such as charge stabilization of intermediates or restriction of free diffusion in bimolecular reactions, we concentrate in the present paper on the influence of steric effects posed by the reaction vessel.

Unimolecular reaction rate theories are now widely developed and in general use throughout the chemical kinetics community. The most straightforward to apply in the case of a reaction carried out under thermal conditions is Transition State Theory.[1, 2] In the context of this theory, the reaction rate can be calculated in terms of partition functions of the reactants and the transition state, both of which can be estimated from thermodynamic considerations. Herein, we propose a simple model which serves as an extension of the ideas of the theory to reaction regions which are geometrically confined. As construed, the present theory has one additional benefit: the reaction enhancement or retardation is obtained from scaling factors applied to the partition functions, so the absolute values of these quantities are not required to obtain the relative rates for the confined and unconfined systems. The largest uncertainty in transition state theory typically arises from the estimation of the transition state parameters which control the absolute rates. In the present case, where we are interested in the relative effects, the absolute rates are less important and such uncertainties in the absolute rates can be avoided.

In general, statistical theories for reaction rate constant have proved accurate, within the uncertainties of the potential surface employed.[2, 3, 4] We use these theories as a point of departure into the present investigation of a comparison of reaction rates for a reaction which occurs in a confined volume to that which is calculated for a free reaction in the gas phase. The applications of the present theory are numerous, however in the present case we restrict ourselves to a single example: a unimolecular reaction which occurs inside a cylindrical carbon nanotube.

In the following section we present a brief outline of methods for estimating the necessary quantities required for calculation of the relative rates as a function of the constraining field. In the Results and Discussion section we obtain results for some simple systems and discuss the results. In the analysis of the examples, we have applied the theory to a simple case of particular interest, where the reaction is confined to a small cylindrical cell (e.g., a carbon nanotube), however, the application of the method is general, and could similarly be applied to reaction cells of arbitrary shape.

Theory

In order to simplify the treatment here, we will concern ourselves only with the *relative* enhancement or retardation of the reaction rate, that is, we will only concern ourselves with the ratio of the rate in the restricted space to that of the free system in the unbound system (or in the consideration of branching ratios below, the ratio of two systems which are geometrically confined, but which have multiple transition states leading to different products).

The ratio of reaction rates is written in terms of standard rate constants as

$$Z = \frac{k_{\text{restricted}}}{k_{\text{free}}}. \tag{1}$$

The individual rate constants are given by the standard transition state theory expression[1, 2]

$$k_{\text{TST}} = \frac{k_B T}{h} \frac{Q^\dagger}{Q}, \tag{2}$$

where T is the absolute temperature, k_B and h are the Boltzmann and Planck constants, and Q and $Q^\dagger$ are the partition functions for the reactants and transition state, respectively. The main difference between Q and $Q^\dagger$ is that the latter lacks a degree of freedom corresponding to the reaction coordinate.

In the context of the expression for the ratio in (1) above, we have, upon application of Eq. (2),

$$Z = \left(\frac{Q^\dagger_{\text{restricted}}}{Q^\dagger_{\text{free}}} \right) \left(\frac{Q_{\text{free}}}{Q_{\text{restricted}}} \right). \tag{3}$$

The two principle quantities which must be obtained to determine the overall effect on the rate constant are the ratios of the restricted and unrestricted partition functions for both the transition state and the reactants.

We now seek to evaluate the partition functions for the different cases, and seek to do so in the classical sense. The classical canonical partition functions (in the present case, we need not distinguish between the transition state and reactant partition functions) are given by[5, 6]

$$Q = h^{-N} \int \int e^{-H(\mathbf{q},\mathbf{p})/k_B T} d\mathbf{q} d\mathbf{p}. \tag{4}$$

Here, h is Planck's constant, k_B is Boltzmann's constant, T is the absolute temperature, $H(\mathbf{q}, \mathbf{p})$ is the Hamiltonian of the system, with N coordinates $\mathbf{q}$ and momenta $\mathbf{p}$. With the intent of discussing partition functions of molecules, we establish a set of coordinates for motion of the center of mass, X, Y, and Z, and a set of coordinates which describe the orientation of the molecule, θ and ϕ. The remaining coordinates describe the internal vibrational motion of the molecule in the present case we assume that the motion is harmonic and described in terms of a set of normal coordinates, η.

For a non-linear molecule in free space, with no interactions with other species, the usual approximation is to separate the Hamiltonian into a series of non-interacting sub-Hamiltonians which describe independent motions,[5, 6]

$$H(\mathbf{q}, \mathbf{p}) = H_{\text{trans}}(X, Y, Z) + H_{\text{rot}}(\theta, \phi, \psi) + H_{\text{vib}}(\eta), \tag{5}$$

where H_{trans}, H_{rot} and H_{vib} are Hamiltonians which describe the translational, rotational and vibrational motion, respectively. The case of the linear molecule has one fewer degrees of rotational freedom, and the coordinate ψ is absent. The integral over the sets of coordinates and momenta are now independent, and the total partition function is now represented as a product of partition functions,[5, 6]

$$Q = Q_{\text{trans}} Q_{\text{rot}} Q_{\text{vib}} \tag{6}$$

with each of the individual partition functions given by Eq. (4) with the appropriate individual Hamiltonian.

The case of the restricted system is somewhat more complicated, as the presence of the geometric boundary couples the various sub-Hamiltonians in Eq. (5), adding additional terms into the Hamiltonians for the vibrational and rotational motion which depend on the orientation of the molecule and the position of the molecule within the reaction volume,

$$
\begin{aligned}
H(\mathbf{q}, \mathbf{p}) \;=\; & H_{\text{trans}}(X, Y, Z) + H_{\text{rot}}(\theta, \phi, \psi) + H_{\text{t}-\text{r}}(\theta, \phi, \psi, X, Y, Z) \\
& + H_{\text{vib}}(\eta) + H_{\text{t}-\text{v}}(\eta, X, Y, Z),
\end{aligned}
\tag{7}
$$

where $H_{\text{t}-\text{r}}$ and $H_{\text{t}-\text{v}}$ represent the Hamiltonians for the translation-rotation and translation-vibration interactions, respectively. If the geometric confinement is that of an infinite barrier, the interaction terms between the translations and rotations and the translations and vibrations require that the potential becomes infinite if any portion of the molecule (or in the approximation treated below, any portion of the molecule in one vibrational period) extends beyond the geometrically allowed region.

For simplicity, we make an approximation that the molecule can be represented by a shape in space with boundary which corresponds to the maximum displacements in any vibrational period. In this case, the vibrations decouple from the rotations and translations, and the vibrational partition function can be evaluated exactly. The expression corresponding to Eq. (6) is now

$$
Q = Q_{\text{trans}-\text{rot}} Q_{\text{vib}}
\tag{8}
$$

with $Q_{\text{trans}-\text{rot}}$ corresponding to the partition function with a Hamiltonian given by the first three terms of Eq. (7). In particular, we notice that the ratio of vibrational partition functions for the restricted and unrestricted case is unity in this approximation.

Inspection of the integral arising from Eq. (7) and (5) indicates that the momentum component of the translational partition function integral is identical in the two cases, and is independent of the other coordinates. As a result, this factor cancels in the ratio, and the ratios of the restricted and unrestricted cases are expressed as

$$
\frac{Q_{\text{rest}}}{Q_{\text{free}}} = \frac{\int F(X, Y, Z, \theta, \phi, \psi) e^{H/k_B T} dX dY dZ d\phi d\theta d\psi dp_\phi dp_\theta dp_\psi}{\int e^{H/k_B T} dX dY dZ d\phi d\theta d\psi dp_\phi dp_\theta dp_\psi},
\tag{9}
$$

where the F function is unity when the molecule is completely inside the cavity, and zero otherwise. H is given by the translational and rotational Hamiltonians with no coupling, as the interactions are accounted for in the function F. In the case of a linear system, there is one fewer degree of freedom, and the coordinate ψ and its conjugate momentum are absent. The integral in the denominator is the product of a translational and a rotational partition function.

We now proceed to find a functional form for F and evaluate the integrals in two limiting cases, the case of a spherical molecule, and a linear molecule,

both inside a carbon nanotube, which has been idealized as a cylinder with a radius R_c. While these two extremes are convenient for the evaluation of the integrals involved, we note that most real molecules will fall somewhere between these two extremes. In the cases below, we will take the approach of evaluating the rotation-translation partition function, and calculating the restriction in terms of the ratio of the restricted rotation-translation partition function to the unrestricted case. Since we are not interested in absolute rate constants, but rather relative rate constants, a number of factors arising from the integration over the momenta which appear in the ratio of partition functions cancel, and we are left with easily calculable scaling factors which depend only on the geometry. Examples of the calculation of this geometric factor in the spherical molecule and linear molecule limits are outlined below.

Spherical Molecule

The initial approximation we make in the spherical molecule is that the rotational Hamiltonian is a spherical top, with a Hamiltonian given by

$$H_{\text{rot}} = \frac{1}{2I} \left[p_\psi^2 + p_\theta^2 + \frac{(p_\psi - \cos\theta p_\psi)}{\sin^2\theta} \right] \tag{10}$$

where I is the moment of inertia of the spherical top. The function F in the integral appearing in Eq. (9) is independent of the orientation of the spherical molecule, and is only dependent on the position of the center of mass of the molecule, the size of the molecule, and the size of the nanotube. In this case, the rotational partition functions cancel, and we are left with the ratio of the translational partition functions,

$$\frac{Q_{\text{rest}}}{Q_{\text{free}}} = \frac{\int_0^{R_c - R_m} \int_0^{2\pi} R dR d\Theta dZ}{\int_0^{R_c} \int_0^{2\pi} R dR d\Theta dZ} \tag{11}$$

where we have made the appropriate conversion to cylindrical coordinates, and where R_c is the radius of the nanotube, and R_m is the radius of the molecule. The ratio is now the ratio of the restricted volume to the volume of the cylinder, given by

$$\frac{Q_{\text{rest}}}{Q_{\text{free}}} = (1 - \xi)^2, \tag{12}$$

where $\xi = R_m/R_c$ is a dimensionless parameter. The value of ξ in this case must be less than unity, with the ratio vanishing for $\xi > 1$.

Linear Molecule

As previously noted, a linear molecule has a reduced number of rotational degrees of freedom, due to the absence of the term corresponding to rotation about the molecular axis. In this case, the rotational Hamiltonian is given by

$$H = \frac{1}{2I} \left(p_\theta^2 + \frac{p_\phi}{\sin^2\theta} \right). \tag{13}$$

In the case of the restricted rotor, there are limits on the coordinates (but not the momenta) of the rotor which depend on the proximity of the molecule to the wall. We work here in the approximation that the center of mass is near the center of the molecule, a distance of R_m from the end. The present treatment can easily be extended to the case where the center of mass is displaced from the end of the molecule, and there are two different distances to the molecular ends, R_m and R'_m.

Returning again to cylindrical coordinates for the position of the molecule within the nanotube, we have, when the integrals over the translational momenta have been carried out,

$$Q_{\text{rest}} = C \int_0^{R_c} \int_0^{2\pi} \int_0^{\pi} \int_0^{2\pi} \int_{-\infty}^{\infty} F(R, \theta, \phi) \exp\left[-\frac{1}{2k_B T I} \left(p_\theta^2 + \frac{p_\phi}{\sin^2 \theta} \right) \right]$$
$$dp_\theta dp_\phi d\theta d\phi d\Theta dR$$
(14)

where C is a constant which includes the terms associated to the integration over the translational momentum. The imposition of the geometric constraints associated with the boundary lead to the condition

$$F(R, \theta, \phi) = \begin{cases} 1 & R^2 + 2R_m R \cos \theta \sin \phi + R_m^2 \sin^2 \phi < R_c^2 \\ 0 & R^2 + 2R_m R \cos \theta \sin \phi + R_m^2 \sin^2 \phi \geq R_c^2 \end{cases}$$
(15)

The integrals over the momenta can still be carried out analytically, leading to the ratio of restricted and unrestricted partition functions, in terms of integrals over the coordinates alone,

$$\frac{Q_{\text{rest}}}{Q_{\text{free}}} = \frac{\int_0^{R_c} \int_0^{2\pi} \int_0^{\pi} F(R, \theta, \phi) \sin \theta d\theta d\phi dR}{\int_0^{R_c} \int_0^{2\pi} \int_0^{\pi} \sin \theta d\theta d\phi dR}.$$
(16)

The integrals can be recast in terms of the dimensionless parameter, $x = R/R_c$ in which case we now have

$$\frac{Q_{\text{rest}}}{Q_{\text{free}}} = \frac{\int_0^1 \int_0^{2\pi} \int_0^{\pi} F(x, \theta, \phi) \sin \theta d\theta d\phi dx}{\int_0^1 \int_0^{2\pi} \int_0^{\pi} \sin \theta d\theta d\phi dx}$$
(17)

with the new restriction

$$F(x, \theta, \phi) = \begin{cases} 1 & x^2 + 2\xi x \cos \theta \sin \phi + \xi^2 \sin^2 \phi < 1 \\ 0 & x^2 + 2\xi x \cos \theta \sin \phi + \xi^2 \sin^2 \phi \geq 1 \end{cases}$$
(18)

where we have introduced the parameter $\xi = R_m/R_c$, which depends only on the ratio of the size of the molecule to the size of the cylinder. We note that, due to the assumption of the center of mass being located in the exact center of the molecule, the restriction function F is symmetric with respect to the transformation $\theta' = \theta + \pi$, and thus, the integral need only be carried out over half of the total range, and thus the integral is only evaluated for $\cos \theta \geq 0$. The

range $\cos\theta \leq 0$ corresponds to the interaction of the opposite end of the molecule with the cylinder, and is identical. In the event that the center of mass is not at the center of the molecule, there would be two slightly different restriction functions which define the interaction of the two ends of the molecule with the cylinder, which could be composed as a product of two restriction functions, $F = F_1 F_2$, where F_1 and F_2 are restriction functions for the two ends.

We find, in this simple case that the ratio of partition functions depends only on the parameter ξ, albeit in a more complex manner than in the case of a spherical molecule. For the present purposes, we find that the most convenient evaluation of the ratio $Q_{\text{rest}}/Q_{\text{free}}$ as a function of ξ is performed *via* a numerical integration.

Results and Discussion

The formulas obtained for the restricted partition functions obtained here are quite straightforward to apply. We note, however, several limitations based on approximations in the present treatment. In effect, we have only treated the translational and rotational motion, and have avoided the vibrational motion. We have made this approximation under the assumption that vibrations do not produce large displacements from the equilibrium position, and that the molecular geometry is defined by the "largest displacement" over a full vibrational cycle. An additional benefit of this treatment is that the reactant and transition states can be treated in an identical fashion. This approximation will certainly fail in the event that there are large amplitude displacements, and in this case, the vibrations need to be treated explicitly. We have also treated the walls of the nanotube as hard boundaries, however, there is likely to be some kind of interaction between the molecule and the walls. We have neglected such effects in the present case, preferring to instead, concentrate on the purely steric effects of the interaction. The rotation-translation configuration integrals we have obtained are all in the limit of classical partition functions, which require that the spacing between the energy levels are small. This is likely to be the case for all rotations except those which have the molecule very near to the wall, and thus have a strong vibrational character. On the other hand, these configurations make up a small part of the total phase space, particularly at modest values of ξ. For translations, the classical treatment is well-founded, since the separations between quantum states are very small for species with masses on the order of amu and for length scales appropriate to carbon nanotubes (nanometers).

In the present theory, we have treated the reaction as a gas phase reaction in a solid state system. The precedent for such a treatment is well-founded, with applications in both diffusion and surface reactions.[2] In the present case, however, we have adopted an additional restriction, where the geometric boundary is "reflective" and constrains the access to the transition state. Such a treatment is similar to that in liquid state systems where solvent molecules induce recrossings of the transition state surface.[2]

The results for the ratios of the restricted and unrestricted partition func-
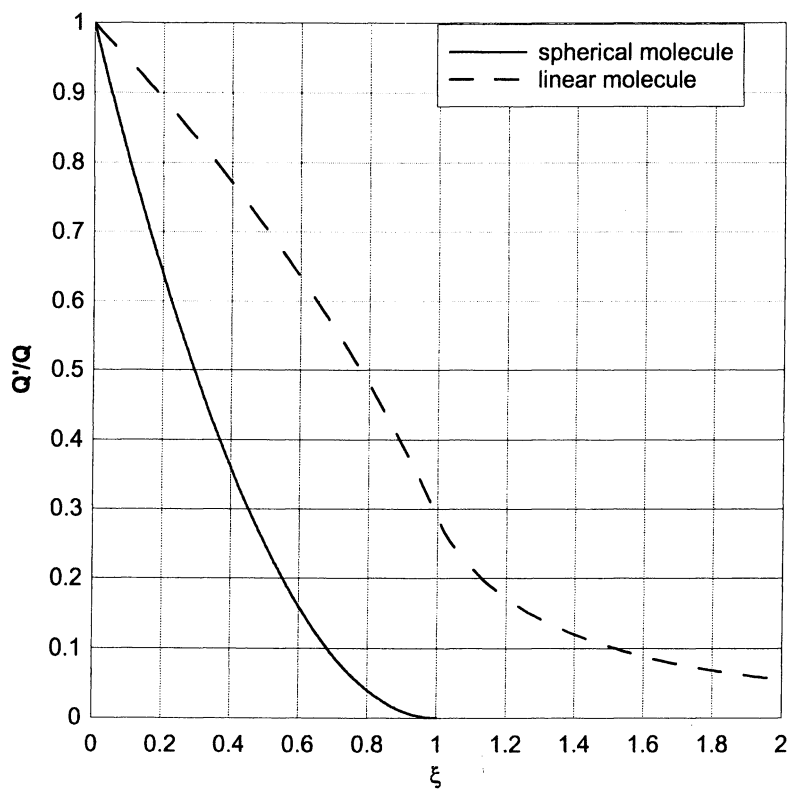
Figure 1: Ratio of restricted and unrestricted partition functions as a function of the dimensionless parameter $\xi = R_m/R_c$.

tions are given in Figure 1, as a function of the dimensionless parameter $\xi = R_m/R_c$. It is immediately observed that the imposition of the boundary condition poses a significantly greater restriction on the spherical molecule than the linear one. The point at which the partition function is reduced by 50% in the linear case is approximately $\xi = 0.75$, whereas the spherical molecule experiences such a reduction at $\xi = (2 - \sqrt{2})/2 \approx 0.29$. In the case of linear molecules, they can be present in the nanotube when $\xi > 1$, although there is significant restriction in the partition function, as the only allowed configurations are those where the molecule is aligned with the cylinder. In the case of spherical molecules, cases with $\xi > 1$ are explicitly disallowed.

We now discuss the application of the results for the ratio of restricted and unrestricted reaction rates, Eq. (3). A determination of the approximate structure of the molecule and transition state, either an extended bond for the case of a molecular fragmentation, or a more spherical molecular shape for an isomerization reaction indicates which of the two cases in Figure 1 is more appropriate. We know that, in general for a fragmentation process, the effective bond lengths are increased, and the result is that the transition state will lie at a value larger than that of the molecule, $\xi_{\text{TS}} > \xi_{\text{react}}$. Consequently, we expect the reaction rate constant to be smaller in the restricted than in the unrestricted case.

For the case of an isomerization reaction, such as a ring closure, we expect the transition state for the typical reaction to have a smaller size than the original molecule, $\xi_{\text{TS}} < \xi_{\text{react}}$ and the reaction will likely be faster. Such an increase of rate neglects, possible effects such as the introduction of new "geometric" transition states, resulting from steric effects, higher in energy, which prevent the molecule from reaching the normal transition state in the gas phase.

The simple model here does, however, open avenues for discussion of several effect which are normally restricted to high pressure chemistry. The usual thermodynamic relationship between the excluded volume and the rate is[7]

$$-RT\frac{\partial k}{\partial p} = \Delta V^\dagger, \tag{19}$$

where p is the pressure and $\Delta V^\dagger$ is the change in volume between the reactants and the transition state. The most notable application of this relationship has been in the investigation of mechanisms and transition state structures for chemical reactions, in particular Diels-Alder type reactions.[7] The present theory shows that it is possible to probe the excluded volume in a chemical reaction without performing the reactions at high pressures, as the presence of the nanotube should serve the same effect of the excluded volume at high pressures.

A second area worth investigating using the present model is the possibility of control of the products of a chemical reaction. In the case where a reactant can form two possible products, the branching ratio will be controlled both by the energetics of the reactions, but also by the effective size of the transition states. It may be possible to construct systems where a reaction which is energetically less favorable dominates because it has a transition state with substantially

smaller volume. The present formulas indicate how systems can be tuned to take advantage of the size of a reaction vessel to promote specific reaction pathways.

We note as well a correlation between the present model, and what would be expected for a microcanonical, RRKM-theory calculation of the reaction rate for a fixed energy. The RRKM expression for the reaction rate is given by[3, 4, 8, 9, 10, 11, 12]

$$k(E) = \frac{N^\dagger(E)}{h\rho(E)} \tag{20}$$

where $N^\dagger(E)$ is the sum of states of the transition state and ρ the density of states of the reactant. The usual method of obtaining these quantities is through either a classical evaluation or a direct count of the associated rotational and vibrational states.[3, 4, 8, 9] In the present case, however, we can utilize the Laplace transform relationship between the quantities,

$$(k_B T)Q^\dagger = \int_0^\infty N^\dagger(E)e^{-E/k_B T}dE \tag{21}$$

$$Q = \int_0^\infty \rho(E)e^{-E/k_B T}dE. \tag{22}$$

The densities and sums of states can thus be obtained by taking the inverse Laplace transform of the partition functions.[3] In the present case, we have obtained the restricted rotation-translation partition function as a multiple of the free translation-rotation partition function. As the Inverse Laplace transform is a linear operator, we find that the translational-rotational density of states contains the same numerical factor as the partition functions. The influence of vibrations can then be handled with a subsequent convolution integral[3, 4, 8, 9] to obtain an approximate sum or density of states to be used in the microcanonical theory. Such a treatment, however, would be limited to the cases of reactions with well-defined transition states. It is well known that for dissociation reactions on a barrierless potential surface, the transition state tightens and moves inward to smaller distances as the energy increases.[11]

In the present illustration, we have treated the molecule and the transition state region as being approximately spherical or approximately linear. One could, if suitable parameters were available, do an exact calculation of the rotational-translational partition function for a real molecular system using numerical techniques. In this case, one would use a asymmetric top Hamiltonian in Eq. (9) and a restriction function F governed by the true molecular dimensions. Alternatively, one could find the restricted phase space density for the microcanonical directly, using monte carlo integration techniques.[10] Such a direct evaluation of the phase space is beyond the scope of the present work, but we expect to return to it in future work.

Acknowledgments

References

[1] Glasstone S.; Laidler K.J.; Eyring H. *The Theory of Molecular Rate Processes*; McGraw-Hill: New York, 1941, and references therein.

[2] Truhlar, D.G.; Garrett, B.C.; Klippenstein, S.J. *J. Phys. Chem.* **1996**, *100*, 12771, and references cited therein.

[3] Gilbert, R.G.; Smith, S.C. *Theory of Unimolecular and Recombination Reactions*; Blackwell Scientific Publications: Boston, 1990, and references cited therein.

[4] T. Baer; W.L. Hase, *Unimolecular Reaction Dynamics, Theory and Experiment*; Oxford University Press: New York, 1996, and references therein.

[5] D.A. McQuarrie, *Statistical Mechanics*; Harper & Row: New York, 1976, and references cited therein.

[6] Hill, T.L. *An Introduction to Statistical Thermodynamics*; Dover Publications: New York, 1986.

[7] See, for example, K.E. Weale, *Chemical Reactions at High Pressures*; E. & F. N. Spon Ltd.: London, 1967, and references therein.

[8] P.J. Robinson; K.A. Holbrook, *Unimolecular Reactions*; Wiley-Interscience: London, 1972, and references therein.

[9] W. Forst, *Theory of Unimolecular Reactions*; Academic Press: New York, 1973, and references therein.

[10] D.M. Wardlaw; R.A. Marcus. *Adv. Chem. Phys.* **1988**, *70*, 231, and references therein.

[11] S.J. Klippenstein, in K. Liu and A. Wagner (eds), *The Chemical Dynamics and Kinetics of Small Radicals*, Part I; World Scientific: Singapore, 1995, and references therein.

[12] W.H. Green Jr., C.B. Moore, and W.F. Polik, *Ann. Rev. Phys. Chem.* **1992**, *43*, 591, and references therein.
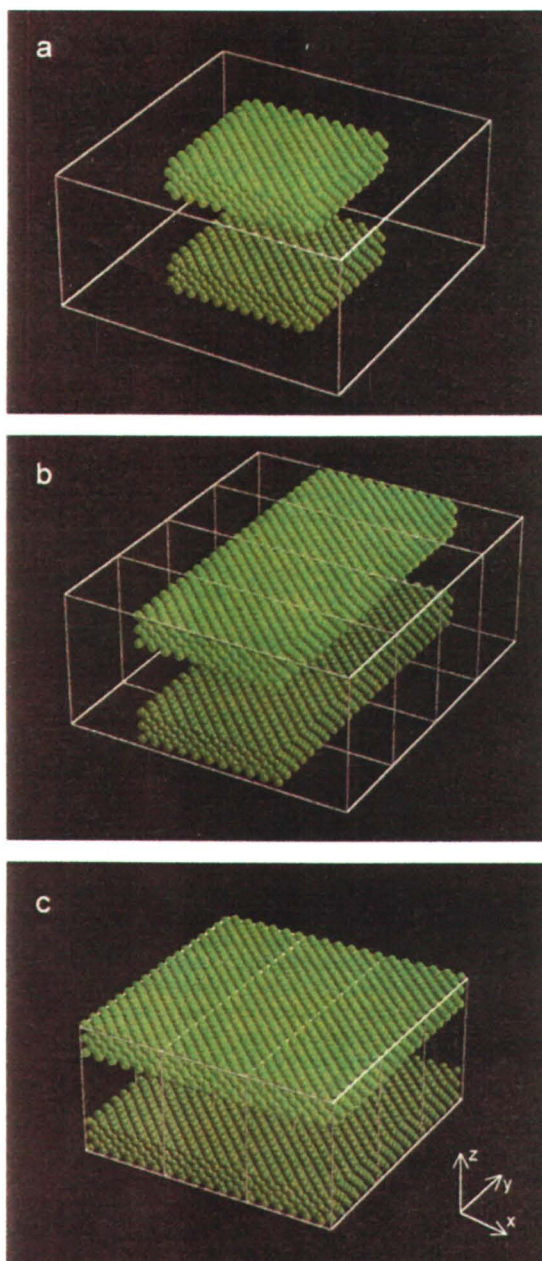
Figure 8. Schematic of the (a) nanoplatelet, (b) nanowire, and (c) infinite slit pore systems. The solid atoms are shown as spheres, and the solid white lines outline the simulation cell. The infinite slit pore is finite in the z direction only, the nanowires are finite in both the x and z directions, and the platelets are finite in all directions. Adapted from Stroud et al. (2001).
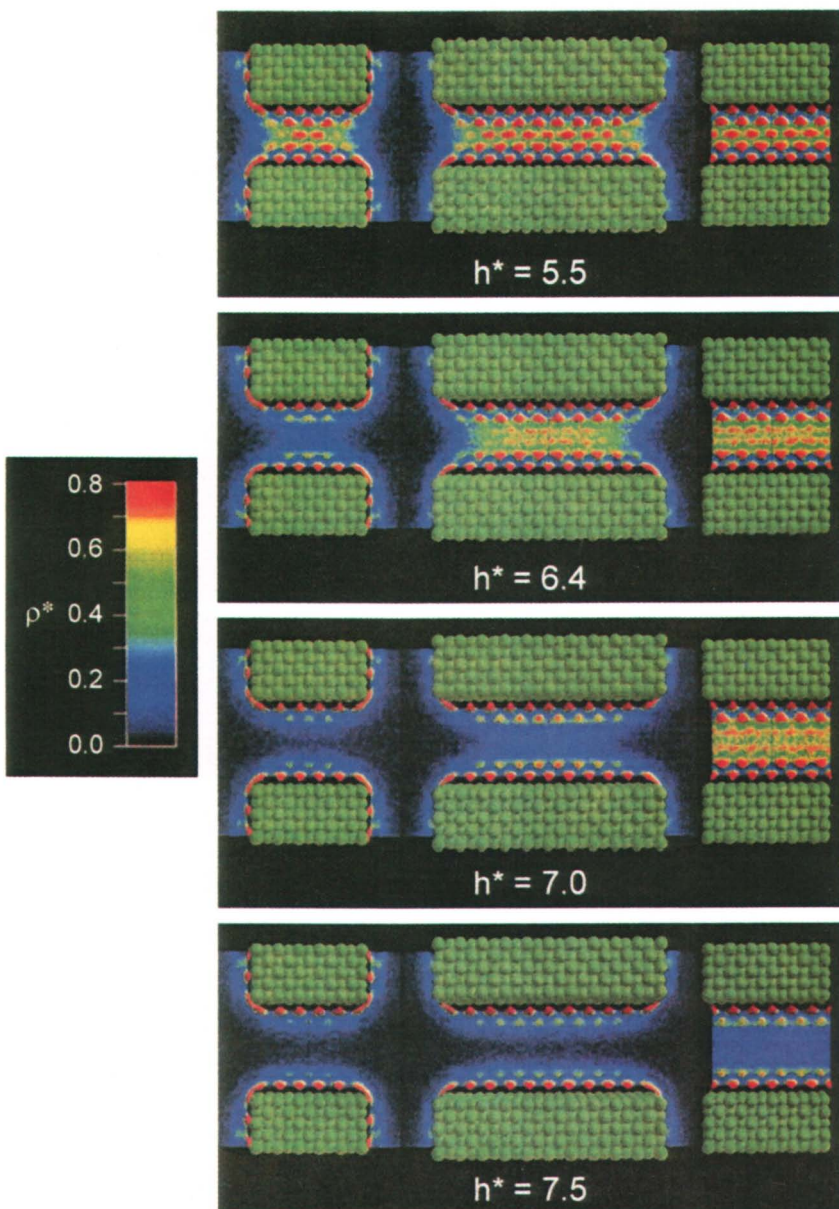
Figure 9. As for Figure 3 but for (from left to right) a 5-wire, 10-wire, and ∞-slit pore at h^8 = 5.5, 6.4, 7.0, and 7.5. Adapted from Stroud et al. (2001).
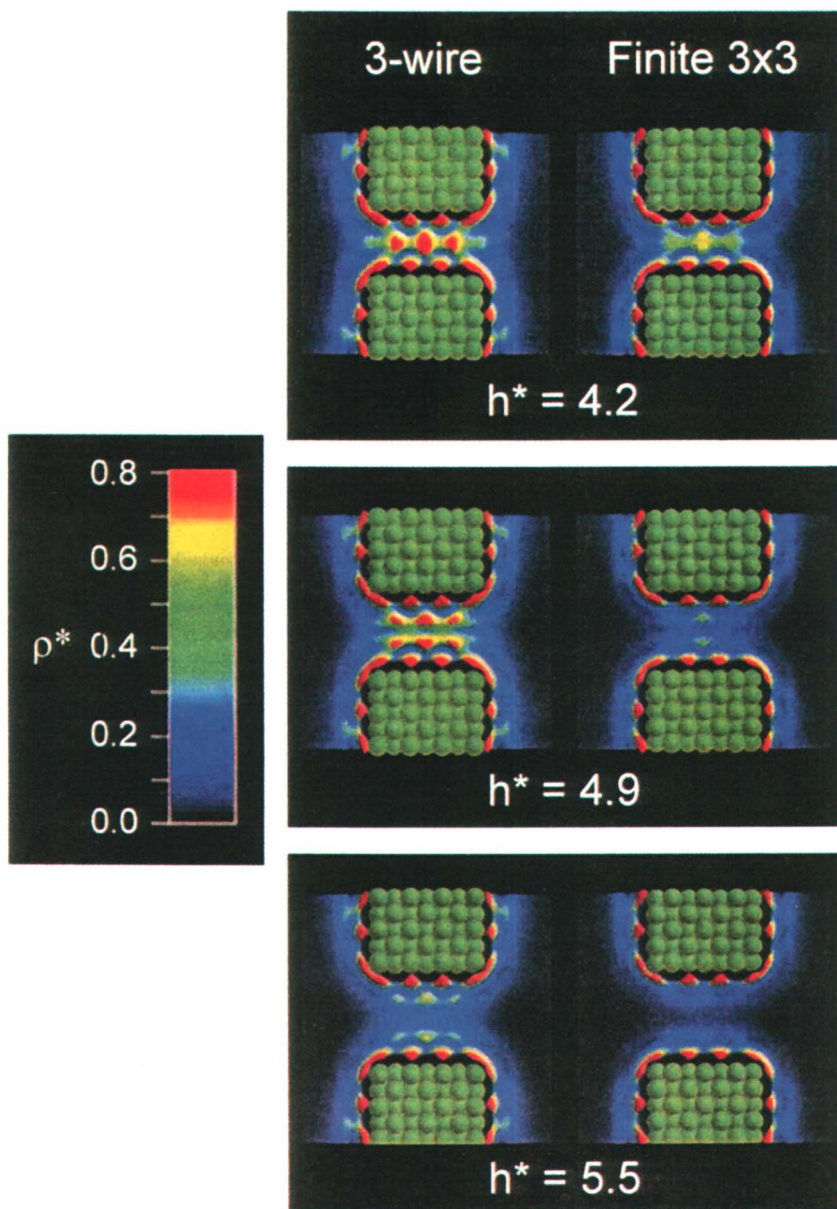
Figure 10. Maps of two-dimensional slices through the three-dimensional, ensemble-average particle density of the fluid condensed between nanowires three unit cells wide (left, slice taken at y = 0.0) and finite platelets with dimensions three unit cells in both the x and y directions (right, slice taken across the center of the contact at y = 0.5) for $\mu^* = -11.7$, $T^* = 1.0$, $\alpha = 0.0$, and $h^* = 4.2$, 4.9, and 5.6. Adapted from Stroud et al. (2001).

Author Index

Subject Index

A

Acid solutions. *See* Ultra thin liquid films

Adhesion
dynamic response of complexes, 37
microscopic parameters of adhesive potential, 38–39
probing mechanical forces, 29
progress, 2
See also Dynamic force spectroscopy (DFS)

Adsorption, equilibrium conditions, 3

Alcohols. *See* Liquids

Algorithms
conformal map, 89–90
controlling friction of sliding nano-arrays, 51
non-Lipschitzian control, 42, 43, 48
terminal attractor, 42
testing proposed, 51
See also Non-Lipschitzian control of friction

Alkanes
dynamic viscosity by simulation and experiment, 142, 143*f*
See also Isoparaffins

Amplitude
quartz crystal microbalance (QCM), 4
tricresylphosphate (TCP), 6*f*, 9*f*

Anomalous diffusion, confined fluids in slit pore, 162, 166*f*, 167*f*

Asphericity parameter, equation, 153

B

Barus equation
parameters for decane isomers, 150*t*
viscosity, 146

Bearings, classical simulations, 102–106

Behavior. *See* Fluid behavior in restricted geometries

Binding forces, quartz crystal microbalance (QCM), 3

Bottlenecks, liquid flow among pores, 191

Boundary lubricants
commensurate walls, 59–61
critical point, 60
effect of higher harmonics, 60–61
incommensurate walls, 62
Morse theory, 60
See also Instabilities in boundary lubricants

Bulk water. *See* Water

t-Butyl phenyl phosphate (TBPP)
lubricated contact, 10, 13–15
See also Tertiary-butyl phenyl phosphate (TBPP)

C

Capillary condensation, particle size and shape, 174, 177*f*, 178*f*, 179*f*

Charge transfer, apparatus for measurement, 26

Classical simulations
bearings and motors, 102–106
drag coefficients showing size, velocity, and temperature

220

O

Octane
  viscosity of isomers of, 144, 145*f*
  See also Isoparaffins
Octanol
  drainage and viscous properties,
    123–124, 127
  sum frequency generation, 125*f*
  See also Liquids
Oils
  structure-property relationships, 140
  See also Isoparaffins
Optical Kerr effect (OKE)
    spectroscopy
  bulk water, 197*f*, 198*f*
  confined water, 195
  See also Water
Orientational autocorrelation function,
    decane isomers, 151, 152*f*
Ornstein–Uhlenbeck equation, fitting
    results to, 37

P

Paraffins. *See* Isoparaffins
Partition functions
  ratios of restricted and unrestricted,
    211, 212*f*, 213
  rotational-translational, for real
    molecular system, 214
  unimolecular reactions, 207–208
Perfluoropolyethers
  drainage, 127–129
  force to drain lubricants, 128*f*
  time evolution of gap separation,
    128, 129*f*
  viscosity, 128–129
Performance, motors, 99
Phase diagram, confining surfaces,
  158
Phenomena, interfaces, 159
Phenomenological models, control
    strategy, 42–43

Physical properties, extraction from
    mapping, 90–91
Pinning
  cluster growth in presence of noise,
    93*f*
  influence of noise on depinning, 94–
    95
  interface of cluster, 91
  model for time development of, 86–
    87
  scaling of radius and size with yield
    stress, 92*f*
  Sher–Turkovitch identity, 92
  transition in laplacian growth, 91–94
  two clusters grown with different
    yield stress, 93*f*
  yield stress, 91
  See also Stick slip laplacian flow
Platinum surface, *t*-butyl phenyl
    phosphate-lubricated, 13–14
Poly(methyl methacrylate) (PMMA)
  force and charge curves collapsing to
    one curve, 23*f*
  friction and charge exchange
    between gold and, 22*f*
  friction between metal and dielectric,
    21–23
Pores. *See* Water
Porous glasses. *See* Supercooled
    liquids in porous glasses
Potentials
  differing strengths, 83–84
  minimum becoming unstable, 82*f*
  See also Dry friction
Power-law, relaxation, 200–201
Prandtl Tomlinson (PT) model
  equation of motion, 57
  motion of atom, 57
  solid friction instability, 56
  thermal effects, 59
  time evolution of potential energy,
    58*f*
  time evolution of trajectories, 58
4-*n*-Propylheptane, viscosity vs.
    temperature, 146, 148*f*